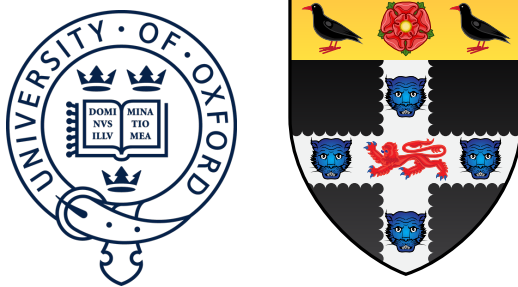


Measurement of Oscillations in Solar Boron-8 Neutrinos and Studies of Optical Scattering in the SNO+ Detector



Daniel Cookman

Christ Church College

University of Oxford

A thesis submitted for the degree of

Doctor of Philosophy

Trinity Term 2023

To my parents

and

To Oscar Jacobsson:

The best of us

Acknowledgements

And I would like to acknowledge ...

Abstract

Formal 1-page summary of the work completed in the thesis.

Table of contents

| | |
|---|-------------|
| List of Figures | xiii |
| List of Tables | xix |
| List of Acronyms | xxi |
| Introduction | 1 |
| 1 The Theory of Neutrino Physics | 3 |
| 1.1 The Standard Model and Neutrinos | 3 |
| 1.2 Neutrino Oscillations and Neutrino Masses | 6 |
| 1.2.1 The Evidence for Neutrino Oscillations | 8 |
| 1.2.2 The Phenomenology of Neutrino Oscillations | 18 |
| 1.2.3 The Origins of Neutrino Mass | 25 |
| 2 The SNO+ Detector | 31 |
| 2.1 Detector Geometry | 31 |
| 2.2 Experimental Phases | 32 |
| 2.3 Detecting and Recording an Event in SNO+: A Journey | 34 |
| 2.3.1 Particle Interactions with Matter | 34 |
| 2.3.2 Optical Processes | 40 |
| 2.3.3 Detection by PMTs | 47 |
| 2.3.4 Data Acquisition and Triggering | 50 |

| | | |
|----------|---|------------|
| 2.3.5 | Operation of the Detector | 52 |
| 2.4 | Calibrations and Detector Modelling | 53 |
| 2.4.1 | Detector Monitoring | 54 |
| 2.4.2 | Electronic and PMT Calibrations | 54 |
| 2.4.3 | Energy and Optical Calibrations | 56 |
| 2.4.4 | Event Reconstruction | 58 |
| 2.4.5 | Event Simulation | 61 |
| 3 | The SMELLIE Calibration System | 63 |
| 3.1 | Lasers | 66 |
| 3.2 | Controlling Laser Intensities | 68 |
| 3.3 | Propagation of Light into the Detector | 73 |
| 3.4 | The Monitoring PMT Unit | 76 |
| 3.5 | Event Triggering and Data Acquisition | 77 |
| 3.6 | Software for SMELLIE Data-taking | 81 |
| 4 | Simulating SMELLIE Events | 85 |
| 4.1 | Improving the SMELLIE Generator Algorithm | 86 |
| 4.1.1 | Previous Attempts at SMELLIE Event Simulation | 86 |
| 4.1.2 | The new generator | 89 |
| 4.2 | Improving the beam profiles | 93 |
| 4.2.1 | Combining beam profile datasets | 97 |
| 4.3 | Comparisons between Data and Simulation | 103 |
| 4.3.1 | Forward Hemisphere Discrepancies | 103 |
| 4.3.2 | Emission Time Discrepancies | 107 |
| 4.3.3 | Backward Hemisphere Discrepancies | 108 |
| 5 | Analysis of SMELLIE Data in the Scintillator Phase | 113 |
| 5.1 | Extinction Length Analysis | 113 |

| | | |
|----------|--|------------|
| 5.1.1 | Mathematical Model | 114 |
| 5.1.2 | Parameter Measurements and Uncertainties | 118 |
| 5.1.3 | Results in Data | 122 |
| 5.2 | Scattering Analysis | 131 |
| 5.2.1 | Historical Approaches and the Problem of Systematics . . | 131 |
| 5.2.2 | New Methodology | 133 |
| 5.2.3 | Results in Data | 140 |
| 5.2.4 | Interpretation | 140 |
| 5.3 | Summary and Suggestions for Future Work | 143 |
| 6 | Solar Oscillation Analysis | 149 |
| 6.1 | Analysis Methodology | 150 |
| 6.1.1 | Observational Principle | 150 |
| 6.1.2 | Background Processes | 153 |
| 6.1.3 | The Log-likelihood Test Statistic | 161 |
| 6.1.4 | The Bayesian Statistical Approach | 162 |
| 6.1.5 | Markov Chain Monte Carlo | 163 |
| 6.1.6 | Choosing Priors | 165 |
| 6.1.7 | Including Systematics in the Fit | 166 |
| 6.1.8 | Including Oscillations in the Fit | 168 |
| 6.2 | Analysis on Scintillator-Phase data | 170 |
| 6.2.1 | Dataset and Livetime | 170 |
| 6.2.2 | Event Selection | 172 |
| 6.2.3 | Expected Rates and their Constraints | 176 |
| 6.2.4 | Systematics | 183 |
| 6.2.5 | Results | 186 |
| 6.3 | Sensitivity Projections | 197 |
| 6.4 | Summary and Suggestions for Further Work | 202 |

| | |
|----------------------|------------|
| 7 Conclusions | 207 |
|----------------------|------------|

| | |
|-------------------|------------|
| References | 209 |
|-------------------|------------|

List of Figures

| | | |
|-----|--|----|
| 1.1 | Diagram of the pp chain and CNO cycle within the Sun | 9 |
| 1.2 | Solar neutrino energy spectrum, and associated uncertainties from the SMM | 10 |
| 1.4 | The two tree-level Feynman diagrams associated with neutrino- electron elastic scattering | 13 |
| 1.5 | Comparison of measured solar neutrino fluxes in the SNO CC, NC, and ES modes to the SSM | 14 |
| 1.7 | Measured survival probability versus mean neutrino energy for each solar neutrino type, as observed by Borexino | 25 |
| 2.1 | 3D model of the SNO+ detector | 32 |
| 2.2 | Comparison of the SNO+ detector media's emission properties, versus optical phase | 36 |
| 2.4 | Scattering lengths in simulation for UPW, LAB, and 2.2 g/L LABPPO | 44 |
| 2.5 | Measured properties of the UPW and acrylic in the water phase . | 45 |
| 2.6 | Refractive indices of acrylic, UPW, and LABPPO as a function of wavelength; also reflectance as a function of incidence angle . . . | 46 |
| 2.8 | Efficiencies of the R1408-type PMTs used as standard within SNO+ | 49 |
| 2.9 | Example charge spectra for a PMT as a function of the true npe generated | 49 |

| | | |
|------|--|----|
| 2.10 | Schematic of the front-end electronics used for data acquisition and triggering in SNO+ | 50 |
| 3.1 | Diagram of the SMELLIE calibration system within SNO+ | 64 |
| 3.2 | A brief history of SMELLIE hardware work and data-taking campaigns | 66 |
| 3.3 | Diagram of the connections between the various bits of SMELLIE hardware and the rest of the SNO+ detector | 67 |
| 3.4 | Emission wavelength and timing spectra of the lasers used in SMELLIE | 69 |
| 3.5 | Typical impact of driving voltage intensity for PQ446 laser on observed maximum occupancy in the detector | 70 |
| 3.6 | Distribution of the number of PMT hits observed per event for laser PQ446 | 71 |
| 3.7 | Picture of the VFA during installation into the ELLIE hardware rack | 72 |
| 3.8 | Maximum occupancy in the detector as a function of the attenuation parameter value used | 73 |
| 3.9 | Fibre emission points and nominal pointing directions | 75 |
| 3.10 | Comparison between typical MPU CAEN traces generated by the PQ495 before and after the Summer 2022 hardware upgrades | 78 |
| 3.11 | Comparison of observed hit times in beamspot before and after TUBii firmware update | 79 |
| 4.1 | Comparison of SMELLIE between data and MC using a 1D generator | 87 |
| 4.2 | Number of attempts taken for existing 2D SMELLIE generator to accept direction | 89 |
| 4.3 | Intensity map of existing beam profile, and interpolated sampling map | 91 |
| 4.4 | Histogram of interpolated intensities within the 2D direction-space | 92 |

| | |
|--|-----|
| 4.5 Comparison of water-phase data to MC generated using both the old and new 2D beam profile generator approaches, with the updated beam profiles | 94 |
| 4.6 Plot of $\Delta\chi^2$ for both single subruns of a typical PMT, and when all relevant subruns are combined | 101 |
| 4.7 Comparison between old and updated beam profiles for fibre FS055, after combining multiple data sets | 104 |
| 4.8 Interpolated intensity map for the new updated beam profile of fibre FS055 | 105 |
| 4.9 Residuals from subruns at two different wavelengths, both compared to the combined beam profile model for fibre FS055 | 106 |
| 4.10 Time residual distribution in the beamspot region for data taken in July 2022 with PQ495 through fibre FS007, as compared to a matching simulation | 108 |
| 4.11 Data–MC comparisons for water phase SMELLIE data in the backscatter PMT region | 110 |
| 4.12 Comparison of Laserball data in the water phase to MC | 111 |
| 5.1 Current RAT models for the extinction lengths of both UPW and scintillator, as a function of wavelength | 114 |
| 5.2 Diagram showing the two PMT regions used in the SMELLIE extinction length analysis | 115 |
| 5.3 Linear interpolation being used on Laserball UPW attenuation coefficient data | 119 |
| 5.4 Time residual distributions of the far and backscatter PMT regions for a simulation using laser PQ407 through fibre FS007, split by the different optical components | 121 |

| | |
|---|-----|
| 5.5 Comparison of the backscatter light region time residual distribution with intensity and emission time calculation choice | 122 |
| 5.6 Unstacked time residual distribution of a simulation of light from the PQ375 laser firing through fibre FS007, split by optical components | 124 |
| 5.7 Far PMT time window selection applied to a simulation of the PQ407 laser fired through laser FS107 | 125 |
| 5.8 Results of the extinction length analysis using the PQ407 laser . . | 127 |
| 5.9 Results of the extinction length analysis using the SuperK laser in the 400–410 nm range | 129 |
| 5.10 Summary of scintillator extinction length measurements made by SMELLIE | 130 |
| 5.11 Comparison of the signal and total hit distribution in the (t_{res}, α) -space using new and old beam profiles for laser PQ495 through fibre FS055 | 134 |
| 5.12 Hit distribution of SMELLIE data taken in run 302,634, with laser PQ495 through fibre FS055, as a function of both t_{res} and α . . . | 135 |
| 5.13 Model of light rays propagating in the SNO+ detector during scintillator phase, emanating from an external source such as SMELLIE | 135 |
| 5.14 Timing distribution of a simulation of the observed hits in the bad light-path PMT selection, split by optical components | 136 |
| 5.15 Comparison of timing distributions in the bad light-path PMT region for simulations of laser PQ495 through fibre FS055, comparing the old and new beam profile | 137 |
| 5.16 Plots of R_1 against R_2 for four pairs of scintillator phase datasets, using the SuperK laser | 141 |
| 5.17 Summary of results from the scattering analysis | 142 |
| 5.18 Observed time residual distributions for the backscattered light region for FS037, comparing May 2021 to June 2023 data | 146 |

| | | |
|------|--|-----|
| 6.1 | True ${}^8\text{B}$ E_ν versus true E_e | 151 |
| 6.2 | The evolution of energy distributions related to ${}^8\text{B}$ solar neutrino detection. | 152 |
| 6.3 | P_{ee} as a function of true neutrino energy, scanned over a variety of oscillation parameter values | 153 |
| 6.4 | The ${}^{238}\text{U}$ and ${}^{232}\text{Th}$ decay chains. | 154 |
| 6.5 | ${}^{214}\text{Bi-Po}$, ${}^{212}\text{Bi-Po}$, and ${}^8\text{B}$ observed energy spectra before and after out-of-window and in-window cuts | 156 |
| 6.6 | Schematic of (α, n) interactions. | 157 |
| 6.7 | (α, n) reconstructed energy spectrum in MC within the analysis ROI, before and after out-of-window cuts have been applied | 158 |
| 6.8 | Radial dependence of external backgrounds considered in this analysis, as compared to the ${}^8\text{B}$ signal | 159 |
| 6.10 | Demonstration of how to handle an energy scaling systematic correctly | 167 |
| 6.11 | Distribution of $\cos \theta_z$, for the events within this dataset | 172 |
| 6.12 | Comparison of tagged ${}^{214}\text{Bi}$ reconstructed energy distributions between data and MC | 185 |
| 6.13 | Examples of the sampled values for parameters within a given MCMC chain as a function of the step number, after tuning the proposal distribution width parameters. | 188 |
| 6.14 | Plot showing the auto-correlation as a function of step delay for three variables in a typical chain | 189 |
| 6.15 | Marginalised 1D posterior density distributions for all non-oscillation parameters. | 190 |
| 6.16 | Correlation matrix between all parameters in the MCMC fit . . . | 192 |
| 6.17 | 2D posterior density distribution marginalised onto Δm_{21}^2 and θ_{12} | 192 |
| 6.18 | Comparison of 1D posterior density distribution marginalised onto θ_{12} for different flux constraints | 193 |

| | |
|---|-----|
| 6.19 Comparison of data to MC for each radial slice | 196 |
| 6.20 Posterior density posterior distributions marginalised onto the two solar oscillation parameters, for each livetime scenario | 199 |
| 6.21 Posterior density posterior distributions marginalised onto each of θ_{12} and Δm_{21}^2 , for each livetime scenario | 200 |
| 6.22 Comparison of projections over 1 year of livetime, with different background expectations. | 203 |

List of Tables

| | | |
|-----|---|-----|
| 1.1 | Global Fit neutrino oscillation parameters | 21 |
| 1.2 | Current best limits on the half-life for $0\nu\beta\beta$ decay for selected isotopes | 29 |
| 2.1 | Current values used to model scintillator emission from electrons in 2.2 g/L LABPPO | 37 |
| 3.1 | SMELLIE fibre names, their associated mounting nodes on the PSUP, and their pointing direction. | 75 |
| 4.1 | Water-phase runs used for new beam profiling. | 96 |
| 5.1 | Datasets used in the SMELLIE extinction length analysis | 123 |
| 6.1 | Cuts used in this analysis. | 173 |
| 6.2 | Impact of each cut on the quantity of events in data. | 175 |
| 6.3 | Combined impact of cuts on each MC process. | 175 |
| 6.4 | Measured rates of the external backgrounds during the water phase of SNO+, by Tony Zummo | 181 |
| 6.5 | Number of events expected both before and after cuts have been applied, along with any constraints. | 182 |

6.6 Comparison of the fit parameter values obtained when getting the HPD values after marginalising onto each parameter, versus looking at the sampled point with the maximal likelihood found. 195

List of Acronyms

$0\nu\beta\beta$ Neutrinoless double beta decay

$2\nu\beta\beta$ Two-neutrino double beta decay

ADC Analogue-to-Digital Converter

AmBe Americium-Beryllium radioactive source

AMELLIE Attenuation Module for ELLIE

AV Acrylic vessel

BD 1,2-Butanediol

BEH Brout-Englert-Higgs (Mechanism)

BHT Butylated hydroxytoluene

BisMSB 1,4-Bis(2-methylstyryl)benzene

BSM Beyond the Standard Model

CC Charged Current (weak interaction)

CI Credible Interval

CTC Crate Trigger Card

DAQ Data acquisition (system)

DB Daughter Board

DDA N,N-Dimethyldodecylamine

ECA Electronic Calibration

ELLIE Embedded LED/Laser Light Injection Entity

ES Elastic Scattering

EW Electroweak (Theory)

EXTA External Asynchronous (Trigger)

FEC Front-End Card

FV Fiducial Volume

GTID Global Trigger Identification number

GT Global Trigger

HPD (The point of) Highest Posterior Density

IBD Inverse β -decay

IH Normal Hierarchy (of neutrino masses)

IW In-window events

LAB Linear alkylbenzene

MPU Monitoring PMT Unit (for SMELLIE)

MSW effect Mikheyev-Smirnov-Wolfenstein effect (of neutrinos)

MTC/A+ Analogue Master Trigger Card

MTC/D Digital Master Trigger Card

NC Neutral Current (weak interaction)

NH Inverted Hierarchy (of neutrino masses)

NI Unit National Instruments DAQ Unit (for SMELLIE)

npe Number of photoelectrons

OOW Out-of-window events

OWLs Outward-looking PMTs

PCA PMT Calibration

PMNS Pontecorvo-Maki-Nakagawa-Sakata (neutrino mixing matrix)

PMTIC PMT Interface Card

PMT Photomultiplier Tube

PPO 2,5-Diphenyloxazole

PQ PicoQuant

PSUP PMT support structure

QE Quantum efficiency (of a PMT)

QHL Charge with high gain over a ‘long’ integration time (390 ns)

QHS Charge with high gain over a ‘short’ integration time (60 ns)

QLX Charge with low gain over a ‘long’ integration time (390 ns)

ROI Region of Interest (of a physics analysis)

SMELLIE Scattering Module for ELLIE

SM The Standard Model of Particle Physics

SNO Sudbury Neutrino Observatory

SNU Solar Neutrino Unit, defined as 10^{-36} neutrino interactions per second

SSB Spontaneous Symmetry Breaking

SSM Standard Solar Model

TAC Time-to-amplitude Converter

TeA Telluric acid, Te(OH)_6

TELLIE Timing subsystem for ELLIE

TeLS Tellurium-loaded liquid scintillator

TIR Total Internal Reflection

TOF Time-of-flight (of a photon)

TTS Transit time spread (of a PMT)

TUBii Trigger Utility Board Mark ii

UPW Ultra-pure water

UPW Ultra-pure water

VFA Remotely-controllable Variable Fibre Attenuator

ZDAB Zebra Database (file format)

MC Monte Carlo

nhit Number of PMT hits in an event

RATDB RAT Database

RAT Reactor Analysis Tool

Introduction

1

Couple of pages outlining document's structure and contents (this is what each of
the chapters is here for). Less formal than the abstract, also explaining what the
expected audience of this thesis is: who will find this document useful!

2

3

4

Chapter 1

1

The Theory of Neutrino Physics

2

Light

Light

The visible reminder of Invisible Light

3

The Rock

T. S. ELIOT

1.1 The Standard Model and Neutrinos

4

The *Standard Model* (SM) of Particle Physics is the culmination of a century's work by scientists to understand the fundamental constituent elements of the Universe, and their interactions. Within the SM, fundamental particles are excitations of associated quantum fields within spacetime. One class of particles in the SM are known as the neutrinos, ν : these are spin-1/2 fermions which are neutral in both the strong and electromagnetic force. The only means by which they are known to interact is through the weak nuclear force. There are three ‘flavours’ of neutrino, one associated with each of their charged lepton counterparts: the electron neutrino ν_e , the muon neutrino ν_μ , and the tau neutrino ν_τ .

5

6

7

8

9

10

11

12

13

1 Crucial to understanding the nature of neutrinos is their interactions with
 2 other particles. Within the SM, the weak nuclear force and electromagnetism are
 3 unified into the Electroweak (EW) Theory by the work of Glashow, Salam, and
 4 Weinberg [1–3]. This is a so-called *chiral gauge field theory*. Gauge field theories
 5 are a special type of quantum field theory which demand that the Lagrangian
 6 density \mathcal{L} is invariant under certain kinds of transformation, in addition to the
 7 usual requirement of Lorentz invariance. For EW, the Lagrangian is invariant
 8 under ‘local’ transformations of the fields’ internal degrees of freedom, defined by
 9 the ‘gauge’ group $SU(2)_L \times U(1)_Y$, where L and Y are known as the left-handed
 10 weak isospin and weak hypercharge, respectively.

11 A local transformation is one which changes values of the fields at all points
 12 in spacetime. By demanding invariance under these gauge transformations, as
 13 well as Lorentz invariance, the theory naturally predicts the existence of vector
 14 (spin-1) boson particles. These are known as the ‘gauge’ bosons of the theory, and
 15 they mediate the interactions defined by the gauge group. The massive W^\pm and
 16 Z^0 bosons, discovered by the UA1 and UA2 experiments in 1983 [4–6], mediate
 17 the weak nuclear force, whilst the massless photon γ mediates the electromagnetic
 18 force.

19 The theory of EW interactions is also *chiral*. Any spinor that defines the
 20 wavefunction of a spin-1/2 field can be split into its left- and right-handed ‘chiral’
 21 components, defined through the projection operators $P_{L,R} = \frac{1 \mp \gamma^5}{2}$. The force
 22 associated with the $SU(2)_L$ part of the EW gauge group only interacts with
 23 the left-handed components of particles, denoted with the subscript L on their
 24 wavefunction.

25 The Lagrangian that defines the weak interactions of neutrinos is:

$$26 \quad -\mathcal{L} = \frac{g}{2 \cos \theta_W} \sum_{\ell,L} \bar{\nu}_{\ell,L} \gamma^\mu \nu_{\ell,L} Z_\mu^0 + \frac{g}{\sqrt{2}} \sum_\ell \bar{\nu}_{\ell,L} \gamma^\mu \ell_L^- W_\mu^+ + \text{h.c..} \quad (1.1)$$

Here, g is the dimensionless coupling constant associated with $SU(2)_L$, and θ_W is the Weinberg angle. The three lepton flavour fields are denoted by $\ell = e, \mu, \tau$, with their associated neutrino fields being given by ν_ℓ . Similarly, the fields associated with the weak gauge bosons are given by W^\pm and Z^0 . The two components of this Lagrangian are known as the Neutral Current (NC) and Charged Current (CC) weak interactions of neutrinos, respectively. Similar Lagrangians exist that define the NC and CC interactions of quarks, as well as the NC interactions of the charged leptons.

Solidifying this theoretical picture are decades-worth of experimental tests of neutrinos and their place in the SM. The first neutrinos to be detected were electron anti-neutrinos, by Cowan and Reines in 1956 [7, 8]. These neutrinos were generated in the β -decay of radioactive isotopes within the Savannah River nuclear reactor: $n \rightarrow p + e^- + \bar{\nu}_e$. This decay arises from a down quark within the neutron of an atom converting into an up quark via a CC interaction, generating a virtual W^- boson that promptly decays into an electron and $\bar{\nu}_e$. The method by which Cowen and Reines detected these anti-neutrinos was through *inverse β -decay* (IBD): $\bar{\nu}_e + p \rightarrow e^+ + n$. This process also originates from CC interactions. Analogous CC interactions allowed Danby *et al* to discover the muon neutrino in 1962 [9], and the DONUT Collaboration to discover the tau neutrino in 2000 [10].

The existence of NC interactions with neutrinos and anti-neutrinos was first demonstrated by the Gargamelle experiment in 1974 [11–14]. In particular, the observation of anti-muon neutrino electron elastic scattering, $\bar{\nu}_\mu + e^- \rightarrow \bar{\nu}_\mu + e^-$ by the experiment was an unambiguous demonstration of NC interactions.

In 1958, Goldhaber *et al* [15] were able to demonstrate experimentally that the helicity of electron neutrinos, i.e. the component of their spin along the direction of motion, is -1 . No evidence of neutrinos with positive helicities (or equally, anti-neutrinos with negative helicities) exists. This stands in firm contrast to all other SM particles.

¹ No flavours of neutrino beyond the electron, muon, or tau types have been
² discovered. A combined analysis of data from the four LEP experiments looking
³ at the decay width of the Z boson was able to indirectly measure the number of
⁴ neutrino species that could undergo NC interactions and had masses less than
⁵ one half of the Z boson: $N_\nu = 2.9963 \pm 0.0074$ [16, 17]. This measurement is very
⁶ strong evidence that no other ‘light’ weakly-interacting neutrinos exist.

⁷ 1.2 Neutrino Oscillations and Neutrino Masses

⁸ So far in this description, no attempt has been made to explain the origin of the
⁹ masses of the fundamental particles. It is certainly straightforward to naïvely add
¹⁰ a mass term such as $m_e \bar{e}_L e_R$ into the SM Lagrangian, where m_e is the mass of
¹¹ the electron. However, one can show that any mass terms added will necessarily
¹² violate the $SU(2)_L \times U(1)_Y$ symmetry that defines the EW interactions [18]. The
¹³ weak vector bosons W^\pm and Z would then need to be massless, in contradiction
¹⁴ with observations.

¹⁵ The solution to this problem comes in the form of the *Brout-Englert-Higgs*
¹⁶ (*BEH*) *Mechanism* [19–21], the final component of the SM. In this Mechanism, an
¹⁷ additional two-component “Higgs” field H is proposed, which is able to interact
¹⁸ with the other fields of the theory in a manner that preserves the SM gauge
¹⁹ symmetries. One part of the added Higgs field interactions are the so-called
²⁰ Yukawa terms, which for interactions with leptons are given by:

$$\text{²¹ } -\mathcal{L}_{\text{Yukawa,lep}} = \sum_{\ell} y_{\ell} \bar{L}^{\ell} H \ell^c + \text{h.c.}, \quad (1.2)$$

²² where y_{ℓ} are the “Yukawa” coupling constants for the three lepton flavours,
²³ $L^{\ell} = \begin{pmatrix} \nu_{\ell,L} \\ \ell_L \end{pmatrix}$ are the left-handed lepton doublets of the SM, and ℓ^c are the
²⁴ right-handed charged leptons.

The key to the BEH Mechanism is *Spontaneous Symmetry Breaking* (SSB):
 the Higgs field is defined in such a way that the ground state takes a non-zero
 ‘vacuum expectation value’, v . By doing so, the underlying gauge symmetry of
 the EW interactions is spontaneously broken as $SU(2)_L \times U(1)_Y \rightarrow U(1)_Q$,
 where $U(1)_Q$ is the residual electromagnetic charge conservation. The above
 Yukawa Lagrangian term after symmetry breaking generates the mass terms for
 the charged leptons:

$$-\mathcal{L}_{\text{Yukawa,lep}} \rightarrow \sum_{\ell} m_{\ell} \bar{\ell}_L \ell^c + \text{h.c.}, \quad (1.3)$$

where $m_{\ell} = \frac{v}{\sqrt{2}} y_{\ell}$ are the charged lepton masses. Other terms associated with Higgs
 interactions in the SM generate mass terms for the quarks and weak vector bosons,
 as seen in data. A further prediction of this BEH Mechanism is the existence of a
 massive scalar boson known as the Higgs particle; this was discovered in 2012 by
 the ATLAS and CMS Collaborations [22, 23].

The one type of fundamental particle not covered by the above argument are
 neutrinos. If neutrinos were massless, then there is no issue: we observe neutrinos
 to have only negative helicities, which is equal to left-handed chiralities if they are
 massless. As the SM contains no right-handed neutrinos, no Yukawa interaction
 can be built to generate masses for the neutrinos. One can also demonstrate that,
 in the SM, neutrinos cannot even obtain masses through loop corrections [24].

This assumption of massless neutrinos appears initially consistent with the
 current observations of direct neutrino mass measurements. The strongest di-
 rect limits come from the KATRIN experiment, which looks at the endpoint of
 the tritium β -decay spectrum. The ‘effective’¹ electron anti-neutrino mass was
 measured to be $m_{\nu} < 0.8$ eV at a 90% confidence level [25]. Even stronger limits

¹ KATRIN measures the ‘effective’ mass and not the actual mass, because of the phenomenon of neutrino oscillations as described in the following sections.

¹ are available from cosmology, by looking in part at the power spectrum of the
² Cosmic Microwave Background. Assuming the so-called Standard ‘ Λ CDM’ Model
³ of Cosmology, limits on the sum of all three neutrino flavours $\sum m_\nu < \mathcal{O}(0.1 \text{ eV})$
⁴ have been achieved [26].

⁵ 1.2.1 The Evidence for Neutrino Oscillations

⁶ Despite the current lack of any direct measurements, we now know that at least
⁷ some neutrino flavours must have mass. This is because of the phenomenon of
⁸ *neutrino oscillations*, which have been observed over a variety of experiments and
⁹ contexts. The critical pieces of evidence for this process are described here; the
¹⁰ underlying mathematical model that is used to explain them quantitatively is
¹¹ described in Section 1.2.2.

¹² The Solar Neutrino Problem

¹³ Neutrinos are generated from the Sun as a by-product of the fusion reactions at its
¹⁴ core. At the highest level, protons fuse into alpha particles by the overall reaction
¹⁵ $4 p \rightarrow {}^4\text{He} + 2 e^+ + 2 \nu_e$, generating also $\sim 25 \text{ MeV}$ of energy that enables the Sun
¹⁶ to shine [27]. This process is known as ‘hydrogen burning’. The Standard Solar
¹⁷ Model (SSM) is the current best quantitative description of stellar evolution for
¹⁸ main sequence stars, and our Sun in particular. It covers the nuclear reactions
¹⁹ that generate both the energy that powers the star and the changes in the relative
²⁰ isotopic abundances, how the energy is transported out through the star via
²¹ radiation of photons and convection, and how the outward pressures caused by
²² this radiation is balanced by gravity to maintain hydrostatic equilibrium. An
²³ introduction to the SSM can be found in [27].

²⁴ In the Sun, two sets of nuclear reactions enable hydrogen burning to occur:
²⁵ the *proton-proton (pp) chain* and *CNO cycle*. Diagrams of these reaction chains

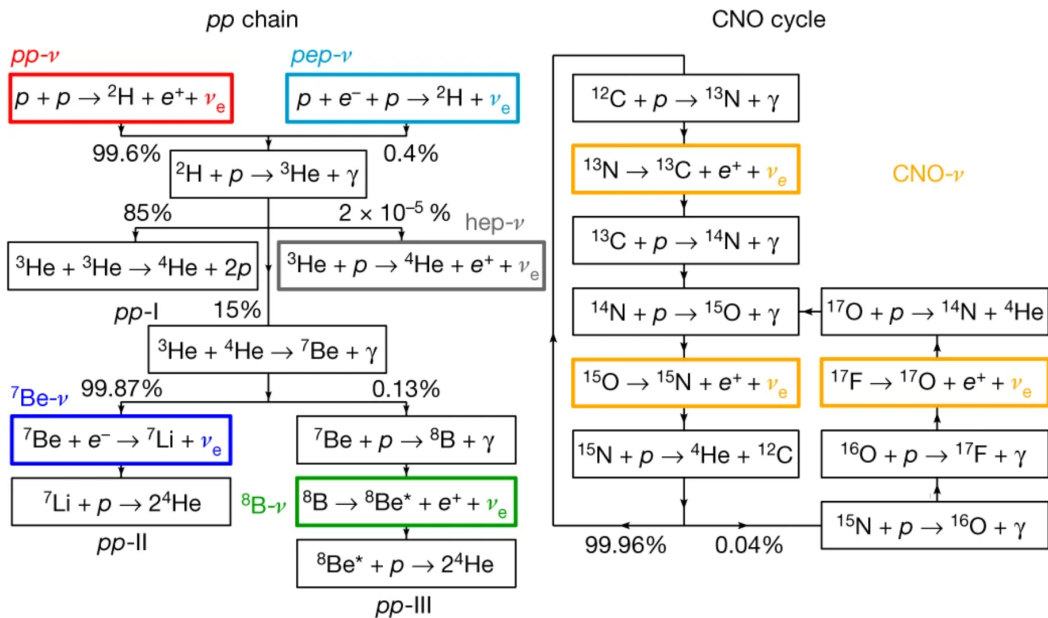


Fig. 1.1: Diagram of the pp chain and CNO cycle within the Sun, with the reactions that generate neutrinos highlighted. Taken from [28].

are shown in Fig. 1.1. In the pp chain, protons are first fused together to form a ^2H nucleus through the ‘pp’ and ‘pep’ reactions, the latter also using an electron. Both of these processes are weak interactions that generate an electron neutrino. Once a deuterium nucleus has been generated, it strongly interacts with a proton to create a ^3He nucleus. The dominant method for hydrogen burning to then terminate is for two ^3He nuclei strongly interact to generate ^4He and two protons.

Two other nuclear reactions with ^3He are possible. In one, ^3He fuses with ^4He to generate a ^7Be nucleus, which can then generate a neutrino either from the creation of ^7Li via electron capture, or from the additional fusing into ^8B which promptly β^+ -decays. These are known as the ^7Be and ^8B solar neutrino generation reactions, respectively. The final and rarest reaction within the pp chain that generates a neutrino is the so-called ‘hep’ reaction, in which ^3He directly fuses with a proton.

The CNO cycle is a secondary means by which the Sun can burn hydrogen. This is achieved through the aid of a ^{12}C nucleus as a catalyst. Part of the cycle

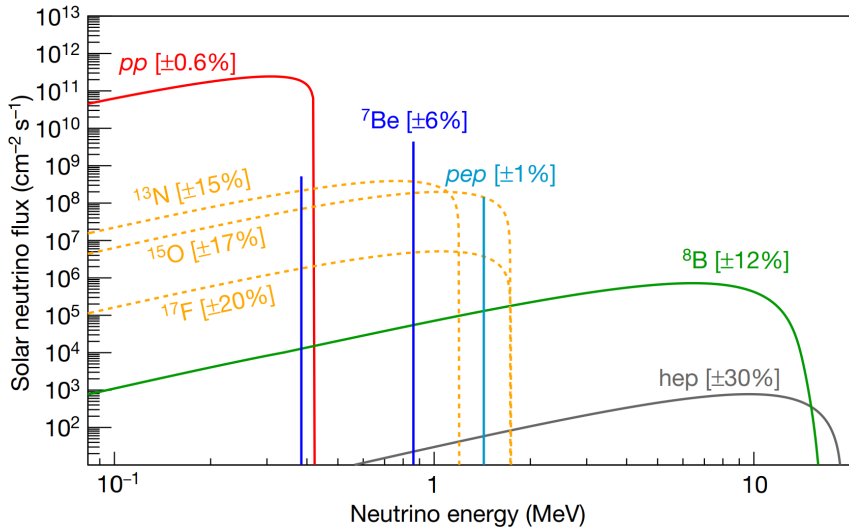


Fig. 1.2: Solar neutrino energy spectra, and associated uncertainties from the SSM. Figure is taken from [28, 30]; note that the flux is given in units of $\text{cm}^{-2} \text{s}^{-1} \text{MeV}^{-1}$ for the continuum sources, and $\text{cm}^{-2} \text{s}^{-1}$ for mono-energetic sources.

1 involves the generation of unstable isotopes ^{13}N and ^{15}O , both of which β^+ -decay,
 2 creating electron neutrinos. In a rare side-chain of the CNO cycle, it is possible
 3 to also generate ^{17}F which also weakly decays to generate a neutrino. This is the
 4 final method of generating neutrinos in our Sun.

5 The SSM quantitatively predicts the flux and energy spectra of neutrinos
 6 generated through each of the above processes, as incident on the Earth. This
 7 is shown in Fig. 1.2. The shapes of the energy spectra are determined by the
 8 nuclear reactions that define the process: for example, the broad shape of the
 9 $^8\text{B} \nu_e$ energy spectrum comes from the β^+ -decay of ^8B isotopes, and has been
 10 measured in nuclear beam experiments to high precision [29].

11 The rate of the ^8B interaction in the Sun, and hence the generated neutrino
 12 flux, depend strongly on the radial temperature distribution of the Sun, the cross-
 13 sections of the pp chain nuclear reactions, and the Sun's chemical composition.
 14 The latter point remains a topic of some controversy: measurements of the relative
 15 abundances in 1998 through spectroscopy of the Sun's photosphere as well as
 16 meteorites give a ‘metal-to-hydrogen’ ratio of $Z/X = 0.023$ [31], whereas a more

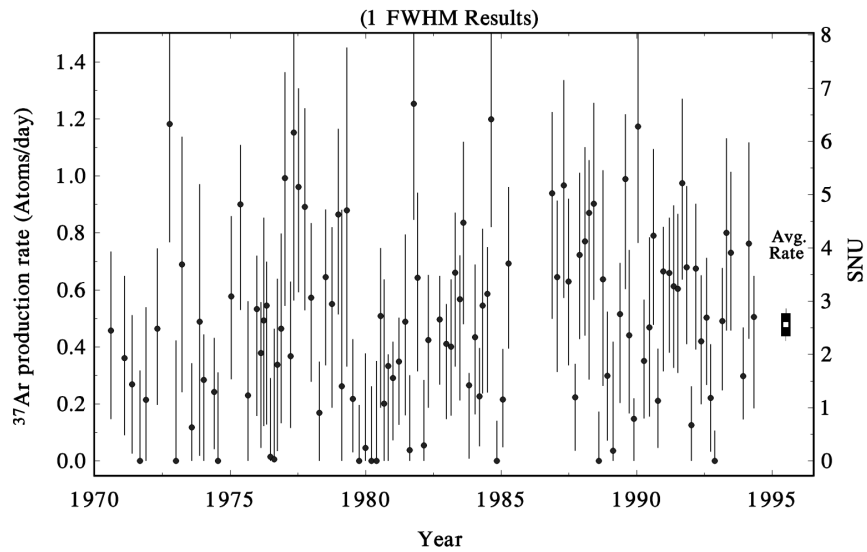


Fig. 1.3: Observed rate in the Homestake Chlorine detector, over the lifetime of the experiment. Taken from [34].

recent study in 2009 has a substantially lower value of $Z/X = 0.018$ [32]. ‘Metal’ here is used in the astrophysical sense: elements heavier than hydrogen or helium. These two models are called the ‘high-metallicity’ GS98 model and ‘low-metallicity’ AGSS09met model, respectively. The current best SSM associated with these two abundance models, denoted B16_GS98 and B16_AGSS09met, have ${}^8\text{B}$ flux predictions of $\Phi_{{}^8\text{B}} = (5.46 \pm 12\%) \times 10^6 \text{ cm}^{-2} \text{ s}^{-1}$ and $\Phi_{{}^8\text{B}} = (4.50 \pm 12\%) \times 10^6 \text{ cm}^{-2} \text{ s}^{-1}$, respectively [30].

The first experiment built to measure solar neutrinos was that of the Homestake Chlorine Detector, starting in the late 1960s [33]. A large tank of C_2Cl_4 was put deep underground, whereby electron neutrinos could be captured by the ${}^{37}\text{Cl}$ nuclei: ${}^{37}\text{Cl} + \nu_e \rightarrow {}^{37}\text{Ar} + e^-$. Through a careful chemical extraction process, any atoms of ${}^{37}\text{Ar}$ generated in the tank could be counted with an efficiency over 90%. After running the experiment for a period of almost 30 years, a final measurement of the solar neutrino interaction rate was $2.56 \pm 0.16(\text{stat.}) \pm 0.16(\text{sys.}) \text{ SNU}$ [34], where 1 SNU (‘Solar Neutrino Unit’) is defined as 10^{-36} events per target atom per second. The results as a function of time can be seen in Fig. 1.3.

¹ In contrast, according to one particular recent SSM using the GS98 metallicity
² model, the expected rate is $8.46^{+0.87}_{-0.88}$ SNU [35], highly inconsistent with the results
³ at Homestake. This disagreement became known as the *Solar Neutrino Problem*,
⁴ and was the first piece of evidence towards neutrino oscillations.

⁵ Since the Homestake experiment, a series of solar neutrino experiments used
⁶ a variety of different target isotopes to measure the rate of solar neutrinos. In
⁷ all cases, the measured rates were substantially below what is expected from the
⁸ SSM. The SAGE and GALLEX/GNO experiments used the capture of electron
⁹ neutrinos on ^{71}Ga to measure the capture rate: the final observations were
¹⁰ $65.4^{+3.1}_{-3.0}(\text{stat.})^{+2.6}_{-2.8}(\text{sys.})$ SNU [36] and $69.3 \pm 4.1 \pm 3.6$ SNU [37], respectively. An
¹¹ SSM expectation is $127.9^{+8.1}_{-8.2}$ [35]. Because the capture on ^{71}Ga has a much lower
¹² energy threshold than ^{37}Cl , these experiments were able to show that the Solar
¹³ Neutrino Problem was associated with the low-energy pp neutrinos as much as
¹⁴ the higher energy ^8B and ^7Be neutrinos.

¹⁵ The Kamiokande experiment, and its successor Super-Kamiokande, are large
¹⁶ water Cherenkov detectors, sensitive to neutrinos through neutrino-electron elastic
¹⁷ scattering (ES): $\nu_x + e^- \rightarrow \nu_x + e^-$. All flavours of neutrino are capable of
¹⁸ scattering through a NC process, but there is an additional CC mode for electron
¹⁹ neutrinos, as shown in Fig. 1.4. The differential cross-section for this interaction
²⁰ as a function of the scattered electron's kinetic energy T is given by [38]:

$$\frac{d\sigma_{\nu_i}}{dT} = \frac{2G_F^2 m_e}{\pi} \left\{ g_L^2(T) \left[1 + \frac{\alpha}{\pi} f_-(z) \right] + g_R^2(T) (1-z)^2 \left[1 + \frac{\alpha}{\pi} f_+(z) \right] \right. \\ \left. - g_R(T) g_L(T) \frac{m_e}{E_\nu} \left[1 + \frac{\alpha}{\pi} f_{+-}(z) \right] \right\}, \quad (1.4)$$

²⁴ where $i = e, \mu^2$, G_F is the Fermi coupling constant, m_e is the electron mass, α
²⁵ is the fine-structure constant, E_ν is the incident neutrino energy, and $z = T/E_\nu$.
²⁶ $g_{L,R}(T)$ are the left- and right-handed running chiral couplings, which have a

² $\frac{d\sigma_{\nu_\mu}}{dT} = \frac{d\sigma_{\nu_\tau}}{dT}$ because both flavours of neutrino only undergo the NC interaction.

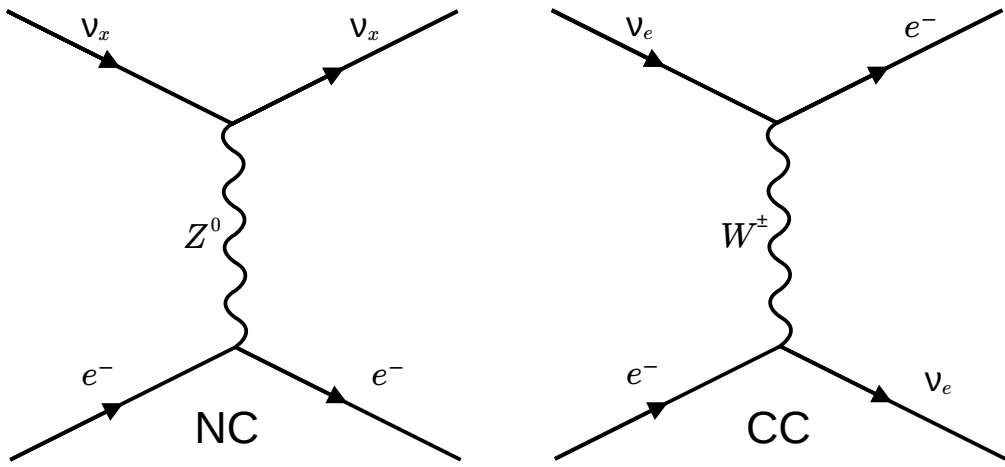


Fig. 1.4: The tree-level Feynman diagrams associated with the NC and CC modes of neutrino-electron elastic scattering.

T -dependence because of radiative corrections. Similarly, $f_-(z)$, $f_+(z)$, and $f_{+-}(z)$ are all QED radiative correction terms.

The most recent combined measurement of the ${}^8\text{B}$ solar neutrino flux in Super-Kamiokande is $(2.345 \pm 0.014(\text{stat.}) \pm 0.036(\text{sys.})) \times 10^6 \text{ cm}^{-2} \text{ s}^{-1}$ [39], roughly half the amount expected from the SSM [30].

One of the most important experiments for demonstrating that neutrino oscillations are the solution to the Solar Neutrino Problem was the Sudbury Neutrino Observatory, SNO. A large spherical acrylic vessel 2.2 km underground was filled with 1000 tonnes of heavy water, D_2O , from which Cherenkov light due to particle interactions could be detected [40]. Neutrinos were able to interact with the heavy water via three complementary modes: the CC process $\nu_e + d \rightarrow e^- + 2\text{p}$, the NC process $\nu_x + d \rightarrow \nu_x + p + n$, and the ES process described above.

Results of the measured fluxes of ν_e and $\nu_{\mu,\tau}$ solar neutrinos for the three detection modes in SNO, ES results from Super-Kamiokande, and comparison to the SSM are shown in Fig. 1.5. Because the NC interaction is insensitive to neutrino flavour, it is able to directly measure the total flux of ${}^8\text{B}$ solar neutrinos, regardless of flavour. One can see that, from the results, the NC flux measurement

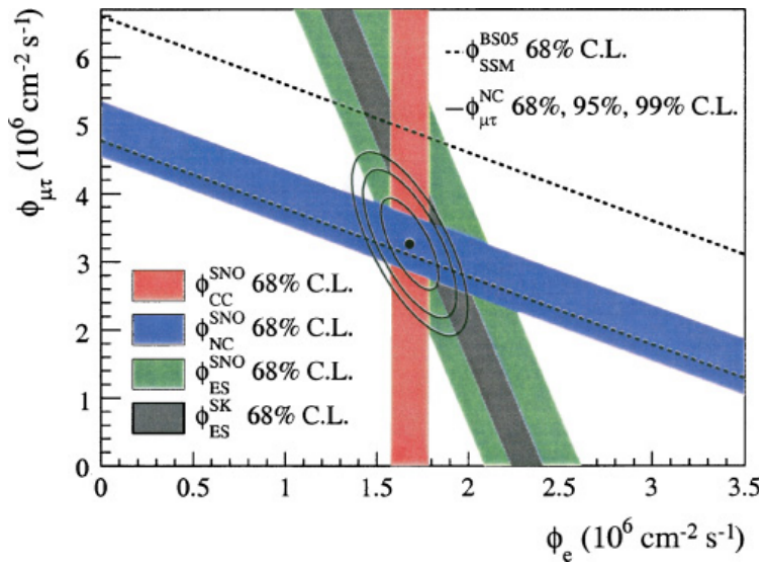


Fig. 1.5: Measured solar neutrino fluxes from electron neutrinos versus muon and tau neutrinos, in the SNO CC, NC, and ES modes (coloured bands). Also shown is the expectation from the SSM (dotted lines), and the ES rate measured from Super-Kamiokande (black band). The combined probability contours are shown in black. Taken from [41].

is consistent with the SSM. In contrast, the CC mode is only sensitive to the ν_e flux, whilst the ES mode is sensitive to an admixture of the different neutrino flavours. The results of all measurements of solar neutrinos from both SNO and Super-Kamiokande lead to consistent values of the flux of ${}^8\text{B}$ neutrinos for each flavour, consistent also with the SSM.

6 The Atmospheric Neutrino Anomaly

Atmospheric neutrinos come from the decays of cosmic ray pions and muons in the Earth's atmosphere. One can show that the expected ratio of the flux of muon neutrinos to electron neutrinos generated in the atmosphere should be about 2 [42]. The IBM [43], Kamiokande [44], and Super-Kamiokande [42] experiments were able to detect atmospheric neutrinos through CC interactions with electrons in the water, generating electron or muon tracks (depending on the neutrino flavour) that could be distinguished by the shape of their Cherenkov rings. In all cases,

the observed ratio of ν_μ to ν_e events was consistently below expectations. This
1
was known as the Atmospheric Neutrino Anomaly.
2

Super-Kamiokande was able to gather enough statistics from atmospheric
3
neutrino interactions to demonstrate that there was a clear dependence on the
4
rate of muon neutrino interactions as a function of the event direction. In particular,
5
the asymmetry A between the number of upward-going muon neutrino events U ,
6
and downward-going events D , was measured in one dataset to be [42]:
7

$$A = \frac{U - D}{U + D} = -0.296 \pm 0.048(\text{stat.}) \pm 0.01(\text{sys.}), \quad 8$$

a deviation from zero by over 6σ . In contrast, the asymmetry measured for
9
atmospheric ν_e events was consistent with zero. Further analysis on the experiment
10
looked at the rate of atmospheric ν_μ events as a function of the ratio L/E ,
11
where L is the estimated distance from production of the neutrino, and E is the
12
neutrino energy. The relative rate compared to expectations is shown in Fig. 1.6a.
13
Taken together, these atmospheric neutrino results demonstrate that there is a
14
disappearance of muon neutrinos which depends on the ratio L/E , whereas there
15
is no similar effect for the electron neutrinos.
16

Reactor Anti-neutrinos

The detection of $\bar{\nu}_e$ from nuclear reactors via IBD has been used not just to first
18
detect the existence of neutrinos by Cowan and Reines [7, 8], but also to provide
19
evidence for neutrino oscillations. For example, the KamLAND experiment is a
20
large-scale liquid scintillator detector based in Japan in which IBD events can be
21
detected [46]. The expected rate of these events could be derived from the known
22
powers of the various Japanese nuclear reactors, as well as their distances from
23
the experiment. The ratio of the measured rate to expectation as a function of
24
 L_0/E , where L_0 is the flux-averaged distance to the reactors, is shown in Fig. 1.6b.
25

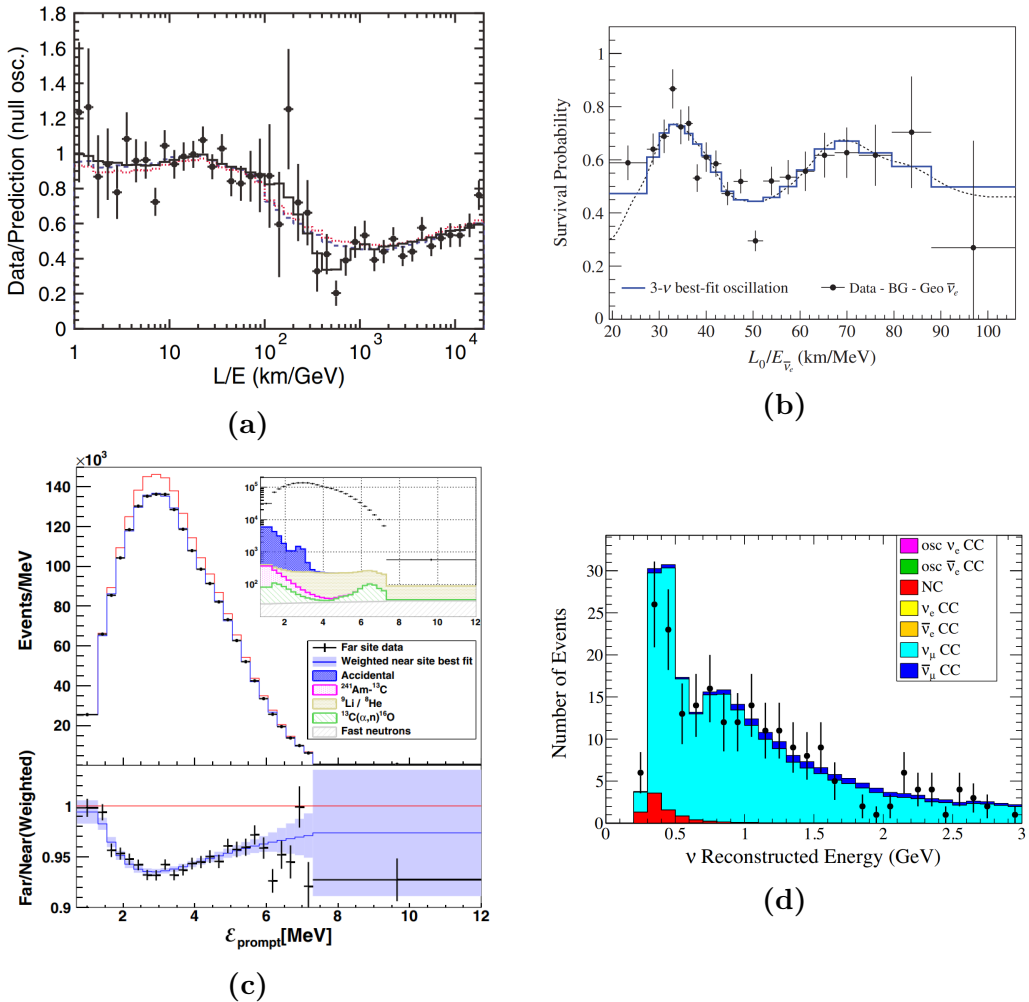


Fig. 1.6: Plots of measured survival probability for various types of neutrinos, in different experiments, as a function of L/E (or just E when L is fixed). **(a)**: Atmospheric neutrinos from Super-Kamiokande [45]. The solid line indicates the best-fit expectation from 2-flavour neutrino oscillations; the dashed and dotted lines correspond to the alternative hypotheses of neutrino decay and decoherence, respectively. **(b)**: Reactor anti-neutrinos from KamLAND [46]. $L_0 = 180$ km is the flux-weighted average reactor baseline; the blue bins and black dotted line correspond to the 3-flavour neutrino oscillation best-fit curve. **(c)**: Reactor anti-neutrinos from Daya Bay [47]. The expected number of events in the far site with/without neutrino oscillations (blue/red lines) based on the observations in the near site is compared to observations in the far site. **(d)**: Accelerator muon neutrinos from T2K [48].

The plot shows clear evidence of $\bar{\nu}_e$ disappearance, with an oscillatory dependence on L_0/E .

The Daya Bay [47], Double Chooz [49], and RENO [50] experiments are all also liquid scintillator detectors that measured IBD interactions from reactors, but unlike KamLAND they were each placed only ~ 1 km from a nuclear reactor. Each detector observed $\bar{\nu}_e$ disappearance over this much shorter length scale, also with a dependence on energy. The results from Daya Bay, as an example, are shown in Fig. 1.6c. Interestingly, the magnitude of the disappearance observed in these ‘short-baseline’ reactor antineutrino experiments is different to those seen in the ‘long-baseline’ KamLAND experiment.

Accelerator Neutrinos

Neutrinos generated from accelerators have been able to demonstrate numerous pieces of direct evidence for neutrino oscillations. These accelerators are able to generate very high intensity beams of ν_μ and $\bar{\nu}_\mu$, with some background of ν_e and $\bar{\nu}_e$. Much like experiments designed for reactor antineutrino measurements, accelerator neutrino detectors tend to come in two main varieties: long- and short-baseline. Typically, long-baseline experiments have two detectors, one near to the point of neutrino generation, and the much-larger far detector where the main oscillation measurements take place. The near-detector is used to ascertain the precise composition of neutrino beam, in order to minimise systematics in the composition of the beam as well as interaction cross-sections.

A wide variety of accelerator neutrino experiments have taken place over the past 25 years. The long-baseline experiments T2K and NOvA have both demonstrated disappearance of both ν_μ and $\bar{\nu}_\mu$ from their accelerator beams with high statistical significance [48, 51]. An example of the observed energy spectrum from a predominantly ν_μ -type beam, as seen by T2K, is shown in Fig. 1.6d. In

¹ contrast to the energy spectrum of the neutrinos at production, which is unimodal,
² this plot shows oscillations in the observed rate as a function of neutrino energy.

³ T2K and NOvA have also been able to observe the appearance of ν_e and $\bar{\nu}_e$ (as
⁴ appropriate) in their far detectors, well above the background rate expected [52, 53].

⁵ Recently, the two experiments have seen evidence for differences in the appearance
⁶ and disappearance rates of neutrinos and antineutrinos [54, 55]. In addition to the
⁷ appearance of ν_e shown by T2K and NOvA, the OPERA long-baseline neutrino
⁸ experiment was able to show the appearance of ν_τ in detector [56].

⁹ 1.2.2 The Phenomenology of Neutrino Oscillations

¹⁰ Oscillations in Vacuum

¹¹ Taken together, the observations described in the previous section naturally lead
¹² to the notion of neutrino oscillations: the idea that as neutrinos propagate through
¹³ space they are capable of changing flavour. Special Relativity precludes massless
¹⁴ particles from experiencing time evolution, so any theory of neutrinos changing
¹⁵ flavour between one another must require non-zero mass states.

¹⁶ The initial theories describing neutrino oscillations were made by Pontecorvo,
¹⁷ Maki, Nakagawa, and Sakata in the 1960s [57, 58]. These theories initially
¹⁸ assumed a two-neutrino model of oscillations, but now that ν_τ particles have
¹⁹ been observed a three-neutrino model has been adopted. The theory starts by
²⁰ assuming that the flavour eigenstates of neutrinos, $\nu_{e,\mu,\tau}$ are different from the
²¹ neutrino mass eigenstates, $\nu_{1,2,3}$, and are instead related to one another through
²² the Pontecorvo-Maki-Nakagawa-Sakata (PMNS) mixing matrix, U :

$$\begin{pmatrix} \nu_e \\ \nu_\mu \\ \nu_\tau \end{pmatrix} = U \cdot \begin{pmatrix} \nu_1 \\ \nu_2 \\ \nu_3 \end{pmatrix} = \begin{pmatrix} U_{e1} & U_{e2} & U_{e3} \\ U_{\mu 1} & U_{\mu 2} & U_{\mu 3} \\ U_{\tau 1} & U_{\tau 2} & U_{\tau 3} \end{pmatrix} \cdot \begin{pmatrix} \nu_1 \\ \nu_2 \\ \nu_3 \end{pmatrix}. \quad (1.5)$$

Because U must be unitary in order to preserve total probability, its components can be parameterised as follows:

$$U = \begin{pmatrix} c_{12}c_{13} & s_{12}c_{13} & s_{13}e^{-i\delta_{CP}} \\ -s_{12}c_{23} - c_{12}s_{13}s_{23}e^{i\delta_{CP}} & c_{12}c_{23} - s_{12}s_{13}s_{23}e^{i\delta_{CP}} & c_{13}s_{23} \\ s_{12}s_{23} - c_{12}s_{13}c_{23}e^{i\delta_{CP}} & -c_{12}s_{23} - s_{12}s_{13}c_{23}e^{i\delta_{CP}} & c_{13}c_{23} \end{pmatrix} \cdot \begin{pmatrix} \nu_1 \\ \nu_2 \\ \nu_3 \end{pmatrix}. \quad (1.6)$$

This matrix uses three “mixing angles” $0 \leq \theta_{12}, \theta_{13}, \theta_{23} \leq \pi/2$, and one further parameter called the “CP-violating phase”, $0 \leq \delta_{CP} \leq 2\pi$, with the abbreviations $s_{ij} = \sin \theta_{ij}$ and $c_{ij} = \cos \theta_{ij}$ used in the above expression.

Given that a neutrino flavour eigenstate $|\nu_\alpha(0)\rangle$ ($\alpha = e, \mu, \tau$) is produced in some CC process at time $t = 0$, because mass eigenstates $|\nu_i(0)\rangle$ ($i = 1, 2, 3$) are simultaneously the energy eigenstates when propagating in free space, the time evolution of the neutrino state is given by:

$$|\nu_\alpha(t)\rangle = \sum_{i=1}^3 U_{\alpha i} e^{-E_i t} |\nu_i(0)\rangle. \quad (1.7)$$

E_i is the energy eigenvalues corresponding to the associated mass eigenstates. The oscillation probability of going from one flavour α to another β is given by $P(\nu_\alpha \rightarrow \nu_\beta) = |\langle \nu_\beta | \nu_\alpha(t) \rangle|^2$. Assuming that the neutrino is ultra-relativistic so that $E_i \gg m_i$, where m_i is the mass of the i^{th} mass eigenstate, and that all mass eigenstates have the same definite momentum, one can show that the oscillation probability becomes [59]:

$$\begin{aligned} P(\nu_\alpha \rightarrow \nu_\beta) = \delta_{\alpha\beta} - 4 \sum_{i < j} \Re \{ W_{\alpha\beta,ij} \} \sin^2 \left(\frac{\Delta m_{ij}^2 L}{4E} \right) \\ - 2 \sum_{i < j} \Im \{ W_{\alpha\beta,ij} \} \sin \left(\frac{\Delta m_{ij}^2 L}{2E} \right), \end{aligned} \quad (1.8)$$

where $\delta_{\alpha\beta}$ is the usual Kronecker delta, $W_{\alpha\beta,ij} = U_{\alpha i}U_{\beta i}^*U_{\alpha j}^*U_{\beta j}$, $\Delta m_{ij}^2 = m_i^2 - m_j^2$, L is the distance between the creation and detection of the neutrinos, and $E_i \approx E$ is the average energy of the neutrino. As can be seen, the probability will oscillate as a function of L/E , in accordance with what was seen in Section 1.2.1.

If anti-neutrinos are produced, then oscillations are governed by U^* , which is equivalent to U but with the CP phase changing sign: $\delta_{CP} \rightarrow -\delta_{CP}$. Therefore, the difference between $P(\nu_\alpha \rightarrow \nu_\beta)$ and $P(\bar{\nu}_\alpha \rightarrow \bar{\nu}_\beta)$ is given by twice the third term of Eq. 1.8.

In a neutrino flavour disappearance measurement, $P_{\alpha\alpha} = P(\nu_\alpha \rightarrow \nu_\beta)$ is the *survival probability* of the neutrinos. In this case, $W_{\alpha\beta,ij} = |U_{\alpha i}U_{\alpha j}^*|^2$ is real, and the survival probability formula simplifies to:

$$P_{\alpha\alpha} = 1 - 4 \sum_{i < j} |U_{\alpha i}U_{\alpha j}^*|^2 \sin^2 \left(\frac{\Delta m_{ij}^2 L}{4E} \right). \quad (1.9)$$

An experiment is only sensitive to neutrino oscillations from mass splitting Δm_{ij}^2 if X_{ij} is $\mathcal{O}(1)$, where X_{ij} is the phase within the relevant oscillation probability term:

$$X_{ij} = \frac{\Delta m_{ij}^2 L}{4E} = 1.27 \frac{\Delta m_{ij}^2 [10^{-3} \text{ eV}^2] L [\text{km}]}{E [\text{MeV}]} \quad (1.10)$$

If $X_{ij} \ll 1$, then $\sin^2(X_{ij}) \rightarrow 0$, and no oscillations are seen due to that mass splitting. If instead $X_{ij} \gg 1$, then what can only be observed is the average effect over many oscillations, $\langle \sin^2(X_{ij}) \rangle = 1/2$.

From the results of a variety of neutrino oscillation experiments, the oscillation parameters and magnitudes of the mass splittings have now been measured, with varying degrees of precision. A global fit of the experimental data by the NuFit group in October 2021 [60] give the values shown in Table 1.1. All the parameters appear to have non-zero values, implying that mixing between all neutrino flavours

| Parameter | Normal hierarchy | Inverted hierarchy |
|--|----------------------------|----------------------------|
| $\theta_{12}[\circ]$ | $33.44^{+0.77}_{-0.74}$ | $33.45^{+0.77}_{-0.74}$ |
| $\theta_{23}[\circ]$ | $49.2^{+1.0}_{-1.3}$ | $49.5^{+1.0}_{-1.2}$ |
| $\theta_{13}[\circ]$ | $8.57^{+0.13}_{-0.12}$ | $8.60^{+0.12}_{-0.12}$ |
| $\delta_{CP}[\circ]$ | 194^{+52}_{-25} | 287^{+27}_{-32} |
| $\Delta m_{21}^2[10^{-5} \text{ eV}^2]$ | $7.42^{+0.21}_{-0.20}$ | $7.42^{+0.21}_{-0.20}$ |
| $\Delta m_{3\ell}^2[10^{-3} \text{ eV}^2]$ | $+2.515^{+0.028}_{-0.028}$ | $-2.498^{+0.028}_{-0.028}$ |

Table 1.1: Global fit results for the neutrino oscillation parameters and mass splittings, as performed in NuFit 5.1 [60]. The results for both the Normal and Inverted Hierarchy are shown: $\Delta m_{3\ell}^2 = \Delta m_{31}^2$ in the former, Δm_{32}^2 in the latter. The results used do not include atmospheric neutrino data from Super-Kamiokande.

is possible. Furthermore, $|\Delta m_{21}^2| \ll |\Delta m_{31}^2| \sim |\Delta m_{32}^2|$, meaning there are two distinct ‘scales’ in L/E that are sensitive to neutrino oscillations.

In addition to this information, we also know from solar data that the sign of Δm_{21}^2 must be positive, for reasons that will be explained in the next section. However, the same cannot be yet said for Δm_{31}^2 . This leads to two possible scenarios of the ordering of the neutrino mass states. If the sign of Δm_{31}^2 is positive, then $m_{\nu_1} < m_{\nu_2} < m_{\nu_3}$, known as the Normal Hierarchy (NH). Alternatively, $m_{\nu_3} < m_{\nu_1} < m_{\nu_2}$, known as the Inverted Hierarchy (IH).

Neutrino Oscillations in Matter

Considering only neutrino oscillations in vacuum is insufficient to understand the results of certain neutrino experiments, especially those detecting high-energy solar neutrinos, such as those from the ${}^8\text{B}$ chain. Using Eq. 1.10 for the case of solar neutrinos, one finds that $X_{ij} \gg 1$ for all i, j , so all effects of neutrino oscillations in the vacuum should be washed out. This leads to an expected

¹ electron neutrino survival probability for solar neutrinos of:

$$\begin{aligned} \text{2} \quad P_{ee} &= 1 - 2 \sum_{i < j} |U_{ei} U_{ej}^*|^2 \end{aligned} \quad (1.11)$$

$$\begin{aligned} \text{3} \quad &= 1 - \frac{1}{2} \sin^2(2\theta_{13}) - \frac{1}{2} \sin^2(2\theta_{12}) \cos^4(\theta_{13}) \end{aligned} \quad (1.12)$$

$$\begin{aligned} \text{4} \quad &= 0.55, \end{aligned} \quad (1.13) \quad \text{5}$$

⁶ using the parameters in Table 1.1. This survival probability value appears some-
⁷ what consistent with those measured in low-energy solar neutrino experiments
⁸ such as SAGE and GALLEX/GNO, but not with experiments with higher energy
⁹ thresholds such as Homestake, Super-Kamiokande, or SNO.

¹⁰ The resolution of this apparent problem is that the effect of matter on neutrino
¹¹ oscillations have not been considered. When neutrinos travel through a medium,
¹² the electrons, protons, and neutrons within that medium interact weakly with
¹³ those neutrinos, leading to coherent forward elastic scattering. The resulting
¹⁴ phenomenon is known as the *MSW effect*, after its discovery by Mikheyev, Smirnov,
¹⁵ and Wolfenstein [61, 62].

¹⁶ One can show that there is an effective potential due to these weak interactions
¹⁷ of the form $V_{CC}(x) = \sqrt{2}G_F n_e(x)$, where $n_e(x)$ is the electron number density
¹⁸ at a position x [63]. This effective potential is only felt by electron neutrinos,
¹⁹ because of the additional CC interaction possible, as seen in Fig. 1.4. All neutrino
²⁰ flavours experience NC interactions identically, and so can be ignored in what
²¹ follows. The effective potential modifies the Hamiltonian, and therefore by the
²² Schrödinger Equation the propagation of the neutrino wavefunctions are modified.

²³ The resulting dynamics of the MSW effect for 3- ν oscillations in a general
²⁴ medium can become quite complex. However, for the case of solar neutrinos two
²⁵ simplifying assumptions can be made that make many of the equations far more
²⁶ tractable: a full discussion can be read in e.g. [64]. Firstly, for solar neutrinos

it can be shown that $A_{CC} = 2EV_{CC} \ll \Delta m_{31}^2$, leading to the evolution of the ν_3 state decoupling from the ν_1 and ν_2 states. There exists a new basis in which the Hamiltonian is diagonalised, known as the matter eigenstate basis, leading to new effective oscillation parameters:

$$\begin{aligned}\tan 2\theta_{12}^M &= \frac{\tan 2\theta_{12}}{1 - \frac{A_{CC}}{A_{res}}}, \\ \Delta m_{M,21}^2 &= \Delta m_{21}^2 \sqrt{\sin^2 2\theta_{12} + \cos^2 2\theta_{12} \left(1 - \frac{A_{CC}}{A_{res}}\right)^2}, \\ A_{res} &= \frac{\cos 2\theta_{12} \Delta m_{21}^2}{\cos^2 \theta_{13}}.\end{aligned}\quad (1.14)$$

A_{res} is the value of A_{CC} at which a resonance occurs, leading to the effective mass splitting $\Delta m_{M,21}^2$ being minimised. In the core of the Sun, this resonance occurs at an energy of $E \sim 2$ MeV. If $A_{CC} \ll A_{res}$, then the effective oscillation parameters reduce back to the vacuum oscillation parameters, as expected. If instead $A_{res} \ll A_{CC} \ll \Delta m_{31}^2$, then $\theta_{12}^M \rightarrow \pi/2$. In this case, ν_e that are created in the medium are completely driven into the $|\nu_2^M\rangle$ effective mass eigenstate.

Because the values of the effective oscillation parameters are a function of the electron density of the medium, calculating the full impact of the MSW effect of a medium with strongly-changing density can be challenging. However, if the rate of change of electron density is slow enough as a function of distance, a second approximation can be made: this is known as the *adiabatic approximation*. For solar neutrinos, this approximation has been shown to be valid assuming the SSM and the measured values of the oscillation parameters. Under this approximation, states that are in a given effective mass eigenstate smoothly transform into one another as the neutrinos propagate. Therefore, an electron neutrino with high-enough energy that it has been driven into the $|\nu_2^M\rangle$ state in the Sun's core will then smoothly transform into the equivalent $|\nu_2\rangle$ mass eigenstate once it has reached the Sun's surface. This state then travels through space without any

¹ further oscillations occurring, because the neutrino has been transformed into a
² mass eigenstate. For such a neutrino, the detection probability becomes simply:

$$\text{3} \quad P(\nu_2 \rightarrow \nu_e) = |\langle \nu_e | \nu_2 \rangle|^2 = |U_{e2}|^2 \quad (1.15)$$

$$\text{4} \quad = \sin^2 \theta_{12} \cos^2 \theta_{13} \quad (1.16)$$

$$\text{5} \quad = 0.30, \quad (1.17)$$

⁷ using the oscillation parameters from Table 1.1. This survival probability is almost
⁸ half of the value seen in Eq. 1.11.

⁹ At intermediate energies, solar neutrinos are only partly driven into the $|\nu_2^M\rangle$
¹⁰ eigenstate, leading to a survival probability that is somewhere in-between the
¹¹ two extremes: $0.30 \leq P_{ee} \leq 0.55$. The value of P_{ee} for a given neutrino will be
¹² dependent on both the neutrino's energy and its location of production in the
¹³ Sun: a neutrino generated closer to the core of Sun will have to travel through
¹⁴ regions of greater electron density, driving the effective mixing angle θ_{12}^M larger.

¹⁵ Looking at data, Fig. 1.7 shows the measured values of P_{ee} for a number
¹⁶ of different types of solar neutrino, each with their own characteristic energy
¹⁷ spectrum. Also shown is the expectation after considering the MSW effect: as
¹⁸ can be seen, the solar neutrino data appears consistent with this model.

¹⁹ Important to note is that the resonance phenomenon of the MSW effect requires
²⁰ a positive sign for Δm_{21}^2 to occur, given that $0 \leq \theta_{12} \leq \pi/4$. If $\Delta m_{21}^2 < 0$, then in
²¹ the case where $|A_{CC}| \gg |A_{res}|$, θ_{12}^M will be driven to 0 instead of $\pi/2$. This would
²² lead to the survival probability of solar neutrinos increasing at higher energies,
²³ entirely counter to what is seen in data. Because of this, the sign of Δm_{21}^2 is
²⁴ known to be positive.

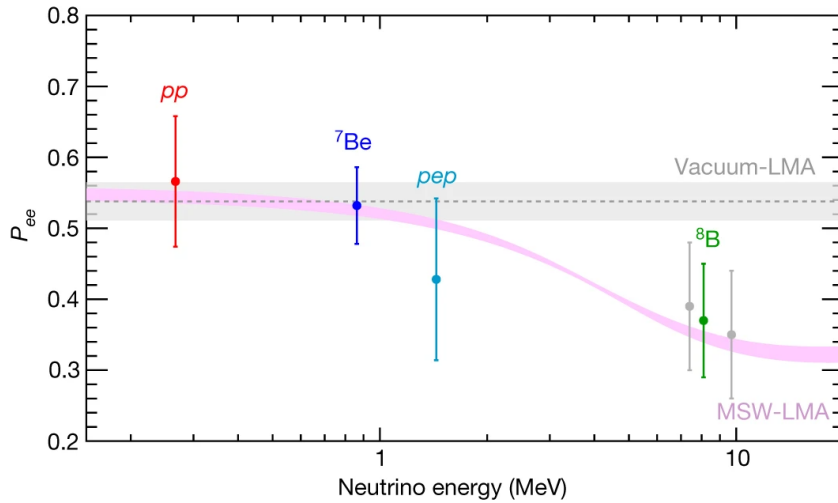


Fig. 1.7: Measured survival probability versus mean neutrino energy for each solar neutrino type, as observed by Borexino. Taken from [28]. For comparison, the expected survival probability due to vacuum oscillations and the MSW effect are shown.

1.2.3 The Origins of Neutrino Mass

Having seen a wide variety of experiments over many decades observe neutrino oscillations, and the phenomenology that describes them requiring at least two neutrino mass states to be non-zero, a critical question is how neutrino masses can be included into the SM. There are two different approaches to doing so. If neutrinos are given a *Dirac mass term*, then a term similar to the one in Eq. 1.2 is added, now using right-handed neutrino terms ν_j^c :

$$-\mathcal{L}_{\text{Dirac}} = \sum_{i,j} y_{ij}^\nu \bar{L}^i C H \nu_j^c + \text{h.c.} \quad (1.18)$$

$$\rightarrow \sum_{i,j} m_{ij}^\nu \bar{\nu}_{i,L} \nu_j^c + \text{h.c..} \quad (1.19)$$

The 3×3 matrix y_{ij}^ν describes the Yukawa coupling strengths between the neutrinos and the charge conjugate of the Higgs doublet, CH . After SSB, a neutrino mass matrix is obtained $m_{ij}^\nu = \frac{v}{\sqrt{2}} y_{ij}^\nu$, which can be related to the PMNS mixing matrix [18]. The theoretical downsides of this approach are two-fold: firstly,

¹ because $v = 246.22 \text{ GeV} \gg m_{\nu_i} \sim \mathcal{O}(10^{-2} \text{ eV}^2)$, this requires fine-tuning of the
² Yukawa coupling parameters down to values $\sim \mathcal{O}(10^{-14})$.

³ A second assumption needed for neutrinos to be Dirac particles is the existence
⁴ of right-handed, ‘sterile’ neutrinos. These are so-called because their right-handed
⁵ nature precludes them from interacting via any of the three main fundamental
⁶ forces of particle physics. The only known means by which sterile neutrinos could
⁷ have any contact with the rest of the SM is via the above mass term of the
⁸ Lagrangian; this implies that neutrinos could oscillate into a sterile neutrino state,
⁹ for example. The LSND and MiniBooNE short-baseline neutrino experiments
¹⁰ have seen excesses at low energies that could be explained by oscillations of a
¹¹ sterile neutrino with a mass splitting of $\Delta m_{41}^2 \sim \mathcal{O}(1 \text{ eV}^2)$ [65, 66]; however, these
¹² results seem at odds with recent results by the MicroBooNE Collaboration [67].

¹³ An alternative approach to generating neutrino masses without needing to
¹⁴ posit the existence of right-handed neutrino states is through a *Majorana mass*
¹⁵ *term*:

$$\mathcal{L}_M = \frac{1}{2} \sum_{i,j} m_{ij}^\nu \nu_{i,L}^T C \nu_{j,L} + \text{h.c.}, \quad (1.20)$$

¹⁶ where there is now no longer a coupling to the Higgs field, and instead the charge
¹⁷ conjugate of the left-handed neutrino states is used. This term breaks SM gauge
¹⁸ symmetry, so in theories Beyond the Standard Model (BSM) that want to include
¹⁹ such a term typically introduce a higher-order term that reduces after SSB down
²⁰ to the Majorana term [68]. Many of these BSM theories, for example ones that
²¹ include a so-called ‘Seesaw Mechanism’, also have a means of explaining why
²² neutrinos have such light masses, without having to resort to ‘unnatural’ Yukawa
²³ coupling strengths [69]. For this term to exist neutrinos must be a ‘Majorana
²⁴ particle’, in which they are their own antiparticle, expressed mathematically as
²⁵ $\nu^c = \nu$. This is named after Ettore Majorana, who realised that a mass term such
²⁶ as the above could exist under these special conditions [70].

The existence of this Majorana mass term would have major consequences, beyond just allowing for neutrino masses. Crucially, the term violates lepton number, as it allows for neutrinos to annihilate one another. Because all other terms in the SM conserve the ‘accidental’ symmetry of lepton number conservation, any evidence of lepton number violation with neutrinos can provide strong evidence that neutrinos are Majorana particles.

One prominent search mode for determining whether neutrinos have a Majorana mass term is by looking for *neutrinoless double beta decay*, $0\nu\beta\beta$. This is a variant of the radioactive decay known as *two-neutrino double beta decay*, $2\nu\beta\beta$, and was first hypothesised by Wendell H Furry [71]. $2\nu\beta\beta$ is a nuclear process theorised by Maria Goeppert-Mayer [72], in which two β -decays occur simultaneously in one nucleus, generating two electrons and two electron anti-neutrinos. This is only possible in the subset of isotopes for which $2\nu\beta\beta$ is energetically favourable, but the usual single β -decay is not (or indeed any other form of nuclear decay).

One example of an isotope capable of $2\nu\beta\beta$ is ^{130}Te . Fig. 1.8 shows the mass excesses of the nuclear ground state energy levels for isotopes in the isobar $A = 130$. As can be seen, ^{130}Te is not capable of β^- -decay to ^{130}I , but decay via $2\nu\beta\beta$ down to the stable isotope ^{130}Xe is possible. This process has been observed by the CUORE experiment [73], and $2\nu\beta\beta$ has been similarly observed in a number of other isotopes such as ^{76}Ge [74], ^{136}Xe [75], and ^{150}Nd [76].

Unlike $2\nu\beta\beta$, $0\nu\beta\beta$ would emit no neutrinos during the decay, and instead a virtual anti-neutrino emitted by one nucleon would be captured on another as a neutrino. Fig. 1.9a shows a Feynman diagram for this process. A theorem by J. Schechter and J.W.F. Valle [78] says that, as long as the weak interaction is governed by some form of local gauge theory, any observation of $0\nu\beta\beta$ guarantees the existence of a Majorana mass term for neutrinos.

The lack of neutrinos generated in $0\nu\beta\beta$ compared to $2\nu\beta\beta$ enables a method for distinguishing between the two processes. In $2\nu\beta\beta$, the energy of the decay is

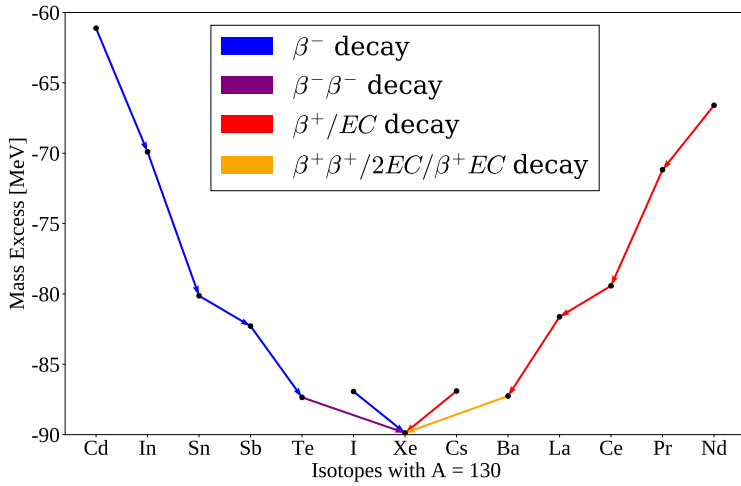


Fig. 1.8: Masses excesses of the $A = 130$ isobar, from [77]. The allowed weak decays between isotopes are shown by coloured arrows; note how both ^{130}Te and ^{130}Ba can only decay via second-order weak processes.

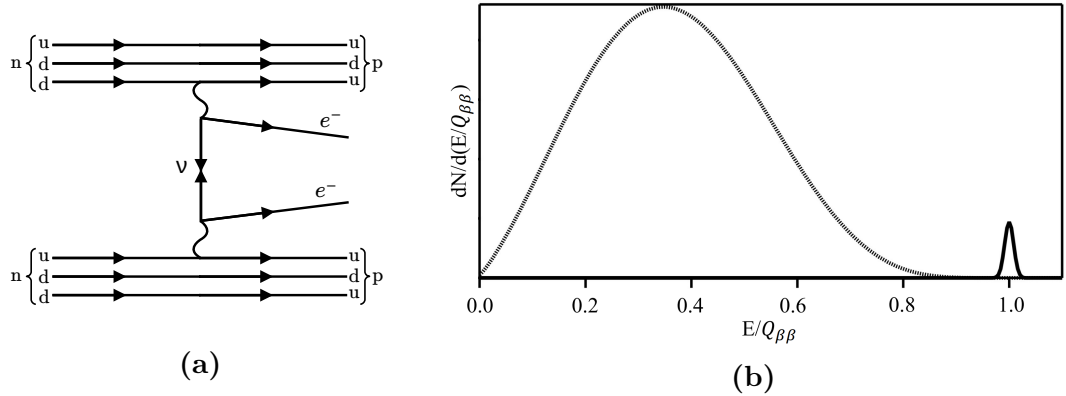


Fig. 1.9: (a): Feynman diagram for $0\nu\beta\beta$ decay. (b): Sketch of the energy spectra for $2\nu\beta\beta$ (dashed line) and $0\nu\beta\beta$ decays (solid line). The Q -value of the decay is written here as $Q_{\beta\beta}$. Taken from [79].

- ¹ shared between the two electrons and two anti-neutrinos generated. Given that the
- ² anti-neutrinos rarely ever interact, the observed energy of the event will come only
- ³ from the electrons (ignoring the negligible kinetic energy of the daughter nucleus).
- ⁴ This leads to a broad observed energy spectrum. In comparison, with $0\nu\beta\beta$ all the
- ⁵ decay energy is passed onto the electrons, and so the observed energy spectrum
- ⁶ will be a thin peak at the Q -value of the decay. This is shown schematically in

Fig. 1.9b. As can be seen, $0\nu\beta\beta$ can be searched for by looking for an excess of radioactive decay events generated by a $2\nu\beta\beta$ -decaying isotope at the Q -value.

No evidence of $0\nu\beta\beta$ has been seen at the time of writing. However, numerous experiments have been searching for the decays in a variety of isotopes, and more are under construction or being planned. A summary of the current state of searches for the most prominent isotopes that could theoretically allow $0\nu\beta\beta$ is shown in Table 1.2. In absence of an observation, experiments report a limit on the minimum possible half-life of $0\nu\beta\beta$, $T_{1/2}^{0\nu\beta\beta}$. If $0\nu\beta\beta$ is observed, the measured half-life can be used to help determine the neutrino masses, through the formula:

$$\frac{1}{T_{1/2}^{0\nu\beta\beta}} = \frac{|m_{\beta\beta}|^2}{m_e^2} G_\nu |\mathcal{M}_{0\nu\beta\beta}|^2, \quad (1.21)$$

where G_ν and $\mathcal{M}_{0\nu\beta\beta}$ are the phase space factor and matrix elements of the decay, and $m_{\beta\beta}$ is known as the ‘effective $0\nu\beta\beta$ mass’, defined as:

$$m_{\beta\beta} = \sum_{i=1}^3 U_{ei}^2 m_{\nu_i}. \quad (1.22)$$

| Isotope | $T_{1/2}^{0\nu\beta\beta}$ [years] | Experiment | |
|-------------------|------------------------------------|-------------|------|
| ^{76}Ge | $> 1.8 \times 10^{26}$ | GERDA | [80] |
| ^{100}Mo | $> 1.5 \times 10^{24}$ | CUPID-Mo | [81] |
| ^{130}Te | $> 2.2 \times 10^{25}$ | CUORE | [82] |
| ^{136}Xe | $> 2.3 \times 10^{26}$ | KamLAND-Zen | [83] |

Table 1.2: Current best limits on the half-life for $0\nu\beta\beta$ decay, for selected isotopes. All limits given are for a 90% CL.

Chapter 2

1

The SNO+ Detector

2

The light-soaked days are coming.

3

JOHN GREEN

2.1 Detector Geometry

4

The SNO+ detector is a large, multi-purpose neutrino detector built in the SNOLAB underground laboratory near Sudbury, Canada. Its main detector structure is taken from the Sudbury Neutrino Observatory (SNO) [40], which can be seen in Fig. 2.1. At the heart of the detector lies the main detector medium, which changes depending on the phase of the experiment — more on the specifics of this in Section 2.2. This medium is held within a 12 m diameter sphere known as the Acrylic Vessel (AV). The AV floats within a body of ultra-pure water (UPW), beyond which is a stainless steel support structure (PSUP) that holds 9362 inward-facing Photomultiplier Tubes (PMTs). It is these PMTs that detect the light generated from physics events that occur within the detector medium. The AV is kept in place relative to the PSUP through a series of ‘hold-up’ and ‘hold-down’ tensylon ropes. All of these components are suspended within a large cylindrical cavity also filled with UPW. 91 outward-looking PMTs (OWLs) are

5

6

7

8

9

10

11

12

13

14

15

16

17

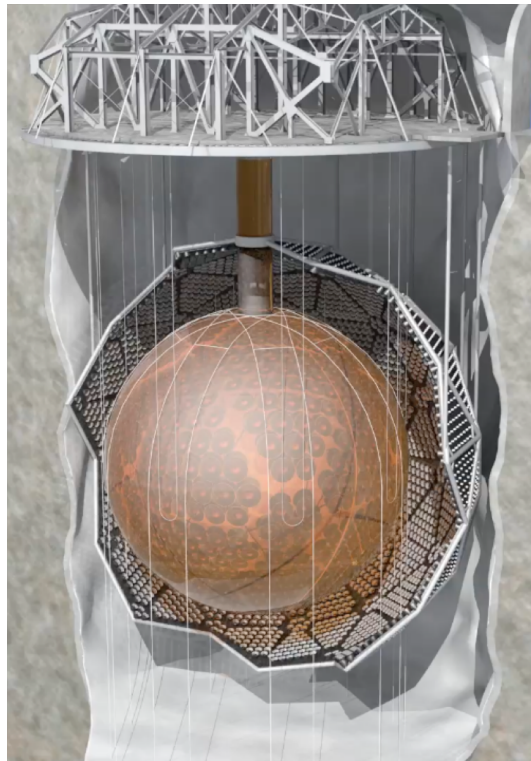


Fig. 2.1: 3D model of the SNO+ detector [84].

¹ also affixed to the outside of the PSUP, allowing for the effective vetoing of cosmic
² ray muons.

³ Directly above the detector is the Deck, within which all the detector electronics
⁴ are kept. Access within the AV for calibration tools and filling is possible only
⁵ through the acrylic ‘neck’ on top of the AV. Full details of the design of the current
⁶ detector can be found in [84].

⁷ 2.2 Experimental Phases

⁸ As mentioned earlier, SNO+ was designed to fulfil a number of physics goals
⁹ over multiple ‘phases’ of the detector’s lifetime. The phases are distinguished
¹⁰ by the medium that fills the AV. The first main phase (after a brief **Air Fill**
¹¹ **Phase** used only for detector commissioning) was that of the **Water Fill Phase**,
¹² with data taken between May 2017 and July 2019. This was used to perform

fundamental optical calibrations of the detector [85], measurements of the solar neutrino flux [86], observation of neutrino oscillations in reactor anti-neutrinos [87], and searches for nucleon decay [88, 89].

After this, the detector was filled with 780 tonnes of liquid scintillator known as linear alkylbenzene (LAB), mixed with the fluor 2,5-diphenyloxazole (PPO). More information on the physics of scintillators can be found in Section 2.3.1. Filling of the LABPPO cocktail had to be paused in March 2020 due to the COVID-19 pandemic, leading to the detector having its bottom half still filled with UPW, and the top half filled with LAB and PPO at 0.5 g/L. This impromptu phase became known as the **Partial Fill**, and allowed for some creative analyses to be performed: an initial neutrino oscillation analysis from reactor anti-neutrinos [90], as well as the first ever observation of directionality in a high light yield scintillator [91, 92]. Eventually, filling of the detector with liquid scintillator completed in May 2021. At that point, the concentration of PPO in the detector was at 0.6 g/L, markedly below the target level of 2.0 g/L. A further ‘PPO top-up’ campaign then proceeded, finishing in April 2022 with a final concentration of 2.2 g/L PPO. Thus began the **Scintillator Phase** of the experiment, which continues on during the time of writing. The main goals for this phase include a number of solar neutrino analyses (including the one described in Chapter 6), a precision measurement of the neutrino oscillation parameter Δm_{21}^2 using reactor anti-neutrinos [90], and further calibrations of the detector and its backgrounds.

Finally, in the near future the detector will be loaded with Tellurium for the **Tellurium Phase**, allowing for the flagship analysis of the experiment to begin: neutrinoless double beta decay. In order to load Te within the liquid scintillator in a stable manner, a chemical loading process has been developed, as described in [93]. The Te starts within Te(OH)_6 (telluric acid, otherwise known as TeA), which after purification will be reacted with 1,2-butanediol (BD) via heating and

¹ addition of N,N-Dimethyldodecylamine (DDA), which acts as a stabiliser. What
² results is tellurium-loaded scintillator, TeLS.

³ Two further chemicals are planned to be added to the scintillator cocktail.
⁴ The antioxidant butylated hydroxytoluene (BHT) will be added to capture any
⁵ free-radicals within the liquid scintillator, hopefully preventing any oxidation
⁶ reactions that could lead to the ‘yellowing’ of the scintillator, a degradation of its
⁷ optical properties. The addition of BHT is not expected to impact the detector’s
⁸ optics in any substantial way. However, the other substance to also be added,
⁹ 1,4-Bis(2-methylstyryl)benzene (bisMSB), will impact the optics. BisMSB acts as
¹⁰ a ‘wavelength-shifter’ which enables the scintillator cocktail to transmit light with
¹¹ a greater overall detection efficiency — more on the details of this in Section 2.3.1.

¹² **2.3 Detecting and Recording an Event in SNO+:**

¹³ **A Journey**

¹⁴ To understand the SNO+ detector well, it is worth thinking about how the
¹⁵ information contained in a physics event, e.g. a solar neutrino interaction, gets
¹⁶ observed. This section follows the journey of such an event.

¹⁷ **2.3.1 Particle Interactions with Matter**

¹⁸ All observable physics events within the detector begin by the generation of some
¹⁹ form of ionising radiation: α , β^\pm , γ , p or n . These can be created via numerous
²⁰ processes, both exciting (e.g. $0\nu\beta\beta$ or interactions of neutrinos) and annoying
²¹ (e.g. decay of background radioisotopes): see Section 6.1.2 for some of them.
²² Regardless of their origin, these particles begin propagating through the detector,
²³ and interacting with the detector medium. A number of mechanisms then allow
²⁴ for the generation of optical-wavelength light as a result of these interactions.

Cherenkov Light Emission

Whenever a charged particle travels through a dielectric medium at speeds faster than the speed of light in that medium, light is generated from the ‘wake’ of induced dipoles. This is known as **Cherenkov light**, a process much akin to the ‘sonic boom’ that occurs when an object travels at supersonic speeds through a medium. This light emanates outwards in a cone along the direction of the charge’s travel; the angle of the cone θ_γ being purely a function of the speed of the charged particle relative to the speed of light in vacuum, β , and the refractive index of the medium $n(\omega)$ at a given frequency ω : $\cos \theta_\gamma(\omega) = \frac{1}{n(\omega)\beta}$. There is then a minimum speed necessary for Cherenkov light to be generated: $\beta_{\min}(\omega) = 1/n(\omega)$.

In addition to the characteristic cone shape of the light, the spectrum of the light generated is also distinctive. Igor Tamm and Ilya Frank determined the expected energy dE emitted per unit length travelled by the charged particle, dx , as [94]:

$$\frac{dE}{dx} = \frac{q^2}{c^2} \int_{\beta n(\omega) > 1} \omega \left(1 - \frac{1}{\beta^2 n^2(\omega)} \right) d\omega. \quad (2.1)$$

Here, q is the charge of the moving particle. The Cherenkov emission spectrum during the water phase is shown in the black dotted line of Fig. 2.2.

All SNO+ detection media allow Cherenkov light to be generated, as long as sufficiently high energy particles traverse it. In the water fill phase of the detector, Cherenkov light was the only means by which light could be generated. Light from Cherenkov emission can still be created in liquid scintillator, but it tends to be swamped by another form of light generation: scintillation.

Scintillation

For certain special classes of material, the excitation and ionisation of atomic electrons nearby a moving charged particle can lead to the generation of optical-wavelength light, in a process known as **scintillation** (often generally referred to

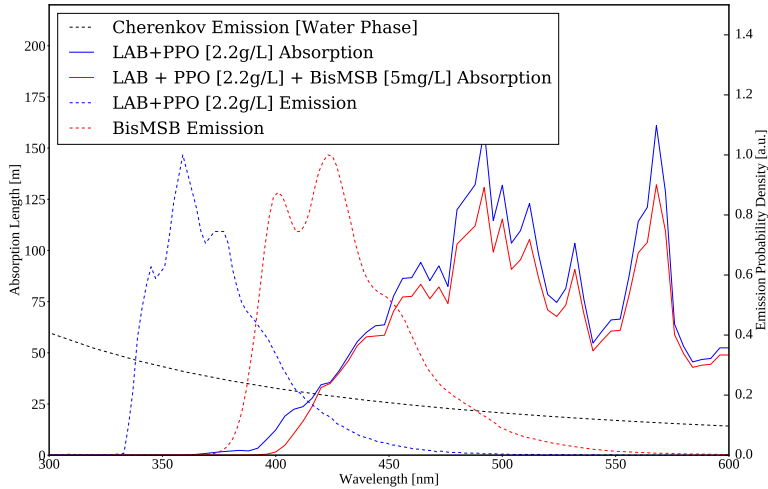


Fig. 2.2: Comparison of the SNO+ detector media’s emission and absorption properties, versus optical phase [95, 96].

as ‘luminescence’ or ‘fluorescence’). Although multiple varieties of scintillator exist, the one used in SNO+ is that of an organic liquid scintillator. For such liquids, scintillation light is generated from the de-excitation of delocalised electrons within carbon–carbon ‘ π -bonds’ [97]. A major example of these π -bonds are found in benzene rings, which are present in LAB, PPO, and bisMSB.

Because of this delocalised structure, excited atomic π -electrons can stay in what is typically the first-excited state for somewhat longer than typical excited states: lifetimes of $\mathcal{O}(10^{-9} \text{ s})$ as opposed to $\mathcal{O}(10^{-12} \text{ s})$. This is what gives scintillation light its characteristic ‘slow’ response relative to the instantaneous light generated by the Cherenkov process. Moreover, decays from this state can emit light typically in the optical-wavelength range. π -electrons can end up in the first-excited state either by direct excitation, or by ionisation followed by recombination. Because the ground state of these electrons are spin-singlet states, atomic spin selection rules [97] strongly prefer any direct excitations to stay in a spin-singlet state. As a result, so-called “inter-system crossing” from an excited singlet state to an excited triplet state is strongly suppressed.

| Component | A_i | τ_i [ns] |
|-----------|--------|---------------|
| 1 | 0.665 | 7.35 |
| 2 | 0.218 | 5.45 |
| 3 | 0.083 | 117.5 |
| 4 | 0.0346 | 425 |
| Rise | – | 0.8 |

Table 2.1: Current values used to model scintillator emission from electrons in 2.2 g/L LABPPO [98, 99].

However, ionised electrons that recombine have no such restriction, and so readily form excited triplet states. Once in such a state, the same spin selection rules strongly suppress the decay of these excited triplet electrons back down to the singlet ground state. This leads to scintillation light having, at the very least, a ‘fast’ and ‘slow’ time component. In SNO+, we currently model emission of scintillation light from LAB with 4 time components, following the timing distribution $f(t)$ given by:

$$f(t) = \sum_i A_i \left(\frac{e^{-t/\tau_i} - e^{-t/\tau_{\text{rise}}}}{\tau_i - \tau_{\text{rise}}} \right), \quad t > 0. \quad (2.2)$$

Here, A_i and τ_i correspond to the fraction of light emitted and decay constant for each component respectively, and τ_{rise} is a common rise time. The current values for these parameters used in simulations for the emission from electron tracks can be seen in Table 2.1. These were obtained by Rafael Hunt-Stokes through the fitting of tagged ^{214}Bi β -decay events within the detector with 2.2 g/L LABPPO [98]. A plot from R. Hunt-stokes showing this fit between data and simulation is shown in Fig. 2.3.

When using just a single scintillating compound, the very same energy levels that can generate scintillation light are those that can absorb it. This can be a problem for large-scale detectors like SNO+, which depend on scintillation light being unobstructed in its path to the PMTs. This problem can be addressed with

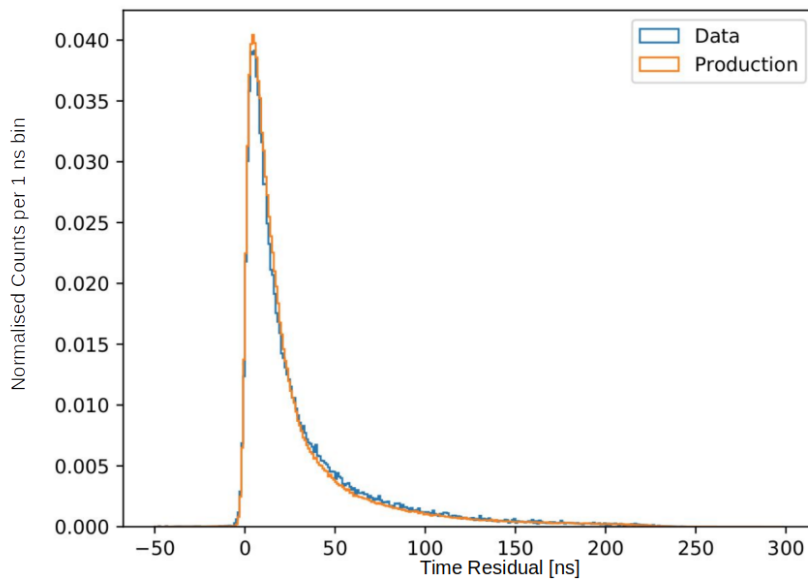


Fig. 2.3: Comparison between the observed emission time distribution of electrons from tagged ^{214}Bi β -decays and a production of matching simulated events, after fitting the timing constants. Taken from [98].

¹ the addition of another scintillating component, known (somewhat confusingly)

² as the primary fluor. In SNO+, this is the PPO added to the LAB.

³ When an LAB molecule is excited, that energy can be transferred to a PPO

⁴ molecule through what is known as a ‘non-radiative transfer’. In short, this transfer

⁵ of energy occurs not through the emission and absorption of optical photons, but

⁶ through the coupling of the molecules’ electric dipoles during a collision. When

⁷ the now-excited PPO molecule de-excites to emit scintillation light, the different

⁸ molecular structure it has generates a different emission spectrum to that of LAB.

⁹ These longer wavelengths of light are no longer able to be absorbed by the LAB,

¹⁰ allowing for a scintillator with less optical absorption.

¹¹ In SNO+ we plan on also adding in the compound BisMSB to the scintillator

¹² cocktail. This is a ‘wavelength-shifter’: scintillation light at short wavelengths is

¹³ absorbed, and then re-emitted at longer wavelengths, where the detection efficiency

¹⁴ of the PMTs is greatest (~ 420 nm). More on the properties of the PMTs in SNO+

¹⁵ can be found in Section 2.3.3. The net effect of the three scintillating components

¹⁶ within SNO+ can be seen in Fig. 2.2. Note how, as energy is transferred from one

scintillation component to another, the wavelength of light emitted gets necessarily longer as energy is lost to heat.

The light yield of a scintillator, i.e. the amount of optical photons generated per unit of energy deposited into the scintillator, is a function not just of the scintillator but also the incident particle’s ionisation strength. In particular, α particles are far more effective at exciting and ionising nearby atoms, and so can deposit far more of its energy into the scintillator per unit volume. However, the strength of this ionisation for α s can actually become at detriment to the generation of scintillation light. Empirically, scintillators follow to first order Birks’ Law for their scintillation light yield [100]:

$$\frac{dL}{dx} = S \frac{\frac{dE}{dx}}{1 + k_{\text{Birks}} \frac{dE}{dx}}, \quad (2.3)$$

where $\frac{dL}{dx}$ is the number of photons emitted per unit track length, $\frac{dE}{dx}$ is the energy loss of the incident particle per unit track length, S is the scintillator’s characteristic light yield constant, and k_{Birks} is the scintillator’s “Birks’ Constant”. For minimum-ionising particles such as a 6 MeV electron $\frac{dE}{dx} \approx 2 \text{ MeV cm}^{-1}$ [], meaning the denominator of this equation is close to 1, and so the amount of scintillation light generated is just $\frac{dL}{dx} \approx S \cdot \frac{dE}{dx}$. However, for α -particles generated in radioactive decays, this denominator can become substantial, and in the limiting case we have merely $\frac{dL}{dx} \approx \frac{S}{k_{\text{Birks}}}$. For example, α -particles are generated at 5.304 MeV from the decays of ^{210}Po nuclei [77]. However, in the 2.2 g/L LABPPO scintillator currently within SNO+, we observe that these events generate light equivalent to a 0.45 MeV event. For this scintillator, S and k_{Birks} are measured to be approximately 14,000 γ/MeV and $0.077 \text{ mm MeV}^{-1}$, respectively [101].

¹ 2.3.2 Optical Processes

² Once optical-wavelength photons have been created within the detector, various
³ processes can then occur that can hinder its path towards a PMT, and therefore
⁴ modify the observed signal. This subsection covers the main optical processes,
⁵ with a focus on Rayleigh scattering, as an understanding of this phenomenon is
⁶ critical for Chapters 3–5.

⁷ Rayleigh Scattering

⁸ Optical scattering is the general process of how light is scattered by particles
⁹ within a medium. This is fundamentally an electrodynamical process: an elec-
¹⁰ tromagnetic wave is incident on the set of particles within the medium, which
¹¹ induces these particles to oscillate within the field, and therefore generating their
¹² own electromagnetic radiation in response. Usually, this ‘scattered’ radiation has
¹³ the same frequency as that of the incident radiation, and therefore the scattering
¹⁴ is said to be *elastic*. It is possible under certain circumstances for this scattered
¹⁵ radiation to be of a longer wavelength than the incident radiation: in which case,
¹⁶ energy was absorbed by the particles and so the scattering was *inelastic*. However,
¹⁷ this latter type of scattering, also known as Raman scattering, is not relevant for
¹⁸ SNO+.

¹⁹ The general solution to elastic optical scattering was first described by Gustav
²⁰ Mie [102] and Ludvig Lorenz [103] in what is now known as *Mie Theory*. In
²¹ this theory, it is assumed that a plane wave of wavelength λ is incident on a
²² dielectric sphere of radius a . While the general solution to the problem of Mie
²³ scattering is somewhat complicated (if tractable), in certain regimes one can
²⁴ make further simplifying assumptions that substantially reduce the complexity
²⁵ of the result. In particular, if one assumes that the size of the particle is much
²⁶ smaller than the wavelength of light, and that any induced dipole moment can

actually be established in the time window allowed by the oscillation period of the electromagnetic field [104], then one can obtain *Rayleigh scattering*. This simpler case is so-called because of its initial formulation by Lord Rayleigh [105].

One can show that the differential cross-section associated with Rayleigh scattering of unpolarised light off a single particle, $\frac{d^2\sigma_{\text{Ray}}}{d\theta d\phi}(\theta, \phi)$, is given by [106]:

$$\frac{d^2\sigma_{\text{Ray}}}{d\theta d\phi}(\theta, \phi) = \frac{8\pi a^6}{\lambda^4} \left(\frac{n_{\text{par}}^2 - 1}{n_{\text{par}}^2 + 2} \right)^2 (1 + \cos^2 \theta). \quad (2.4)$$

Here, θ and ϕ correspond respectively to the polar and azimuthal angles of the scattered waves relative to the incoming wave, and n_{par} is the refractive index of the scattering particle. Most important to notice about this equation is that the cross-section follows a strong $1/\lambda^4$ dependence, meaning that short wavelengths of light will be scattered to far greater extents than that of longer wavelengths. Secondly, the light is not scattered isotropically, but according to a $1 + \cos^2 \theta$ dependence. This means that most light is either scattered directly forwards or backwards, and little gets scattered orthogonally to the direction of the incident light. This is useful when it comes to trying to measure scattering in the SNO+ detector, as it provides a handle upon which to distinguish scattered light from isotropically-emitted scintillation light.

Of course, we care about the scattering that occurs within an entire bulk medium, not just the scattering off of a single molecule. From a macroscopic perspective, the key quantity of interest is a material's *Rayleigh scattering length*, l_{Ray} : the mean distance a photon is expected to travel before Rayleigh scattering. One can show that, assuming the above differential scattering cross-section, the Rayleigh scattering length is given by [107]:

$$l_{\text{Ray}} = \left[\frac{16\pi}{3} R \right]^{-1}. \quad (2.5)$$

¹ R is the *Rayleigh ratio*, $R = \frac{1}{V} \frac{d^2\sigma_{\text{Ray}}(90^\circ)}{d\theta d\phi}$, where V is the volume taken up by
² one scattering particle within the medium. R is then equivalent to the power of
³ the scattered light per unit volume of the scattering medium per unit incident
⁴ intensity at $\theta = 90^\circ$.

⁵ This can lead to a few changes to Rayleigh scattering that are worth noting.
⁶ Firstly, unlike for a single particle, the electric polarisability of a material can be
⁷ *anisotropic*. Anisotropic materials have a modified angular dependence on their
⁸ differential cross-section, governed by the *depolarisation ratio*, δ . In particular, the
⁹ $(1 + \cos^2 \theta)$ dependence becomes $\left(1 + \frac{1-\delta}{1+\delta} \cos^2 \theta\right)$. For isotropic materials, $\delta = 0$,
¹⁰ and so the angular dependence reduces to the original form.

¹¹ Secondly, the above model has been shown to be insufficient to describe liquids
¹² or solids [108], because of the non-negligible strength of their inter-molecular forces.
¹³ Fortunately, Einstein [109], Smoluchowski [110], and Cabannes [111] developed
¹⁴ a theory for describing how photons can scatter off of the local charge density
¹⁵ fluctuations that naturally are present in a medium because of the thermal motion
¹⁶ of molecules. The theory shows that the Rayleigh ratio of a medium is related to
¹⁷ the medium's dielectric constant, ε , by:

$$\text{¹⁸} R = \frac{\pi^2}{2\lambda^4} \left[\rho \left(\frac{\partial \varepsilon}{\partial \rho} \right)_T \right]^2 k_B T \kappa_T \frac{6 + 6\delta}{6 - 7\delta}, \quad (2.6)$$

¹⁹ where ρ is the density of the medium, $\left(\frac{\partial \varepsilon}{\partial \rho} \right)_T$ is the partial derivative of the dielectric
²⁰ constant with respect to a changing density assuming a constant temperature T ,
²¹ k_B is the Boltzmann Constant, and κ_T is the medium's isothermal compressibility.
²² This latter quantity is given by the rate of change of volume given a changing
²³ pressure of the medium, all at a constant temperature.

²⁴ Furthermore, the Eykman Equation [107, 112] has been shown to be an
²⁵ effective empirical formula relating how ε is impacted by density fluctuations to

the medium's refractive index, n_{med} :

$$\rho \left(\frac{\partial \varepsilon}{\partial \rho} \right)_T = \frac{(n_{\text{med}}^2 - 1)(2n_{\text{med}}^2 + 0.8n_{\text{med}})}{n_{\text{med}}^2 + 0.8n_{\text{med}} + 1}. \quad (2.7)$$

This leads to a final empirical formula for the Rayleigh scattering length:

$$l_{\text{Ray}} = \left[\frac{8\pi^3}{3\lambda^4} \left(\frac{(n_{\text{med}}^2 - 1)(2n_{\text{med}}^2 + 0.8n_{\text{med}})}{n_{\text{med}}^2 + 0.8n_{\text{med}} + 1} \right)^2 k_B T \kappa_T \frac{6 + 3\delta}{6 - 7\delta} \right]^{-1}. \quad (2.8)$$

In-situ measurements of the scattering of the UPW were made indirectly during SNO [113], and then subsequently in the water phase of SNO+ had a divisive scaling factor of $(1.28 \pm 0.05(\text{stat.}) \pm 0.14(\text{sys.}))$ determined by Esther Turner [114]. Ex-situ measurements of the Rayleigh scattering within LAB and LABPPO have also been made by groups in both the SNO+ and JUNO Collaborations [115–119], but no in-situ measurements have been made prior to this thesis. Fig. 2.4 shows the scattering lengths for UPW, LAB, and 2 g/L LABPPO from these measurements, with the lines showing what is currently being used in simulations for SNO+. Measurements of the scattering lengths in scintillator are a major focus of Chapters 3–5.

Absorption and Re-emission

In addition to scattering, an optical medium is also able to absorb light that propagates through it. For a given medium, the *absorption length* l_{abs} is analogous to l_{Ray} described above, and is typically strongly a function of wavelength. For most materials, absorbed light is forever lost, converted into heat. However, for the special case of scintillators, re-emission of absorbed light is possible: this is because of the physics described in Section 2.3.1.

Because both scattering and absorption impede a photon's ability to propagate through a medium directly, it is often possible to measure their combined impact

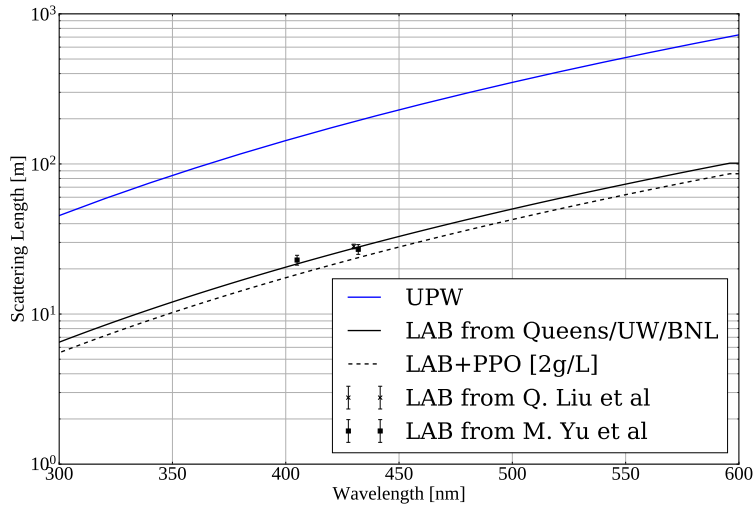


Fig. 2.4: Scattering lengths used in simulation for UPW, LAB, and 2 g/L LABPPO. The UPW shape is taken from indirect in-situ measurements in [113] with an additional divisive scaling factor from [114]. The LAB shape is taken from ex-situ measurements by SNO+ members at Queen’s University, University of Washington, and Brookhaven National Laboratory [115, 116]. An additional divisive scaling factor of 1.176 due to PPO was made by [117]. For comparison, measurements by members of the JUNO Collaboration for LAB are also shown [118, 119].

1 through what is known as the attenuation/extinction length, l_{ext} :

$$2 \quad \frac{1}{l_{\text{ext}}} = \frac{1}{l_{\text{abs}}} + \frac{1}{l_{\text{Ray}}}. \quad (2.9)$$

3 In the water phase, the ‘Laserball’ calibration system was used by Ana Sofia Inácio
4 to measure various optical properties of the detector, including the extinction
5 lengths of the UPW and acrylic as a function of wavelength [79, 85]. Using the
6 water phase scattering measurements made by E. Turner, Eq. 2.9 allowed for the
7 estimation of the absorption lengths of these two materials, shown in Figure 2.5.
8 Measurements of the extinction length in the scintillator phase is discussed in
9 detail in Chapter 5.

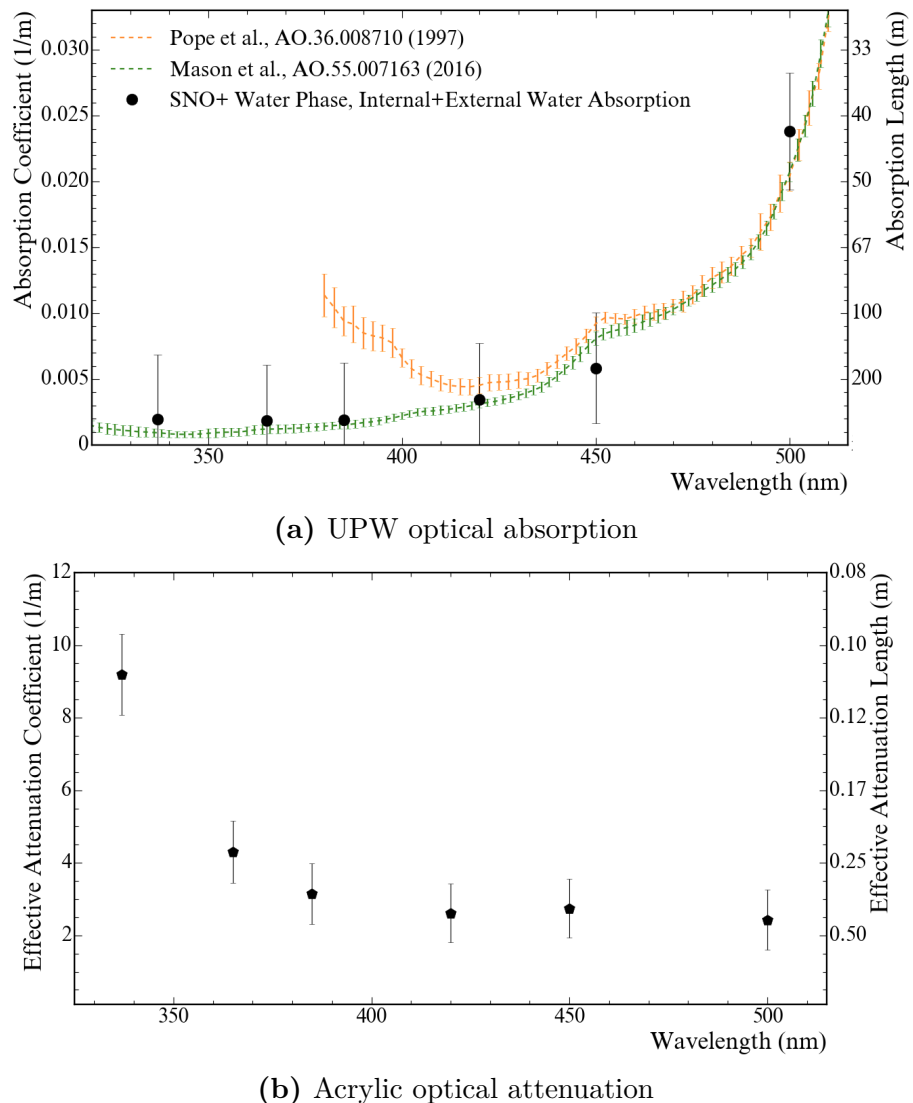


Fig. 2.5: Properties of the UPW and acrylic in the water phase, measured by A. S. Inácio in [79, 85].

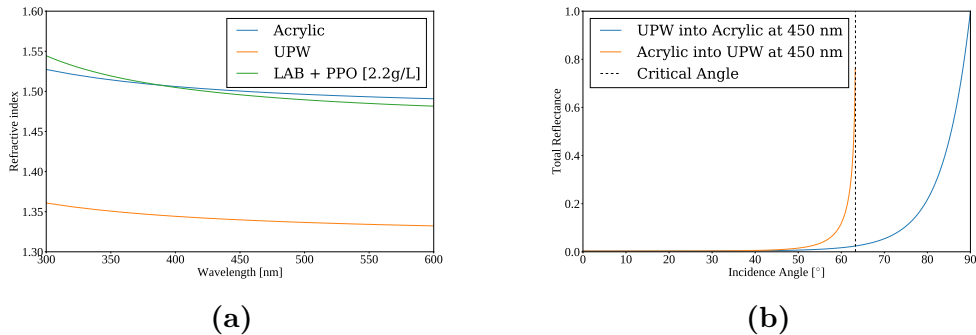


Fig. 2.6: (a): Refractive indices of acrylic, UPW, and LABPPO as a function of wavelength. The values for acrylic and UPW come from model fits to data made in SNO [113, 120], whereas those for LABPPO come from data taken in [121]. (b): Reflectance of an unpolarised beam of light at 450 nm going between UPW and acrylic.

1 Surface reflection and refraction

2 When light travels through the boundary of one medium to another, both reflection
 3 and refraction can be possible, depending on the relative refractive indices of
 4 the two media as well as the angle of incidence. The refractive indices of the
 5 UPW, acrylic, and LABPPO are shown as a function of wavelength in Figure 2.6a.
 6 Note that, for most optical wavelengths, LABPPO has a very close refractive
 7 index to acrylic, whereas UPW is somewhat farther away. By consequence,
 8 negligible refraction is expected in most cases for light travelling between the
 9 liquid scintillator and the acrylic; however, substantial refraction and reflection are
 10 possible for light travelling between acrylic and UPW. Because of this, isotropically-
 11 emitting point-like physics events within the AV that are close enough to the
 12 acrylic will have some of their light undergo Total Internal Reflection (TIR) at
 13 the AV, reflecting back into the AV instead of continuing outward into the outer
 14 water.

15 Even when not undergoing TIR, some light at a boundary will still reflect.
 16 The fraction of light that reflects is known as the *reflectance* R , compared to that
 17 which is able to transmit through the boundary, the *transmittance* $T = 1 - R$.

The *Fresnel Equations* determine the reflectance of an interface [122]:

$$R_s = \left| \frac{n_1 \cos \theta_i - n_2 \cos \theta_t}{n_1 \cos \theta_i + n_2 \cos \theta_t} \right|^2, R_p = \left| \frac{n_1 \cos \theta_t - n_2 \cos \theta_i}{n_1 \cos \theta_t + n_2 \cos \theta_i} \right|^2, \quad (2.10)$$

where R_s and R_p are the reflectances of s - and p -polarised light, n_1 and n_2 are the refractive indices of the first and second optical media, and θ_i and θ_t are the angles of incidence and refraction, respectively. For SNO+, we are only interested in unpolarised light, so the total reflectance $R = (R_s + R_p)/2$.

The total reflectance going from UPW into acrylic, as well as from acrylic into UPW, for an unpolarised beam of light with wavelength 450 nm is shown in Fig. 2.6b. For the latter case, the critical angle at which TIR occurs is clear.

2.3.3 Detection by PMTs

The final step for photons in our journey is detection by a PMT. Almost all PMTs in SNO+ are of the Hamamatsu R1408 design [40]. These PMTs within SNO+ are housed within an 18-segment reflecting Winston cone known as a ‘concentrator’. The combined PMT–concentrator ‘bucket’, shown in Fig. 2.7a, is designed to maximise the collection efficiency of light emanating from within the AV, whilst minimising the collection efficiency of light outside the AV [123]. The so-called ‘angular response’ of the PMT buckets has been measured in both SNO and SNO+ using the Laserball, which describes the relative collection efficiency as a function of the polar angle of the incident light ray relative to the direction in which the PMT bucket points. The results of this can be seen in Fig. 2.7b.

Once a photon is incident on the PMT’s photocathode, it is possible for that photon to be absorbed and generate a photoelectron. The probability of this happening is governed by the photocathode’s Quantum Efficiency (QE) at the photon’s wavelength, as well as the collection efficiency of a photoelectron onto the first dynode of the PMT. The combined measured efficiency of PMTs tested

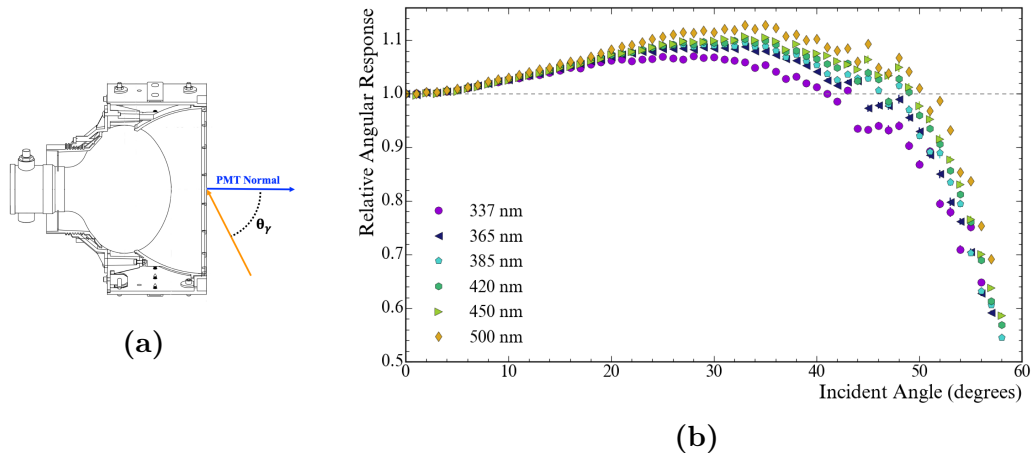


Fig. 2.7: (a): Diagram of the PMT and concentrator ‘bucket’ used within SNO+, showing also the definition of the incidence angle. (b): Plot of the measured relative angular response of the PMTs in SNO+, as a function of both incidence angle and wavelength. Both figures taken from [85].

¹ *ex-situ* for SNO can be seen in Fig 2.8. Once this photoelectron has been created,
² the dynodes within the PMT generate a cascade of electrons that produce an
³ observable voltage signal. The dynamics of this cascade are such that there is
⁴ a natural spread of possible times between the creation of a photoelectron and
⁵ the generation of the voltage pulse in the PMT’s anode. This is known as the
⁶ ‘Transit Time Spread’ (TTS) of the PMTs: for SNO+, the RMS of the TTS for
⁷ the R1408-type PMTs is ~ 1.7 ns [40].

⁸ Finally, if multiple photons generate photoelectrons on the same PMT close
⁹ enough in time, the amount of charge generated increases in proportion to the
¹⁰ number of photoelectrons (npe). Much like with the transit time, the strength
¹¹ of the signal observed by the PMT is governed by a distribution, a function
¹² of the npe generated. Examples of these distributions can be seen in Fig. 2.9.
¹³ The relatively large widths of these charge distributions precludes the ability to
¹⁴ straightforwardly determine the npe purely from charge when the npe is small.
¹⁵ To work around this, various techniques can be employed to try and estimate the
¹⁶ npe in a given PMT — an example of one such method can be seen in Section 4.2.

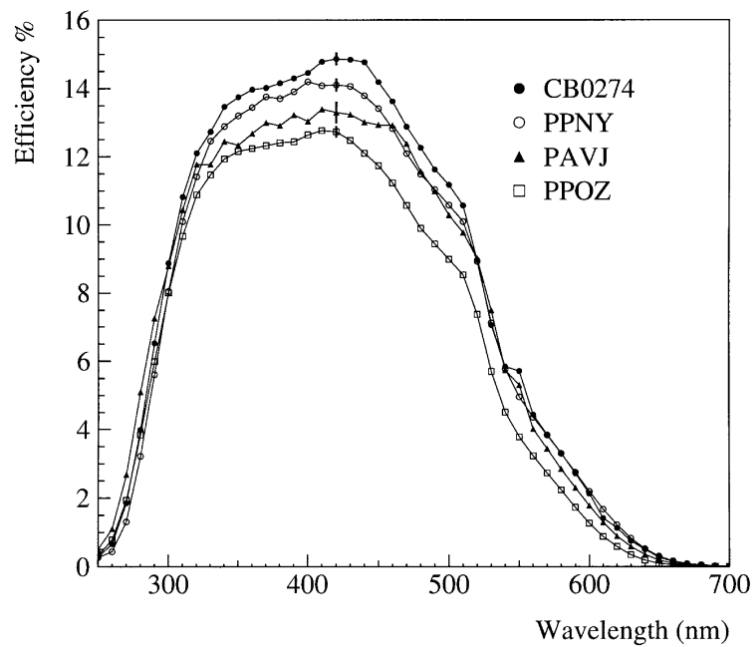


Fig. 2.8: Efficiencies of four R1408-type PMTs tested for calibration by [124].

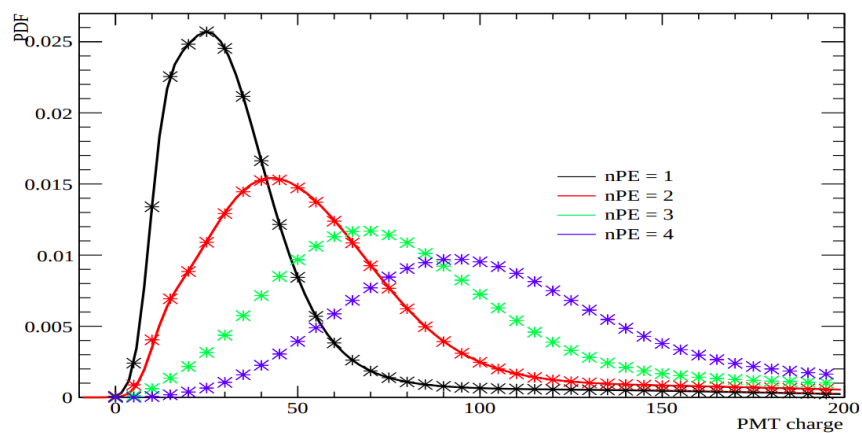


Fig. 2.9: Example charge spectra for a PMT as a function of the true npe generated. Figure taken from [125].

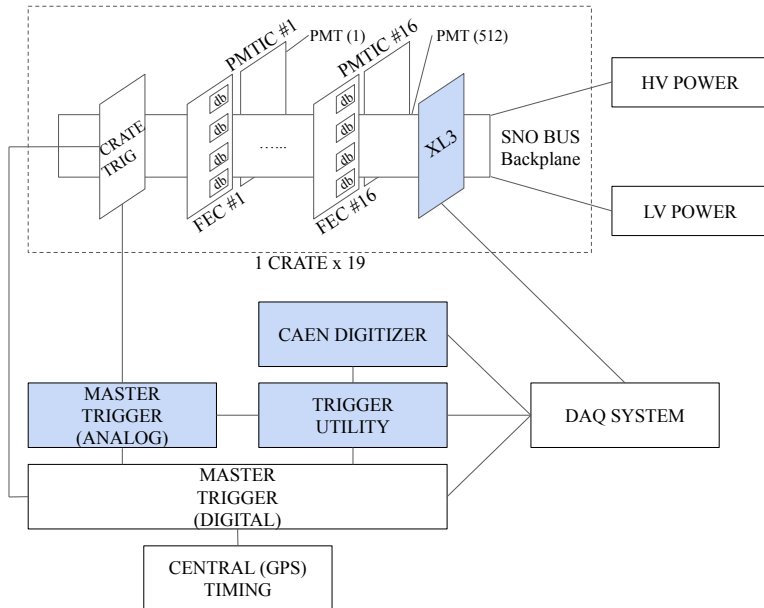


Fig. 2.10: Schematic of the front-end electronics used for data acquisition and triggering in SNO+, taken from and discussed in [84].

2.3.4 Data Acquisition and Triggering

Once a signal reaches the cable attached to a PMT, it travels along up to the front-end electronics on the deck above the detector. The job of these electronics, known as the data acquisition (DAQ) and triggering system, is to convert raw electronic signals from the PMTs into recorded digital ‘events’ that can be used for analysis. A schematic showing the setup of the electronics is shown in Fig 2.10, with full details in [84].

A signal passes first through the PMT Interface Card (PMTIC), which then sends it through to one of the Daughter Boards (DBs) which are stored on Front-End Cards (FECs) within one of 19 electronic crates on deck. The DBs determine if the analogue signal along a given PMT channel has crossed a pre-defined charge threshold, at which point we say that we have detected a ‘hit’ on that PMT’s channel. When this occurs, the DB performs a set of important actions:

1. Begins a timer for that channel, in the form of a Time-to-Amplitude Con-
2 verter (TAC). TAC also corresponds to the resulting analogue voltage on
3 the output of the TAC being measured.

4. Begins integrating the total charge signal for that channel in three ways,
5 known as QHS, QHL, and QLX. These correspond to using different inte-
6 gration times and gain settings.

7. Generates trigger pulses for that channel for each available trigger type.
8 Three main trigger signals are the ‘N20’ (a square pulse for 20 ns), ‘N100’
9 (a square pulse for 100 ns), and ‘ESUMHI’ (a pulse copying the shape of
10 the voltage signal for that channel). The reason for these names will be
11 explained shortly.

Whilst the TAC, QHS, QHL, and QLX are being calculated, the trigger signals
from each channel are sent over to the Crate’s Trigger Card (CTC), where the
signals are then summed for each trigger type. These crate-level trigger signals are
then sent over to the 7 detector-level Analogue Master Trigger Cards (MTC/A+),
which further sum the signals by trigger type from all the crates in the detector.
It is at this point of the process where the names of the trigger types becomes
clear: the combined N20 and N100 signals are proportional to the total number
of hit PMTs within a 20 ns and 100 ns time window, respectively, whilst the total
ESUMHI signal corresponds to the total charge seen over all the PMTs.

If these trigger signals go above certain pre-defined thresholds, then a signal
is sent for that trigger type to the Digital Master Trigger Card (MTC/D). The
MTC/D receives all trigger signals from the detector, and if a given trigger type
has been ‘masked in’ (i.e. activated) the Card will generate a Global Trigger
(GT) for the detector with a time stamp from its 50 MHz clock. Under certain
circumstances, such as calibrations, a trigger signal can be generated externally
and asynchronous to the MTC/D: these are ‘EXTA’ triggers. Any such EXTA

¹ trigger signal is first handled by an electronics box named ‘TUBii’ (Trigger Utility
² Board Mark ii), before then being passed onto the MTC/D. TUBii functionality
³ will become relevant when discussing the calibration electronics described in
⁴ Chapter 3.

⁵ Once a GT signal is generated, it is then sent back to all the CTCs, which
⁶ then orders the integration of time and charge to be stopped on all channels for
⁷ that crate. The time and charge information that has been temporarily stored
⁸ on each channel’s CMOS chip on the FEC is then sent to the crate’s ‘XL3’ card,
⁹ which packages the crate’s raw information via ethernet over to a set of computers.
¹⁰ The trigger signals for a triggered event are also digitised by a CAEN brand
¹¹ Analogue-to-Digital Converter (ADC), and sent to the same DAQ computers. The
¹² total window of time in which data is gathered from one GT signal is 400 ns, with
¹³ data from up to 180 ns before and 220 ns after the GT has arrived. There is then
¹⁴ a necessary ‘dead time’ of 420 ns after a given GT has been given in which no
¹⁵ further GTs can be made.

¹⁶ Finally, the raw data from the crates and trigger system arrives in a set of
¹⁷ computers, which organise all of this into an individually-packaged ‘event’, stored
¹⁸ on disk in the ‘Zebra Database’ (ZDAB) format. A given built event contains the
¹⁹ TAC and charge information from each hit PMT, the CAEN digitised waveforms,
²⁰ a unique identifying number for that triggered event (the GTID), as well as the
²¹ times from both the MTC/D’s 50 MHz clock and a GPS-calibrated 10 MHz clock.
²² The former time is used for measuring relative times between events whilst the
²³ latter is used for knowing the time of day of an event: both are used in Chapter 6.

²⁴ **2.3.5 Operation of the Detector**

²⁵ Control of the detector’s DAQ system is handled through a custom-built GUI
²⁶ known as ORCA [126]. This program allows operators of the detector to modify

settings in the detector electronics at both a low- and high-level. It also allows operators to monitor the current status of the detector, such as voltage and current levels within each crate.

ORCA allows for the detector to have its data split into ‘runs’ of different types. For the majority of the time, the detector is run in the ‘Physics’ mode, with individual runs split into 1 hour periods. It is this data that is used for almost all high-level physics analyses, such as the one described in Chapter 6. To help with the movement and processing of data, runs of raw data are split into ZDAB files of maximum size 1 GB. Because of this, the number of files generated per run is proportional to the trigger rate of the detector. In the current 2.2 g/L LABPPO scintillator phase under nominal conditions, the trigger rate is ~ 2.5 kHz, leading to 15 ZDAB files being generated per run of 1 hour in length.

Other detector run types include ones for detector maintenance, as well as for calibrations of various kinds. During certain calibration runs, data can be further split into ‘subruns’ where necessary. This allows for data taken from a given calibration source to have the different settings used (e.g. different wavelength settings) all kept within one run, but still appropriately separated. Operation of specific calibration sources, including the one described in Chapter 3, can be performed through the ORCA GUI.

2.4 Calibrations and Detector Modelling

Once the raw data from triggered events has been stored in files, certain extra steps must be taken before effective analysis of that data can be achieved. This section covers those steps.

¹ 2.4.1 Detector Monitoring

² No data taken from the detector can reasonably be used for analysis unless its
³ quality has been approved. This is done in a number of ways on SNO+. Firstly,
⁴ a number of automated systems monitor all aspects of the detector, including
⁵ voltage levels in the crates, trigger rates, as well as ‘slower’ quantities such as
⁶ the tensions on the ropes holding the AV in place. Problems in any of these
⁷ measured parameters trigger an automatic alarm system, which notifies a human
⁸ detector operator. A human detector operator monitors the detector 24/7 whilst
⁹ the detector is live.

¹⁰ In addition to systems that monitor whether anything has gone wrong, infor-
¹¹ mation about the state of the detector during each run is stored in a database
¹² known as RATDB. This information includes, amongst other things, a recording of
¹³ which PMT channels have actually been raised to high voltage for that run, as
¹⁴ well as any channels/cards/crates that have been flagged for having a known poor
¹⁵ data quality (e.g. being overly noisy).

¹⁶ 2.4.2 Electronic and PMT Calibrations

¹⁷ The lowest level of calibrations performed in SNO+ are the Electronic and PMT
¹⁸ Calibrations: ECAs and PCAs, respectively. These calibrations convert the raw
¹⁹ time and charge values recorded by the DAQ into quantities that can actually be
²⁰ used in analysis.

²¹ During an ECA, two main quantities are measured. Firstly, because of noise
²² the integrated charge measured on each channel is offset by some amount. This
²³ offset, known as the ‘pedestal’, is recorded for each channel. The other quantity
²⁴ is the ‘time slope’ for each channel, which allows one to convert from the ADC
²⁵ TAC counts into an uncalibrated hit time of that channel’s PMT in ns. Both
²⁶ of these quantities are measured by sending external signals to channels in the

crates, forcing them to start measuring TAC and charge even though no PMTs were actually hit. Running ECAs also enable us to spot any channels with unusual behaviour, so that they are not used during analysis. ECAs are typically done on a fortnightly basis, or after maintenance to the DAQ system has been performed.

Using ECAs alone is not enough to have fully-calibrated time and charge data. The lengths of cables between PMTs and PMTICs are all slightly different, leading to differences in the so-called ‘cable delay’ of each channel. This means that two PMTs that have a photoelectron generated at the same time can generate slightly different TAC values. Furthermore, because the start time of the TAC is determined by when the channel’s signal goes above a constant threshold, if a signal is very large (e.g. when numerous photoelectrons have been generated on one PMT) then the start time of the TAC will be systematically earlier. This is known as the ‘time walk’. Both of these quantities get measured during PCAs.

PCAs can be performed by either the Laserball or by the TELLIE calibration system. The latter is a series of 92 optical fibres attached at various points of the PSUP, through which optical-wavelength light can be fired from LEDs. TELLIE is the Timing subsystem of the ELLIE calibration system: the Embedded LED/Laser Light Injection Entity. The other two fibre-based optical calibration subsystems, AMELLIE and SMELLIE, are introduced in Section 2.4.3. For both the Laserball and TELLIE calibration systems, the cable delay and time walk are measured by firing light from the source at a known time and with a known hit occupancy, and observing when the signal arrives in each PMT channel.

On top of calibrating the PMT hit times, PCAs also further calibrate the charge information. In particular, the charge spectrum generated by a single photoelectron is determined for each channel. This allows us to convert the pedestal-corrected charge ADC counts into an approximate number of photoelectrons.

Using the data gathered from both ECAs and PCAs, the raw data stored in ZDABs is processed into a new file format known as RATDS files. These files

¹ contain all the information of an event, but now the timing and charge information
² have been calibrated. It is this file type used in the optical calibration work of
³ Chapters 3–5.

⁴ 2.4.3 Energy and Optical Calibrations

⁵ The next stage of calibrating the detector is modelling its optical properties. These
⁶ properties include all the processes covered in Section 2.3.2, such as scintillator
⁷ emission, optical absorption, re-emission, and Rayleigh scattering. This is crucial,
⁸ as it allows us to reconstruct information about events within the detector: more
⁹ on event reconstruction shortly.

¹⁰ In addition to deployments of the Laserball (discussed in Section 2.3.2), two
¹¹ further calibration sources are used in SNO+ to measure properties of light
¹² propagation: AMELLIE and SMELLIE. These are the ‘Attenuation Module’ and
¹³ ‘Scattering Module’ for the ELLIE calibration system. Like TELLIE, AMELLIE
¹⁴ and SMELLIE consist of optical light sources that shine through optical fibres
¹⁵ into the detector. The former uses LEDs from TELLIE, whilst the latter uses
¹⁶ optical wavelength lasers. Despite the names both subsystems are similar enough
¹⁷ that they are both capable of measuring attenuation and scattering within the
¹⁸ detector. More details about the SMELLIE hardware can be read in Chapter 3.

¹⁹ Another critical component of the detector to calibrate well is the energy
²⁰ response: given a specific amount of energy deposited in the water/scintillator,
²¹ how many hits are observed? For this, a number of radioactive sources are used
²² at a variety of energies. In the scintillator phase, there are three main sources.
²³ The first is an americium-beryllium (AmBe) source inherited from SNO [127],
²⁴ which contains ^{241}Am that α -decays, which can be captured by the ^9Be within
²⁵ the source. This capture leads to the emission of a neutron as well as production
²⁶ of a ^{12}C nucleus, which 60% of the time is in an excited state. When this excited

state decays, a 4.4 MeV γ is emitted promptly. Eventually the neutron is captured by hydrogen in the detector, leading to a characteristic 2.2 MeV delayed γ being generated [84]. Both the prompt and delayed peak energies from the AmBe source can be used for energy calibration. In addition to this, one can calibrate the neutron detection efficiency with the AmBe source [127], which is important for the analysis of antineutrino IBD events.

Another deployable radioactive source is the ^{16}N source, also originally used for SNO [128]. The ^{16}N isotope β -decays to ^{16}O , with a distinctive 6.1 MeV γ also being generated 66% of the time. It is the γ that can make it out to the detector, whilst the β can be tagged by a block of scintillator and PMT held within the source container.

In theory, sources can be deployed both within the AV ('internally') and in the water shielding ('externally'). Both internal and external deployments were used for the optical calibration of the water phase with the Laserball [85]. Although external deployments during the scintillator phase with the Laserball, N16, and AmBe sources have been made, there have been no such internal source deployments. This is a result of the substantial work currently underway [129] to overhaul the internal deployment hardware, in order to satisfy the much more stringent radiopurity requirements of the scintillator phase over the water phase.

Alongside these deployed sources, a different kind of radioactive source has been used during the scintillator phase for energy calibration: the existing radioactive background spectra within the detector. Backgrounds such as ^{14}C , ^{210}Po , $^{214}\text{BiPo}$, and ^{208}Tl all have distinctive peaks in the energy spectrum of SNO+ during the scintillator phase, and can be used to calibrate the scintillator's energy response. Using $^{214}\text{BiPo}$ events in particular has been used for energy scale calibration with the solar oscillation analysis, as discussed in Section 6.2.3.

¹ 2.4.4 Event Reconstruction

² Once the detector has been calibrated, event ‘reconstruction’ becomes possible.
³ This is the process of deriving high-level physics quantities about a triggered event
⁴ within the detector, based upon the calibrated hit information. In SNO+, our
⁵ base assumption in most cases of event reconstruction is that a triggered event was
⁶ due to a single electron track. Reconstructing an event involves running a number
⁷ of algorithms, which in the scintillator phase are together called the **ScintFitter**.

⁸ The first critical pieces of information that gets determined by **ScintFitter**
⁹ is the event’s position and time. The reconstructed position corresponds to the
¹⁰ point in the detector where the triggered event most likely came from (assuming
¹¹ the event was approximately point-like in extent), whilst the reconstructed time
¹² is the starting emission time of the event, relative to the event’s trigger time. The
¹³ position of an event is critical to know, as far fewer background events occur near
¹⁴ the centre of the detector compared to the edges. It is also important to know the
¹⁵ emission time of an event, as this allows us to build the so-called ‘time residual’
¹⁶ (t_{res}) distribution of an event. For a point-like physics event in the detector, t_{res}
¹⁷ for a given PMT hit is defined as:

$$\text{18} \quad t_{res} = t_{\text{hit}} - t_{\text{TOF}} - t_{\text{emm}}, \quad (2.11)$$

¹⁹ where t_{hit} is the calibrated hit time of the PMT, t_{TOF} is the time one expects
²⁰ for light to travel directly from the reconstructed position to that PMT (the
²¹ time-of-flight), and t_{emm} is the reconstructed emission time.

²² Whilst a number of algorithms have been developed for reconstructing position
²³ and time in SNO+, they all work on the same basic principle. Because of the
²⁴ spherical symmetry of the detector, if an event occurs at the centre of the detector

one expects direct light to hit PMTs throughout the detector at the same time¹.
 However, if an event happens some distance away from the detector’s centre then
 direct light will arrive at the PMTs it is closer to sooner. Therefore, by looking
 at the distribution of hit times for PMTs that were hit earliest as a function of
 the PMTs’ positions in the detector (ignoring PMT hits that arrived much later,
 presumably because the photon paths were not direct) one can try and estimate
 where the position of the event was. Reconstructed positions and reconstructed
 times are linked by the time residual equation described above.

Currently on SNO+, a likelihood-based approach is used to reconstruct position
 and time. The algorithm endeavours to maximise the combined likelihood of
 the observed calibrated hit times of the hit PMTs, given proposed points in the
 four-dimensional (position, time) parameter space [130–132]. However, regardless
 of algorithm there are two factors that limit the position and timing reconstruction
 of an event. The TTS of the PMTs used as well as the speed of the scintillator
 emission timing defines the fundamental timescale — and hence also length scale
 — by which events can be reconstructed. Secondly, if more photons are able to
 generate prompt hits in the detector from a given event, then more information
 can be used to determine the position and time. Under current conditions, a
 2.5 MeV event in the centre of the detector will have a position resolution of
 100 mm [133].

The other critical piece of reconstructed event information is the event’s energy.
 More precisely, this is the kinetic energy of an electron that has been assumed
 to have generated the event. By consequence, events due to α -decay will obtain
 reconstructed energies well below the actual energy of the α particle, because of
 scintillator quenching (see Section 2.3.1 for details).

¹It is possible for the centre of the AV and PSUP to not be completely aligned, i.e. there is an ‘AV offset’. Then, the spherical symmetry can be very slightly broken by refraction through the AV. Fortunately, we account for this when coordinating our position fitters.

At its simplest, assuming that an event is from an electron of moderate energy (e.g. at 2.5 MeV), then we can expect the number of PMT hits observed to be directly proportional to the energy of the event. Given that the number of hits observed in an event (called the `nhit`) is governed by a Poisson distribution, then the uncertainty in energy will just be proportional to the square root of the number of hits. As a result, the reconstructed energy resolution in SNO+ is determined by the scintillator’s light yield and absorption length, as well as the coverage and QE of the PMTs.

There are second-order corrections to the energy reconstruction that need to be considered to minimise bias. At low energies, scintillator quenching becomes non-negligible, so an understanding of the scintillator’s Birks’ constant is needed. At high energies, many PMTs will have had multiple photoelectrons generated, so merely using the `nhit` will give an underestimate of the true energy. Finally, the detection efficiency of photons is non-uniform as a function of position in the detector. The current energy reconstruction algorithm used within SNO+ attempts to deal with all of these effects [134, 135].

After position, time, and energy reconstruction, **ScintFitter** calculates a number of additional quantities from what are known as classifiers. These describe a wide number of properties about an event, often using the derived t_{res} distribution of an event as the basis for classification. Some examples of classifiers used in analysis are discussed in Section 6.1.2.

All Physics data runs, as well as certain calibration data such as AmBe and ^{16}N , has the **ScintFitter** algorithm run over it after having been processed for time and charge calibration. This results in what is known as a fully-processed RATDS file, as well as a new file type known as an `ntuple`. This latter file type has much of the hit-level information removed, and contains only event-level information such as the reconstructed energy and position. Because these files are

much smaller, they are the ones typically used in the high-level physics analyses
on the experiment, such as the one described in Chapter 6.

2.4.5 Event Simulation

Simulations of events in SNO+ are performed using the software **RAT** [84]. Built
on the **GEANT4** particle physics software framework, **RAT** is capable of simulating
all aspects of the physics of an event within the detector via a Monte Carlo (MC)
approach. This includes any particle physics that defines an event’s generation,
propagation and interactions of those particles in the detector media, the generation
of light by both scintillation and Cherenkov processes, the propagation of that light,
as well as the detection of that light by PMTs and simulation of the expected DAQ
response. **RAT** is then used to process both simulation and data in the same way.
In addition to being highly customisable, **RAT** can use the **RATDB** tables generated
from a given data run when simulating to try and match those particular run
conditions as closely as possible. **RAT** also offers a suite of tools to assist with
analysis of data. The software is constantly being updated with new features —
the work done in this thesis uses **RAT** versions between 6.18.8 and 7.0.9, inclusive.

Chapter 3

1

The SMELLIE Calibration

2

System

3

There's a certain Slant of light,

Winter Afternoons —

That oppresses, like the Heft

4

Of Cathedral Tunes —

EMILY DICKINSON

As mentioned in Section 2.4.3, one of the principal systems for calibrating the optics of the SNO+ detector is SMELLIE. This calibration device consists of 5 different optical wavelength lasers able to be fired through 15 optical fibres, whose endpoints are attached to the PSUP. A collimator is attached at the end of each fibre, ensuring the emitted light forms a narrow beam across the detector. A diagram of SMELLIE in the detector is shown in Fig. 3.1.

5

6

7

8

9

10

The primary goal of SMELLIE is the measurement and monitoring of optical scattering within the detector over the lifetime of the experiment. By firing light from SMELLIE into the detector, some fraction of the photons will be scattered by the detector medium, a fraction of those scattering at large angles relative to

11

12

13

14

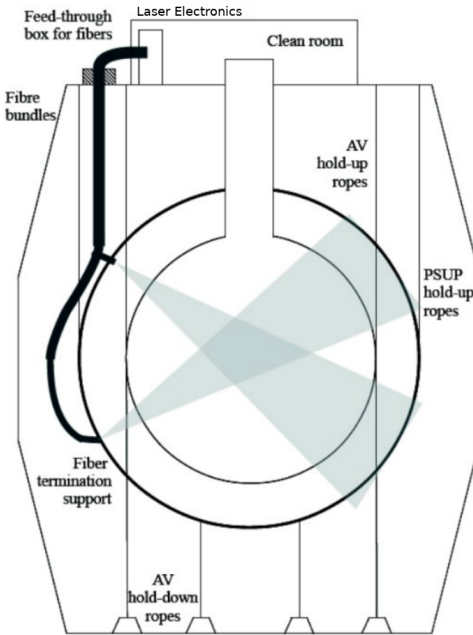


Fig. 3.1: Diagram of the SMELLIE calibration system within SNO+. Modified from [136].

the direction of the SMELLIE beam. This strongly scattered light can be detected by PMTs far from the ‘beamspot’, and will also arrive substantially later than light which travelled directly from the fibre to those PMTs. By isolating this scattered light signal, and comparing the quantity observed in data to equivalent simulations with varying scattering lengths, in principle one can measure the detector medium’s scattering length. If one takes SMELLIE data with various wavelengths of light at various points in time, one can get a dynamical picture of the optical scattering in SNO+. An analysis of optical scattering in the scintillator phase is made in Section 5.2.

Another substantial measurement that can be made with SMELLIE is the extinction length of the detection media as a function of wavelength and time. This can be done by comparing the fraction of light emitted by the fibre that gets observed in the beamspot after passing through the detector. Section 5.1 covers this analysis in the scintillator phase. Once measurements of both the scattering

length and extinction length have been made, it is then possible to derive the
absorption length from Eq. 2.9.

Both the scattering and absorption lengths of the detector medium impact
the propagation of light from physics events, and hence which PMTs get hit
along with the times of those hits. If these lengths are systematically off within
simulation, this can lead to negative consequences for reconstructing events. In
particular, for the scintillator phase, if there is more optical absorption occurring
than expected, then because not all absorbed light is re-emitted a larger fraction of
photons are lost. Therefore, because energy reconstruction is strongly dependent
on the number of PMT hits observed in an event, the energy of events will be
systematically under-estimated. Alongside this, light that is re-emitted will only
do so after some time delay, and the direction of this re-emission unlikely to be in
the same direction as before. This leads to systematic changes in the observed time
residual distributions, impacting position reconstruction, as well as any classifiers
that use the time residual distribution.

If there is more optical scattering than expected within the scintillator, this
also indirectly leads to a greater loss of light because of the increased path length
that a photon will typically have to travel before being detected. By consequence,
there will be a second-order impact on the energy reconstruction from systematics
in the scattering length. Much like changes in the quantity of re-emitted light,
increasing the amount of scattering will also systematically effect the position
reconstruction and many classifiers.

A full description of the initial hardware setup of SMELLIE that was used
during the air fill and early parts of the water fill phase can be read in [137, 138].
Since then, a series of hardware upgrades have been made, with [114, 139] covering
the hardware status used in data taken throughout the water phase. Fig. 3.2
shows a timeline of the hardware upgrades as well as some of the calibration data
taking campaigns performed using SMELLIE. The current layout of the SMELLIE

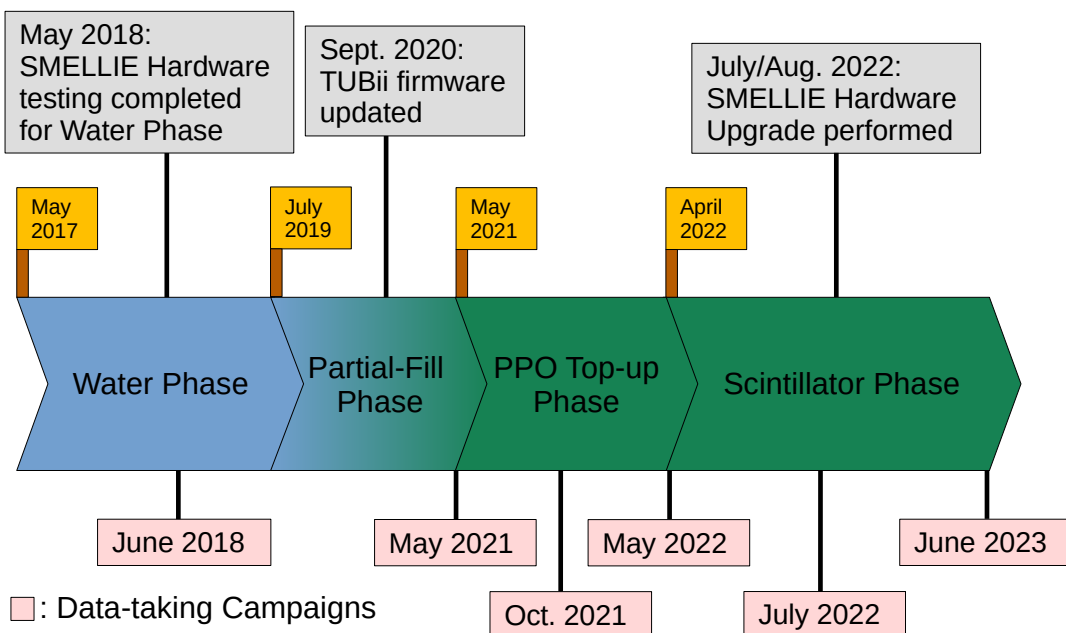


Fig. 3.2: A brief history of the SMELLIE hardware work and calibration data-taking campaigns of interest for this thesis.

¹ hardware, showing the connections between each of the devices within the system,
² can be seen in Fig. 3.3. This chapter briefly summarises the current contents of
³ the calibration system, along with descriptions of the major hardware changes
⁴ made since the water phase.

⁵ 3.1 Lasers

⁶ Fundamental to the SMELLIE calibration system are 5 optical-wavelength lasers.
⁷ Four of these are fixed-wavelength pulsed-diode laser heads from the company
⁸ PicoQuant. These ‘PQ’ laser heads each emit with a different narrow wavelength
⁹ spectrum, peaking at 375 nm, 407 nm, 446 nm, and 495 nm. These are referred
¹⁰ to as the PQ375, PQ407, PQ446, and PQ495 lasers, respectively. In addition to
¹¹ these lasers, a SuperK Compact laser made by NKT Photonics (hereafter referred
¹² to as the SuperK laser) is also used¹. Unlike the PQ laser heads, the SuperK

¹ Apologies to those more familiar with ‘SuperK’ referring to the SuperKamiokande experiment based in Japan: this laser bears no relation.

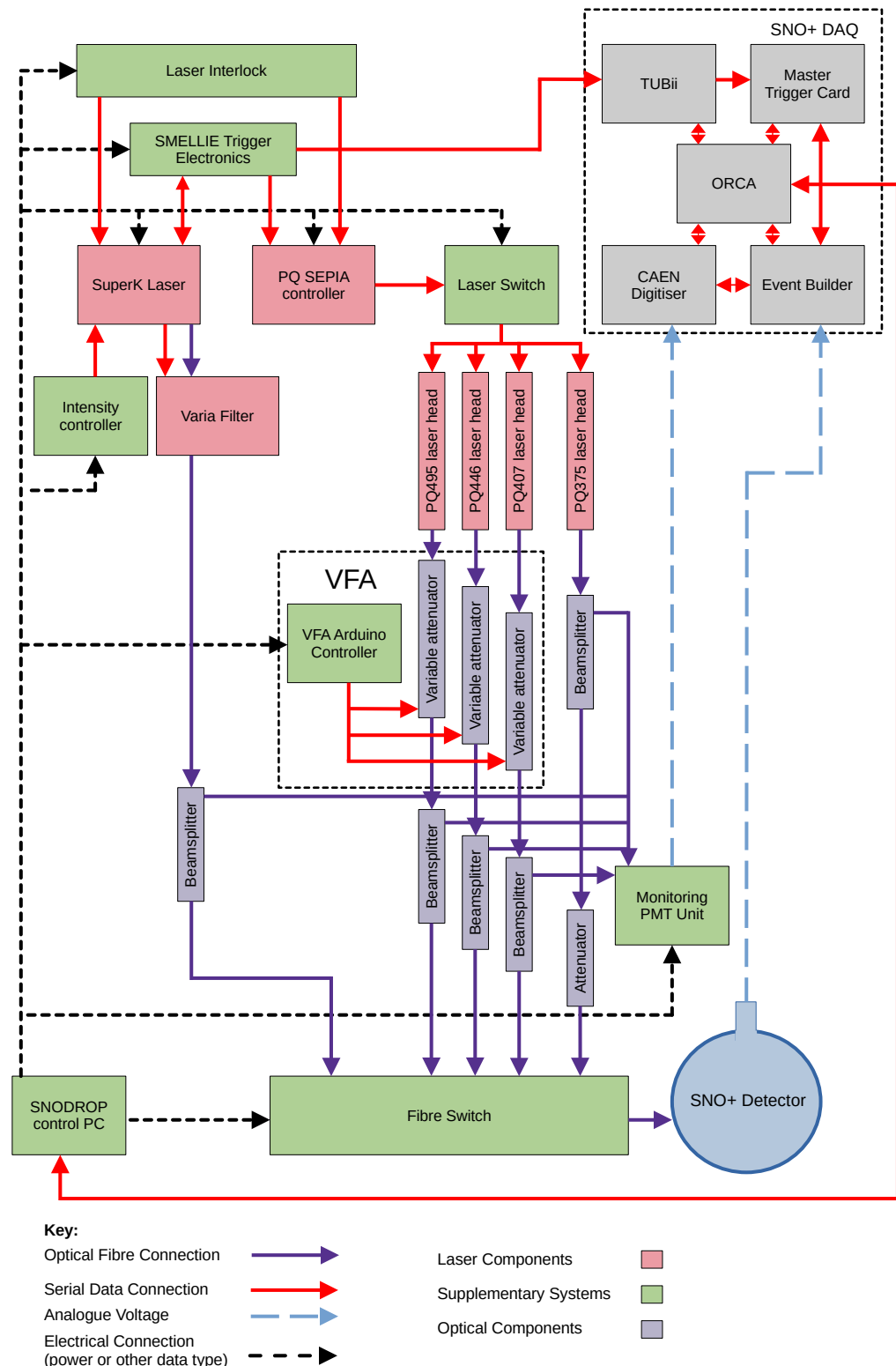


Fig. 3.3: Diagram of the connections between the various bits of SMELLIE hardware and the rest of the SNO+ detector, after the changes made in the Summer of 2022. Adapted from [114].

¹ is a super-continuum laser able to produce laser light over the whole optical
² wavelength spectrum. Because the interest is almost always in determining optical
³ properties at specific wavelengths, a variable bandpass filter also built by NKT
⁴ Photonics known as the SuperK Varia has been included. This allows the user to
⁵ select any wavelength interval between 400–700 nm, with a minimum bandwidth
⁶ of 10 nm. The wavelength and emission timing characteristics of all five lasers
⁷ are shown in Fig. 3.4. The $\mathcal{O}(1\text{ ns})$ time widths for the lasers are essential for
⁸ scattering analyses as they allow for much greater precision in knowing when
⁹ photons should arrive at PMTs in the detector than with an LED source. This
¹⁰ is why SMELLIE uses lasers for its light generation, unlike the LEDs used for
¹¹ AMELLIE and TELLIE.

¹² **3.2 Controlling Laser Intensities**

¹³ It is important to be able to control the quantity of light that enters the detector
¹⁴ from a given pulse of one of the lasers. This is done in two parts. For the
¹⁵ SuperK laser, the raw power of the beam in a pulse can be set as a percentage of
¹⁶ the maximum possible power for that wavelength. Once a light pulse has been
¹⁷ generated, it is then attenuated by a neutral density filter contained within the
¹⁸ SuperK laser hardware.

¹⁹ For the PQ lasers, a PicoQuant-brand SEPIA II laser driver is used to set the
²⁰ raw pulse intensity and firing rate. Unlike the SuperK, the intensity control is
²¹ given by the laser driver’s driving voltage, as a fraction of the maximum possible
²² voltage. For both types of laser, the driving voltage is given as a number between
²³ 0 and 1000, where 1000 indicates the maximum allowed driving voltage for that
²⁴ laser. Problematically, the dependence on the raw output intensity of the PQ laser
²⁵ heads are highly nonlinear with respect to the amplitude of the driving voltage.
²⁶ To demonstrate, consider the observed fraction of events in which each PMT was

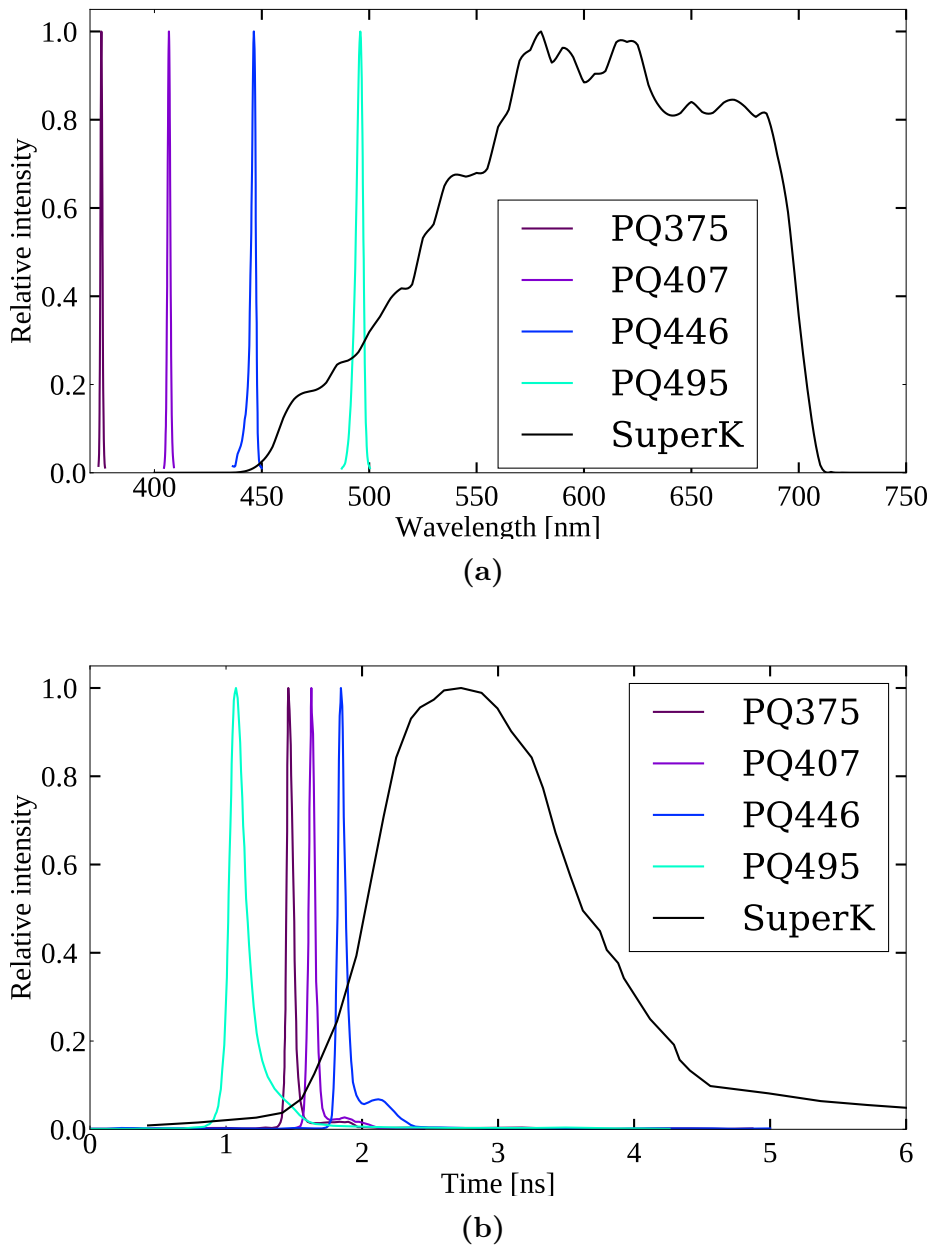


Fig. 3.4: Emission wavelength (a) and timing (b) spectra of the lasers used in SMELLIE. PQ spectral information taken from the manufacturer; SuperK information measured by J. Lidgard [140].

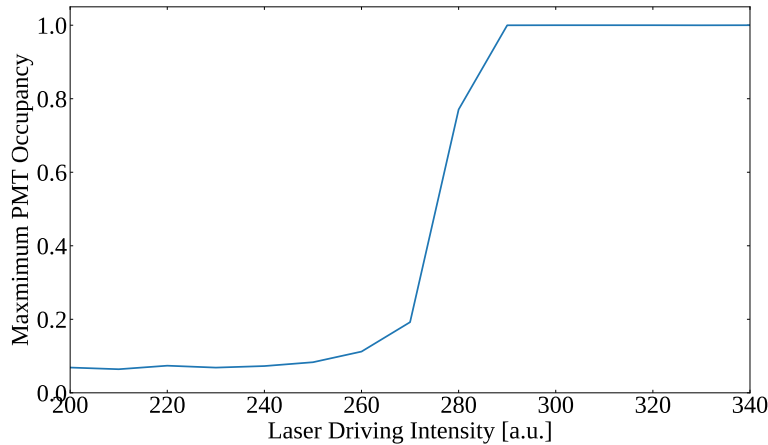


Fig. 3.5: Typical impact of driving voltage intensity for PQ446 laser on observed maximum occupancy in the detector. Data taken on February 22nd, 2021.

hit. This is known as the PMT occupancy, and the maximum PMT occupancy is shown as a function of driving voltage for SMELLIE events using the PQ lasers in Fig. 3.5.

For low driving voltages, the resulting maximum PMT occupancy is very small, and rises slowly. However, near the ‘lasing threshold’ the occupancy observed rapidly climbs. Above this threshold, some PMTs in the beamspot ‘saturate’, having an occupancy of 1. As will be seen in Chapter 4, information about the light intensity incident on a given PMT can be derived in a straightforward manner only if the light level is stable for a given set of data, and the occupancy on the PMT is below 1. When driving a laser head near its lasing threshold the shot-to-shot variation in observed light intensity in the detector can also become substantial: see Fig. 3.6 for an example of this occurring.

During the water and scintillator phases up until Summer 2022, some data taken, especially using the PQ407 and PQ446 lasers, suffered from large shot-to-shot intensity variations. Throughout this period, after the light was generated by a PQ laser head it would then be passed through an attenuator, fixed to some nominal attenuation setting for each laser. In theory, one could solve the intensity

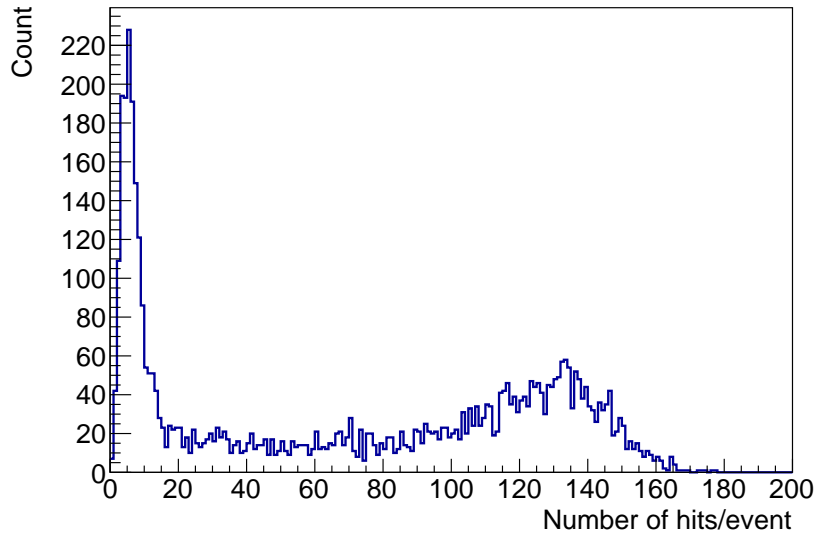


Fig. 3.6: Distribution of the number of PMT hits observed per event in the detector for laser PQ446 when the driving voltage value is 280. Data taken on February 22nd, 2021.

variation problem by deliberately setting the intensity well beyond the lasing threshold, and then changing the attenuation of the attenuator to obtain the occupancies within the detector one is interested in. However, under the original hardware this was untenable as this would require someone to manually change the attenuations in-person every time a different set of SMELLIE run conditions were proposed.

Instead, Jeff Lidgard built a piece of hardware called the remotely-controllable Variable Fibre Attenuator (VFA), shown in Fig. 3.7. Contained within a metal housing were a ‘precision variable attenuator’ from DiCon Fibreoptics [141] for each PQ laser, along with an Arduino running firmware written by J. Lidgard to enable communication with each of the attenuators. Commands could be sent to a given attenuator asking for a specific attenuation expressed as a number between 0 and 3000, where the number divided by 100 gives the theoretical attenuation. Following ex-situ testing by J. Lidgard and Jasmine Simms, the VFA was installed

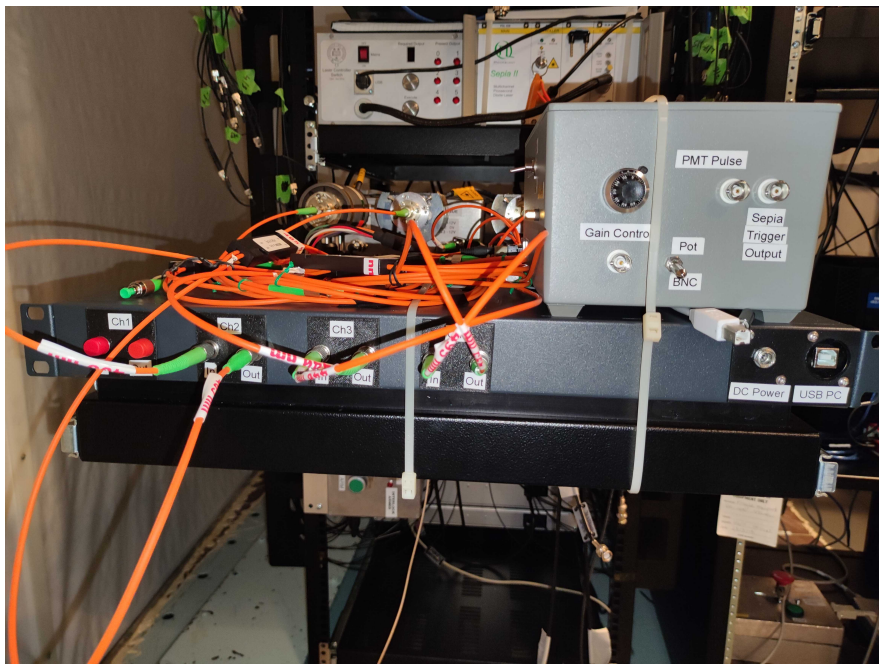


Fig. 3.7: Picture of the VFA during installation into the ELLIE hardware rack. The VFA box rests beneath the fibres connecting to the beam splitters, as well as the newly-installed Monitoring PMT Unit (see Section 3.4 for details).

¹ underground by myself and Armin Reichold in July 2022, with some assistance
² from J. Lidgard in integration of the hardware and SMELLIE server software.

³ During testing of the VFA in-situ, it was discovered that the actual attenuation
⁴ of the variable attenuator at the minimum setting of 0 dB for the PQ375 laser
⁵ was so strong that negligible light was ever observed in the detector. This is likely
⁶ because the precision variable attenuator components were primarily designed
⁷ by the manufacturer with infrared fibre-optic transmission in mind. Because of
⁸ this, the PQ375 was not hooked up to the VFA, and kept its original attenuator
⁹ setup. After fixing the driving voltage settings for PQ407, PQ446, and PQ495 to
¹⁰ be 1000, 750, and 750 respectively, the observed maximum PMT occupancy in the
¹¹ detector was once again compared to the input laser intensity setting. For PQ375
¹² this input parameter remained the driving voltage; for the others, the attenuation
¹³ setting was now used. The results can be seen in Fig. 3.8. As hoped for, the three

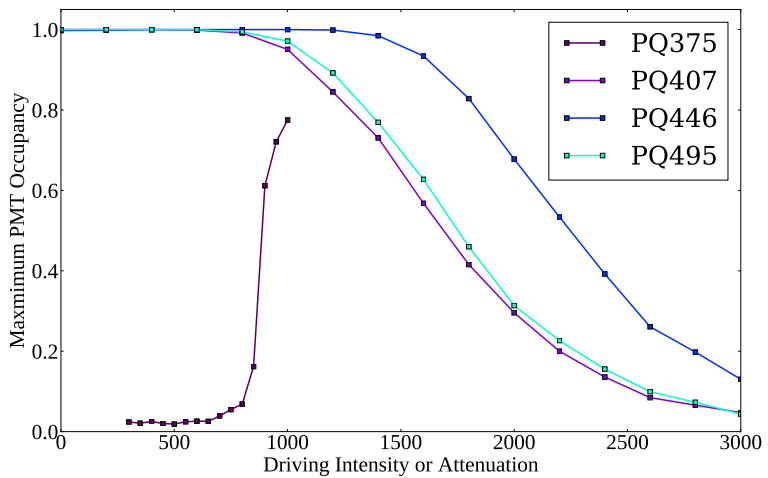


Fig. 3.8: Maximum occupancy in the detector as a function of the attenuation parameter value used, for each of PQ407, PQ446, and PQ495. Because PQ375 is not plugged into the VFA, its dependence on the driving intensity is shown instead. Data taken on the 12th of January, 2023.

PQ lasers hooked up to the VFA can now have stable intensities of light observed in the detector over multiple orders of magnitude of observed intensity.

3.3 Propagation of Light into the Detector

Once a pulse of optical light has been generated by the lasers and attenuated to the desired intensity, the next step is to navigate that light into the detector. This is achieved through a network of Corning-brand “InfiniCor SXi” multimode optical fibres [142]. These fibres were chosen in part for their low intrinsic radioactivity [143], as well as having a graded index as a function of radius. This latter property enables lower dispersion between different modes of the light, so that the initial sharpness of any given light pulse in time is maintained. However, because these fibres were mainly designed for telecommunication purposes, their nominal operating wavelengths are out in the near-infrared, 750–1450 nm. As SMELLIE only fires wavelengths in the range 375–700 nm, there is a small but non-negligible amount of light lost when propagating through the fibres.

After some light is split off by a beamsplitter to allow for ex-situ monitoring of the light pulse (see Section 3.4), it is sent to the Fibre Switch, two boxes manufactured by Laser Components UK that allows a user to remotely-control which of the fibres to send the light down into the detector.

Finally, the light that passes through the fibre switch propagates along one of the 15 optical fibres that have been submerged in the SNO+ cavity, whose ends are mounted to the PSUP. Specifically, sets of three fibres are mounted to a given node of the PSUP, with associated node numberings: nominally 07, 25, 37, 55, and 21. These provide for a variety of positions within the detector from which light can be emitted. Each mounting which holds three of the optical fibres also contains collimators, designed to reduce the possible range of angles with which the light can be emitted from. This is particularly important for SMELLIE, because unlike the other ELLIE systems, a thin ‘pencil’ beam of light across the detector is ideal for measuring scattering [137]. The mounting also points each of the three fibres in different directions: 0°, 10°, and 20° from the direction radially towards the centre of the detector.

Each fibre is given a name that nominally refers to both its mounting position and its pointing direction. For example, the label ‘FS107’ corresponds to the SMELLIE fibre mounted at node 07 with a pointing direction of 10°. Unfortunately, during installation some fibres were mislabelled, leading to the node mounting points and pointing directions of some fibres being inconsistent with the labelling convention. The actual mounting nodes and pointing directions for each fibre can be seen in Table 3.1. The 3D positions and pointing directions of all the fibres are determined in [139], and shown in Fig. 3.9.

When performing analysis with SMELLIE, a fibre-centric spherical-polar coordinate system is used. This coordinate system was first fully-developed by E. Turner; full details can be read in [114]. A position \mathbf{x} is measured relative to a given fibre’s mounting position, \mathbf{f} (hereafter referred to as simply the fibre’s

| Fibre | Node | Pointing direction |
|-------|------|--------------------|
| FS007 | 07 | 0° |
| FS107 | 07 | 10° |
| FS207 | 07 | 20° |
| FS025 | 25 | 0° |
| FS125 | 25 | 10° |
| FS225 | 25 | 20° |
| FS037 | 37 | 10° |
| FS137 | 37 | 0° |
| FS237 | 37 | 20° |
| FS055 | 55 | 10° |
| FS155 | 55 | 20° |
| FS255 | 55 | 0° |
| FS093 | 21 | 0° |
| FS193 | 21 | 10° |
| FS293 | 21 | 20° |

Table 3.1: SMELLIE fibre names, their associated mounting nodes on the PSUP, and their pointing direction. Taken from [114].

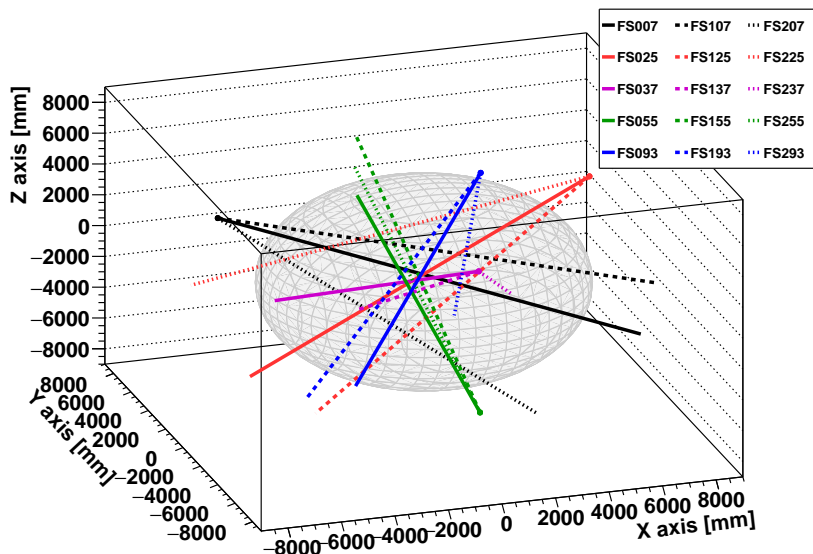


Fig. 3.9: Fibre emission points and nominal pointing directions within the detector.

¹ position). Polar angles, labelled α , are measured relative to the fibre's pointing
² direction, $\hat{\mathbf{u}}$. As a result, a line from the fibre position along $\alpha = 0$ across the
³ detector should in theory hit the centre of the fibre's beamspot. Finally, in order
⁴ to define the azimuthal angle ϕ , the plane orthogonal to $\hat{\mathbf{u}}$ is considered. Both \mathbf{x}
⁵ and the unit vector in the vertically-upwards direction, $\hat{\mathbf{z}}$, are projected onto this
⁶ plane, forming the vectors \mathbf{x}_{proj} and $\hat{\mathbf{z}}_{proj}$, respectively. ϕ is then defined as the
⁷ angle going from $\hat{\mathbf{z}}_{proj}$ to \mathbf{x}_{proj} if one were to look at the plane in the direction of
⁸ $\hat{\mathbf{u}}$. Mathematically, this can be written as:

$$\tan \phi = \frac{(\mathbf{x}_{proj} \times \hat{\mathbf{z}}_{proj}) \cdot \hat{\mathbf{u}}}{\mathbf{x}_{proj} \cdot \hat{\mathbf{z}}_{proj}}. \quad (3.1)$$

¹⁰ 3.4 The Monitoring PMT Unit

¹¹ As mentioned in the previous section, part of the light generated by the lasers
¹² gets split off from the main fibre path down into the detector, and is used for
¹³ monitoring purposes. This is achieved with a box known as the Monitoring
¹⁴ PMT Unit (MPU). As the name suggests, the MPU contains a small PMT that
¹⁵ generates an electronic signal pulse from the laser light. This signal is then shaped
¹⁶ by electronics, and passed to the detector's central CAEN digitiser to have that
¹⁷ pulse digitised.

¹⁸ One problem with the existing MPU within SMELLIE was that the pulse
¹⁹ it produced was so broad that 300 ADC samples were needed to capture the
²⁰ full shape (the CAEN samples at a rate of 1 every 4 ns). This led to a large
²¹ fraction of data being generated by SMELLIE events coming not from the PMT
²² hit information, but simply the MPU's signal digitisation. A natural consequence
²³ of this was the rate at which the lasers could be fired had to be limited to
²⁴ typically 1 kHz, otherwise the detector was not able to handle the rate of data
²⁵ being generated.

Because of this, a new MPU was commissioned. Built by Adam Baird and 1
Johan Fopma from the Oxford Physics Central Electronics Group, this MPU had 2
updated electronics such that the pulse was shaped shorter. In addition, the rise 3
time of the pulse was made faster, in the hopes that the emission time of the light 4
pulse for a given event could be captured more accurately. The new MPU was 5
installed by myself and A. Reichold at the same time as the VFA, in Summer 6
2022. 7

Alongside the installation of the new hardware, the settings in ORCA for the 8
CAEN digitisation of the MPU signal were updated. In particular, the number of 9
samples made by the CAEN was shortened from 300 down to 124. The timing 10
of the CAEN sampling and delay on the TUBii trigger (more on the trigger 11
shortly) was also modified. As a result of these changes, a much shorter trace was 12
now being generated, without missing any part of the MPU pulse or moving the 13
observed TAC for hits in the detector outside the trigger window. Fig. 3.10 shows 14
a comparison between typical MPU pulses taken before and after the upgrades. 15

3.5 Event Triggering and Data Acquisition

As mentioned in Section 2.3.4, it is possible to trigger the SNO+ detector elec- 17
tronics via an external asynchronous trigger, EXTA. Taking data with SMELLIE 18
takes advantage of this capability: instead of waiting for the normal ‘physics’ 19
triggers such as N100 to pick up the event, an EXTA signal can be sent from 20
the firing laser to trigger the detector precisely when a light pulse is within the 21
detector. 22

Trigger signal pulses are created by the National Instruments DAQ Unit 23
(the ‘NI Unit’), in place alongside the rest of the SMELLIE electronics. These 24
trigger pulses are sent to either the PQ’s SEPIA controller or the SuperK laser 25
to induce the firing of the relevant laser. If a PQ laser was fired, a trigger pulse 26

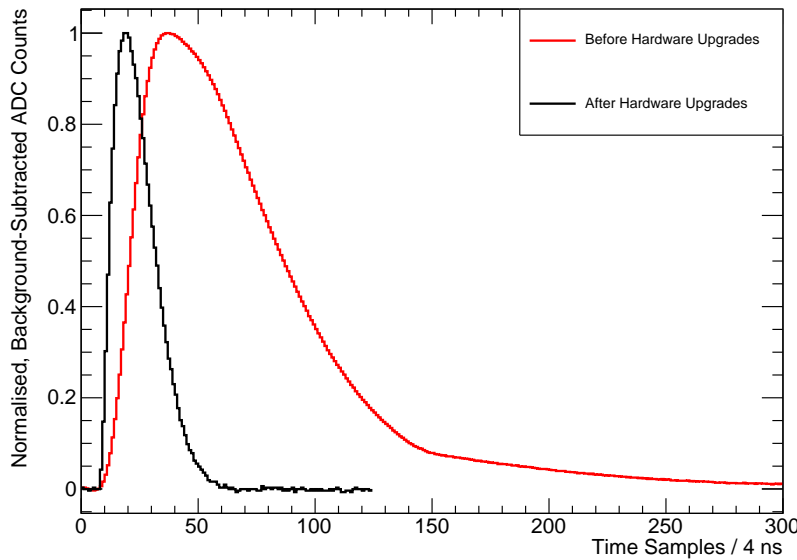


Fig. 3.10: Comparison between typical MPU CAEN traces generated by the PQ495 before and after the Summer 2022 hardware upgrades. The data before was taken on July 24th 2022, whilst the data after was taken on June 17th 2023. The traces have had their baselines subtracted off, and their peak values normalised to 1.

1 is simultaneously sent to TUBii, which after a delay sends an EXTA trigger
 2 signal to the MTC/D, which then issues a GT. In contrast, the SuperK has a
 3 substantial variation in the emission time of laser light relative to a given driving
 4 pulse. Instead of sending the trigger signal to TUBii in parallel to the SuperK
 5 laser, a photodiode contained within the SuperK laser system is able to detect
 6 any generated light, and from that detection a new trigger signal is sent to TUBii.

7 A major problem with the handling of the trigger signal delay by TUBii was
 8 present throughout the collection of water phase SMELLIE data. This delay was
 9 ‘latched’ to the 100 MHz clock present within the electronics of TUBii. As a result,
 10 the observed hit times of PMTs in the detector (which are relative to the GT time)
 11 was a convolution of the hit times without the latching and a top hat function of
 12 width 10 ns.

13 An example of this effect in action can be seen in Fig. 3.11. Light from the
 14 PQ495 laser was fired through fibre FS007 by E. Turner in June 2018, during

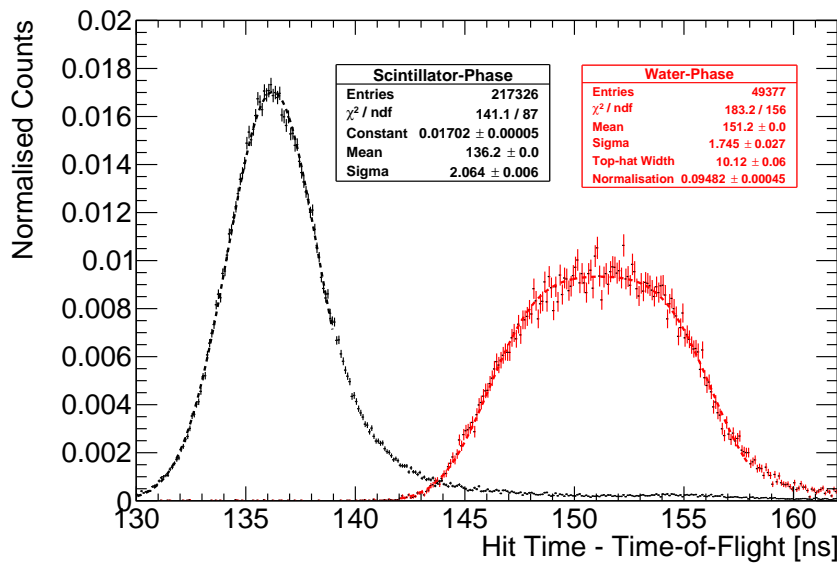


Fig. 3.11: Comparison of observed hit times in beamspot for laser PQ495 through fibre FS007, before and after T. Zummo's firmware update to TUBii. The initial data was taken by E. Turner June 20th 2018 during the water phase, whilst the data post-fix was taken by myself on June 24th 2023 during the scintillator phase. The peak of the former is fit to the convolution of a Gaussian with a top-hat function, whilst the latter is just fit with a Gaussian function.

the water phase. Looking only at PMTs that were hit in the beamspot, defined here as PMTs with $\alpha < 3^\circ$, the trigger times can be fit to the convolution of a Gaussian with a 10 ns top hat.

During the partial fill phase, Tony Zummo updated the firmware of TUBii so that this latching would no longer occur, and the arrival times to the MTC/D were truly asynchronous to any clocks. The results are also shown in Fig. 3.11: notice how the width of the peak is now much sharper. This width is determined by the TTS of the hit PMTs, with the width of the PQ495 timing pulse being a subdominant effect.

Because this fix to TUBii was not in place until after all water phase data taking had been completed, any analysis of SMELLIE data from the water phase had to contend with this 10 ns trigger ‘jitter’. Fortunately, this jitter was global to all hit times of a given event, so if measured a correction could be made.

1 In this thesis, two similar approaches are used to measure the event-by-event
2 emission time t_{emm} , the time at which laser light first emanates from the fibre in
3 a given event. In both, the calibrated hit times of PMTs within the beamspot t_{hit}
4 have the time-of-flight of light travelling from the fibre to the given PMT, t_{TOF}
5 subtracted. t_{TOF} is calculated by using the “Light Path Calculator” algorithm
6 developed within **RAT**. In one method, used both within the analysis work of E.
7 Turner [114] and in Chapter 4 of this thesis, t_{emm} is measured as the second-earliest
8 value of $t_{\text{hit}} - t_{\text{TOF}}$ in the beamspot. This method, called the “ $t_{\text{emm}} = t_2$ ” approach,
9 skips the earliest event in the beamspot to be robust to noise hits.

10 Alternatively, in the “ $t_{\text{emm}} = t_{\text{med}}$ ” approach, the median value of $t_{\text{hit}} - t_{\text{TOF}}$
11 in the beamspot is used. We shall see in Chapter 5 that using t_2 has a bias as
12 a function of the number of hits in the beamspot in a given event, whereas t_{med}
13 does not.

14 This event-by-event approach to reconstructing t_{emm} is only necessary when
15 the trigger system has unresolved problems. Because of the fix to the TUBii
16 firmware, data taken using the PQ lasers during the scintillator phase did not in
17 theory require using either of the t_{emm} reconstruction methods described above.
18 However, for the SuperK laser a new problem was made clear. In Fig. 3.12 one can
19 see the hit times of beamspot PMTs for SuperK light of wavelengths in the interval
20 [490, 500] nm from fibre FS125, taken on June 17th 2023. A clear double-peaked
21 structure can be seen. Also shown on the plot is the distribution of t_2 values. If
22 the laser light were being emitted in two pulses for a given event, then it would
23 be expected to see only one bump in this distribution. However, the shape of the
24 t_2 is clearly bimodal in a manner matching that of the overall timing distribution:
25 this indicates that the actual emission times of light from the fibre can come at
26 two different times relative to the GT time.

27 The origin of this double-peaked structure for SuperK events remains unre-
28 solved. However, the fact that events from the PQ lasers do not see this effect

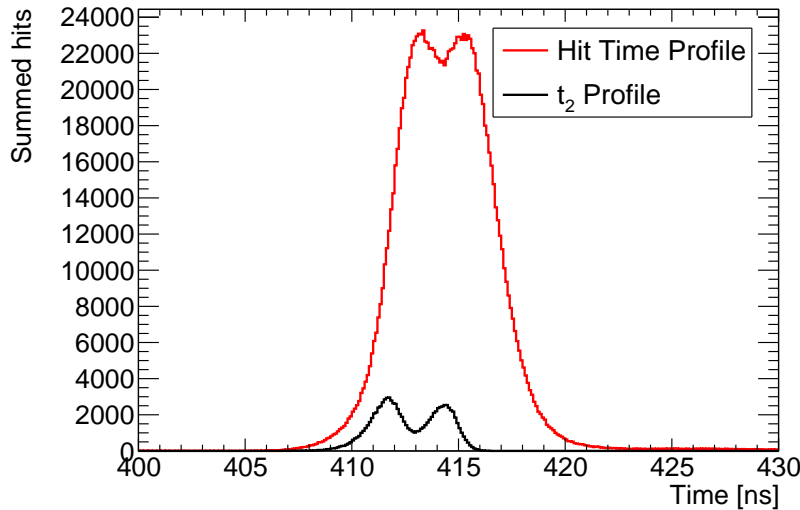


Fig. 3.12: Hit time and t_2 distributions for a subrun of SMELLIE data taken with the SuperK laser in the [490, 500] nm range through fibre FS125 on June 17th 2023. The double-peaked structure is clear in both distributions.

indicates that the issue likely lies somewhere in the part of the triggering system unique to the SuperK laser. For work within this thesis, it was decided to continue to use an event-by-event approach to t_{emm} for data from all phases and lasers, to ensure consistency.

3.6 Software for SMELLIE Data-taking

The process of taking data with SMELLIE is largely automated. The user begins by deciding on the settings — the number of laser pulses and their frequency, as well as which fibre, laser, wavelength, intensity, and attenuation (if relevant) — that will be used for each subrun. One run of SMELLIE data taking can have an arbitrary number of subruns within it, each with their own setting. This is organised into a “run plan” JSON file for that run, and uploaded to a central CouchDB server for storage.

¹ To begin data taking, ORCA is used to put the DAQ into a ‘SMELLIE’ run
² type, which disables almost all the usual ‘Physics’ triggers such as N100 and N20.
³ The only triggers still masked into the MTC/D are:

- ⁴ • EXTA: This is needed to capture the trigger signals sent from SMELLIE.
- ⁵ • ESUMHI: This residual physics trigger is kept in with a high threshold, to
⁶ capture any high-nhit events not coming from SMELLIE, e.g. if a supernova
⁷ were to go off whilst SMELLIE data taking was occurring.
- ⁸ • PULSEGT: This is a special trigger that fires at a rate of 50 Hz independent
⁹ of all other systems. With this trigger, the noise rate can be calculated on a
¹⁰ run-by-run basis for each channel.

¹¹ The noise rates derived from the PULSEGT triggers are automatically calculated
¹² during the processing of runs, and are stored in RATDB tables. As mentioned
¹³ in Section 2.4.5, RAT can use these tables to replicate the noise levels in each
¹⁴ PMT when generating simulations to match data. When performing analysis on
¹⁵ SMELLIE data, only events from an EXTA trigger are usually considered.

¹⁶ With ORCA, one can then load in any run plan already uploaded to the
¹⁷ CouchDB server, and then execute it. ORCA then sends commands describing
¹⁸ the instructions laid out in the run plan to a server running on a computer called
¹⁹ SNODROP, which is housed in the same pair of electronic racks as the rest of the
²⁰ SMELLIE hardware. This server converts these high-level commands into the low
²¹ level instructions understood by the specific pieces of SMELLIE hardware needed
²² to actually send the correct number of pulses of laser light of the right wavelength
²³ and intensity through the correct fibre. Details of the integration of SMELLIE
²⁴ with ORCA can be found in [144]

²⁵ Whilst SMELLIE data is being taken, a “run description” JSON file is generated
²⁶ and then uploaded to the SMELLIE CouchDB server, describing the settings of

the SMELLIE run actually executed. This differs from the run plan slightly in two main ways: firstly, the same run plan can be run on multiple occasions. However, a run description file is associated to exactly one run of data that was actually taken. Secondly, if a SMELLIE run was terminated early either by the detector operator, or from a hardware problem, the run description file will correctly show only the subruns that were actually performed. The code repository used in all SMELLIE analysis has been updated by myself to use a given run description file in concert with the associated SMELLIE data file, so that the subrun-level metadata can be known during analysis.

Chapter 4

1

Simulating SMELLIE Events

2

Max Power : *Kids. From now on there are three ways of doing things: the right way, the wrong way, and the Max Power way.*

Bart Simpson : *Isn't that just the wrong way?*

Max Power : *Yes, but faster!*

THE SIMPSONS

Critical to extraction of scattering information from SMELLIE data is an accurate MC simulation of the SMELLIE system. By modelling the laser light emission into the detector correctly, we can simulate how SMELLIE light will be impacted by changing scattering lengths in the detector. Because of the complexity of the optics of the optical fibres used to direct the laser light into the detector, a given SMELLIE event is simulated as a partially-collimated “flash” of visible photons emanating from the emission point of the fibre into the detector. This flash then requires a number of parameters to be correctly described. In particular:

- **Fibre emission positions** were recorded during the installation of the fibres.

13

- **Wavelength and emission timing distributions** of light pulses were taken from measurements of the laser heads by their manufacturers [], or by colleague Jeff Lidgard in the case of the SuperK wavelength distribution [].
- **The “pulse magnitude”**, defined as the mean number of photons simulated per event, is determined on a subrun-by-subrun basis, and is assumed to fluctuate as a Poisson distribution.
- **The beam profiles**, which describe the angular emission distributions of each fibre, is the focus of this chapter. These are necessary because unlike scintillation light, the light emitted from SMELLIE fibres is not isotropic.
- **Nominal fibre emission directions** attempt to define the centre of the beam for a given fibre.

This chapter is split into three sections. Improvements to the existing simulation algorithm for the beam profiles are first made, and then the beam profiles themselves are updated. Finally, comparisons between data and simulation are made after the upgrades to investigate any remaining discrepancies.

4.1 Improving the SMELLIE Generator Algorithm

4.1.1 Previous Attempts at SMELLIE Event Simulation

Before we can determine the beam profiles, we must first decide how to specify them. Previous observations show that different fibres can have notably different beam profiles [137], so we let each fibre’s beam profiles be unique. We assume for now that a given fibre’s beam profile is stable over time, and independent of the wavelength of light fired. A straightforward, naïve approach to parameterising a beam profile

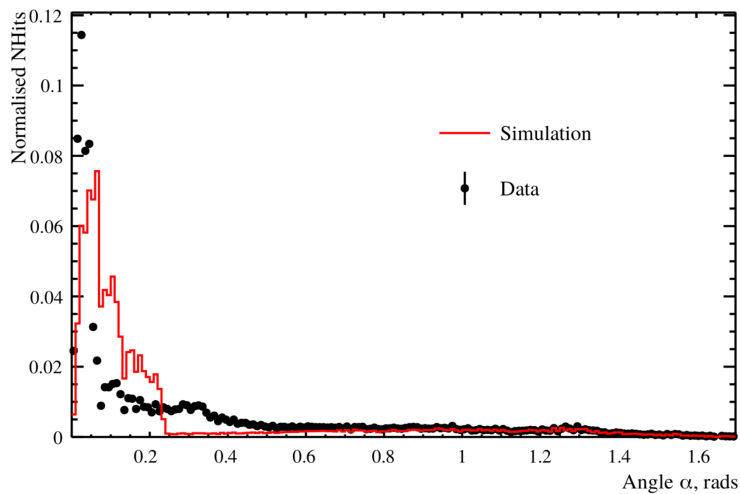


Fig. 4.1: Comparison between a simulation of one of the fibres, made from the 1D beam profile generator (red), with the associated data subrun that was used to create that beam profile (in black). For both MC and data, what is plotted is the PDF of observed PMT hits, as a function of the α angle. Poissonian errors have been added to the data points, but are too small to see. Clearly, this 1D generator does not replicate the observed beam profile correctly. Figure taken from [114].

would be as follows: specify some nominal fibre direction, corresponding to the direction light takes travelling from the fibre to the centre of the “beamspot” observed on the other side of the detector. Then, specify a 1D beam profile, corresponding to the probability density of firing a photon at a given polar angle α relative to the nominal direction. One might even assume this distribution is Gaussian. The distribution in azimuthal direction, ϕ , is assumed to be uniform.

This 1D beam profile approach was used initially for SMELLIE, and remains in use for the other ELLIE sub-systems within SNO+. However, when SMELLIE data was taken in the water-phase of the experiment, simulations using these beam profiles failed to match them well at all - see figure 4.1 for an example. Not only was the distribution in α not Gaussian, a distinct speckle-pattern can be observed within the beamspot that is not uniform in ϕ . This fact led to colleague Esther Turner building a SMELLIE generator that could handle 2D beam profiles: dependent on both α and ϕ . The distribution was stored as a map from each inward-pointing PMT in the detector to a relative intensity value. This was chosen

¹ because the beam profile shapes were calibrated from existing SMELLIE data —
² more on this in section 4.2.

³ This original 2D generator then sampled the beam profile via a rejection
⁴ sampling approach, outlined as follows:

⁵ 1. Propose a test direction (α, ϕ) , by generating ϕ uniformly in the interval
⁶ $[0, 2\pi]$, and α according to some pre-determined Gaussian distribution,
⁷ known as the Gaussian envelope.

⁸ 2. Given this test direction, calculate where a line following this direction from
⁹ the fibre of interest will hit the PSUP on the other side of the detector. Find
¹⁰ the 3 closest PMTs to that point.

¹¹ 3. From those PMTs, obtain their relative intensity values from the beam
¹² profile mapping, and perform an interpolation based on how close each
¹³ PMT is to the PSUP intersection point. This gives an interpolated relative
¹⁴ intensity value for this test direction.

¹⁵ 4. Because we are sampling using the angular coordinates (α, ϕ) , differential
¹⁶ area elements over this space of directions do not have the same size. We
¹⁷ can correct for this fact by multiplying our interpolated relative intensity by
¹⁸ $\sin \alpha$, which corresponds to the Jacobian of the direction-space.

¹⁹ 5. Calculate the value for the Gaussian envelope along this test direction.

²⁰ 6. Throw a random number uniformly between 0 and the Gaussian envelope
²¹ value. If the random number is less than the interpolated intensity, then
²² this test direction is accepted, and a photon is generated with that direction.
²³ Otherwise, we reject the direction and try the whole process again.

²⁴ This generator certainly works, but has a key problem: efficiency. The 1D
²⁵ generator was able to generate a SMELLIE event (that is, to fully specify the

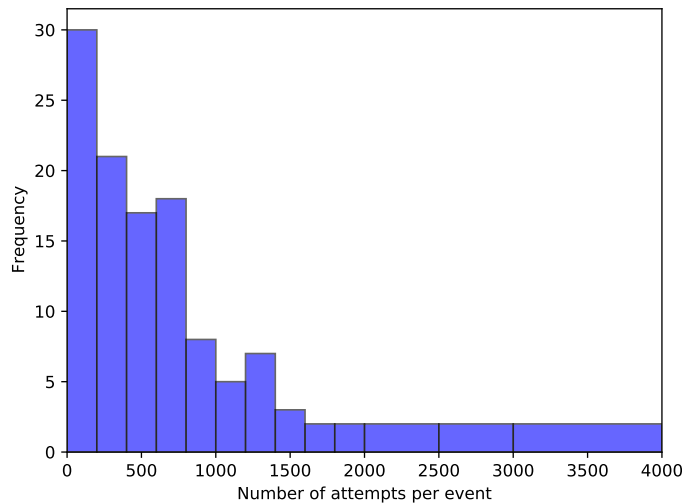


Fig. 4.2: Typical distribution of the number of attempts it takes for the existing 2D generator before the test direction gets accepted, per event.

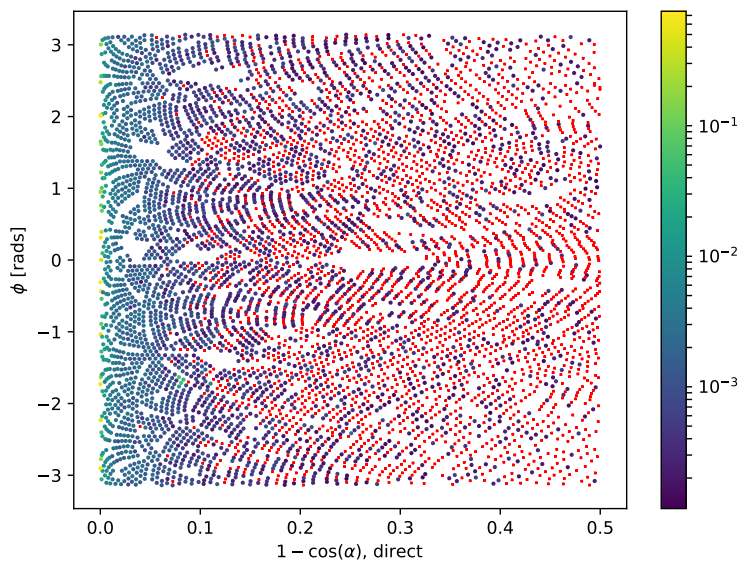
starting parameters of all the photons emitted from a fibre) at a speed of $\sim 1\text{ ms}$.
 However, the 2D generator specified here could take upwards of $\sim 50\text{ s}$ *per event* to
 generate. Because a typical SMELLIE analysis requires simulating many millions
 of events, the CPU time taken to perform this quickly became unfeasible. Fixing
 this generator speed problem was a high priority for the SMELLIE analysis.

4.1.2 The new generator

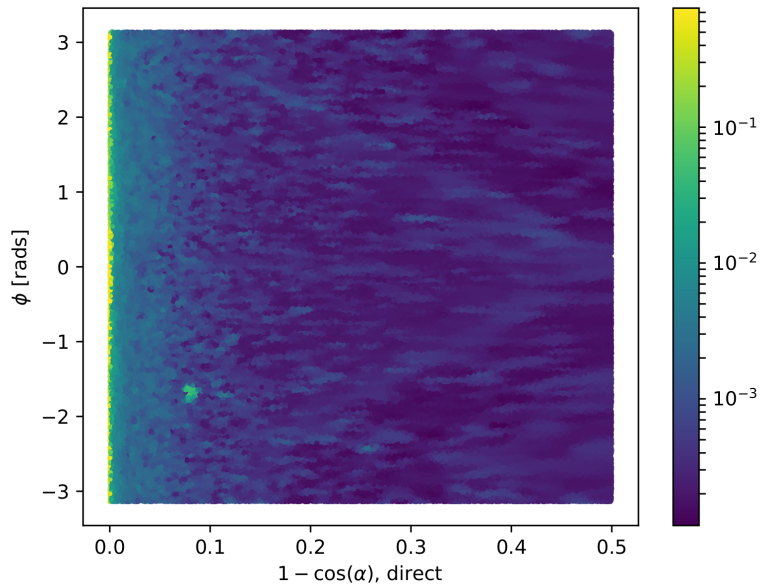
On careful inspection of the existing 2D generator, the main reason for the slowness
 of the algorithm is the use of a rejection approach. Even with use of the Gaussian
 envelope, which was included to help with speed, the vast majority of proposed
 directions are never selected. Figure 4.2 shows a histogram of number of attempts
 per event it took for a valid direction to be chosen for a representative SMELLIE
 simulation. Moreover, the calculations needing to be done for every proposed
 direction are relatively complex, notably trying to find the 3 nearest PMTs to
 some point on the PSUP.

A new 2D generator was built with these thoughts in mind. Firstly, the rejection method would no longer be used, given its inefficiency. We would also endeavour to try and “pre-calculate” as much as possible before run-time. Starting with the existing PMT relative intensity maps, we plot these in the 2D direction-space ($1 - \cos \alpha, \phi$): see Figure 4.3a. In a toy-MC simulation, 500,000 directions are then thrown uniformly in this 2D space per fibre. For each direction, the same method of obtaining an interpolated intensity value from the nearest PMTs to the corresponding point on the PSUP as from the original 2D generator was performed, the only difference being that these calculations were done well before any actual SMELLIE simulation. Figure 4.3b shows the interpolated intensities obtained for one fibre.

Following this, the sampled intensities were then binned into a 2D histogram, where the bin value corresponds to the sum of all intensities for all directions found within this bin. Choosing a sensible binning procedure is important: too few bins, and necessary information about the shape of the beam is lost, whilst too many bins can oversample the data and capture statistical artefacts in the sampling process instead of just the beam profile. As a balance, 15 bins were chosen along the ϕ direction, and 60 in $r = 1 - \cos \alpha$. This was chosen to ensure that a reasonable number of PMTs were located within each bin, lessening the impact of any statistical fluctuations. Although the bins in ϕ were chosen to have uniform width, this was decided to be not the case for the other axis, as there is far more important information near $r = 0$ (the beamspot). Instead, the width of the bins in r were calculated so that roughly the same total probability was contained in each r -strip. By consequence, bins near the beamspot typically are of significantly smaller size than ones much further out. This allows us to both capture any rapid changes in intensity near the beamspot, where this matters greatly, and smooth out the very-low intensities seen at larger polar angles. One of these histograms can be seen in Figure 4.4: the large change in bin widths as a



(a) PMT relative intensity map



(b) Interpolated intensity map

Fig. 4.3: The first step in the new method for preparing the new generator. In (a), the relative intensities used for the existing beam profile of fibre labelled FS055 are shown for each PMT, the position on the plot indicating the location of that PMT in the fibre coordinates. The colour indicates the relative intensity; PMTs marked red have an intensity of zero. Figure (b) shows the result of throwing 500,000 directions uniformly over this 2D space, the intensity of each point given by interpolating the intensities of nearby PMTs.

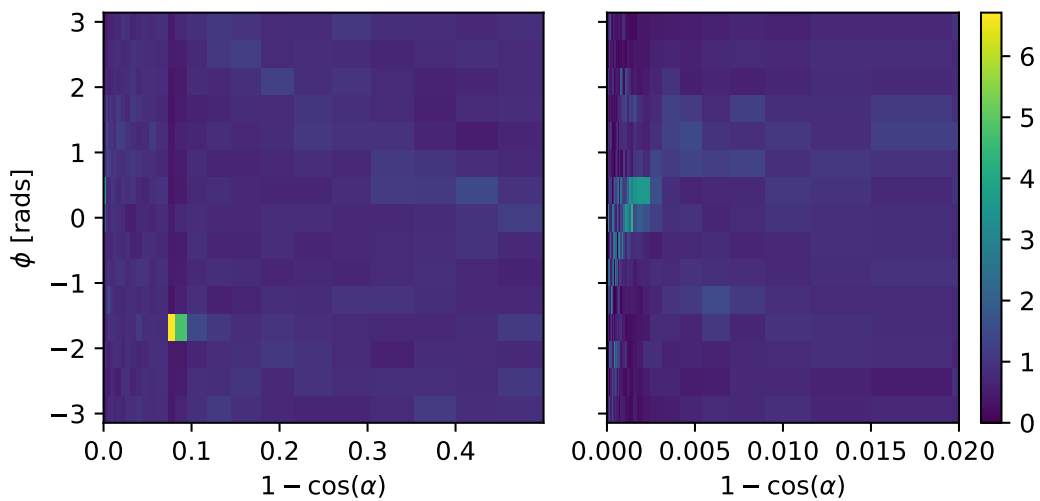


Fig. 4.4: Histogram of interpolated intensities within the 2D direction-space. The left view shows the full histogram; the right is a zoomed-in version near the beamspot. Unlike the binning in ϕ , the bin widths in r are not at all uniform. Instead, they have been determined such that the area summed over a given “strip” of bins of constant r will be the same.

function of r is clear. One can also see that near the beamspot notable dependence on the intensity as a function of ϕ . The mysterious “spot” at $r = 0.08$, well out of the beamspot, is an indication that the underlying beam profile data being used requires improvement: more on this in section 4.2.

The Cumulative Density Function (CDF) of this intensity histogram as a function of bin was then produced, where the bins were ordered through a raster-scan: scanning first over ϕ , and then r . The CDF was then normalised to 1 so that it was well-defined. It is this CDF object that is then loaded in and sampled from during event generation. To do this, an “inverse-CDF” approach was used, which has the major benefit over rejection sampling of always producing a valid direction for every sample made. The algorithm works as follows:

1. Throw a random number uniformly in $[0, 1]$.
2. Perform a binary search to find the bin that has the largest CDF value below this random number.

-
3. Look at the bin edges in ϕ of this selected bin: use linear interpolation of
the random number to obtain a ϕ value located between these two ϕ -values. 1
4. Look at the selected bin's r -bin edges, and select a value of r by throwing a
second random number uniformly between the two edges. Convert this r 3
into a polar angle α . 4
5. The photon's direction is defined by the (α, ϕ) chosen by this process. 5

Because of the relative simplicity of this algorithm compared to the previous 2D
generator, the speed improvement was very large: generation now took ~ 1 ms per 7
SMELLIE event, a speed improvement of nearly 50,000. Event generation became 8
as fast as it was when the 1D generator was being used. Furthermore, because 9
of the approach taken, this major speed improvement comes at no sacrifice in 10
accuracy. Figure 4.5 shows a comparison of the average number of photoelectrons 11
(npe) per event per PMT between water-phase SMELLIE data and simulations 12
with both the old and new 2D generator. One can see clearly that both generators 13
are as accurate as one another. Note that this plot uses the updated beam profiles 14
as explained in the next section. 15

4.2 Improving the beam profiles

Even with the new 2D profile generator, a problem remains: the simulation fails 17
to reasonably recreate data, and much of this appears to be because of the poor 18
beam profile data being used. The curious “spot” for one of the fibres was already 19
noted in the previous section that doesn't seem to be physical, and more broadly 20
at large angles for all the fibres there are large swathes of PMTs with an intensity 21
of zero, providing little useful information about the beam shape. It was shown 22
in [114] that with the old 2D generator, the systematic uncertainty on the beam 23
24

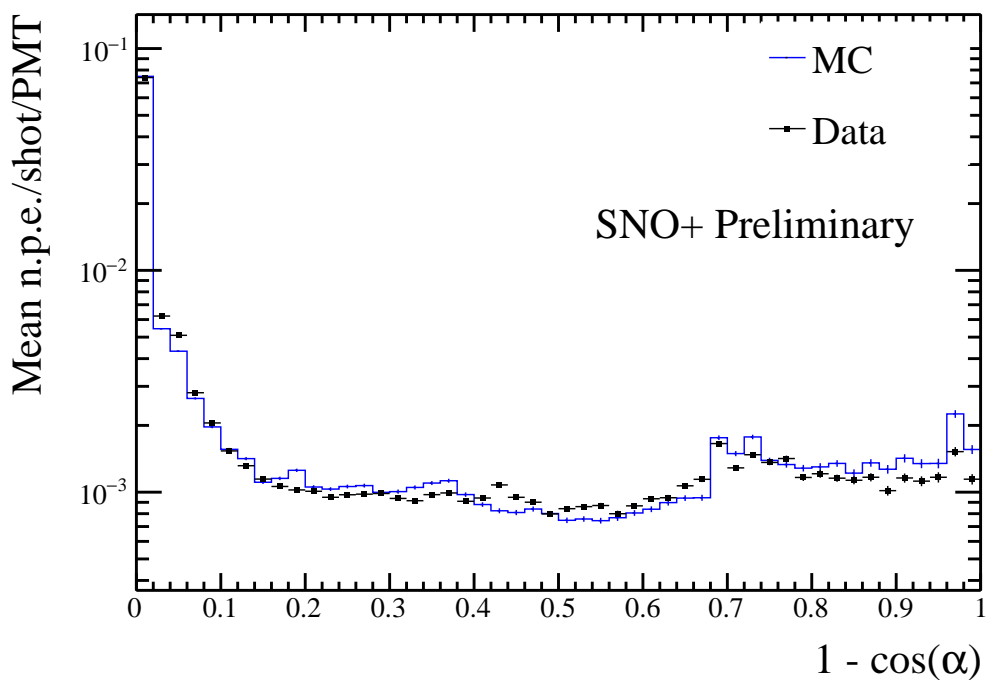


Fig. 4.5: Comparison of water-phase data to MC generated using both the old and new 2D beam profile generator approaches, with the updated beam profiles. Both versions of the generator are consistent with one another, but the new generator is many times faster.

profiles was the dominant source of error in the main SMELLIE analysis. To help improve this situation, it was decided to update the existing beam profiles.

These old beam profiles were originally determined by looking at SMELLIE data taken during the water-phase. Specifically, a “medium”-intensity subrun with one of the lasers firing at a wavelength of 495 nm, was chosen for each fibre. “Medium”-intensity corresponds to firing the relevant laser at a set intensity determined during an earlier commissioning process, for which the maximum occupancy of PMT hits at that intensity, i.e. the proportion of hits per event, corresponded to roughly 80%. This value was chosen as it allowed for high statistics in a relatively short run-time, but not so intense that the occupancy of any given PMT in the beamspot was 100%. Because Rayleigh scattering is strongly-dependent on wavelength, the long wavelength of light was chosen so that impacts from this scattering were small in the data.

SNO+ PMTs are unable to distinguish the exact number of photoelectrons being generated. One is typically only able to know if a PMT has been triggered at all, by any number of photoelectrons. As a result, the occupancy of a PMT over a number of SMELLIE events, o , is a biased estimator of the mean number of photoelectrons generated, μ . Assuming the number of photoelectrons generated in a given event follows Poisson statistics, the probability of generating k photoelectrons is:

$$P(k|\mu) = \frac{\mu^k e^{-\mu}}{k!}. \quad (4.1)$$

The probability of observing a “hit” in a given PMT corresponds to generating at least one photoelectron:

$$P(\text{hit}|\mu) = P(k \geq 1|\mu) = 1 - P(k = 0|\mu) = 1 - e^{-\mu}, \quad (4.2)$$

| Run Number | Run Type | Comments |
|------------|---|---|
| 114,018 | All PQ lasers; SuperK laser in 400–500 nm range | Only PQ495 laser and SuperK at 495 nm is used |
| 114,023 | SuperK laser in 500–600 nm range | Part 1 of this wavelength range; crash occurred on last subrun, so that subrun is ignored |
| 114,034 | SuperK laser in 500–600 nm range | Part 2 of this wavelength range |

Table 4.1: Water-phase runs used for new beam profiling.

- ¹ which implies after rearrangement that one can determine the mean number of
² photoelectrons per event from the occupancy by:

$$\mu = \ln(1 - o). \quad (4.3)$$

- ⁴ This is the reason why we want to avoid PMTs with occupancies of 100%: they
⁵ preclude one's ability to convert into a value for μ by looking at occupancy alone.
⁶ We call this conversion from occupancy into npe the “multi-hit correction”. The
⁷ impact of this correction is typically small for most PMTs, but can become very
⁸ significant in a fibre's beamspot.

⁹ Once the npe mapping from data was obtained, a correction was then made for
¹⁰ the detector's optics: even ignoring a fibre's beam profile, we still expect certain
¹¹ PMTs to be illuminated more than others because of e.g. reflections off the AV, or
¹² the solid angle subtended by the PMT bucket opening. For each fibre, a simulation
¹³ was made where the beam profile was set as isotropic, and the corresponding
¹⁴ npe mapping obtained: this map held information about the detector optics only.
¹⁵ The beam profile mapping was then derived by simply dividing each fibre's npe
¹⁶ mapping from data to its associated isotropic MC npe map. It is these maps that
¹⁷ were first used in section 4.1.2.

4.2.1 Combining beam profile datasets

Fortunately, much more SMELLIE data was taken during the water-phase than was used for the original beam-profiling analysis. This additional data can be combined with that which was already used to far better constrain the beam profiles. In particular, given the existing assumption that scattering effects are minimal above wavelengths of ~ 490 nm, all data taken with wavelengths above this can also be used. The specific runs (and associated comments about their specifics) are described in Table 4.1. Because high-intensity runs require a different analysis approach (PMTs with high occupancies must use charge, not occupancy, to estimate npe), for this analysis we only considered subruns that used low or medium intensity set-points.

For each subrun j of data per fibre, we look only at PMT hits for each PMT i that has been identified as “good” for that subrun¹, $i \in G_j$. G_j here represents the set of good PMTs in subrun j . In particular, a “good” PMT must have valid electronic and timing calibrations, be at high voltage and masked into the detector’s trigger system for that subrun. In addition, an angular cut of $\alpha < 60^\circ$ was made to remove PMTs that are well outside any reasonable beam direction. To isolate the hits arriving directly from the fibre without reflecting, scattering, or being noise, a time cut was also made. Because what matters is the time relative to emission from the fibre, and the expected time-of-flight from fibre to different PMTs varies, a quantity known as the time residual was used. Starting with the calibrated hit time of a given PMT relative to the event’s trigger time, t_{hit} , the expected time-of-flight t_{TOF} from the fibre to the PMT was subtracted, estimated with the collaboration’s “Light Path Calculator”. Then, the emission time was also subtracted, t_{emm} , estimated by looking at the second-earliest value of $t_{hit} - t_{TOF}$ within the fibre’s central beamspot, defined as the PMTs for which $\alpha < 3^\circ$. It

¹Strictly speaking, a PMT’s “goodness” is only determined on a run-by-run, not a subrun-by-subrun level, but this has no impact on the analysis.

1 was found that a “loose” time residual cut of $t_{res} \in [-10, +12]\text{ns}$ was sufficient
 2 to remove the vast majority of non-direct light with little signal sacrifice. In the
 3 situation where a subrun with intensity was very small, it would not regularly
 4 have at least two hits in the beamspot, and so the time residuals calculated would
 5 not be valid for many events. To avoid this situation, a cut was made on any
 6 subruns with mean intensities below 9 within their beamspot. This value was
 7 chosen as it would mean a 2σ fluctuation downwards of $2 \cdot \sqrt{9} = 2 \cdot 3 = 6 \text{ npe}$
 8 would still have more than the 2 hits necessary for timing reconstruction. One
 9 fibre, FS207, has no data subruns that satisfy this condition, and as such will
 10 have to be dealt with separately. For the time being, this fibre was ignored.

11 Extracting the underlying beam profiles from these data required some careful
 12 thought, especially because different subruns could have different intensities.
 13 Considering a PMT i in subrun j , the mean number of photoelectrons generated
 14 per event in that PMT for that subrun, μ_{ij} can be decomposed as follows:

$$15 \quad \mu_{ij} = I_j k_i = I_j b_i f_i. \quad (4.4)$$

16 I_j is the intensity of the subrun, i.e. the mean number of photons generated
 17 from the fibre in that subrun per event. k_i is the probability that a given photon
 18 generated at the fibre source ends up generating a photoelectron in PMT i .
 19 This itself can be further split into two components: b_i , the probability that a
 20 given photon at the fibre source points in the direction of PMT i ; and f_i , the
 21 probability that a given correctly-pointed photon actually makes it to the PMT
 22 and successfully generates a photoelectron. It is b_i that is the actual beam profile
 23 we would like to measure.

24 Letting p_{ij} be the probability of observing a hit for a given event on a given
 25 PMT, the probability of observing m_{ij} hits out of N_j events in the subrun will be

binomially-distributed:

$$P(m_{ij}|\mu_{ij}) = L(\mu_{ij}|m_{ij}) = \binom{N_j}{m_{ij}} p_{ij}^{m_{ij}} (1-p_{ij})^{N_j-m_{ij}} = \binom{N_j}{m_{ij}} (1-e^{-\mu_{ij}})^{m_{ij}} e^{-\mu_{ij}(N_j-m_{ij})}. \quad (4.5)$$

Here we have used equation 4.2, and noted that this probability distribution in m can be re-framed as a likelihood function for the parameter μ_{ij} . Considering only a single subrun of data, the maximum likelihood estimate of the parameter μ_{ij} can be shown to be:

$$\langle \mu_{ij} \rangle = -\ln \left(1 - \frac{m_{ij}}{N_j} \right) = \ln (1 - o_{ij}) \quad (m_{ij} \neq N_j), \quad (4.6)$$

where o_{ij} is just the occupancy of PMT i in subrun j . This is just the multi-hit correction formula seen in equation 4.3, which makes sense.

When looking at multiple subruns for the same fibre, the total likelihood function for a given PMT when considering all the data for a given fibre will be the product of the likelihoods from each dataset,

$$L(\{I_j\}, k_i | \{m_{ij}\}) = \prod_j L(I_j, k_i | m_{ij}) = \prod_j \binom{N_j}{m_{ij}} (1-e^{-I_j k_i})^{m_{ij}} e^{-I_j k_i (N_j-m_{ij})}. \quad (4.7)$$

This leads to a log-likelihood distribution of

$$\mathcal{L}(\{I_j\}, k_i | \{m_{ij}\}) = \sum_j \left[\ln \left(\binom{N_j}{m_{ij}} \right) + m_{ij} \ln (1 - e^{-I_j k_i}) - I_j k_i (N_j - m_{ij}) \right]. \quad (4.8)$$

Formally, one could combine the likelihoods of all the PMTs together, and by looking at the maximum likelihood estimates for each of the parameters measure the parameter values this way. However, the set of equations one obtains through this approach quickly become analytically intractable, because the PMTs are coupled by the intensity values I_j . Even a direct numerical approach would be

¹ liable to fail: for a given fibre there can be dozens of subruns, and many thousands
² of PMTs of relevance, so the dimensionality of the system of equations would be
³ far too large.

⁴ Because of this, a different approach was taken. It is expected that in a subrun
⁵ the total npe, summed over all good PMTs, should be proportional to the intensity
⁶ value I_j . One must be careful about this construction — different subruns can
⁷ have different sets of good PMTs, so two subruns with identical I_j values could
⁸ have a larger summed npe merely because more PMTs were good in that subrun.
⁹ To counter-act this effect, only PMTs that were classified as good in *all* subruns
¹⁰ being analysed for that fibre would be used for the npe summation. In other
¹¹ words, we use data from PMT i for summing only if:

$$\text{12} \quad i \in \mathcal{I} = \bigcap_j G_j. \quad (4.9)$$

¹³ We can then define the summed npe for a given subrun as $S_j = \sum_{i \in \mathcal{I}} \text{npe}_{ij}$, and
¹⁴ assert that $I_j = cS_j$. By finding a value proportional to I_j , there is now enough
¹⁵ information to maximise the log-likelihood $\mathcal{L}(k_i | \{m_{ij}\}, \{I_j\})$ with respect to k_i
¹⁶ for each PMT independently, and hence obtain estimates for these k_i parameters.

¹⁷ Of course, what is actually wanted are the underlying b_i values, not k_i . This is
¹⁸ where isotropic simulations come in. For each run of data used, a matching isotropic
¹⁹ MC was produced. As an example, a simulation for run 114,023 contained 200,000
²⁰ events for each fibre using an isotropic beam profile, over the full wavelength
²¹ range considered in this run, 500–600 nm, using the same run conditions as in
²² data (which PMTs were at high voltage, etc.).

²³ For each isotropic MC run, both I_j^{MC} and k_i^{MC} were calculated via the method
²⁴ described above. Because the simulations were isotropic, the underlying value
²⁵ for b_i was constant across all the PMTs, and so $ak_i^{MC} = f_i$. By doing some

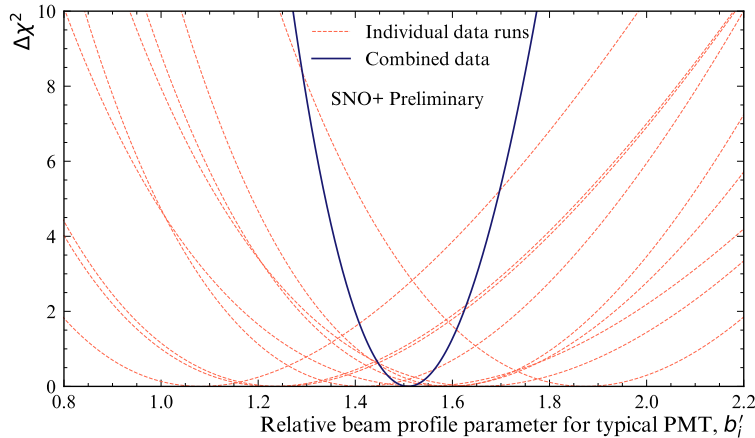


Fig. 4.6: Plot of $\Delta\chi^2 \simeq X_i$, twice the negative log-likelihood ratio, for both single subruns of a typical PMT, and when all relevant subruns are combined.

rearranging of equation 4.4, we find that:

$$\mu_{ij} = I_j b_i f_i = c S_j b_i a k_i^{MC} = (acb_i) S_j k_i^{MC}. \quad (4.10)$$

As a result of this, given the set $\{S_j\}$ and k_i^{MC} , one can maximise the log-likelihood \mathcal{L} with respect to $b'_i = acb_i$ numerically, to obtain the maximum likelihood estimate of b'_i . Because a and c were global constants of proportionality, they would become irrelevant as soon as the beam profile was normalised in the CDF-creation process outlined in 4.1.2.

Figure 4.6 shows the shape of this log-likelihood distribution for a particular PMT when considering fibre FS007's beam profile. One can see how individual subruns provide much more information when combined than if one looked at a single subrun alone.

Another benefit of using this log-likelihood approach is that the resulting distribution's shape can be used for uncertainty estimation. In almost all cases, Wilks Theorem [145] allows us to produce 1σ confidence intervals about the

maximum likelihood estimate for b'_i , $\langle b'_i \rangle$, because

$$X(b'_i) = -2 [\mathcal{L}(b'_i) - \mathcal{L}(\langle b'_i \rangle)]$$

¹ approximates a χ^2 -distribution. As a result, the error bounds on our parameter
² estimate are given by when $X = 1$. The fact that the shape of X can be well-
³ approximated by a quadratic in the region near $X = 0$ indicates the validity of
⁴ Wilks' Theorem being used here.

⁵ Only a couple of exceptions to this approach of parameter estimation are
⁶ possible. In the case where $m_{ij} = N_j$, i.e. a PMT has 100% occupancy, no
⁷ maximum likelihood estimate exists: we need not worry about this, as subruns
⁸ where this occurs have not been used. On the other end, however, there are some
⁹ PMTs for certain fibres where after all subruns of data have been included, there
¹⁰ remains no hits. In this scenario, one can show that the log-likelihood becomes
¹¹ linear in the beam profile parameter:

$$\mathcal{L}(b'_i | \{m_{ij} = 0\}) = b'_i k_i^{MC} \cdot \sum_j [I_j N_j]. \quad (4.11)$$

¹² This scenario is very much reminiscent of rare-decay searches, and a similar
¹³ approach can be used. A 1σ upper limit on the possible value for b'_i can be
¹⁴ analytically-calculated to be:

$$b'_{i,ulim} = -\frac{k_i^{MC} \sum_j [I_j N_j]}{\ln [1 - \text{erf} (1/\sqrt{2})]}, \quad (4.12)$$

¹⁵ where $\text{erf}(x)$ is the error function.

4.3 Comparisons between Data and Simulation 1

In this section, the major systematic differences between simulations of SMELLIE and data that remain after the above improvements have been made are discussed. These fall into three broad categories. The two of these are the differences seen in the forward and back hemispheres of the detector relative to a given fibre; the third are differences in the timing distributions of the light. 2
3
4
5
6

4.3.1 Forward Hemisphere Discrepancies 7

Figure 4.7 shows the impact of using additional subruns of data on a typical beam profile. One can clearly see the great reduction in the number of PMTs with no hits in data. That many more data sets were included allowed for the major increase in dynamic range available for measuring these b'_i values. One can also note that by including additional data the curious spot that was seen in the old beam profile our at $r \approx 0.08$ has gone, further indicating that it was an artefact of that single data set. 8
9
10
11
12
13
14

Further details can be gathered from the interpolated intensity maps, one of which can be seen in figure 4.8. There are two curious stand-out features that can be seen here: firstly, there are multiple distinct parabolic arcs. These correspond to the shadows of the ropes that hold up/down the AV. More precisely, they are the mismodelling of those shadows — if the shadows were in the right place in the isotropic MC, then they would correctly cancel out any decreased intensity seen in the data of shadowed PMTs. These shadows could be mismodelled either because the positions of the ropes in the MC are in the wrong place, or the fibre's emission position is wrong. Note that any mismodelling of the fibre's nominal emission direction has no impact on this shadowing problem, as changing that direction merely causes a change of basis in the (r, ϕ) -space. The latter possibility 15
16
17
18
19
20
21
22
23
24
25

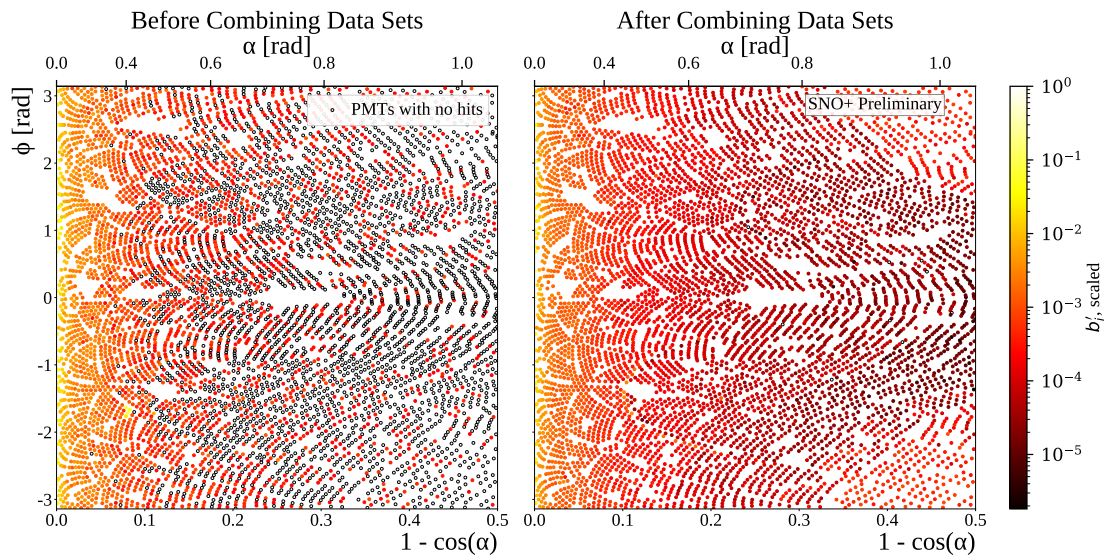


Fig. 4.7: Comparison between old and updated beam profiles for fibre FS055, after combining multiple data sets. Once again, the relative intensities (b'_i) for each PMT are given by the colour of each point, the position of each plotted in the 2D (r, ϕ) -space. The relative intensities have been both scaled here so that the largest value equals 1. Hollowed-out points are PMTs that, even after all relevant subruns have been combined, have no PMT hits.

of incorrect fibre positions are more likely, and in fact these arcs in the beam profiles could be used as an effective way to correct for this problem.

The second distinctive feature of this intensity map is the large band of lower intensity varying between $r \approx 0.2 - 0.5$, followed by larger intensity out at large r values. This feature comes from light reflecting off the AV surface, or internally-reflecting. The reason for this band's functional dependence on ϕ is that this particular fibre, FS055, has a nominal fibre direction $\sim 10^\circ$ from pointing radially-towards the detector's centre. This feature appears in the updated beam profiles of all fibres, but its shape depends on the particular fibre's direction — for fibres pointing directly towards the detector's centre, there is little ϕ -dependence observed. Like the ropes, this feature must come from some form of mismodelling of the optics of the AV. A de-facto shadowing of PMTs in line with tangents from the AV surface which intersect the fibre position is to be expected. One also expects PMTs at polar angles larger than this to have their observed intensities boosted

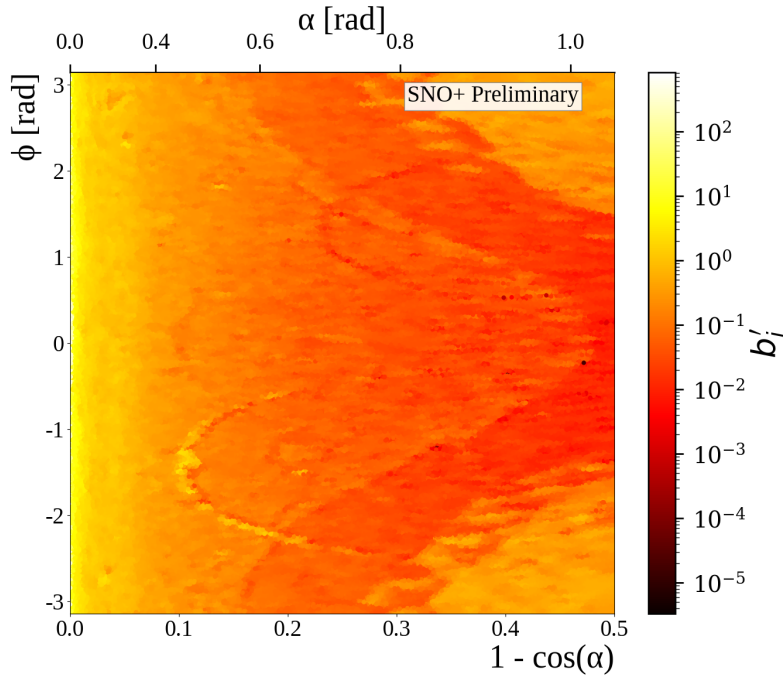


Fig. 4.8: Interpolated intensity map for the new updated beam profile of fibre FS055. The misalignment of rope shadows and AV effects, can both be seen.

from reflected light off the AV. However, the discontinuities seen in the beam profiles indicate that for whatever reason this effect has been over-emphasised in the simulation.

There is a further phenomenon that can be seen, by comparing beam profile values obtained from a single subrun to the updated combined beam profile. This can be done by calculating the residuals corresponding to the single subrun, relative to the combined data set. The residual is negative if the combined data sets have a b'_i below the equivalent for a given single subrun; that is, the combined model underestimates this subrun for that PMT.

This information was plotted for two different subruns from the same fibre, seen in figure 4.9. One subrun was the same one used by Esther Turner for the original 2D beam profiling, with a wavelength of 495 nm; the latter was at the longer wavelength of 595 nm. For both subruns, most PMTs are seen to have intensities well-modelled by the combined model. However, their appears

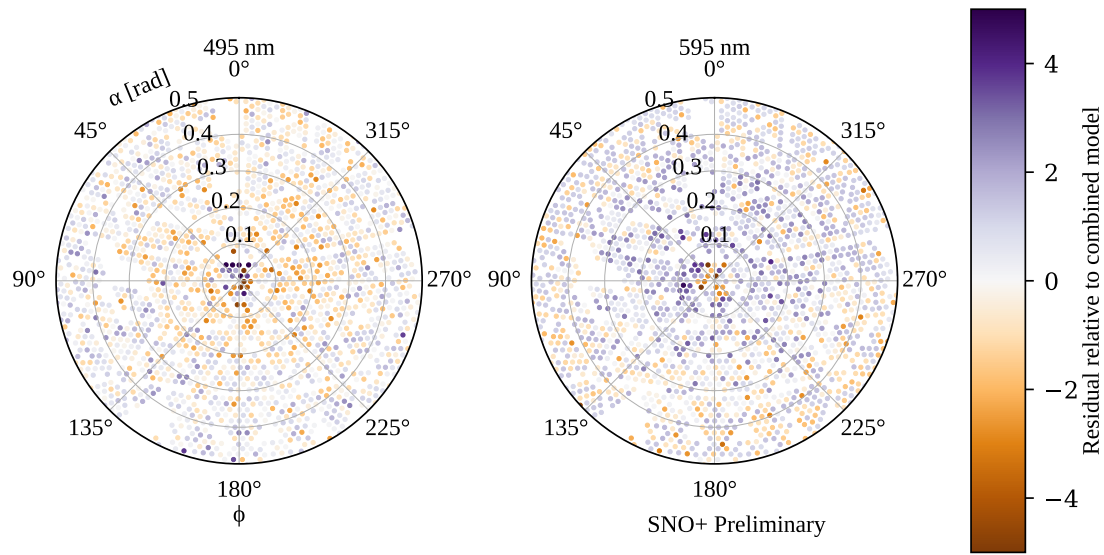


Fig. 4.9: Residuals from subruns at two different wavelengths, both compared to the combined beam profile model for fibre FS055. A negative sign, and hence bluer colours, indicate that the combined model underestimates the observed intensity for that particular subrun. Values with a magnitude beyond 5 are shown capped at this maximal value for the purposes of this plot. These PMTs are plotted in the polar fibre coordinates (α, ϕ).

1 to be a significant amount of mismodelling within the beamspot. There also
 2 appears to be some systematic shift between data and model at somewhat larger
 3 polar angles. Moreover, this mismodelling seems not to be merely random, but
 4 a function of wavelength: at shorter wavelengths the beamspot tends towards
 5 being overestimated and then underestimated at larger values of α . At longer
 6 wavelengths, the beamspot becomes underestimated, with larger angles getting
 7 overestimated. This indicates that there appears to be a wavelength-dependence
 8 on the beam profiles, contradicting one of the main assumptions which we used
 9 to combine the water-phase data in the first place! All three of these features
 10 — rope shadows, AV reflections, and wavelength dependence — add systematic
 11 uncertainty to the beam profiles, beyond the statistical uncertainty as measured
 12 by the width of the likelihood distribution. Certainly if one wanted to further
 13 improve the uncertainties in the beam profiles, tackling these challenges would be
 14 key.

4.3.2 Emission Time Discrepancies

In addition to systematics in the spatial distribution of light observed in the forward distribution, for two sets of lasers there are notable emission timing discrepancies. The first is the double-peaked timing structure of the SuperK laser, which was discussed in Section 3.5. The other main difference is associated with the PQ495 laser.

Fig. 4.10 shows the time residual distribution of hits in the 10° beamspot PMT region of fibre FS007, due to PQ495 laser light fired in July 2022. The “ t_{med} ” approach to determining the emission time was used, as described in Section 3.5. Also shown in this plot is the time distribution from a simulation of this same setup. The spike at $t_{\text{res}} = 0$ for both distributions corresponds to events with only a single hit in the beamspot. Almost all hits shown here are known to come from direct light. The shape of the distribution in MC is largely determined by the transit time distribution of the PMTs, which give rise to the four peaks seen in the MC. Aside from the prompt peak around $t_{\text{res}} = 0$, the earlier peak is associated with PMT pre-pulsing, and the latter two peaks with PMT late-pulsing [146].

The two major discrepancies between data and MC seen for this laser is the much broader prompt peak seen in data than expected, and the bump at ~ 19 ns. Neither of these effects are seen in the other PQ lasers. Because these hits come almost exclusively from direct light, the most likely explanation for this difference is a change in the emission time distribution of the PQ495 laser, relative to the timing distributions used in RAT which were provided by the laser’s manufacturer. One method for resolving this problem could be to measure the laser’s emission timing distribution with an oscilloscope, in the same manner used by J. Lidgard to determine the timing distribution for the SuperK laser [140].

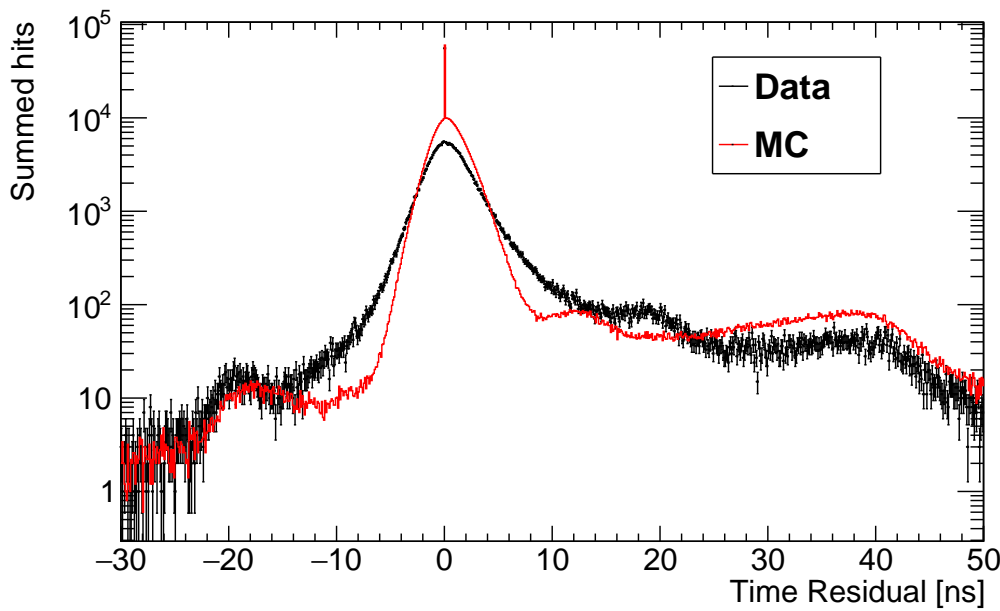


Fig. 4.10: Time residual distribution in the beamspot region for data taken in July 2022 with PQ495 through fibre FS007, as compared to a matching simulation. The width of the data’s prompt peak is much broader than expected, and there is a notable bump at 19 ns not present in the MC.

4.3.3 Backward Hemisphere Discrepancies

A third class of systematic differences between data and simulation of SMELLIE events are those discrepancies observed in the distributions of hits near a given fibre emission point. Consider the region of 50 PMTs closest to a given fibre. This defines what shall be called the “back-scatter” region of PMTs, because these will be the PMTs which will see the greatest intensity of light that has Rayleigh scattered in the UPW outside the AV. For a given subrun, only the subset of these PMTs which were ‘good’ in the sense described in Section 4.2.1 were used.

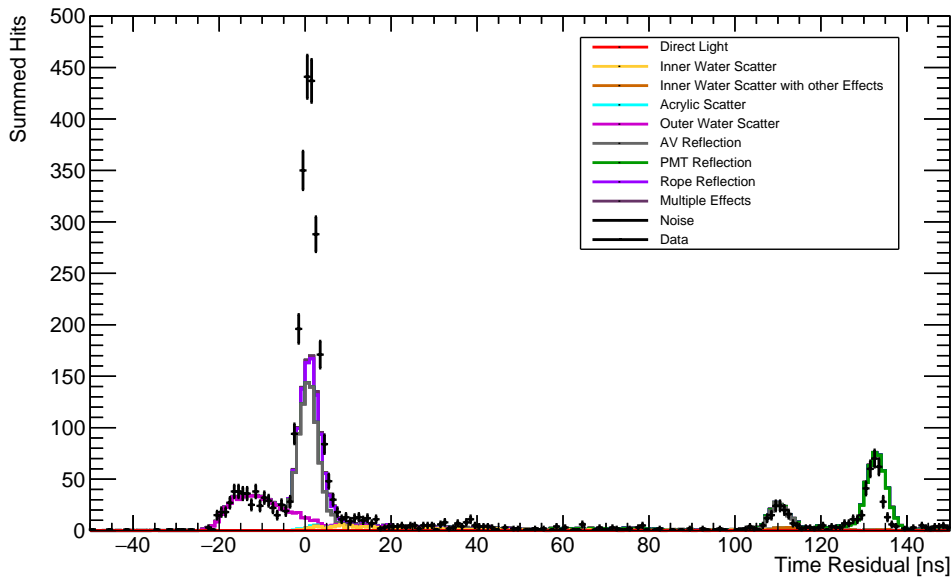
This PMT region will become useful to the analyses described in Chapter 5.

Fig. 4.11 shows the time residual distributions for data taken in water phase run 114,018 in the back-scatter PMT region, using the SuperK laser in the wavelength range 490–500 nm. The method of emission time calculation used here is that of t_{med} . Because it is not possible for light to travel straight from the fibre emission

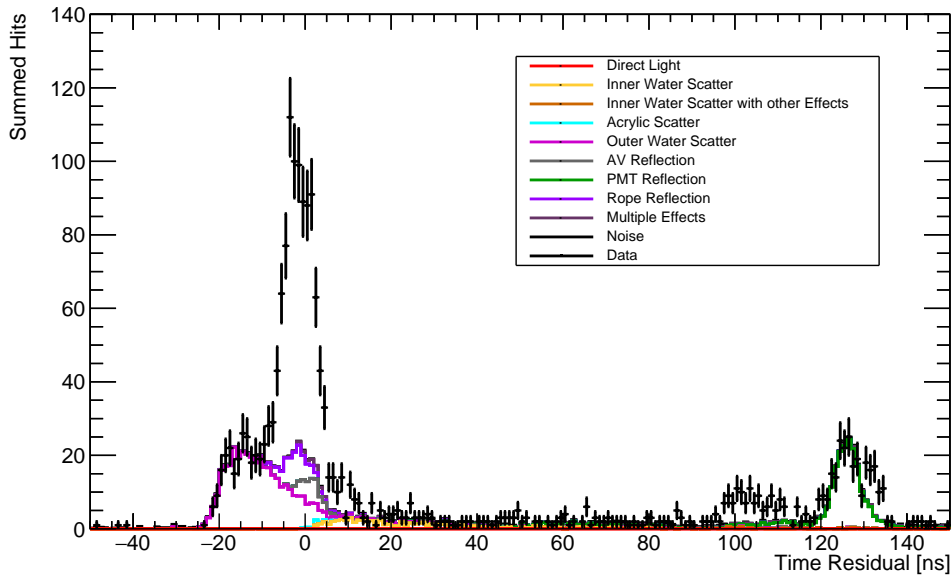
point to a PMT in the back-scatter region, the light-paths used for calculating the time-of-flight in the time residuals here correspond to those which reflect off of the AV surface. Also shown in these plots are matching simulations of these subruns. The distributions from simulation are displayed as stacked histograms, where each individual histogram corresponds to the subset of hits associated with photons that underwent specific types of path. The overall intensity of the simulation has been scaled so that the number of hits in the $[-30, -10]$ ns time residual window is equal in data and MC, corresponding to a window in which only light that back-scattered in the outer water was observed.

Looking at Fig. 4.11a in particular, corresponding to the 0° fibre FS007, both data and simulation observe five distinct regions of interest. After the earliest peak from light which back-scattered in the outer water, there is a prominent peak near 0 ns arising from reflections off of the AV surface nearest to the fibre, as well as reflections from ropes. After this, in the 10–50 ns range, there is a long tail of hits due to a number of effects, including back-scattering in the inner water. Much later, there are two further peaks: one at 110 ns due to reflections off of the far AV surface, and one at 132 ns due to reflections off of the PMTs and concentrators on the far side of the detector.

Although all the features described above are seen qualitatively in both data and MC, there are a couple of notable discrepancies. The first to note are the differences in shape seen in the PMT reflection peaks of both fibres shown. The FS007 data has a tighter peak than expected from simulation, whilst the FS155 data sees the opposite. These differences are likely due to the current limitations of the PMT reflection model used in RAT. Fig. 4.12 shows the best-fit of Laserball data to simulations with varying PMT reflection models, taken from [85]. The last peak in this plot comes from PMT reflections, which shows a small disagreement between data and MC. It is presumably this residual systematic in the modelling



(a) Fibre FS007



(b) Fibre FS155

Fig. 4.11: Plots showing comparisons between the time residual distributions in the ‘back-scatter’ PMT region for water phase SMELLIE data taken in run 114,018, with the SuperK laser in the wavelength range 490–500 nm for two different fibres, and matching MC.

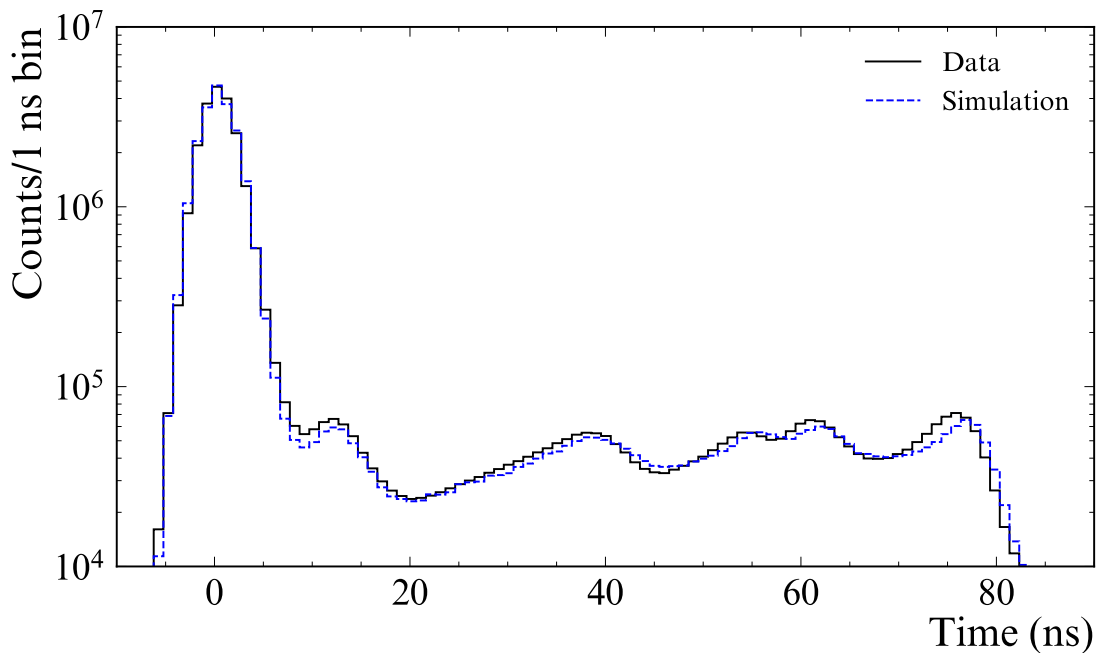


Fig. 4.12: Comparison of Laserball data in the water phase to MC, with a wavelength of 420 nm. The latest peak comes from PMT reflections. From [85].

of the PMT reflections that leads to the shape differences in the peaks seen in the SMELLIE data.

The other prominent difference is the magnitude of the peak at 0 ns, with data appearing to have a peak over twice the size of simulation. This can clearly be seen for the results of both fibres in Fig. 4.11. What could cause this discrepancy? One simple explanation is that the intensity calibration of the MC is wrong. Because the intensity of the simulation shown here has been forced to match that of the outer water back-scattered light, if the scattering length of this water is systematically off in simulation then so too would the intensity calibration. If this were the case, then the true Rayleigh scattering length of the outer water would have to be substantially longer than expected in order to explain the discrepancy in the peak at 0 ns. However, this would cause a substantial change in the magnitudes of the two later peaks. Given that these two late peaks have magnitudes which appear to agree with data under the current intensity calibration, a large systematic in the UPW scattering length does not seem like the primary cause of this systematic.

1 A second hypothesis for explaining the difference in peak heights at 0 ns is
2 that there is far more light being reflected off of the AV surface than expected.
3 As discussed in Section 2.3.2, standard specular reflection is entirely determined
4 by the refractive indices of the two media, and the angle of incidence of the light.
5 The refractive indices of the UPW and acrylic are well-known, and because FS007
6 is a 0° fibre, the angles of incidence of light rays will be close to 0° also. The
7 fact that there appears to be good agreement between data and MC in the peak
8 from reflections off of the far AV surface casts strong doubt on a substantial
9 miscalculation of the specular reflection. An alternative theory is the existence of
10 a diffusive reflection component on the AV surface, due to a surface roughness.
11 This could possibly explain the existence of a peak seen in data in Fig. 4.11b, but
12 not in the MC.

13 There are two further hypotheses which could possibly help to explain the 0 ns
14 peak discrepancy. One is that the extra light in this peak comes from scattering
15 in the acrylic, with the scattering length being much shorter than currently
16 modelled. The current RAT model indicates that only a negligible fraction of light
17 gets scattered in the acrylic, so there would need to be a dramatic change in the
18 scattering length. The final hypothesis is that the rope reflections are currently
19 being mismodelled. Currently, the model for rope reflections in RAT assumes 60%
20 reflectivity with the reflections being purely diffusive. However, this is based on
21 preliminary estimates only, with no formal calibration to back this reflection model
22 up. It could be the case that a different reflection model could help to alleviate
23 the tension between data and model in the peak, although it is challenging to see
24 how the all the difference could be attributed to purely this.

Chapter 5

Analysis of SMELLIE Data in the Scintillator Phase

Due to Local Education Authority cuts,

*The light at the end of the tunnel has been
switched off.*

DR. FRANK CHEW

In this chapter, two novel analyses using data from SMELLIE are built and implemented. The first is a method for measuring the extinction lengths of the SNO+ scintillator as a function of both wavelength and time; the second is a way of monitoring changes in Rayleigh scattering. A key theme of both is the careful design of their methodologies to avoid the known systematics discussed in Section 4.3.

5.1 Extinction Length Analysis

The first analysis discussed in this chapter is the measurement of the extinction lengths of the liquid scintillator deployed in the SNO+ detector, as a function of both wavelength and time. As seen in Fig. 3.2, SMELLIE data was taken during

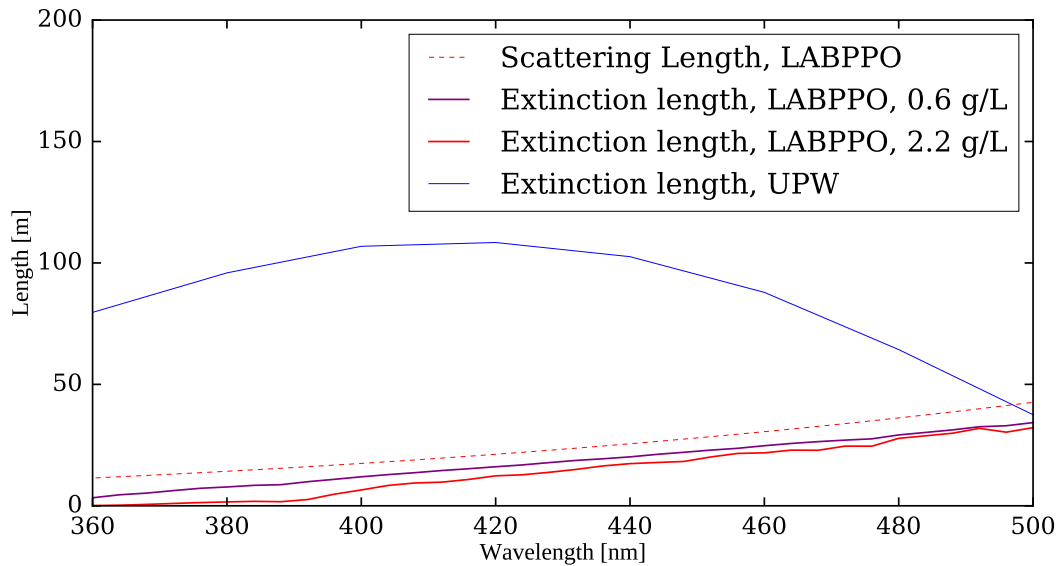


Fig. 5.1: Current RAT models for the extinction lengths of both UPW and scintillator, at different PPO concentrations as a function of wavelength. For the scintillator, the scattering length distribution is also shown as a dotted line, showing that it is expected for scattering to dominate over absorption in the 400–500 nm range.

the water phase, and in the scintillator phase when the PPO concentration of the LABPPO was at a variety of levels. Fig. 5.1 shows the changes in extinction length with detector phase, as a function of wavelength, according to the optical model described in Section 2.3.2, and implemented in RAT. This will be discussed further in Sections 5.1.3 & 5.2.4.

5.1.1 Mathematical Model

To begin, consider light emission from a particular SMELLIE fibre of fixed wavelength λ_j , with a mean emission intensity of I_j photons emitted per event in subrun j during detector phase p . Modifying Eq. 4.4, a general PMT i will have a mean npe per event of $\mu_{ij,p}(\lambda_j) = I_{j,p} b_{i,p}(\lambda_j) f_{i,p}(\lambda_j)$. A detector phase-dependence has been added to all terms, because:

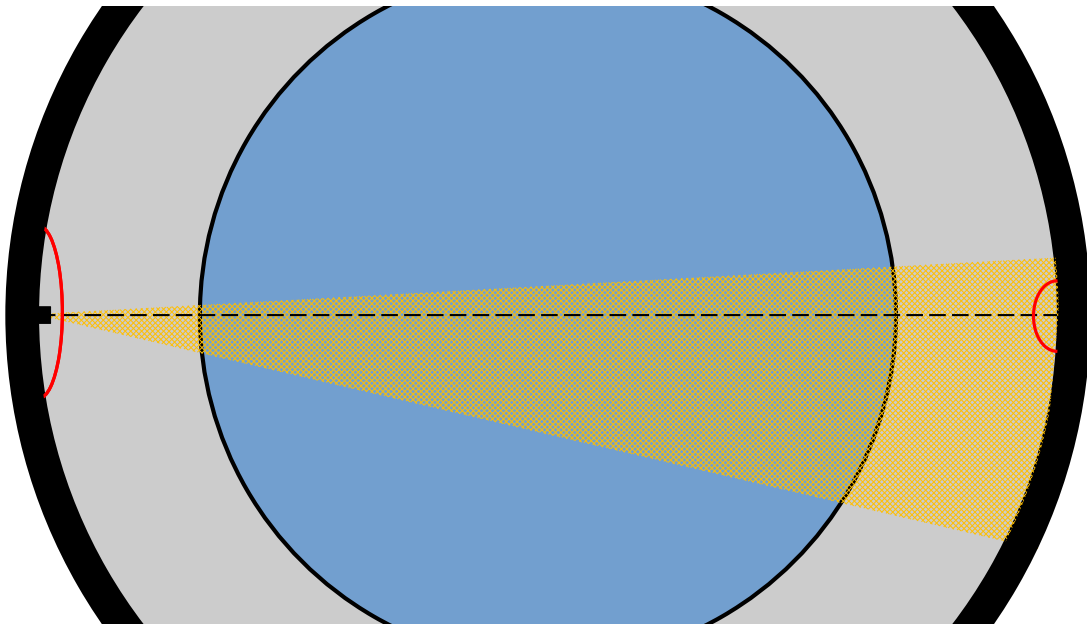


Fig. 5.2: Diagram showing the two PMT regions used in this analysis, indicated by red rings.

- The emission intensities chosen, $I_{j,p}$, can vary between different data-taking campaigns. These changes are due to changes in hardware (as detailed in Chapter 3), as well as changes in the settings used to run SMELLIE.
- The beam profile of a given fibre at a given wavelength is not expected to change with detector phase. However, if the refractive index of the inner detector medium changes (e.g. from the water phase to scintillator phase), then the fraction of light emitted that is pointed in the correct direction to be detected by PMT i , $b_{i,p}(\lambda_j)$, *can* change.
- In a different phase of the detector, the optics of the inner detector can change. As a result, the probability that a photon pointing in the correct direction for PMT i actually makes it across the detector and generates a photoelectron, $f_{i,p}(\lambda_j)$, *can* change.

In this analysis, two regions of PMTs will be used for a given fibre; Fig. 5.2 shows a schematic of the PMT selections. The first region corresponds to PMTs *radially-opposite* the fibre emission point in the detector, i.e. the lightpaths travel

¹ orthogonally through all surface boundaries. The reason for this choice will be
² explained shortly. Considering the various contributions to the value of $f_{i,p}(\lambda_j)$, a
³ PMT in this ‘far’ selection will have a mean npe per event, $\mu_{ij,p}^{\text{far}}(\lambda_j)$, of:

$$\mu_{ij,p}^{\text{beam}}(\lambda_j) = I_{j,p} b_{i,p}(\lambda_j) \exp\left(-\frac{L_{ij,p}^{\text{extern}}(\lambda_j)}{l_p^{\text{extern}}(\lambda_j)}\right) \exp\left(-\frac{L_{ij,p}^{\text{acr}}(\lambda_j)}{l_p^{\text{acr}}(\lambda_j)}\right) \exp\left(-\frac{L_{ij,p}^{\text{inner}}(\lambda_j)}{l_p^{\text{inner}}(\lambda_j)}\right) \\ \cdot T_{ij,p}(\lambda_j) \epsilon_{ij,p}(\lambda_j). \quad (5.1)$$

⁷ Here, $L_{ij,p}^{\text{extern,acr,inner}}(\lambda_j)$ is the length of a path in a given detector medium through
⁸ which light travels, for the external water, acrylic, and inner detector medium,
⁹ respectively. $l_p^{\text{extern,acr,inner}}(\lambda_j)$ is the extinction length of each detector medium
¹⁰ for a given wavelength — it is assumed that only the inner detector medium has
¹¹ changing optics in different phases. Some fraction of light is lost when passing
¹² between two mediums with different refractive indices: this is captured by $T_{ij,p}(\lambda_j)$,
¹³ the product of the Fresnel transmission components for all optical boundaries
¹⁴ along a photon’s path. Finally, $\epsilon_{ij,p}(\lambda_j)$ is the probability that a photon along
¹⁵ a given path, incident on a given PMT, will generate a photoelectron that is
¹⁶ detected.

¹⁷ The second selection of PMTs are those near the fibre emission point. The first
¹⁸ light observed by these PMTs will be from photons which have ‘back-scattered’ in
¹⁹ the UPW outside the AV. This is followed by light reflected off of the AV surface.
²⁰ The details of isolating this backscattered light is discussed in Section 5.1.2.
²¹ Assuming that the Rayleigh scattering properties of the UPW outside the AV
²² have been unchanged throughout the lifetime of the detector, then the expected
²³ number of photoelectrons observed in a selection of these PMTs during a time
²⁴ period in which only back-scattering can occur will be simply:

$$\mu_{j,p}^{\text{back}} = k I_{j,p}. \quad (5.2)$$

k here is just some general constant of proportionality. Therefore, observing this back-scattered light can be used as a measure of the relative intensity of the subrun.

Because $\mu_{j,p}^{\text{back}}$ is proportional to the intensity, the ratio $R_{ij,p} = \mu_{ij,p}^{\text{beam}}(\lambda_j)/\mu_{j,p}^{\text{back}}$ will be independent of $I_{j,p}$. A similar trick can be used to remove the dependence of $R_{ij,p}$ on k , by taking the ratio of $R_{ij,p}$ with $R_{ij,\text{H}_2\text{O}}$, where $R_{ij,\text{H}_2\text{O}}$ is the measured values of $R_{ij,p}$ in the water phase. This ratio becomes:

$$\begin{aligned} \frac{R_{ij,p}}{R_{ij,\text{H}_2\text{O}}}(\lambda_j) &= \frac{k}{k} \frac{b_{i,p}(\lambda_j)}{b_{i,\text{H}_2\text{O}}(\lambda_j)} \frac{T_{ij,p}(\lambda_j)}{T_{ij,\text{H}_2\text{O}}(\lambda_j)} \frac{\epsilon_{ij,p}(\lambda_j)}{\epsilon_{ij,\text{H}_2\text{O}}(\lambda_j)} \exp\left(-\frac{L_{ij,p}^{\text{extern}}(\lambda_j) - L_{ij,\text{H}_2\text{O}}^{\text{extern}}(\lambda_j)}{l^{\text{extern}}(\lambda_j)}\right) \\ &\quad \cdot \exp\left(-\frac{L_{ij,p}^{\text{acr}}(\lambda_j) - L_{ij,\text{H}_2\text{O}}^{\text{acr}}(\lambda_j)}{l^{\text{acr}}(\lambda_j)}\right) \exp\left(-\frac{L_{ij,p}^{\text{inner}}(\lambda_j)}{l_p^{\text{inner}}(\lambda_j)} + \frac{L_{ij,\text{H}_2\text{O}}^{\text{inner}}(\lambda_j)}{l_{\text{H}_2\text{O}}^{\text{inner}}(\lambda_j)}\right) \\ &= \frac{b_{i,p}(\lambda_j)\epsilon_{ij,p}(\lambda_j)}{b_{i,\text{H}_2\text{O}}(\lambda_j)\epsilon_{ij,\text{H}_2\text{O}}(\lambda_j)} \frac{T_{ij,p}(\lambda_j)}{T_{ij,\text{H}_2\text{O}}(\lambda_j)} \exp\left(-\frac{L_{ij,p}^{\text{inner}}(\lambda_j)}{l_p^{\text{inner}}(\lambda_j)} + \frac{L_{ij,\text{H}_2\text{O}}^{\text{inner}}(\lambda_j)}{l_{\text{H}_2\text{O}}^{\text{inner}}(\lambda_j)}\right), \end{aligned} \quad (5.3)$$

where it has been assumed that any change in path length through the external UPW or acrylic relative to their extinction lengths is negligible.

Importantly, when considering the first PMT selection, a further simplification can be made to the above formula. Because the light travels orthogonally through the AV boundaries, its path is unaffected by changes in the refractive index of the inner detector medium. Therefore, the impact of the beam profile and PMT efficiency will be unchanged, and so the formula simplifies to:

$$R_{ij,\text{H}_2\text{O}}(\lambda_j) = \frac{T_{ij,\text{H}_2\text{O}}(\lambda_j)}{T_{ij,p}(\lambda_j)} \exp\left(\frac{L_{ij,p}^{\text{inner}}(\lambda_j)}{l_p^{\text{inner}}(\lambda_j)} - \frac{L_{ij,\text{H}_2\text{O}}^{\text{inner}}(\lambda_j)}{l_{\text{H}_2\text{O}}^{\text{inner}}(\lambda_j)}\right) \cdot R_{ij,p}(\lambda_j). \quad (5.4)$$

The measurable quantities $R_{ij,\text{H}_2\text{O}}(\lambda_j)$ and $R_{ij,p}(\lambda_j)$ are then proportional to one another, with the constant of proportionality being a function of the variable of interest $l_p^{\text{inner}}(\lambda_j)$.

¹ 5.1.2 Parameter Measurements and Uncertainties

² As a result of Eq. 5.4, measuring the extinction length of the scintillator requires
³ first measuring a number of other quantities with knowledge of their uncertainties.

⁴ UPW Extinction Lengths

⁵ As discussed in Section 2.3.2, the attenuation lengths of the UPW were measured
⁶ as a function of wavelength in the water phase with the Laserball. It is assumed
⁷ that the optics of the UPW inside and outside the AV were the same, and outer
⁸ UPW has not changed since.

⁹ In this analysis, the measured values of the attenuation coefficients $\alpha_w(\lambda) =$
¹⁰ $1/l_{\text{H}_2\text{O}}^{\text{inner}}(\lambda)$ and their associated errors were taken from [85]. The wavelength range
¹¹ this Laserball data was taken over was 337–500 nm, so avoid extrapolation only
¹² wavelengths in this range were considered in this analysis. For a given SMELLIE
¹³ subrun with wavelength λ_j , $l_{\text{H}_2\text{O}}^{\text{inner}}(\lambda_j)$ was estimated by linearly interpolating
¹⁴ between Laserball α_w data points, and then taking a reciprocal. Because the
¹⁵ systematic uncertainties dominated for each Laserball data point, which were
¹⁶ likely to be highly correlated between data points, the uncertainty in $\alpha_w(\lambda_j)$ was
¹⁷ estimated by linearly interpolating the quadrature sum of the statistical and
¹⁸ systematic uncertainties at each Laserball data point. Fig. 5.3 shows this process
¹⁹ in action from the wavelength 375 nm. At its largest, the uncertainty in $l_{\text{H}_2\text{O}}^{\text{inner}}$ is
²⁰ $\sim 50\%$. Fortunately, the impact of this large error is mitigated in Eq. 5.4 because
²¹ $L_{ij,\text{H}_2\text{O}}^{\text{inner}}(\lambda_j) \ll l_{\text{H}_2\text{O}}^{\text{inner}}$.

²² Path Lengths and Transmission Coefficients

²³ Section 2.3.2 also discusses the measured refractive indices as a function of
²⁴ wavelength for the UPW, acrylic, and LABPPO. For a given detector phase, subrun,
²⁵ and PMT, the Collaboration’s Light Path Calculator is able to determine the

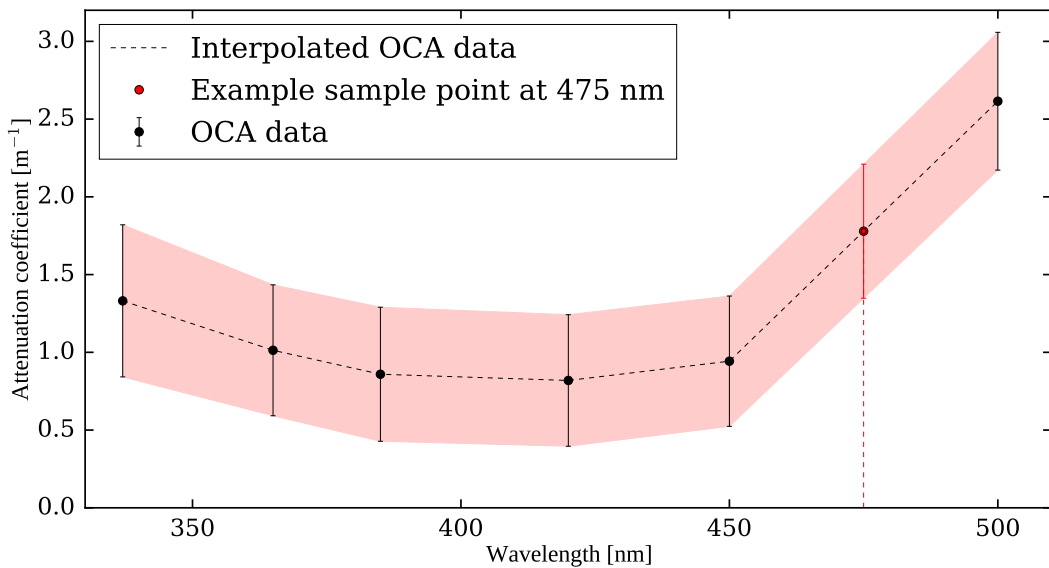


Fig. 5.3: Plot showing how linear interpolation has been used on the Laserball water phase UPW attenuation coefficient data. An example point at 475 nm is shown explicitly.

values of $L_{ij,p}^{\text{inner}}(\lambda_j)$ as well as the combined Fresnel transmission coefficient $T_{ij,p}(\lambda_j)$. 1

It is assumed that there is negligible uncertainty in these values. 2

Measuring the Number of Photoelectrons 3

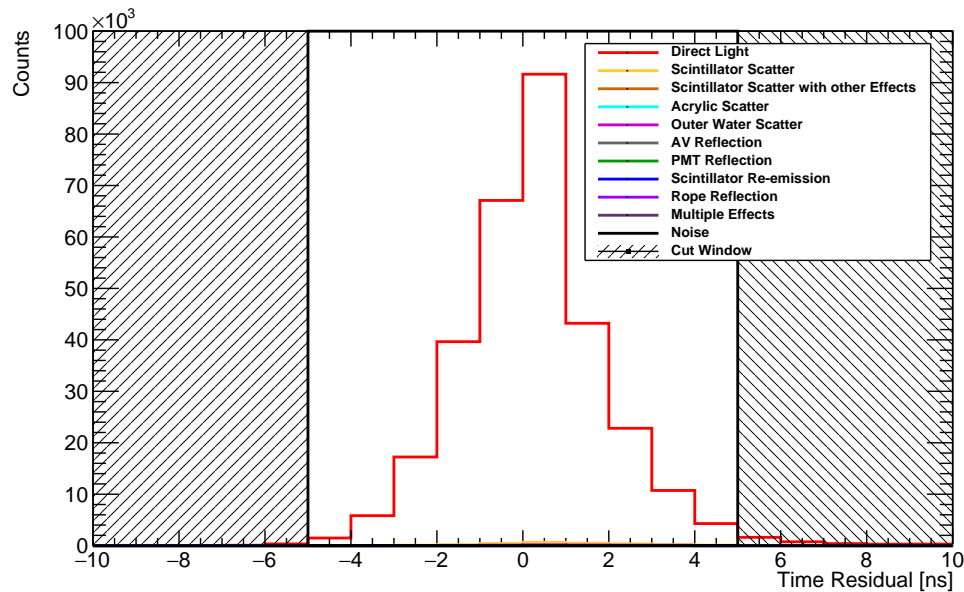
Critical to this analysis is the determination of the mean npe per event in both ‘far’ and ‘backscatter’ PMTs. These two PMT selections have to be approached slightly differently. 4 5 6

The ‘far’ PMTs were selected by first finding the intersection point on the PSUP with a line that passes through both the fibre emission point and the centre of the AV. The 20 PMTs closest to this point were chosen. For a given analysis between a scintillator phase subrun j and a matching water phase subrun, only PMTs inside this selection which were identified as “good” (as defined in Section 4.2.1) in both subruns were used. For a given far PMT being used, direct light was isolated by calculating the time residuals of all hits on the PMT, using the “ $t_{\text{emm}} = t_{\text{med}}$ ” approach mentioned in Section 3.5. Then, the number of hits observed in a “tight” time residual window of $[-5, +5]$ ns was measured for the 7 8 9 10 11 12 13 14 15

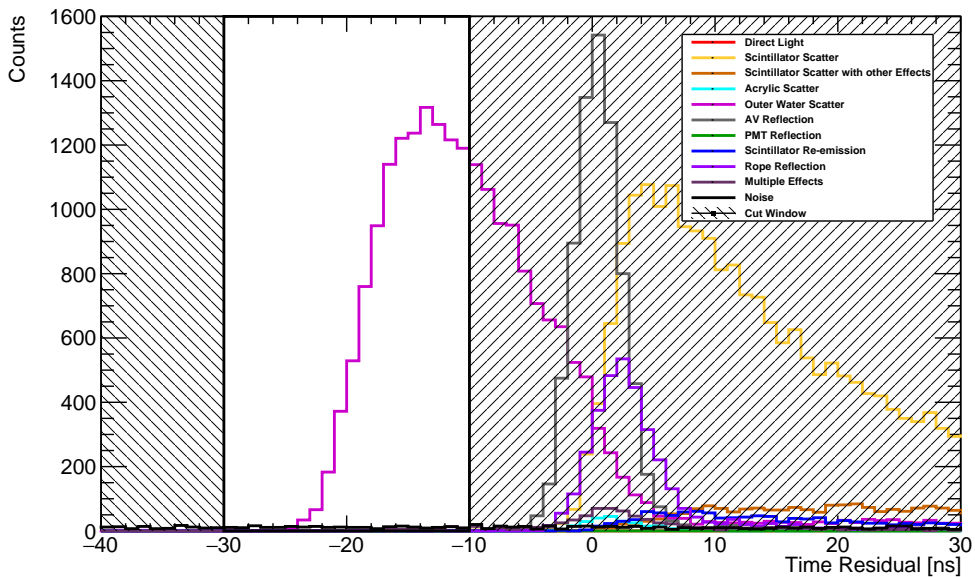
1 PMT of interest. By converting to occupancy and then using a multi-hit correction
 2 as described in Eq. 4.3, the total npe per event for that PMT was estimated. The
 3 uncertainty in this value was given by the Poisson error of the calculated npe. In
 4 order to minimise the statistical uncertainty, all individual far npe measurements
 5 for a given subrun were combined into one value of the ‘far’ light npe per event,
 6 $\mu_{j,p}^{\text{far}}$.

7 Backscattered PMTs were selected for each fibre by finding the 50 PMTs
 8 closest to the fibre emission point. A t_{res} window of $[-30, -10]$ ns was used for
 9 the isolation of backscattered light in each subrun. Like above, the total hits for
 10 each PMT was converted into a total npe with associated Poisson error. A final
 11 correction was made to account for noise hits: the measured noise rate of a given
 12 PMT was calculated using the PULSEGT triggers, as described in Section 3.6.
 13 After accounting for the width of the time window, the corresponding expected
 14 number of noise hits was subtracted off of the total measured npe to give the npe
 15 per event from direct light only. The npe from these PMTs were combined into
 16 one value of the backscattered light npe per event, $\mu_{j,p}^{\text{back}}$. The variables R_s and
 17 R_w are the ratios of the far light npe to the backscattered light npe for a given
 18 scintillator or water phase subrun, respectively. The subrun j subscript has been
 19 dropped for simplicity.

20 Fig. 5.4 shows the time residual distributions for both PMT selections of
 21 a simulation of the PQ407 laser being fired through fibre FS007 during the
 22 scintillator phase, with 2.2 g/L PPO loading. The simulation used the optical
 23 model described in Section 2.3.2. The earliest photon track associated with a given
 24 PMT hit was classified by the optical processes it underwent. A hit associated with
 25 a photon that travelled unimpeded through the detector is classified as ‘direct’.
 26 For this fibre and wavelength combination, the time residual windows used allow
 27 for a signal-to-background ratio of 98.8% for the far PMTs, and 99.7% for the
 28 backscattered PMTs, ignoring noise hits.



(a) Far region



(b) Backscatter region

Fig. 5.4: Time residual distributions of the far and backscatter PMT regions for a simulation using laser PQ407 through fibre FS007, split by the different optical components. The time windows defining the signal regions are shown in both.

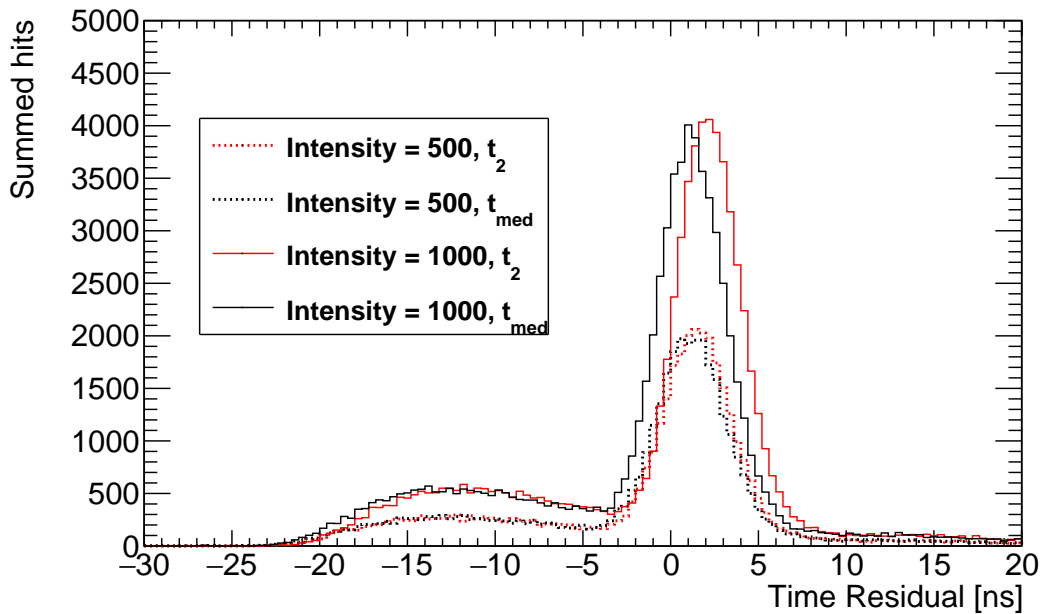


Fig. 5.5: Comparison of the backscatter light region time residual distribution, as a function of both emission intensity and emission time calculation choice. A clear intensity-dependence can be seen when using t_2 , whereas t_{med} is much more robust.

¹ t_{med} was used in this analysis instead of t_2 because it was found to be far
² more robust to changes in emission intensity. Fig. 5.5 shows a comparison of the
³ t_{res} distribution for backscattered PMTs between using t_2 and t_{med} , at different
⁴ emission intensities. As can be seen, the t_2 distribution is biased towards positive
⁵ t_{res} values as intensity increases. This is not the case when using t_{med} .

⁶ 5.1.3 Results in Data

⁷ Datasets Used

⁸ The datasets used in this analysis are summarised in Table 5.1. The water phase
⁹ data all came from run 114,018; scintillator phase data was taken at five different
¹⁰ points during the scintillator phase, two during the loading of PPO and three
¹¹ afterwards. These datasets match those highlighted in Fig. 3.2.

¹² ‘Medium’ intensity subruns from the PQ407, PQ495, and SuperK lasers were
¹³ used in this study. Results from the PQ446 laser are not shown, as many extinction

| Date | Detector Phase | Runs used |
|--------------|------------------------------------|---------------------------------------|
| June 2018 | Water Phase | 114,018 |
| May 2021 | Scintillator Phase, 0.6 g/L PPO | 270,856, 270,857, 270,858, 270,862 |
| October 2021 | Scintillator Phase, 1.1 g/L PPO | 275,676; 275,680 |
| May 2022 | Scintillator Phase, 2.2 g/L PPO | 300,708; 300,712; 300,715; 300,748 |
| July 2022 | Scintillator Phase, 2.2 g/L PPO | 302,630; 302,634; |
| June 2023 | Scintillator Phase, 2.2 g/L PPO | 310,294; 310,298; 310,303 |

Table 5.1: Datasets used in the SMELLIE extinction length analysis.

length values produced were unphysical, likely due to the very substantial intensity instabilities seen in much of their water and scintillator phase subruns. The PQ375 laser was also not used, for reasons discussed shortly. Fibres FS193 and FS293 were not used as they failed to ever allow a substantial amount of light through them; FS207 was also not used as there was no beam profile distribution made for that fibre. Every scintillator phase subrun being used was matched to an equivalent water phase subrun.

The sensitivity of the extinction length measurement is strongly dependent on the ratio of that extinction length to the length scale of the AV. Very long extinction lengths are difficult to measure because only a small amount of light is expected to be lost due to scattering or absorption. In contrast, at short extinction lengths only a very small amount of light will reach the other side without being extinguished; the dominant source of hits will come from scattered or re-emitted light.

As an example, Fig. 5.6 shows the expected optical component breakdown for hits from far PMTs from fibre FS007 due to laser PQ375, using the current RAT model of the 2.2 g/L LABPPO scintillator phase detector. Because the short extinction length at this wavelength relative to the diameter of the AV,

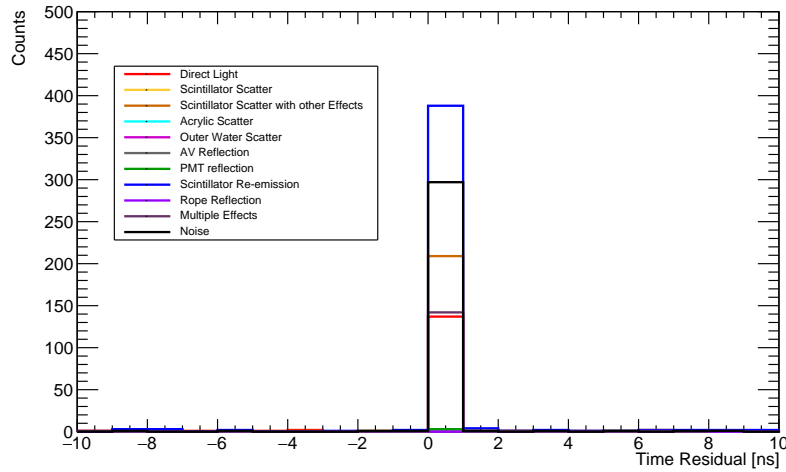


Fig. 5.6: Unstacked time residual distribution of a simulation of light from the PQ375 laser firing through fibre FS007, split by optical components. The direct light is clearly subdominant to light that has been absorbed and re-emitted by the scintillator. The spike at 0 ns arises from only one hit being observed in the beamspot for that event.

1 typically there would rarely be more than one hit in the beamspot region per
 2 event. This meant that t_{med} would correspond to that hit's time, and because
 3 there is an overlap between the beamspot and far PMTs for this fibre, a large
 4 spike at $t_{\text{res}} = 0$ can be observed. Importantly, the amount of direct light seen in
 5 the far PMTs in this simulation is entirely sub-dominant to the re-emitted light.
 6 Without accounting for this re-emitted light, this analysis would over-estimate the
 7 extinction length substantially. In contrast, it has already been shown in Fig. 5.4a
 8 that the contribution of re-emitted light to the PQ407 laser is expected to be
 9 negligible.

10 Although re-emitted light is sub-dominant in the far region, scattered light
 11 remains an important background. This becomes most relevant for the 10° and 20°
 12 fibres, as the direction of the far PMTs are somewhat distant from the beamspot,
 13 so the intensity of direct light is substantially less than that of the 0° fibres. A
 14 simulation of this is shown in Fig. 5.7 for fibre FS107 in the 2.2 g/L scintillator
 15 phase. The proportion of direct light signal to background components in the

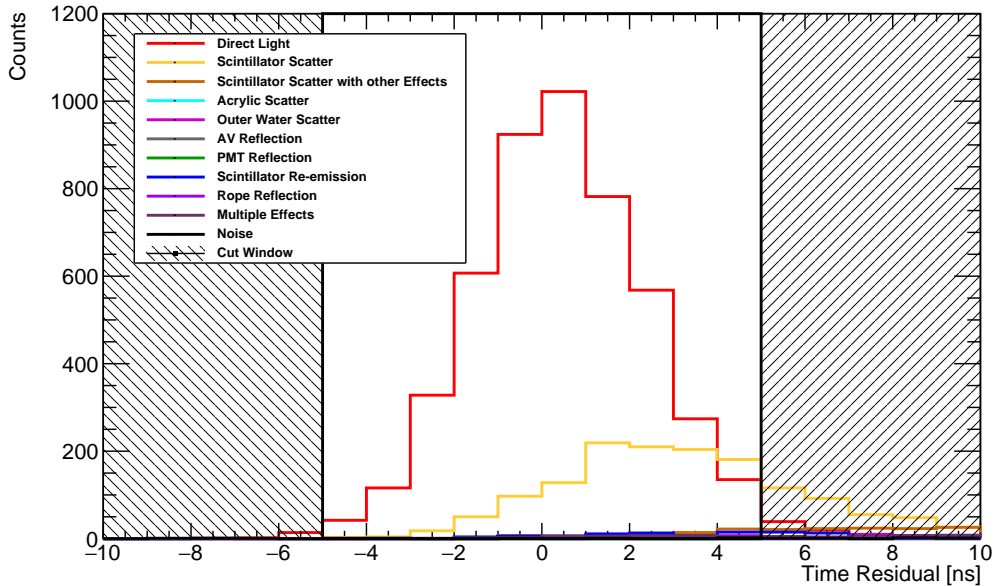


Fig. 5.7: Far PMT time window selection applied to a simulation of the PQ407 laser fired through laser FS107. The substantial background contribution from scattered light can be seen.

[-5, +5] ns window is substantial. As a result, any measurement of R_s would be systematically off.

With similar simulations for all other fibres, it was found that all 0° fibres apart from FS093 achieved a signal-to-background ratio of over 95%. No other fibres were able to achieve a signal purity close to this value. Because of this, only these ‘pure’ fibres were used for actual extinction length calculations in this analysis. Data from the other fibres was still processed, but only used for comparison, as will be seen in the next section. Unlike all other fibres, FS093 was found to have a strong contribution to the far PMT hits from light reflected off of ropes. Although this rope reflection contribution should not be impacted by changes to the inner detector medium, it was decided to leave this fibre out of the extinction length calculations.

¹ Results

² The analysis results from the PQ407 laser are shown in Fig. 5.8. These have been
³ split into a different plot for each time period. Each fibre is represented by an
⁴ individual colour and marker shape pairing associated with the fibre's pointing
⁵ angle and node, respectively. Because 0° fibres had the far PMT region nearest
⁶ the beamspot, they observed the largest values of R_w and R_s compared to the 10°
⁷ and 20° fibres. This necessitated the use of log-log plots to effectively show the
⁸ data. Lines of constant gradient, associated with scintillator extinction lengths
⁹ in the range 5–120 m in 5 m steps, are shown as dashed grey lines. These lines
¹⁰ increase in extinction length from the top left down to the bottom right, and in
¹¹ so doing show that longer extinction lengths are much harder to measure with
¹² the same precision as shorter extinction lengths.

¹³ As explained in the previous section, each plot had a straight line of the form
¹⁴ $R_w = mR_s$ fit to the 0° data points, excluding fibre FS093. Because there were
¹⁵ comparable uncertainties in both axes, this fit was performed by minimising the
¹⁶ χ^2 term:

$$\chi^2(m) = \sum_j \frac{(R_{j,w} - mR_{j,s})^2}{\sigma_{R_{j,w}}^2 + m^2\sigma_{R_{j,s}}^2}. \quad (5.5)$$

¹⁸ An uncertainty on the gradient of the fit was found by determining the change in
¹⁹ m required to increase the value of $\chi^2(m)$ by 1. Re-arranging Eq. 5.4, one can
²⁰ derive the formula:

$$l_{\text{scint}} = \frac{L_s}{\ln m + \ln \left(\frac{T_s}{T_w} \right) + \frac{L_w}{l_w}}, \quad (5.6)$$

²² from which the extinction length in scintillator at a given wavelength at a given
²³ time period with propagated uncertainties was found.

²⁴ As the concentration of PPO is increased in the detector, the extinction length
²⁵ at 407 nm appears to decrease in tandem. Then, the first two datasets taken in
²⁶ the 2.2 g/L scintillator phase appear consistent with one another. This is not true

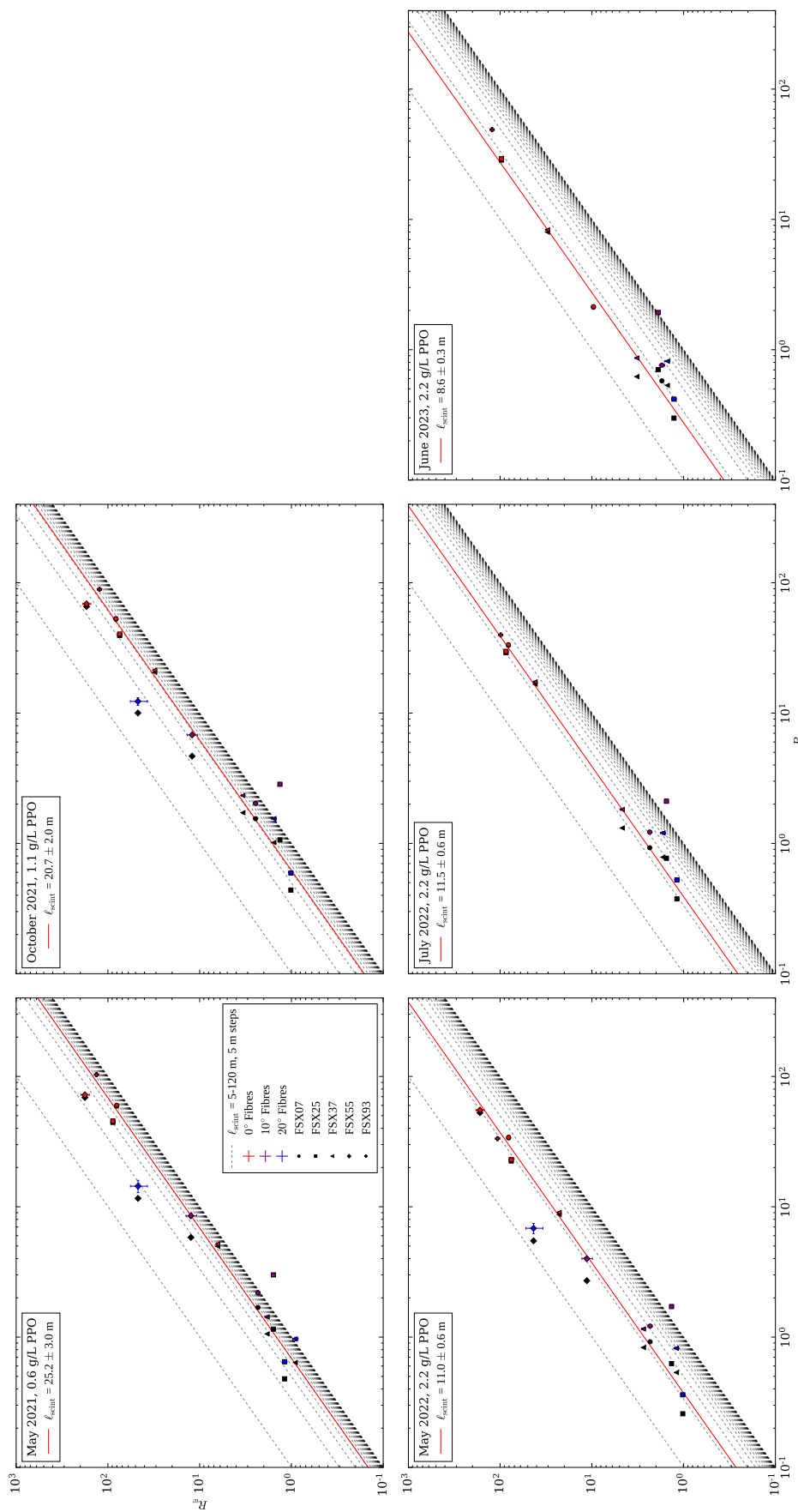


Fig. 5.8: Results of the extinction length analysis using the PQ407 laser.

1 of the final dataset taken at the end of the scintillator phase, which measured a
2 shorter extinction length again. The origin of this change is unknown.

3 Also shown in the plot are the results of fibres not included in the fit. As
4 an example, fibre FS125 (shown as the purple square) is found to be generally
5 in the non-physical region corresponding to negative extinction lengths, in the
6 bottom-right half of the plots. This can be explained by the substantial scattering
7 background expected in the far PMTs of this fibre. Assuming the simulation
8 discussed in the previous section for this fibre in the 2.2 g/L scintillator phase, as
9 well as matching simulations for the other PPO concentrations, this systematic
10 effect in R_s was corrected for and shown with a black square. This was also shown
11 for all other fibres. As can be seen, by using the nominal correction from the
12 existing scintillator optics models, the FS125 measurements are pushed into the
13 physical regime, quite close to the line of best-fit.

14 Fig. 5.9 shows the data from the SuperK laser in the 400–410 nm range, for
15 the May 2021, May 2022, and June 2023 datasets in which SuperK data was
16 taken. Once again, there appears to be a substantial shortening of the scintillator’s
17 extinction length as PPO was added. These values differ from the PQ407 result,
18 but this is not too surprising as what is measured with the SuperK laser is the
19 extinction length averaged over a whole 10 nm range, weighted by the intensity
20 spectrum of the laser. The third measurement result increases compared to the
21 second here, another contrast to the PQ407 laser.

22 Fits to the SuperK data at wavelengths between 400–500 nm during May 2021,
23 May 2022, and June 2023 were performed in the same manner as described above.
24 The combined results for all of these measurements, as well as the PQ407 laser, are
25 shown in Fig. 5.10. All three SuperK datasets show an increase in the extinction
26 length with wavelength, as expected. There is also a substantial shortening in
27 the extinction length going from the 0.6 g/L dataset to the 2.2 g/L dataset. This

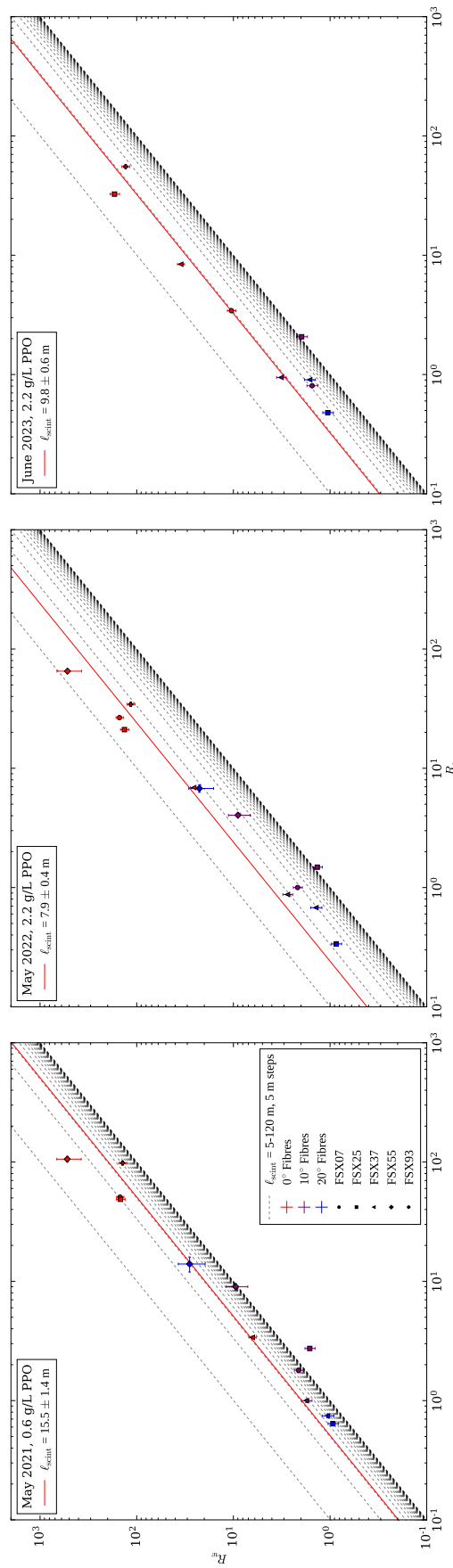


Fig. 5.9: Results of the extinction length analysis using the SuperK laser in the 400–410 nm range.

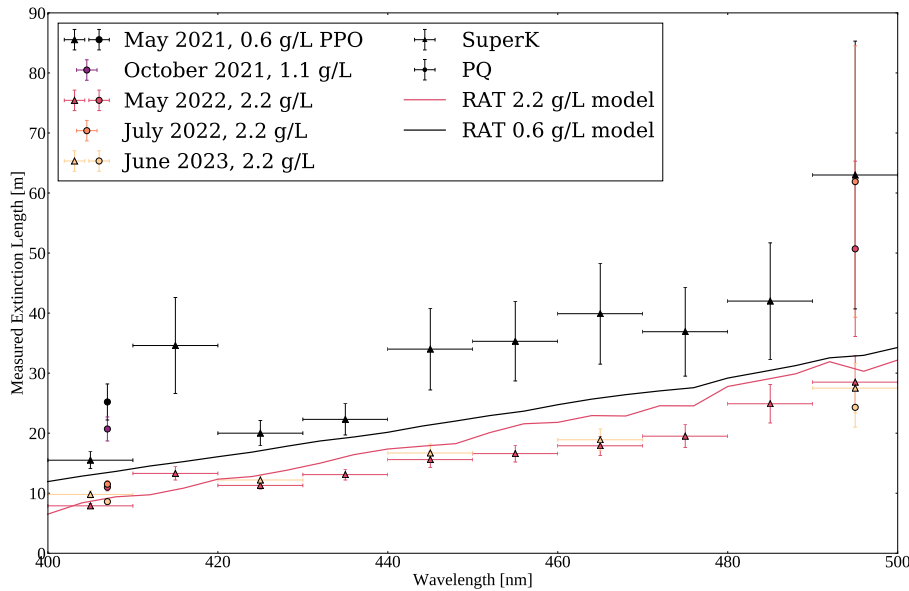


Fig. 5.10: Summary of scintillator extinction length measurements made by SMELLIE, with a comparison to the current 2.2 g/L optics model used in RAT.

- ¹ is matched qualitatively with the PQ data. Generally, data from May 2022 and
- ² June 2023 appear to be consistent with one another.

³ Comparisons with other Measurements

- ⁴ It is important to compare the measurements of the scintillator extinction lengths
- ⁵ using SMELLIE to other methods used by the Collaboration. The optical model
- ⁶ used in RAT for the 0.6 g/L scintillator was built from bench-top measurements
- ⁷ prior to scintillator phase [95, 116]. The extinction length associated with this
- ⁸ model is shown as a black line in Fig. 5.10. The results from my analysis with
- ⁹ SMELLIE data give longer extinction lengths than the existing model, for both
- ¹⁰ the PQ and SuperK laser over all wavelengths in the 400–500 nm region.

¹¹ For the 2.2 g/L scintillator, more techniques were used for measurement of the
¹² extinction length. One approach by Ben Tam was to use ‘UV-vis’ spectroscopy
¹³ on samples of the scintillator extracted from the detector [147]. Another method,

used by Serena Riccetto, was to look at the `nhits` distribution of the radioactive background ^{210}Po within the detector: a discussion of this and other backgrounds in the detector can be found in Section 6.1.2. The peak `nhit` value associated with this background varies with the position of the event, because of the changing lengths of scintillator the event’s scintillation light must travel through. Different optical models could then be tested by comparing the peak `nhits` of the ^{210}Po in simulation to data [148].

The current model of the 2.2 g/L scintillator absorption and scattering used in `RAT` was developed by combining the measurements of B. Tam and S. Riccetto with older bench-top measurements made before the scintillator phase: details about this model-building can be found in [96, 101]. The extinction lengths obtained from this model are shown as a red line in Fig. 5.10. There appears to be good agreement between these model values and the results from the analysis with `SMELLIE` data taken in May 2022 for wavelengths in the ranges 400–430 nm and 490–500 nm. At medium wavelengths, `SMELLIE` appears to measure extinction lengths somewhat shorter than the existing `RAT` model. These results appear consistent between the May 2022 and June 2023 datasets.

5.2 Scattering Analysis

5.2.1 Historical Approaches and the Problem of Systematics

A method for measuring scattering lengths in the detector using `SMELLIE` was first developed by K. Majumdar [137]. This method was used by E. Turner to measure the scattering length of the UPW in the water phase [114]. A similar approach was built by S. Langrock, and tested on fake water phase data [139]. The general analysis technique was as follows:

1 1. Using simulations under nominal conditions, a region of PMTs and associated
2 time windows was selected that optimised the sensitivity to hits from photons
3 that were scattered inside the AV. This signal region was defined by a
4 geometric region of the 2D (t_{res}, α) parameter space.

5 2. Data was taken using the SMELLIE system.

6 3. A calibration curve of the fraction of hits in the scattered signal region to
7 that of the whole detector as a function of the scattering length for a given
8 fibre and wavelength, was built using simulations.

9 4. The fraction of hits in the signal region was determined for each subrun of
10 SMELLIE data, and then the calibration curve was used to derive values of
11 the scattering length at that wavelength.

12 The challenge with this analysis approach is that it relies on the use of
13 SMELLIE simulations to derive results. There are substantial systematic un-
14 certainties in the modelling of the SMELLIE beam profiles, which can readily
15 propagate into the uncertainty of the scattering length measurement. Both S.
16 Langrock and E. Turner found this in their analyses [114, 139]. Furthermore,
17 the signal regions chosen historically had a substantial background contribution,
18 which often appeared to not be modelled with sufficient accuracy.

19 As a demonstration of these problems, consider a comparison between PQ495
20 laser data taken in July 2022, through fibre FS055, to a simulation of the same
21 setup. This is shown in Figs. 5.11a & 5.12. Also shown in these plots is the
22 scattering signal region as determined by K. Majumdar and E. Turner’s method.

23 One can observe qualitatively features that differ between the data and MC:
24 there are differences in the distribution along the line $t_{res} = 0$ due to beam
25 profile systematics, as well as differences in the features at large angles and
26 times. Although the signal region was chosen to try and optimise the statistical

significance, it failed to account for the systematic uncertainties present in the SMELLIE model. To further emphasise this, Fig. 5.11b shows the impact of using a modified beam profile in the simulation. Instead of using the beam profile developed for that fibre in Section 4.2.1, one was used that had data from only one water phase subrun, as shown in Section 4.1.2. The fraction of hits in the signal region changes from 31.2% to 27.7%.

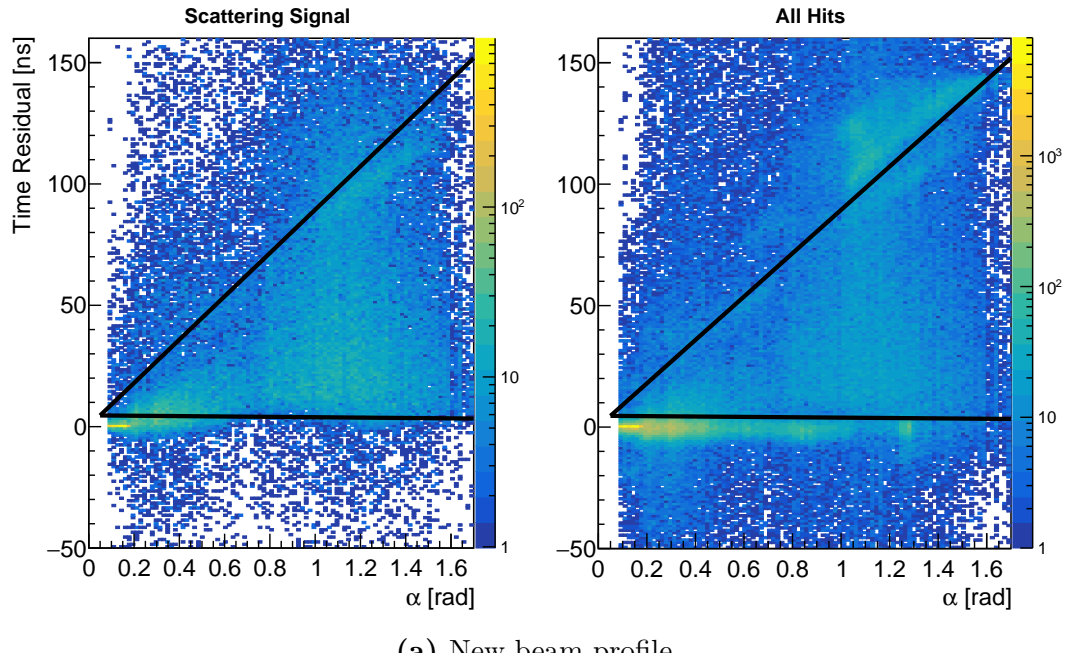
There are two major approaches to handling the problems described above. One approach is to build an optical model of the detector and SMELLIE that has negligible systematic uncertainties, so that the existing analysis approach can be used with minimal problems. An alternative approach, and the one used in this thesis, is to build a new analysis that is more robust to the existing systematic uncertainties in both the SMELLIE beam profile and detector optics.

5.2.2 New Methodology

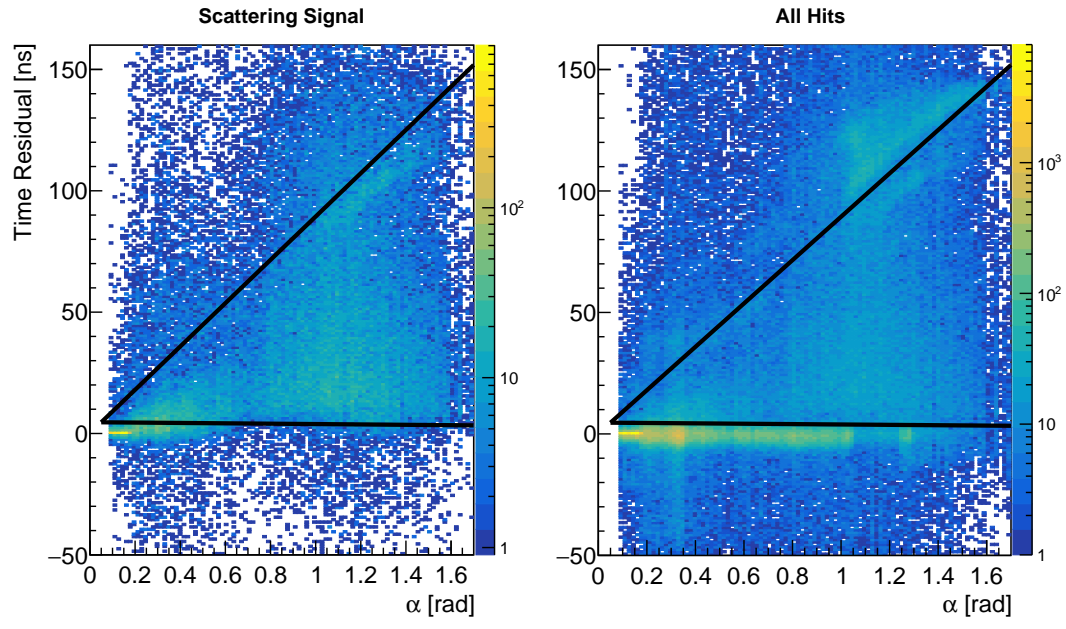
Signal Region Selection

A new PMT and time region was found that had substantially higher scattered signal purity than previous selections, whilst maintaining large signal statistics. Fig. 5.13 shows a simple 2D model of the geometric optics of SMELLIE in the scintillator phase. As can be seen, refraction due to the larger refractive index of LAB and acrylic compared to UPW causes a substantial region of the PSUP to be unreachable by direct light-paths. In the full three dimensions of the detector, this region corresponds to a broad ring of PMTs.

For this analysis, this new scattering signal region will be known as the “bad light-path” region, because no direct light-paths can be found. By consequence, it is impossible to calculate a time residual for hits in this region, as no direct light-path time-of-flight calculation is possible. Instead, times are calculated



(a) New beam profile



(b) Old beam profile

Fig. 5.11: Comparison of the signal and total hit distribution in the (t_{res}, α) -space using new and old beam profiles for laser PQ495 through fibre FS055. The triangular scattering signal region of K. Majumdar's analysis are shown, optimised for the new beam profile simulation. The fraction of all hits in this signal is 31.2% for the new beam profile simulation, and 27.7% for the old beam profile.

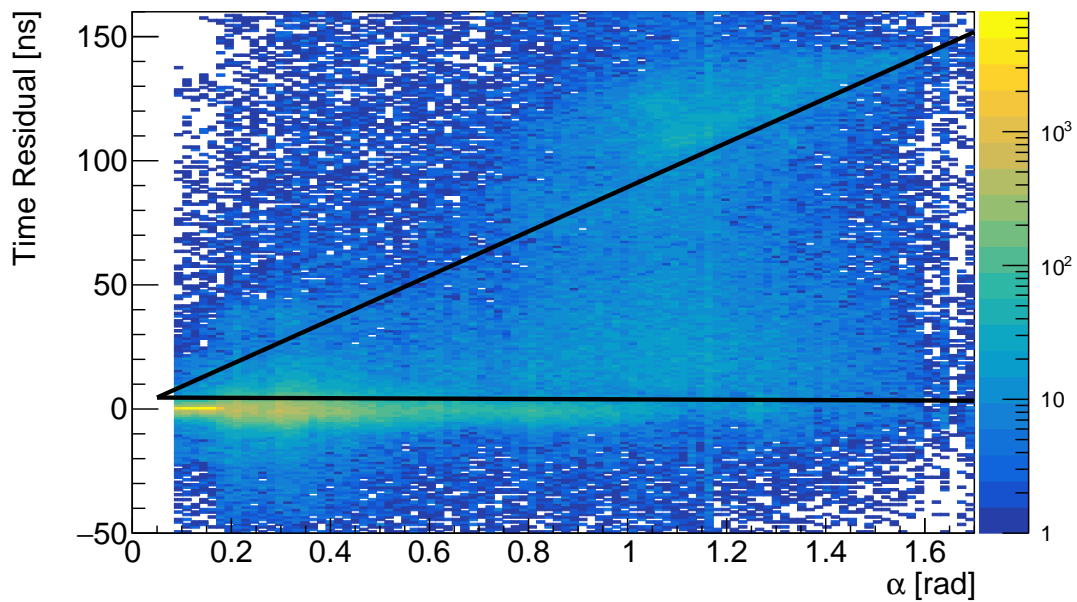


Fig. 5.12: Hit distribution of data taken in run 302,634, with laser PQ495 through fibre FS055, as a function of both t_{res} and α . The triangular scattering signal region optimised from Fig. 5.11a.

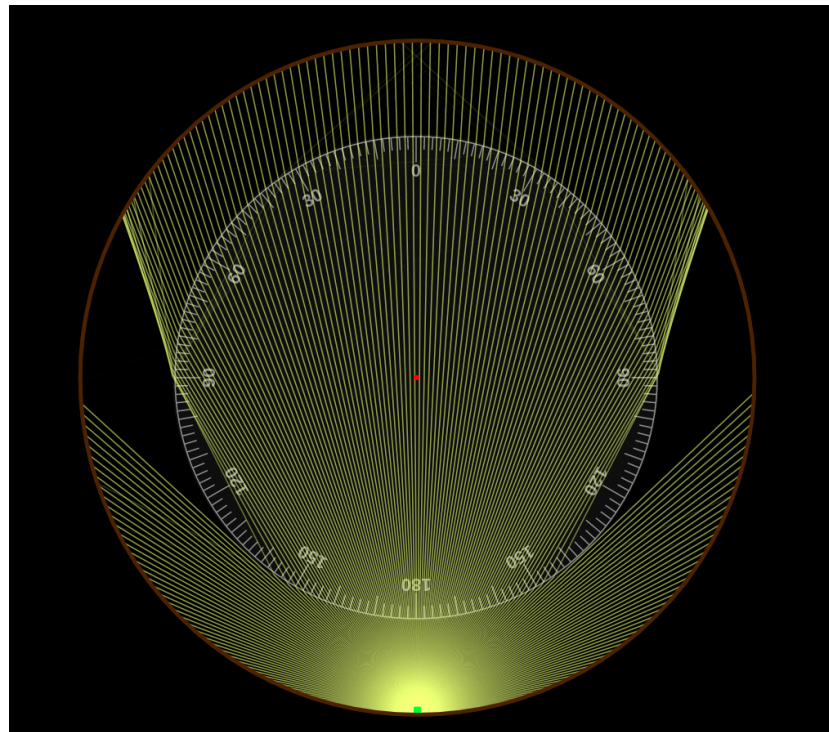


Fig. 5.13: Model of light rays propagating in the SNO+ detector during scintillator phase, emanating from an external source such as SMELLIE. Because of refraction, a large ringed region is formed where no direct light can reach the region from the source. This forms the basis of the new scattering signal region.

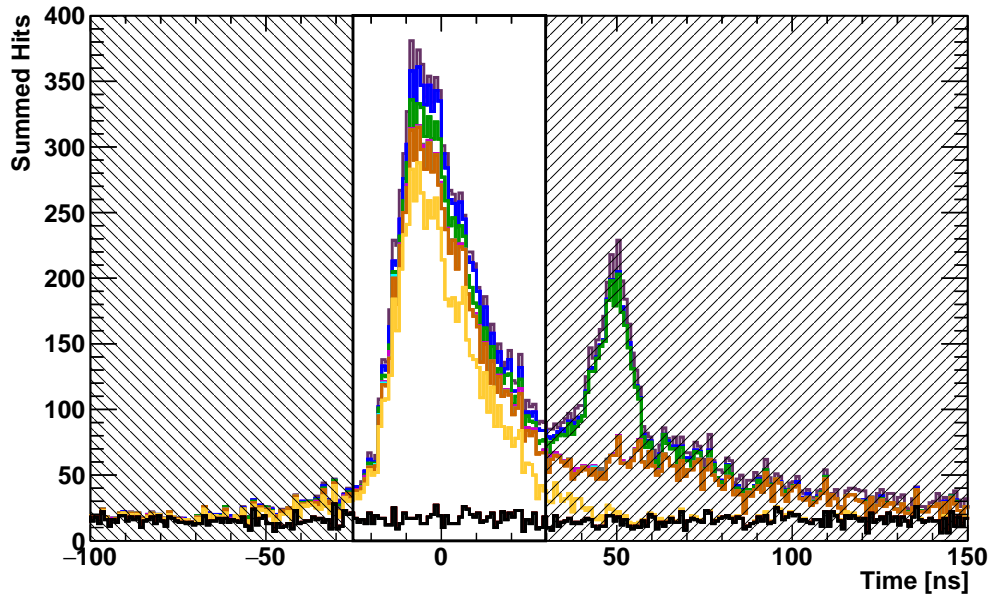


Fig. 5.14: Timing distribution of a simulation of the observed hits in the bad light-path PMT selection through fibre FS055, using the PQ495 laser. The distribution is split into the different optical components.

¹ simply by $t = t_{\text{hit}} - t_{\text{emm}}$, where the usual t_{med} method is used for calculating the
² emission time.

³ In order to try and ensure that the bad light-path region really contained no
⁴ contribution from direct light, SMELLIE simulations were performed for each
⁵ fibre, and only PMTs in the forward hemisphere relative to the fibre that also
⁶ observed no hits from direct light were chosen.

⁷ Fig. 5.14 shows the time distribution of hits in the scattering signal region,
⁸ split by the different components of a simulation, using the PQ495 through fibre
⁹ FS055. As can be seen, in the $[-25, +30]$ ns time window there is a large peak
¹⁰ that is dominated by light scattered by the scintillator. It is this time window
¹¹ that is used in this analysis to isolate the scattered signal for all fibres.

¹² In addition to having a high signal purity, this new scattered signal region
¹³ has the benefit of being robust to beam profile uncertainties. Although beam
¹⁴ profile systematics impact the intensity distribution of the direct light, no such

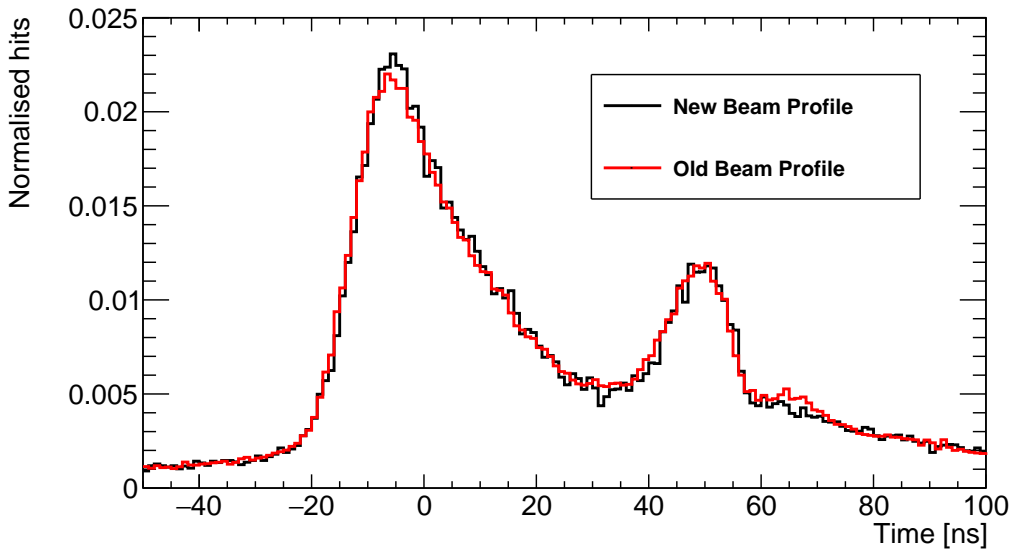


Fig. 5.15: Comparison of timing distributions in the bad light-path PMT region for simulations of laser PQ495 through fibre FS055, comparing the old and new beam profile. Both distributions have been normalised by the number of non-skipped events. The fractional difference in the number of hits in the signal time window is 1.0%.

light is seen in the signal region. Moreover, because scattered light must have a large scattering angle to reach the signal region, the beam profile shape is ‘washed out’ by the scattering. As a demonstration of this effect, Fig. 5.15 compares the observed time distribution in the bad light-path region for the new and old beam profiles of FS055, still using the PQ495 laser. One can see that there is little difference between the distributions a change of 1.0% in the signal time window, compared to the more substantial differences seen in Fig. 5.11.

In the new signal region, some backgrounds to scattering are still present. These can come from PMT noise, scintillator re-emission, reflections off of PMTs and their concentrators, and combinations of multiple optical effects. A substantial fraction of the paths which undergo multiple processes scatter in the scintillator, and so are treated as signal for the purposes of this analysis. The contribution due to noise hits can be readily determined through the use of PULSEGT triggers, through the same approach used in Section 5.1.2. In the example shown in

¹ Fig. 5.14, 82% of non-noise hits in the signal region were from photons which
² underwent scattering in the scintillator.

³ Another thing to check was whether natural changes in the relative position
⁴ of the AV centre with respect to the PSUP over time could leak direct light
⁵ into the signal region. This offset is determined through a calibration system
⁶ stationed at the top of the neck of the detector, known as the Neck Sense Ropes,
⁷ whose measurements have been validated during the partial fill phase with a laser
⁸ survey [149, 150]. These AV offset measurements are saved in the RATDB, and used
⁹ within any simulation of a given data run in RAT. Of the five SMELLIE scintillator
¹⁰ datasets mentioned in Table 5.1, the largest recorded change in AV offset was
¹¹ between May and July 2022, in which the AV moved vertically by 39.5 mm. The
¹² bad light-path PMT region used simulations with run conditions from July 2022
¹³ data; for comparison, a simulation equivalent to the that of Fig. 5.15 was made
¹⁴ using the run conditions of the May 2022 dataset. Only a negligible amount of
¹⁵ hits from direct light leaked into the signal region in this alternative simulation.

¹⁶ **Observing Changes in Scattering**

¹⁷ If the absolute shot-to-shot intensity of a SMELLIE subrun is known, and the
¹⁸ models of the scintillator re-emission and PMT reflections are well-enough known
¹⁹ for the wavelengths of interest, then the scattering length of the scintillator can
²⁰ be determined by comparing data in the signal region to matching simulations of
²¹ varying scattering length. Sadly, at the time of writing, no method for determining
²² the absolute intensity which is sufficiently robust to systematic uncertainties in
²³ the modelling of MC is known. Instead, it was decided for this analysis to use
²⁴ the back-scattered light region described in Section 5.1.2 as a measure of relative
²⁵ intensity.

²⁶ Without knowledge of the absolute intensity, absolute scattering lengths cannot
²⁷ be measured. However, by calculating the ratio of npe in the signal region to

that of the back-scatter region for two equivalent scintillator subruns, denoted R_1 and R_2 , any substantial change in the scattering length between datasets can be observed. Another restriction that this analysis has is that changes in the scattering length cannot be distinguished from changes in the background processes, in particular PMT reflections and scintillator re-emission. The reflectivity of the PMT concentrators is known to be changing slowly with time as the reflective petals of the concentrators degrade in the outer water [85]. A. S. Inácio determined from comparing Laserball data taken in SNO and SNO+ that the PMT angular response had worsened over a period of 12 years by up to 8% in the incident angle range up to 42° [79]. Therefore, an upper estimate of the fractional change in the PMT bucket reflectivity over the course of the two-year period in which SMELLIE scintillator phase data was taken is 1.4%, assuming the same trend. Using the example shown in Fig. 5.14, 6.5% of non-noise hits in the signal region came from PMT reflections, meaning that the overall systematic effect of concentrator degradation is expected to be merely 0.09%.

The other dominant source of background is scintillator re-emission. This is expected to change as a function of PPO concentration. However, because the absorption length of the scintillator at 2.2 g/L is substantially longer than the scattering length in the 400–500 nm range according to the current RAT model, the proportion of this background component is expected to be small: see Figs. 2.2 & 2.4. According to the simulation shown in Fig 5.14, 7% of non-noise hits in the signal region come from scintillator re-emission. According to simulations which use the current RAT model, this fraction of re-emitted light stays roughly constant over the 400–500 nm range.

1
2
3
4
5
6
7
8
9
10
11
12
13
14
15

16
17
18
19
20
21
22
23
24

¹ **5.2.3 Results in Data**

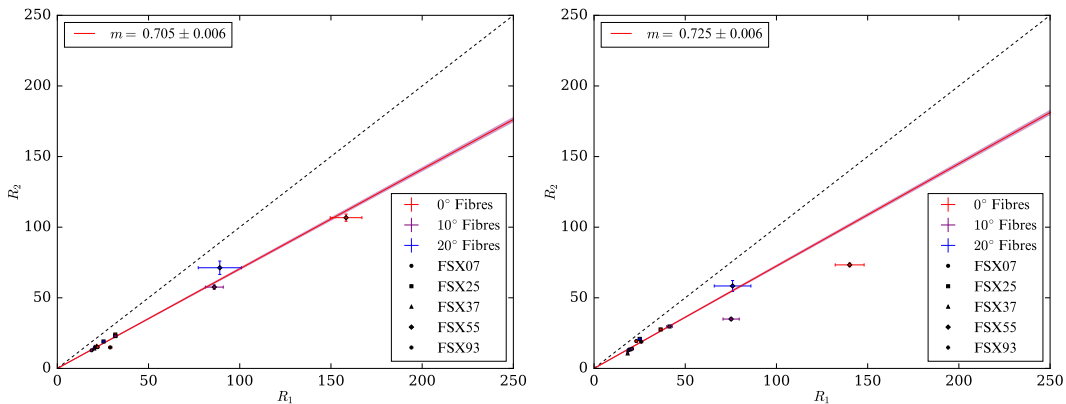
² The datasets used in this scattering analysis are the subset of those described in
³ Table 5.1 which were taken in the scintillator phase by the SuperK laser between
⁴ 400 nm and 500 nm. Only three scintillator datasets had SuperK data taken: May
⁵ 2021, May 2022, and June 2023. The npe ratio for the first dataset is denoted by
⁶ R_1 , and used as the baseline to compare to the later two datasets, denoted R_2 .

⁷ Results from the same wavelength for the same dataset pair were combined
⁸ onto a plot, as shown in Fig. 5.16. Because far more hits are observed in the signal
⁹ region compared to the backscatter light region for all subruns, the dominant
¹⁰ source of statistical uncertainty in R comes from the latter region. As a result,
¹¹ data points with large R values had much larger uncertainties, because these
¹² corresponded to subruns with lower statistics in the backscatter light region.
¹³ In order to account for the non-negligible uncertainties along both axes, the
¹⁴ same fitting procedure from Section 5.1.3 was used. This found the best-fit line
¹⁵ $R_2 = m \cdot R_1$ for each plot with an associated uncertainty.

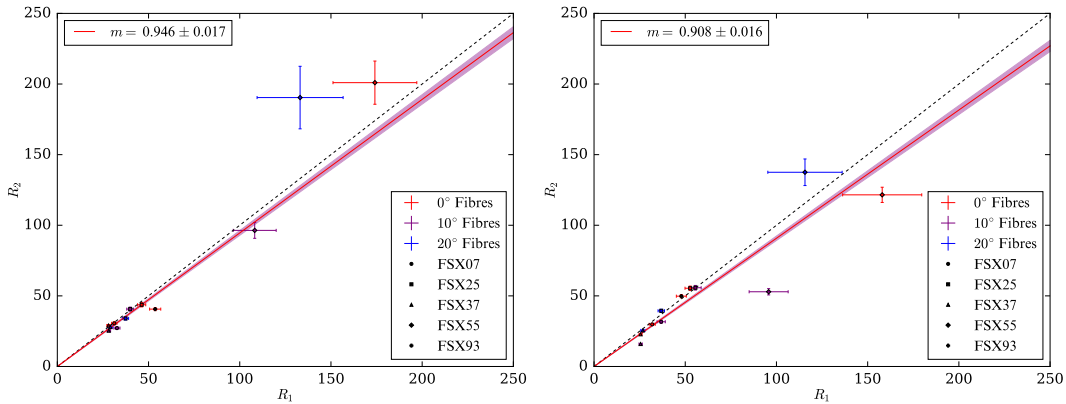
¹⁶ The results for the gradient of all the data considered in this analysis are
¹⁷ shown in Fig. 5.17. All values for the ratio R_2/R_1 are found to be less than
¹⁸ 1. This implies that, at all wavelengths in the range 400–500 nm, less light was
¹⁹ observed in the scatter signal region of the 2.2 g/L scintillator than the 0.6 g/L
²⁰ scintillator. Furthermore, there is a strong wavelength-dependence to this effect,
²¹ such that shorter wavelengths observe a substantially lower fraction than at longer
²² wavelengths. These results appear consistent to within statistical uncertainties
²³ for both 2.2 g/L scintillator datasets considered.

²⁴ **5.2.4 Interpretation**

²⁵ A naïve reading of the above results would say that the scattering length has
²⁶ increased substantially between May 2021 and May 2022. However, that would



(a) May 2021 versus May 2022, 400–410 nm. (b) May 2021 versus June 2023, 400–410 nm.



(c) May 2021 versus May 2022, 490–500 nm. (d) May 2021 versus June 2023, 490–500 nm.

Fig. 5.16: Plots of R_1 against R_2 for four pairs of scintillator phase datasets, using the SuperK laser.

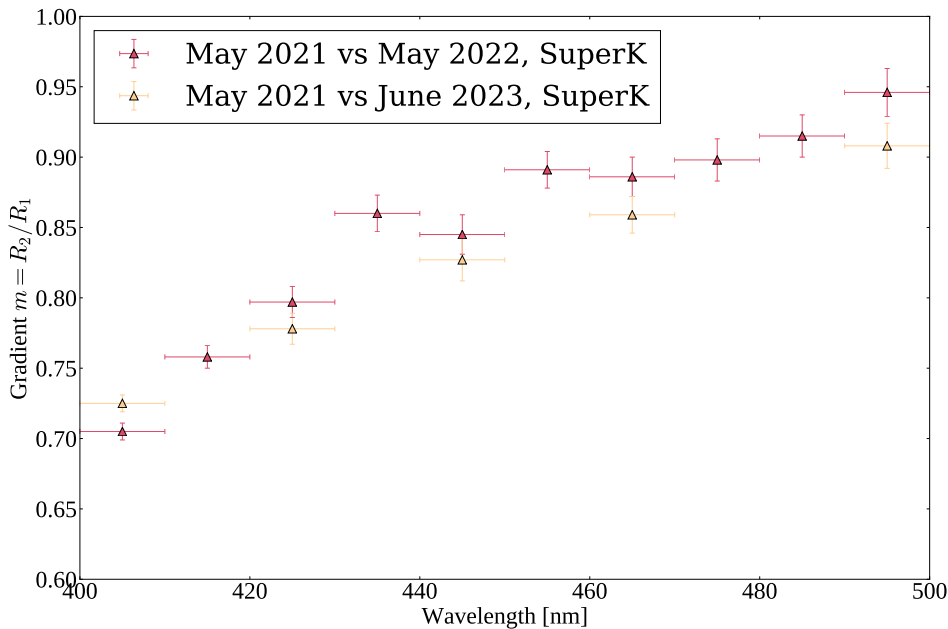


Fig. 5.17: Summary of results from the scattering analysis, shown as a function of wavelength.

1 be in strong tension with the results of the analysis of the previous section, which
 2 clearly shows a significant decrease in the observed extinction length over the
 3 same time period. It is also very difficult to explain from a theoretical perspective
 4 how the addition of PPO to the scintillator cocktail could decrease the amount of
 5 Rayleigh scattering.

6 There is an alternative interpretation which fits the observations of both
 7 analyses. Suppose that the scattering length did not change with time, but
 8 there was an additional non-re-emitting component of the scintillator added
 9 during the PPO loading. Then, this new component of the scintillator would be
 10 capable of absorbing light, shortening the observed extinction length, but the
 11 amount of re-emitted light could be much less than expectation in the wavelength
 12 range considered in this work. This would lead to a decrease in the amount of
 13 light observed in the scattered signal region, as the background re-emitted light
 14 substantially decreased in quantity. The expected fraction of light arriving in this

region due to scintillator re-emission is, as seen in Section 5.2.2, of the correct magnitude to explain the change in the scattering signal region.

In the process of building the current 2.2 g/L scintillator absorption and scattering model, S. Riccetto and B. Tam found that adding a non-re-emitting absorption component was necessary to fit their calibration data simultaneously [96]. The origin of this new component was investigated by B. Tam, who concluded that near the end of the PPO top-up campaign some contaminants were likely added from the accidental overheating of the LABPPO during one of the distillation processes [151]. There is a slight difference between their results and the implication from work in this thesis. S. Riccetto and B. Tam sought little evidence of this new component impacting longer wavelengths, and instead preferred causing a significant impact at short wavelengths $\lambda \lesssim 400$ nm.

5.3 Summary and Suggestions for Future Work

In this chapter, two analyses were developed and performed on data taken with the SMELLIE calibration system, to understand the optical properties of the scintillator within SNO+. The first analysis measured the extinction length of the scintillator as a function both of time and wavelength, through comparison to the already-calibrated water phase data. The extinction lengths found had some differences with existing models, although both see an increase the extinction length seen as a function of wavelength. A substantial decrease in the extinction lengths were observed between the May 2021 and May 2022, when the PPO concentration of the scintillator increased from 0.6 g/L to 2.2 g/L. However, the change in extinction length was far greater than the expected change to the absorption length of PPO. Data taken one year later, in June 2023, shows no indication of any further change to the scintillator’s extinction length distribution.

1 In the second half of this chapter, another analysis was built, designed to be
2 sensitive to changes in Rayleigh scattering. Simulations indicated that this new
3 analysis was also sensitive to changes in the scintillator's re-emission properties
4 or changes in the PMT bucket reflectivity. By performing relative measurements
5 between scintillator datasets, it was found that the amount of light seen in signal
6 region decreased between May 2021 and May 2022, with similar results being
7 seen when comparing May 2021 to June 2023 data. This could only be explained
8 by a decrease in the quantity of scattered light, scintillator re-emission, or PMT
9 reflections in the 400–500 nm range. A significant wavelength-dependence was
10 also seen in these results, with shorter wavelengths observing greater decreases in
11 the amount of light seen.

12 The best physical explanation that combines these results is the existence of
13 a new component of the scintillator cocktail that absorbs, but does not scatter
14 or re-emit light substantially in the 400–500 nm range. This would generate a
15 significant shortening of the extinction lengths over these wavelengths, but decrease
16 the amount of light seen in the signal region of the scattering analysis. This theory
17 has similarities to the observations seen by B. Tam in ex-situ measurements, as
18 well as the fits to the spectra of in-situ backgrounds performed by S. Riccetto.
19 However, there remain some notable differences between my measurements and
20 these others, in particular that there appears to be a non-negligible effect above
21 400 nm.

22 The key insight that enabled both of the analyses in this chapter is the building
23 of analysis methods that were robust to the major systematics present in SMELLIE.
24 By not comparing SMELLIE data to simulation, the discrepancies between the
25 RAT model of SMELLIE and reality, described in Section 4.3, could be avoided.
26 However, not using simulations in these analyses does come at a price. Firstly, the
27 extinction length analysis becomes fundamentally dependent on the water phase
28 data taken by both the Laserball and SMELLIE. The former had large systematic

uncertainties in their UPW attenuation measurements that puts a firm limit on
1
the precision that any extinction length measurement can make.
2

As an example, consider a measurement of the scintillator’s extinction length
3
at 446 nm, with a ‘true’ value of the extinction length of 12 m. If the uncertainties
4
from all other factors could be made negligible, because the derived attenuation
5
length from the water Laserball data is (108 ± 49) m, this propagates to an
6
uncertainty on the extinction length of the scintillator of 5%. This effect becomes
7
even larger as the extinction length increases.
8

This limitation is further compounded by the limited statistics taken in the
9
SMELLIE water phase subruns used in this analysis. The extinction length
10
analysis used ‘medium’ intensity subruns, with the rare UPW backscatter light
11
being used for intensity calibration, where for multiple PQ lasers there were very
12
large shot-to-shot intensity variations. In addition, by needing to determine the
13
emission time for each event independently, instead of being able to rely on the
14
EXTA trigger timing, a small fraction of events may have leaked into or out of
15
the time windows used in both analyses. This effect would be most predominant
16
in data with a low number of hits in the beamspot region.
17

The other major source of uncertainty in the results of both analyses comes
18
from the scatter between fibres around the line of best fit for a given plot. For
19
example, in Fig. 5.16d one of the points with the strongest pull on the fit value of
20
the gradient is the purple triangle associated with fibre FS037. The backscattered
21
light distributions that give rise to this data point are shown in Fig. 5.18. As can
22
be seen, there is a prominent change of shape of the peaks near $t_{res} = 0$ ns, which
23
appears to leak into the backscattered light time window. The origin of this shape
24
change is not yet known, but only appears to affect this fibre in the most recent
25
scintillator dataset. This problem could have minor impacts on the particular
26
fit values which use this data, but all the qualitative results of this chapter will
27
remain.
28

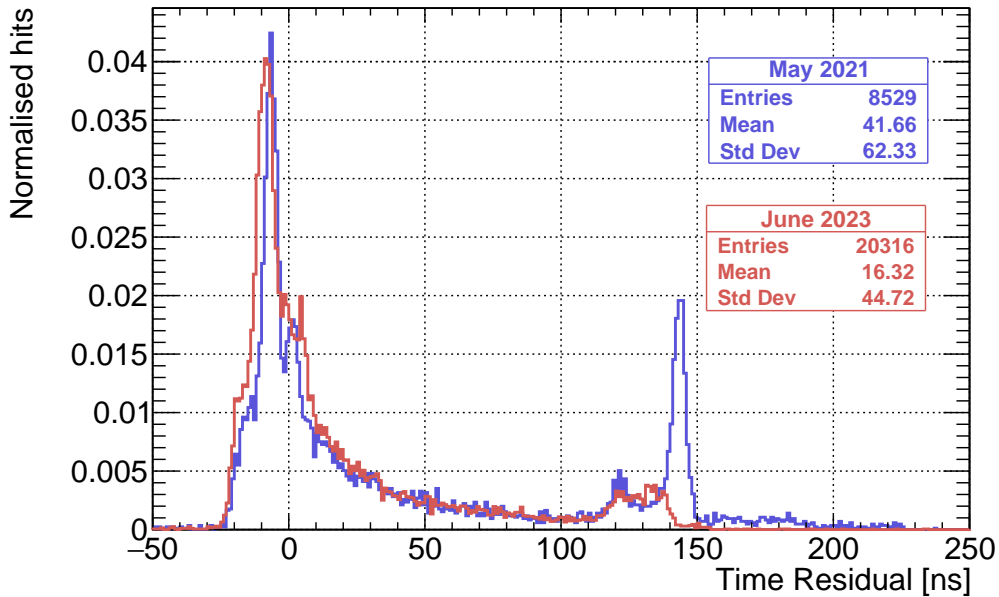


Fig. 5.18: Observed time residual distributions for the backscattered light region of PMTs, with the SuperK laser in the 490–500 nm range through fibre FS037. The distributions from both May 2021 and June 2023 are compared, with both of their distributions normalised to 1.

1 There are a series of improvements that can be made to these two SMELLIE
 2 analyses, based upon the comments above. Major progress could be achieved if a
 3 robust measure of a fibre's absolute emission intensity could be found. In so doing,
 4 measurements of the extinction lengths and scattering properties of the detector
 5 media could be made independent of Laserball data or having to make merely
 6 relative measurements. This could become even more powerful if the beam profiles
 7 of the fibres for different wavelengths could be known with sufficient precision.

8 Another important set of considerations that will need to be made in the future
 9 in order to make precision scattering length measurements is the calibration of the
 10 scintillator re-emission and PMT reflections. It is worth noting that the analysis
 11 of Section 5.2, despite being designed for measuring changes in scattering length
 12 in the scintillator, actually appears to have measured a change in the re-emission
 13 properties of the scintillator. The impact of PMT reflections over time can be
 14 constrained by isolating regions of PMTs and time for which there is high purity

of reflected light, such as the peak seen at 50 ns in Fig. 5.14. Alternatively, these could be calibrated through a deployment of the Laserball during the scintillator phase.

A possible approach to disambiguating between re-emission and scattering in scintillator is through their different scattering angle distributions. Whilst the former emits light isotropically, Rayleigh scattering has the angular form $(1 + \frac{1-\delta}{1+\delta} \cos^2 \theta)$, as discussed in Section 2.3.2. To do this, a secondary measurement of the scattered and re-emitted light could be made in the far PMT region. Because it is known that it is this light which are the dominant backgrounds to the direct light for the extinction length analysis, the amount of this background light which enabled the 10° and 20° fibres to best line up with the fit results of the 0° ones could be determined. Then, this amount could be compared to the amount seen in the bad light-path signal region. One expects a difference in the observed amounts of scattered and re-emitted light in these two regions, because of the anisotropy of the Rayleigh scattering. With the differing values of these two different datasets, one might be able to tease apart the individual contributions of scattering and re-emission, and hence measure both.

Chapter 6

1

Solar Oscillation Analysis

2

Driving out into the Sun

Let the ultraviolet cover me up

Looking for a Creation Myth

Ended up with a pair of black lips

3

This is the End

PHOEBE BRIDGERS

Measuring the “solar” neutrino oscillation parameters Δm_{21}^2 and θ_{12} is one of the principal aims of the SNO+ detector during the scintillator phase. There are, in fact, two complementary methods of measuring these parameters: the oscillations of anti-neutrinos from terrestrial nuclear reactors, and the oscillations of neutrinos from the Sun.

4

5

6

7

8

9

10

11

12

13

14

This chapter focuses on the latter approach, using ${}^8\text{B}$ neutrinos coming from the Sun to measure the solar oscillation parameters. An initial background-free study was performed by Javi Caravaca [152], which demonstrated that it was indeed possible to make such a measurement in the detector. The work in this chapter builds substantially from that analysis. This chapter also draws on the associated reactor anti-neutrino analysis built by Iwan Morton-Blake [90], and

¹ more broadly from the general techniques used in the $0\nu\beta\beta$ analysis of Tereza
² Kroupova [135] and Jack Dunger [153].

³ This chapter begins by explaining how it is possible to measure the solar
⁴ oscillation parameters via ^8B events. Then, the framework used to perform the
⁵ analysis is explained: that of a *Bayesian Analysis using Markov Chain Monte*
⁶ *Carlo techniques*. After the method has been described, the dataset upon which
⁷ the analysis is performed is then introduced. The results and associated validation
⁸ are then given. Given these results, a projection is then made for the expected
⁹ sensitivity to θ_{12} as a function of livetime.

¹⁰ 6.1 Analysis Methodology

¹¹ 6.1.1 Observational Principle

¹² How can we measure neutrino oscillation parameters via solar neutrinos in the
¹³ SNO+ detector? As discussed in Chapter 1, it is possible to detect all flavours
¹⁴ of neutrino through elastic scattering with electrons in the detector. If this
¹⁵ interaction was purely neutral-current, then there would be no way of telling
¹⁶ the flavour-state of an interacting neutrino. However, electron neutrinos are
¹⁷ able to interact through an additional charged-current mode. This modifies the
¹⁸ cross-section for electron neutrinos, and means that as the survival probability
¹⁹ for electron neutrinos generated from the Sun, P_{ee} , is modified, the interaction
²⁰ probability of neutrinos with the detector will also. The resulting differential
²¹ interaction rate R for solar neutrinos as a function of the neutrino’s energy, E_ν , is
²² given by:

$$\frac{dR}{dE_\nu} = \Phi_{^8\text{B}} S_\nu(E_\nu) n_e \left[P_{ee}(E_\nu) \sigma_{\nu_e}(E_\nu) + (1 - P_{ee})(E_\nu) \sigma_{\nu_{\mu,\tau}}(E_\nu) \right], \quad (6.1)$$

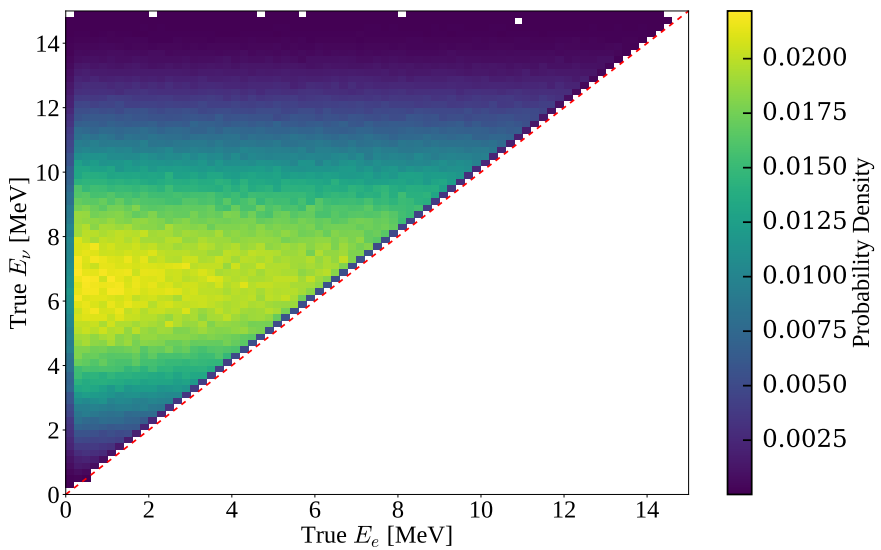


Fig. 6.1: 2D probability distribution comparing the true neutrino energy from a ${}^8\text{B}$ ν_e to the true energy of the scattered electron. Also shown in red is the line $E_\nu = E_e$.

where $\Phi_{{}^8\text{B}}$ is the total flux of ${}^8\text{B}$ solar neutrinos, S_ν is the normalised incident energy spectrum of the solar neutrinos, n_e is the number of electron targets in the detector detection medium, and σ_{ν_i} is the neutrino-electron elastic scattering cross-section for flavour i .

Of course, we do not directly measure neutrino energies in the detector — only the associated scattered electron. If there were no correlation between the observed electron energy and its associated neutrino, then the only effect of neutrino oscillations would be to change the overall observed rate of events due to this process. There would be no change in the shape of the event's energy spectrum, even though neutrino oscillations are a function of neutrino energy. Fortunately, there is some dependence of E_ν on that of the scattered electron, E_e . This dependence can be seen in Fig. 6.1 for ${}^8\text{B}$ electron neutrinos interacting in SNO+. As can be seen, the dependence is weak, and comes mostly from basic energy conservation: If one observes a 10 MeV electron event in the detector, it cannot have come from a 5 MeV neutrino.

In Fig. 6.2 we can see the impact each physical process has on the energy spectrum that we eventually observe. We start with a broad energy distribution

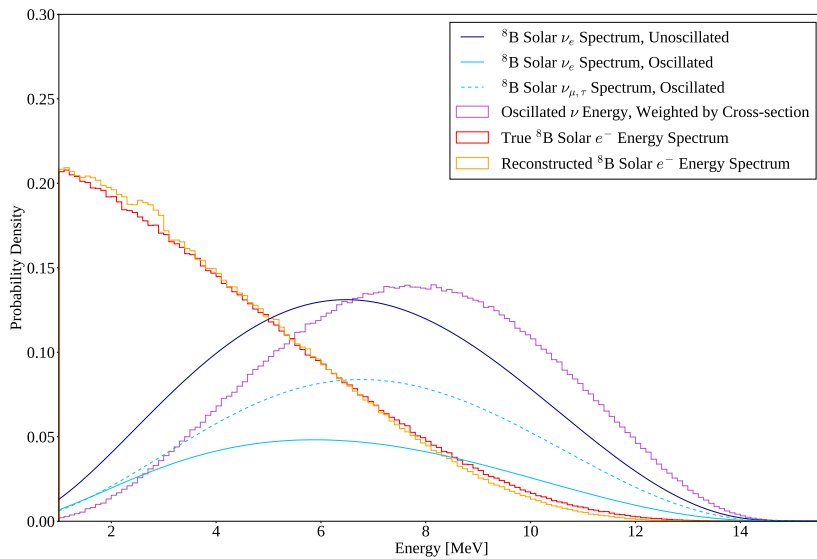


Fig. 6.2: The evolution of energy distributions related to ${}^8\text{B}$ solar neutrino detection. The unoscillated neutrino spectrum is taken from [29]; neutrino oscillations assume oscillation parameters from the current global fit results [60] and ν_e survival probabilities calculated via the method described in Section 6.1.8. The latter three distributions were obtained from MC production as described in Section 6.2.1, with the cross-section formula coming from [38].

of ${}^8\text{B}$ electron neutrinos generated in the Sun. These neutrinos then oscillate their flavour state as they propagate to the detector, in an energy-dependent manner. When a (tiny) fraction of these neutrinos interact with the electrons in our detector, there is both an energy- and flavour-dependence on the cross-section. The scattered electrons gain a kinetic energy with some mild dependence on the inciting neutrino's energy, which is then measured by the detector to within some energy resolution.

Let us now consider the dependence of P_{ee} on the individual neutrino oscillation parameters. Recall from Eq. ?? that, after considering matter-induced oscillations due to neutrinos passing through the Sun and possibly the Earth, $P_{ee} = P_{ee}(\tan 2\theta_{12}^M, \sin \theta_{13}^M, \Delta m_{21,M}^2) = P_{ee}(\theta_{12}, \theta_{13}, \Delta m_{12}^2, \Delta m_{13}^2)$. Fig. 6.3 shows the dependence of each of these four oscillation parameters on $P_{ee}(E)$. We can see that in reality only the two parameters Δm_{21}^2 and θ_{12} have a substantial impact on $P_{ee}(E)$ and hence the observed electron energy spectrum. Because of this, for

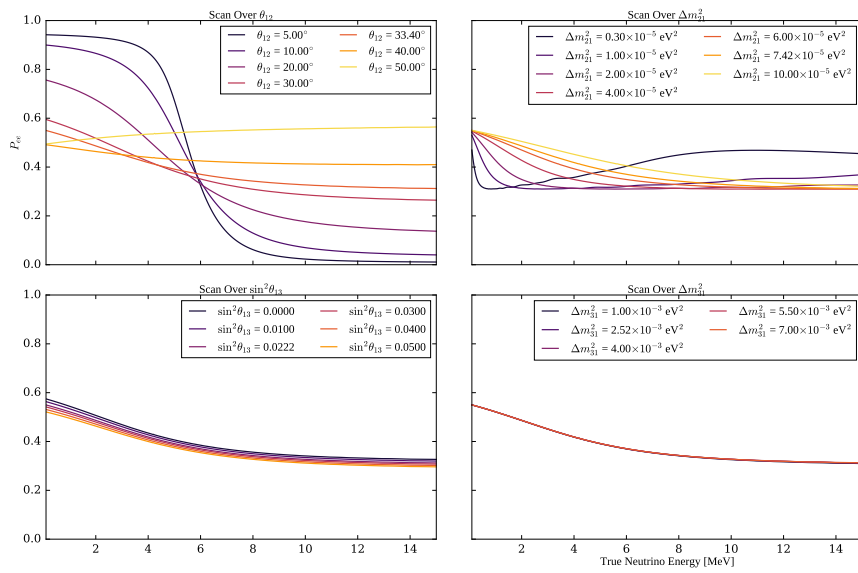


Fig. 6.3: P_{ee} as a function of true neutrino energy, scanned over a variety of oscillation parameter values. For a given oscillation parameter being scanned over, all other oscillation parameters are set at the NuFit 5.1 global fit values. P_{ee} values are calculated using the `PSelmaa` algorithm, as described in Section 6.1.8.

this analysis we will only ever vary these two oscillation parameters, and keep θ_{13} and Δm_{13}^2 at their current “NuFit 5.1” global fit values¹ of $\sin^2 \theta_{13} = 0.0222$ and $\Delta m_{13}^2 = +2.515 \times 10^{-3} \text{ eV}^2$ [60].

6.1.2 Background Processes

Sadly, elastically-scattered electrons from ${}^8\text{B}$ neutrinos are not the only events we see in the SNO+ detector during the scintillator phase. There are a number of background processes that our signal must compete against. Below a reconstructed energy of ~ 2.5 MeV, it is known that various backgrounds completely swamp any possible ${}^8\text{B}$ signal, and so for this analysis we only consider processes that can generate reconstructed energies of at least $E_{\min} = 2.5$ MeV. The following subsections explain each of these backgrounds, as well as methods that have been used to mitigate them as much as possible.

¹We use the global fit results excluding Super-Kamiokande’s atmospheric data, and assuming normal ordering of the neutrino mass hierarchy. This choice has a tiny impact on the magnitudes of these two fixed parameters, the main impact being the sign of Δm_{13}^2 .

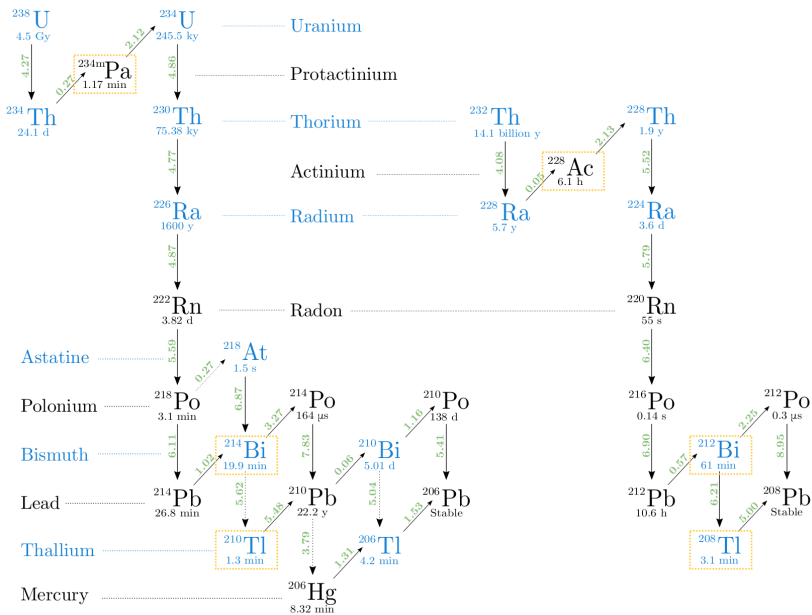


Fig. 6.4: The ^{238}U and ^{232}Th decay chains, taken from [135]. Isotopic half-lives are given below their symbol; the Q-values for each decay, in MeV, is given in green. Downward arrows indicate an α -decay; diagonal arrows indicate β -decay. Isotopes highlighted in gold are potential backgrounds for this solar analysis.

¹ Internal Uranium- and Thorium-Chain Backgrounds

Although every effort has been made to make the scintillator cocktail that fills SNO+ to be as radio-pure as possible, there inevitably remain trace amounts of the radioactive isotopes that derive from the decay chains of the ^{238}U and ^{232}Th isotopes. Fig. 6.4 shows these two decay chains. Fortunately, only a fraction of the radioactive isotopes in these chains actually are capable of generating events in the detector with energies above E_{\min} : these have been highlighted in Fig. 6.4 in gold.

Of particular note are the decays of ^{212}Bi and ^{214}Bi . Both are capable of either α - or β -decays to Tl or Po isotopes, respectively. For the former, it is the subsequent β -decay of the Tl that can have a reconstructed energy above E_{\min} . For the latter, the Bi decay is the part of the pair of decays that can lie above E_{\min} . Although the α -decays here certainly have Q-values well above 2.5 MeV, the liquid scintillator quenches the observed energy well below E_{\min} . The so-called

“Bi–Po” decays are particularly special because the lifetimes of ^{212}Po and ^{214}Po are 1
300 ns and 164 μs , respectively, which are short enough to allow for highly-effective 2
coincidence tagging. 3

There are two main classes of Bi–Po event in the detector: “out-of-window” 4
(OOW) events for which the Bi and Po occur in separate triggered event windows, 5
and “in-window” (IW) events whereby the Bi and Po occur within the same event 6
window. These lead to two distinct strategies for tagging these kinds of events. For 7
out-of-window Bi–Pos, we look for a delayed coincidence of two events. Using the 8
tagging algorithm suggested in [135, 154] as a starting point, the chosen procedure 9
was as follows. There must be two events that trigger the detector within 4 μs of 10
one another, and both have a valid `scintFitter` position reconstruction within 11
2 m of one another. The delayed candidate event must also have at least 100 12
cleaned PMT hits. This very broad coincidence tagging procedure was designed 13
to ensure that the cut was as *efficient* in tagging (and hence, rejecting) Bi–Pos 14
as possible, whilst negligibly impacting the solar signal. This is in contrast to the 15
cuts chosen by Rafael Hunt-Stokes in [155], which try and obtain a highly *pure* 16
sample of Bi–Po tags. 17

Of course, the above delayed coincidence procedure cannot catch any of the 18
in-window Bi–Po events. For these, we use a different approach. Because two 19
decays happened in the same event window, we expect to see two distinct peaks 20
in the event’s time residual spectrum. In order to look for this event topology, a 21
likelihood-ratio classifier was run over events, first developed by Eric Marzec [156] 22
and re-coordinated for the 2.2 g/L LABPPO scintillator optics by Ziping Ye [157]. 23
This classifier calculates the likelihood ratio between the null hypothesis of a $0\nu\beta\beta$ 24
event (a proxy in this analysis for single-site events such as our ^8B signal) and 25
the alternative hypothesis of an in-window Bi–Po event. The more negative the 26
value of the result, `alphabeta212`, the greater the evidence there is for rejecting 27

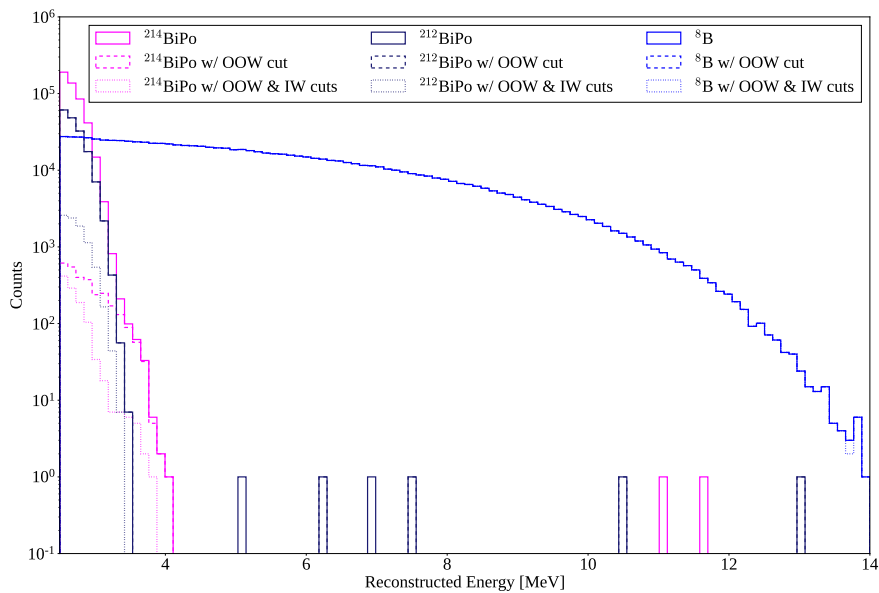


Fig. 6.5: $^{214}\text{Bi-Po}$, $^{212}\text{Bi-Po}$, and ^8B observed energy spectra in MC before and after out-of-window and in-window cuts. The relative normalisations before these cuts have been applied is arbitrary.

the null hypothesis of a single-site event. Events with `alphabeta212 < 0`, or the equivalent for $^{214}\text{Bi-Po}$ events, `alphabeta214`, were then rejected.

Combining both out-of-window and in-window Bi-Po tagging, the impact on $^{212}\text{Bi-Po}$, $^{214}\text{Bi-Po}$, and ^8B ν_e events can be seen in Fig. 6.5. We consider here only events that pass all other cuts used in this analysis (other than the cuts for externals defined shortly): see Section 6.2.2 for the specifics of the cuts used. Because of the different lifetimes of the decays, $^{214}\text{Bi-Po}$ decays predominantly fall out-of-window whilst $^{212}\text{Bi-Po}$ events are typically in-window. This explains why the out-of-window tagging is substantially better at cutting $^{214}\text{Bi-Po}$ decays, whereas the in-window tagging far better tags $^{212}\text{Bi-Po}$ decays. Overall, within the analysis region of interest (ROI), the two combined cuts are able to tag 99.77% of $^{214}\text{Bi-Po}$ triggered events, 94.84% of $^{212}\text{Bi-Po}$ triggered events, whilst retaining 99.85% of ^8B ν_e signal events.

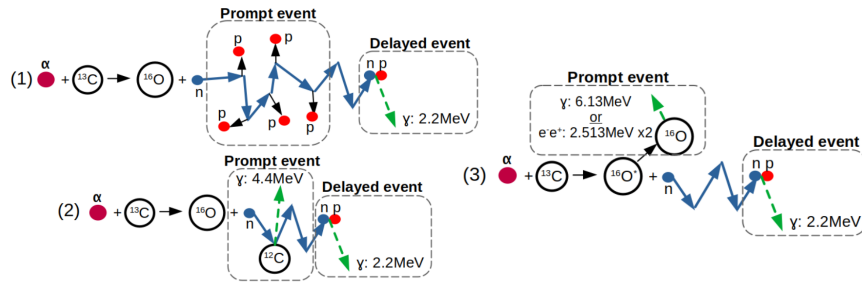


Fig. 6.6: Schematic of the three dominant modes of (α, n) interaction, taken from [90].

(α, n) Reactions

The impact of ^{238}U - and ^{232}Th -chain isotopes does not simply end at their direct decays. It is possible for the α s generated during these decays to undergo their own interactions with nuclei in the detector. Within the organic scintillator of SNO+, the dominant interaction of this type is when an α collides with a ^{13}C nucleus, emitting a neutron: $\alpha + ^{13}\text{C} \longrightarrow ^{16}\text{O} + n$. This is known as an (α, n) reaction.

The topology of this reaction in the detector is a delayed coincidence, as shown in Fig. 6.6. The prompt signal can be generated through a number of processes, including the decay of an excited ^{16}O state. The neutron generated in the interaction then thermalises and gets captured by another nucleus — usually hydrogen in SNO+ — which creates an excited state that then eventually decays, creating a γ that creates the delayed signal in the detector.

As can be seen in Fig. 6.7, (α, n) interactions can lead to events reconstructed at a wide variety of energies, which could be an issue for this analysis. However, because they are delayed coincidence events with a typical decay time of ~ 100 ns, the aforementioned out-of-window and in-window Bi–Po tagging algorithms also efficiently tag (α, n) events. Looking again at Fig. 6.7, simply by using the out-of-window and in-window Bi–Po taggers without any further modifications 99.37% of events in the ROI are cut.

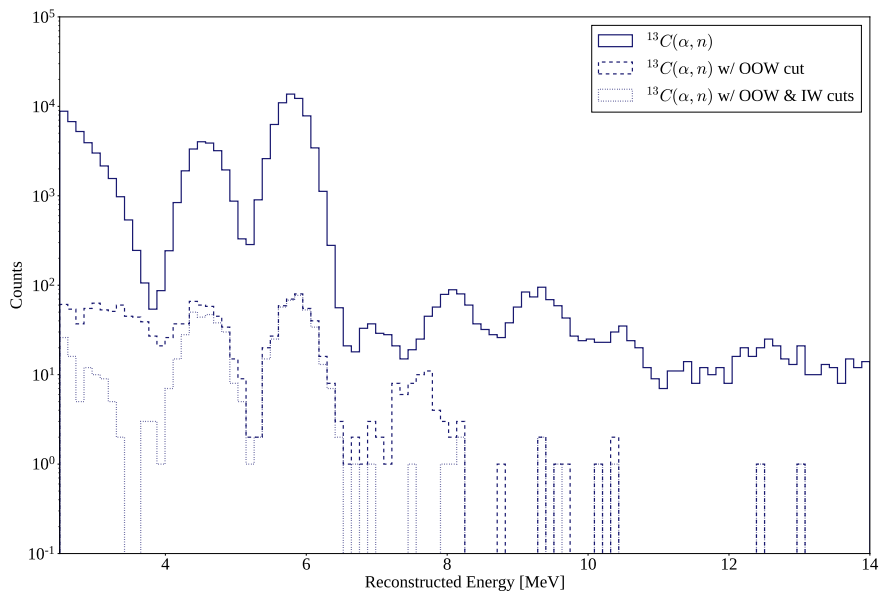


Fig. 6.7: (α, n) reconstructed energy spectrum in MC within the analysis ROI, before and after out-of-window cuts have been applied. The relative normalisation of the distribution before the additional cuts have been applied is arbitrary.

1 External Backgrounds

2 All materials within the SNO+ detector are radioactive, not just the liquid
 3 scintillator cocktail. This includes the acrylic, ropes, external water, and PMTs.
 4 These components have had their radiopurity “assayed” (that is, measured)
 5 throughout the detector’s lifetime, often back to the construction of the original
 6 SNO detector itself. The materials other than the liquid scintillator are known to
 7 have far higher background levels, especially in the important ^{238}U - and ^{232}Th -
 8 chain backgrounds [158]. To distinguish between the inherent backgrounds within
 9 the scintillator, and the backgrounds from materials at larger radii, we use the
 10 terminology “internal” and “external”, respectively.

11 Although there are numerous external backgrounds, with a suitably accurate
 12 and precise position reconstruction algorithm they can be suitably handled. The
 13 simplest approach is with a so-called “fiducial volume” (FV) cut: just throw out
 14 all events that reconstruct beyond some radius. The only external background
 15 events that will reach within the FV are those that have reconstructed very poorly,

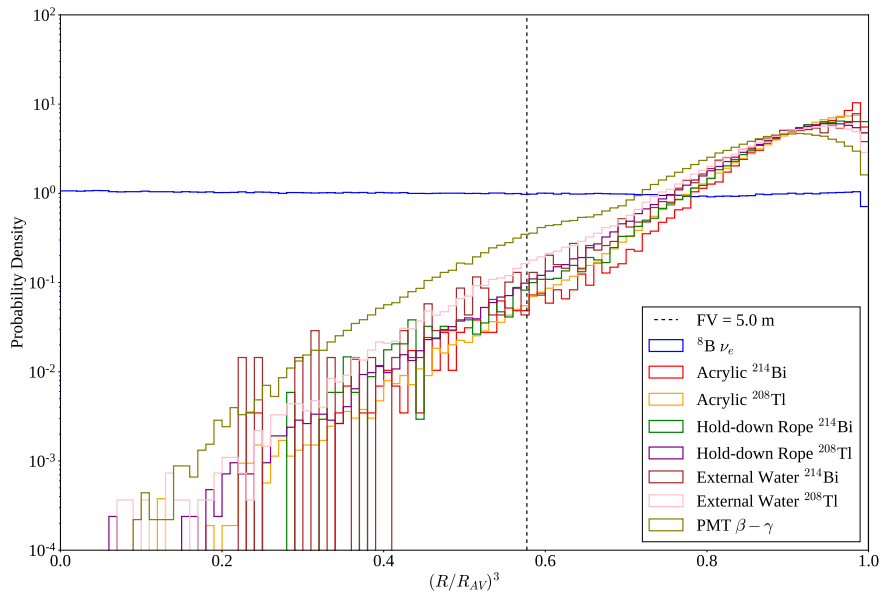


Fig. 6.8: Radial dependence of external backgrounds considered in this analysis, as compared to the ${}^8\text{B}$ signal. Events for all processes shown here had to pass the first 6 cuts of Table 6.1.

or have some long-distance radiation that manages to deposit radiation close to the centre of the AV. Because α and β radiation can only travel short distances through the detector, it is only γ radiation that can realistically travel far enough into the detector to be able to reconstruct anywhere near the centre. Moreover, the intensity of this γ radiation attenuates exponentially towards the centre of the detector, meaning only a tiny fraction of the total number of external events reconstruct within a 3.5 m FV, say. This strong radial-dependence can be seen in Fig. 6.8.

What this figure also demonstrates is that our solar signal has a completely different radial dependence to these backgrounds. As a result, if one considers not just the energy of events but also their reconstructed radius, then it is possible to get an additional handle on the external backgrounds. The FV cut can then be pushed further out to larger radii, allowing one to gain more signal statistics.

Work by Tereza Kroupova [135] allows for additional means of distinguishing external backgrounds from the solar signal. The underlying assumption in the

1 reconstruction of SNO+ events is that there was an electron at a single point, which
2 is entirely valid for ^8B elastic scattering events. However, external backgrounds can
3 fail this assumption in two ways. Firstly, these radioactive decays often generate
4 γ radiation in addition to the main α/β particle, which creates a multi-site event.
5 Because the **scintFitter** position reconstruction algorithm is not prepared for
6 a distribution of energy depositions in the scintillator, the t_{res} distribution will
7 broaden. This allows an event classifier to be built that distinguishes between
8 the t_{res} distributions of single-site events and externals, known as the “external
9 background timing classifier” (**ext0NuTimeTl208AVNaive**).

10 Secondly, because external backgrounds that do reconstruct close to the centre
11 of the detector typically have a γ that travelled a long distance towards the centre
12 of the detector, we expect the earliest light that hits the PMTs to arrive most
13 often along the direction of the reconstructed position vector. A distribution of
14 PMT hits for a given event as a function of their angular distribution relative
15 to the direction of position reconstruction can be built, and compared to the
16 expected distributions for single-site and external background events. This is
17 known as the “external background topological classifier” (**ext0NuAngleTl208AV**).
18 Much like the classifier described in Section 6.1.2, the single-site events used for
19 comparison were $0\nu\beta\beta$ events, but these have a similar single-site structure to the
20 solar signal of interest in this analysis.

21 Fig. 6.9 shows the correlation between the two classifier results for both acrylic
22 ^{208}Tl and $^8\text{B} \nu_e$ events in MC. These events were within the analysis ROI and
23 also below 5 MeV, as external backgrounds never reconstruct above this energy.
24 The other external backgrounds in MC have a similar distribution to that of the
25 acrylic ^{208}Tl .

26 As can be seen, the external background is far more spread out along both axes
27 compared to the signal. This allows for discrimination of external backgrounds from
28 the signal in the 2.5–5.0 MeV range. For this analysis, a cut on both discriminants

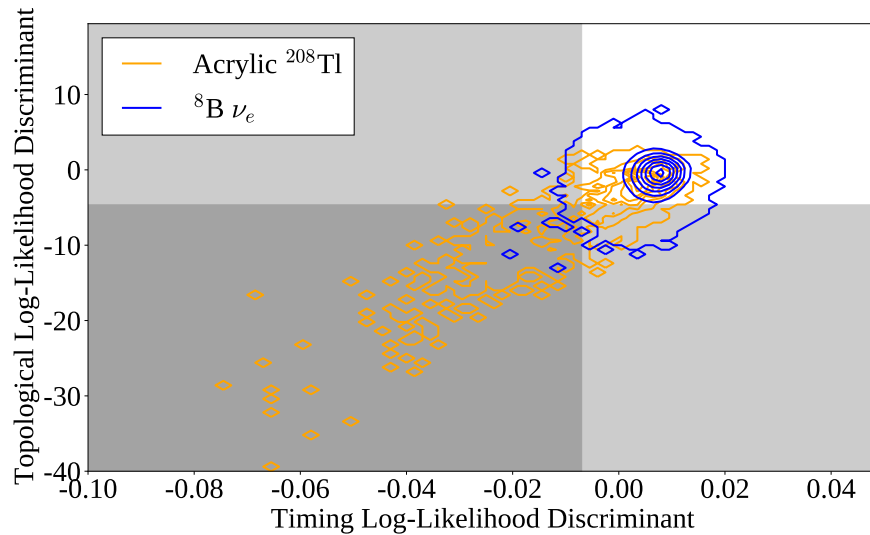


Fig. 6.9: Distributions of the two external classifiers, for both the ${}^8\text{B}$ signal and acrylic ${}^{208}\text{Tl}$ background MC. Contours indicate lines of equal probability density. All events shown were not just in the analysis ROI, but also below 5 MeV. Grey regions indicate the cuts used in this analysis.

were used: to pass, an event required `ext0NuTimeTl208AVNaive > -0.007` and `ext0NuAngleTl208AV > -4.7`. By using these cuts, 37.4% of external acrylic ${}^{208}\text{Tl}$ were cut in the analysis ROI in MC, whilst keeping 99.3% of the ${}^8\text{B} \nu_e$ signal.

6.1.3 The Log-likelihood Test Statistic

At the highest level, this analysis involves taking the data observed in the scintillator-fill after applying a certain set of cuts, along with simulated PDFs for all processes believed to build up the observed data with those same cuts applied, and then attempting to fit the combined energy and radial distributions of the MC to that of the data. Given a set of PDFs, to try and match the distribution of observables in data we can modify a number of parameters. These consist of the normalisations of each PDF (i.e. the total number of events observed due to that process), and any systematic parameters that could modify the shapes of these distributions. For this analysis, the neutrino oscillation parameters act as *de facto* systematic parameters, as they modify the shape of the ${}^8\text{B}$ PDFs. Of course,

¹ unlike usual systematics the oscillation parameters are what we are actively trying
² to measure.

³ The test statistic used for this analysis is the *binned extended log-likelihood*:

$$\mathcal{L}(\mathcal{N}, \boldsymbol{\theta} | \mathbf{n}) = - \sum_{i=1}^{N_{\text{PDFs}}} \mathcal{N}_i + \sum_{j=1}^{N_{\text{bins}}} n_j \ln \left(\sum_{i=1}^{N_{\text{PDFs}}} \mathcal{N}_i P_{ij}(\boldsymbol{\theta}) \right), \quad (6.2)$$

⁴ where \mathcal{N}_i is the normalisation parameter for the i^{th} PDF out of N_{PDFs} in total,
⁵ n_j is the number of observed events in the j^{th} bin of data out of N_{bins} total bins,
⁶ and $P_{ij}(\boldsymbol{\theta})$ is the probability of observing an event of type j in bin i , assuming a
⁷ set of systematic parameters $\boldsymbol{\theta}$. \mathcal{N} and \mathbf{n} are the set of normalisation parameters
⁸ and observed bin values, respectively.

¹¹ 6.1.4 The Bayesian Statistical Approach

¹² There are two main schools of statistical inference, “Frequentist” and “Bayesian”.
¹³ In the former, probabilities describe the fraction of times a situation can be found
¹⁴ within the whole ensemble of possible worlds. For the latter, we care not about an
¹⁵ ensemble of worlds but instead our degree of belief about matters in this current
¹⁶ one. We update our beliefs as we acquire knowledge about the world through
¹⁷ Bayes’ Theorem:

$$\mathbb{P}(\boldsymbol{\mu} | \mathbf{x}) = \frac{\mathcal{L}(\boldsymbol{\mu} | \mathbf{x}) \mathbb{P}(\boldsymbol{\mu})}{\mathbb{P}(\mathbf{x})}. \quad (6.3)$$

¹⁸ Here, $\boldsymbol{\mu}$ is the set of parameters that model our system, $\mathbb{P}(\boldsymbol{\mu})$ is our *prior* (pre-existing) distribution for those model parameters, and \mathbf{x} is the data taken in our experiment. The updated, *posterior* distribution $\mathbb{P}(\boldsymbol{\mu} | \mathbf{x})$ is then the prior multiplied by the likelihood of parameters $\boldsymbol{\mu}$ given observations \mathbf{x} , $\mathcal{L}(\boldsymbol{\mu} | \mathbf{x})$, and divided by the total probability $\mathbb{P}(\mathbf{x})$ of observing \mathbf{x} under any circumstance.

¹⁹ Both approaches to statistics are widely-used in statistical analysis, in both
²⁰ particle physics and beyond. The Bayesian approach was used for this analysis,

as it was believed that this helps keep transparent what assumptions are being
made in the analysis.

Now, if one is able to determine the overall posterior distribution, then it is
possible to derive best-fit values with uncertainties for all parameters in the fit.
This is done by “marginalising” the posterior distribution, i.e. integrating over
all parameters other than the one of interest. A sensible best-fit value is then
the point of Highest Posterior Density (HPD). The uncertainty on this value is
derived from the spread of the marginalised posterior, by the calculation of the
 1σ Credible Interval (CI): this is the set of values for a given parameter which has
a total posterior probability of 68.3%, and contain the best-fit value. There are
in fact an infinite number of CIs that satisfy this property; for this analysis, the
values are chosen in decreasing order of marginalised posterior probability density.

6.1.5 Markov Chain Monte Carlo

Of course, all of this assumes that one can accurately determine the posterior
density distribution. Whilst the likelihood and prior distribution are straight-
forward enough to calculate, often-times $P(\mathbf{x})$ (which acts as a normalisation)
is very challenging to determine. This is because calculating this normalisation
involves integrating the likelihood over all the parameter space, and if there are
a large number of parameters this can become enormously numerically complex.
An alternative approach is needed!

That alternative comes in the form of *Markov Chain Monte Carlo*, MCMC. A
Markov Chain is any mathematical system for which the next state of the system
is dependent only on its current state; the system is in some sense “memoryless”.
For a large class of Markov Chains — those that are “ergodic” and “aperiodic” —
one can prove that regardless of the initial position on the chain, the probability
distribution converges to the same distribution [159]. MCMC uses such a Markov

¹ Chain which attempts to converge towards the posterior density distribution in
² particular. In MCMC, after choosing the initial position in the parameter space,
³ successive states are chosen at random with a probability dependent only on the
⁴ properties of the current position in parameter space and the proposed position.
⁵ The convergence property of Markov Chains means that the set of steps made in
⁶ the parameter space will have a distribution that converges to that of the posterior
⁷ density distribution.

⁸ There are a number of MCMC algorithms, and the particular one used in this
⁹ analysis is that of the *Random-Walk Metropolis Algorithm*. In this algorithm,
¹⁰ given an initial position in the parameter space $\boldsymbol{\mu}$, a new step is proposed, $\boldsymbol{\mu}'$.
¹¹ This step is chosen at random from a multivariate Gaussian distribution centred
¹² on the current position, with widths in each dimension of the parameter space
¹³ chosen beforehand as constants for tuning the MCMC process. This choosing of a
¹⁴ new proposed step at random is what gives the algorithm its Monte Carlo and
¹⁵ Random Walk titles. Once a new step is proposed, it is accepted as the new step
¹⁶ with a probability $S(\boldsymbol{\mu}'|\boldsymbol{\mu})$ according to the condition of *detailed balance*:

$$\begin{aligned} S(\boldsymbol{\mu}'|\boldsymbol{\mu}) &= \min\left(1, \frac{P(\boldsymbol{\mu}'|\mathbf{x})}{P(\boldsymbol{\mu}|\mathbf{x})}\right) = \min\left(1, \frac{L(\boldsymbol{\mu}'|\mathbf{x}) P(\boldsymbol{\mu}')}{L(\boldsymbol{\mu}|\mathbf{x}) P(\boldsymbol{\mu})}\right) \\ &= \min\left(1, \exp\left[\mathcal{L}(\boldsymbol{\mu}'|\mathbf{x}) - \mathcal{L}(\boldsymbol{\mu}|\mathbf{x}) + \ln \frac{P(\boldsymbol{\mu}')}{P(\boldsymbol{\mu})}\right]\right). \end{aligned} \quad (6.4)$$

²⁰ It is the detailed balance condition that ensures convergence of the MCMC
²¹ algorithm to specifically the posterior density distribution. Crucially, because
²² it is only dependent on the ratio of posterior densities, the hard-to-calculate
²³ normalisation $P(\mathbf{x})$ in both posterior density terms cancels out, meaning one only
²⁴ needs to calculate the likelihood and priors for each step.

²⁵ The specific implementation of MCMC used for this analysis is that of **OXO**, a
²⁶ C++ analysis framework first developed by Jack Dunger [153] and built on for

this analysis. `OXO` is able to run the Metropolis algorithm on multidimensional binned data, using the log-likelihood defined in 6.1.3. This framework also allows one to include systematic parameters that can float within the fit, and define non-uniform priors for normalisations and systematics that have constraints.

6.1.6 Choosing Priors

For this analysis, the suggestions made by Biller & Oser in [160] about choosing prior distributions are followed: for parameters that do not have some pre-existing constraint, a flat prior is used. A nice consequence of this choice is that $\ln \frac{P(\mu')}{P(\mu)} = 0$, so the actual value of the prior for these variables never needs to be calculated when running the MCMC algorithm. For this analysis, uniform priors are assumed on the neutrino oscillation parameters Δm_{21}^2 and θ_{12} , as the magnitudes of these parameters are now well-established.

For parameters with existing asymmetric constraints $\beta_{-\sigma_-}^{+\sigma_+}$, this analysis uses an asymmetric Gaussian prior, equivalent to the logarithm of the prior being an asymmetric quadratic:

$$\ln P(\mu) = \mathcal{A} - \begin{cases} \frac{(\mu-\beta)^2}{2\sigma_+^2} & \text{if } \mu \geq \beta, \\ \frac{(\mu-\beta)^2}{2\sigma_-^2} & \text{if } \mu < \beta. \end{cases} \quad (6.5)$$

Here, \mathcal{A} is the logarithm of the prior's normalisation constant, and cancels out in the detailed balance condition. For parameters with symmetric constraints, $\sigma_+ = \sigma_-$, then $\ln P(\mu)$ reduces to a quadratic with maximum at $\mu = \beta$.

Fit parameters often also have basic physical limits on what values they can hold. Normalisation parameters, for example, must be positive. We also restrict the oscillation parameters to be in the very broad range $3.0 \times 10^{-6} \text{ eV}^2 \leq \Delta m_{21}^2 \leq 1.0 \times 10^{-3} \text{ eV}^2$ and $5^\circ \leq \theta_{12} \leq 65^\circ$. The prior density beyond these limits is zero,

¹ meaning that any proposed step outside the allowed region can be immediately
² rejected.

³ 6.1.7 Including Systematics in the Fit

⁴ One important implementation detail is how systematics are applied within the
⁵ MCMC fitting process. Once systematics are added to the fit, at every step the
⁶ binned PDFs for all the processes considered in the fit must get modified appropri-
⁷ ately, which can become extremely computationally-intensive if not approached
⁸ carefully. The strategy used in the `OXO` framework starts by thinking of the
⁹ contents of a binned PDF as a vector of bin probabilities, $\mathbf{p} = (p_1, p_2, \dots, p_{N_{\text{bins}}})^T$.
¹⁰ Then, we can think of a systematic acting on the PDF as a linear transformation,
¹¹ and hence a matrix S acting on this vector: $\mathbf{p}' = S\mathbf{p}$. We only need to calculate
¹² this matrix once for a given set of systematic parameter values, and can then
¹³ use the same matrix on all the PDFs in the fit. Furthermore, when multiple
¹⁴ systematics are applied, the matrix for each systematic can then be combined via
¹⁵ matrix multiplication into one single “detector response” matrix. `OXO` uses the
¹⁶ `Armadillo` [161, 162] linear algebra package for efficient matrix manipulation.

¹⁷ There is a problem that can arise when considering the impact of systematics
¹⁸ near the edge of the analysis ROI. Many systematics such as shifts, scalings,
¹⁹ and convolutions use information about the contents of nearby bins to determine
²⁰ the contents of a particular bin. However, for bins near the edge some of that
²¹ information does not exist — it has been lost to the cuts that define the ROI.
²² This can lead to a bias in the generation of the modified PDFs, and therefore also
²³ the posterior distribution.

²⁴ As an example, consider the impact of an energy scale systematic on the
²⁵ energy distribution of PMT $\beta - \gamma$ events in the detector, shown in Fig. 6.10.
²⁶ Because the events seen for this process in the ROI are merely the high-energy

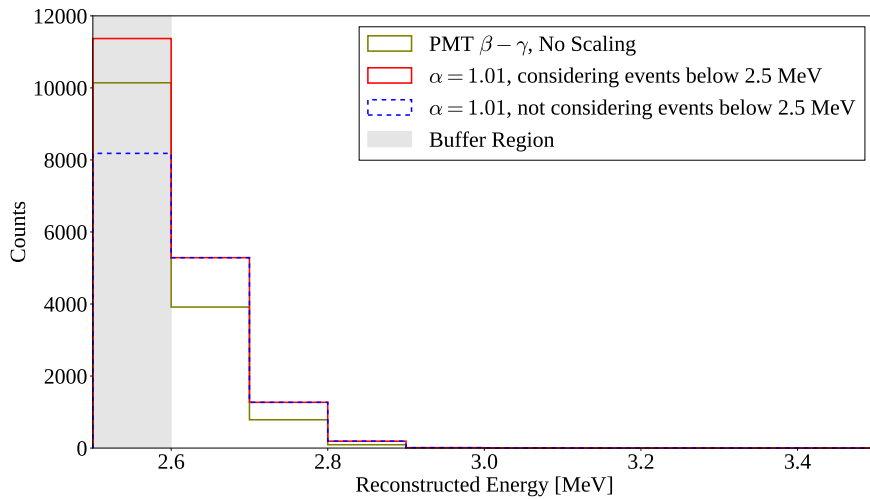


Fig. 6.10: Demonstration of how to handle an energy scaling systematic correctly. The distribution of PMT $\beta - \gamma$ events in the analysis ROI is shown in energy, both before and after an energy scaling of $\alpha = 1.01$ has been applied. If the distribution below 2.5 MeV is not known, then the scaled distribution is biased systematically. This is solved through the use of a buffer region, as indicated.

tail, any systematic energy scaling $E'_{\text{reco}} := \alpha E_{\text{reco}}$ should have a large impact on the number of events observed at the low end of the ROI. However, given that the information about data below E_{\min} is lost to the ROI cuts, any energy scaling of $\alpha > 1$ will not be applied correctly at all.

The solution to this problem is defining a “buffer region” of bins on either side of the ROI, which allow for tracking of events in and out of the ROI due to systematics, but aren’t considered when calculating the likelihood. This is also shown in Fig. 6.10. After the scaling systematic is applied, although incorrect bin values are found in the buffer region, this is fine because we are no longer calculating the likelihood with those bins. Note that because of this modification, the normalisation parameters we put into the model no longer represent the expected number of events in the ROI. Instead, they represent the number of events expected in both the ROI and buffer region, before any systematics have been applied.

¹ 6.1.8 Including Oscillations in the Fit

² Within the analysis MCMC code, the process of neutrino oscillations are thought
³ of as a *de facto* systematic that acts only on the ${}^8\text{B}$ ν_e and ν_x signal spectra.
⁴ Three parameters relevant to the signal are floated within the MCMC fit: Δm_{21}^2 ,
⁵ θ_{12} , and $\varphi_{{}^8\text{B}} = \Phi_{{}^8\text{B}}^{\text{meas}} / \Phi_{{}^8\text{B}}$, the unoscillated ${}^8\text{B}$ flux relative to the expected rate.
⁶ For the two signal PDFs, a third “bookkeeping” dimension is added on top of
⁷ reconstructed energy and radius: the true neutrino energy, E_ν . This is necessary
⁸ for correctly applying oscillations, as the oscillation probability is a function of
⁹ the neutrino’s energy, not the scattered electron’s. Before the fit, these 3D PDFs
¹⁰ are given normalisations corresponding to the expectation of the number of events
¹¹ for each type, ν_e and $\nu_{\mu,\tau}$, after cuts but before oscillations have been applied.
¹² Strictly speaking there should be zero $\nu_{\mu,\tau}$ events before neutrino oscillations: the
¹³ pre-oscillation rate used here is the post-cut number of events expected if 100% of
¹⁴ the neutrinos oscillated to the $\nu_{\mu,\tau}$ type.

¹⁵ During the MCMC fit, for a given set of parameters $\boldsymbol{\theta} = (\Delta m_{21}^2, \theta_{12}, \varphi_{{}^8\text{B}})$ the
¹⁶ following is performed to oscillate the signal PDFs. Firstly, the normalisations
¹⁷ are scaled by the factor $\varphi_{{}^8\text{B}}$. Then, for each E_ν bin the survival probability
¹⁸ $P_{ee}(E_\nu, \Delta m_{21}^2, \theta_{12})$ is calculated. Each bin then has their probability scaled by
¹⁹ either P_{ee} or $1 - P_{ee}$, for ν_e and $\nu_{\mu,\tau}$ respectively. Of course, within the structure
²⁰ of the **OXO** framework these bin-by-bin scaling aren’t immediately applied, but
²¹ instead a matrix describing the impact of oscillations on each of the PDFs is
²² made. Because the oscillation transformation is purely a bin-by-bin scaling, the
²³ resulting matrices are diagonal, with diagonal elements $\varphi_{{}^8\text{B}} \cdot P_{ee}(E_\nu, \Delta m_{21}^2, \theta_{12})$
²⁴ or $\varphi_{{}^8\text{B}} \cdot (1 - P_{ee}(E_\nu, \Delta m_{21}^2, \theta_{12}))$ for ν_e and $\nu_{\mu,\tau}$ respectively. After the oscillation
²⁵ matrix along with all other systematic matrices are applied to the signal PDFs,
²⁶ the PDFs are then marginalised over the E_ν dimension so that the signal PDFs
²⁷ match the dimensionality of all other PDFs.

Calculations of the survival probability are handled with **PSelmaa**, an algorithm written by Nuno Barros for the SNO 3-phase Analysis [163]. This considers not only the neutrino oscillations through the vacuum of space between the Sun and Earth, but also the impact of matter effects in both the Sun and Earth. This can usually be a very computationally-intensive process, but **PSelmaa** takes advantage of the assumption that the solar oscillation parameters are in the so-called “Large Mixing Angle” regime, making the calculation much faster. As seen in Section 1.2.1, previous solar oscillation experiments demonstrate that this assumption is reasonable. For this analysis, the standard MSW effect is assumed with neutrinos obeying the Normal Hierarchy, with the Sun following the **B16_GS98** metallicity model [30] and the **PREM** model being used for the Earth [164].

One final thing **PSelmaa** needs to know to calculate survival probabilities is the distribution of solar zenith angles during the data-taking. The solar zenith θ_z is the angle between the two following vectors: one going from the centre of the Earth through the centre of the SNO+ detector, and another starting from the detector’s centre and pointing towards the Sun. As an example, if the Sun were ever to be directly above the detector, both vectors would be along direction \hat{z} in detector coordinates, leading to a solar zenith angle of $\theta_z = 0$. The position of the SNO+ detector on Earth, as well as the times at which the detector was live, determine the solar zenith angle distribution. If not accounted for, this can lead to a bias in the result of the analysis, as a preponderance of livetime taken at night (say) would lead to a larger fraction of solar neutrinos having to pass through the bulk of the Earth to get to the detector, and hence the impact of the MSW effect would be greater.

Even after using the Large Mixing Angle approximation, having to call **PSelmaa** numerous times for every step in the MCMC algorithm would lead to exorbitant run times for the fitting. Therefore, a further approximation is made. Before running the MCMC fit, **PSelmaa** is used to calculate P_{ee} over the necessary 3D

¹ space of parameters. To get a fine scan of this space, 101 E_ν values from 1 MeV
² to 20 MeV, 101 Δm_{21}^2 values from 3×10^{-6} eV² to 1×10^{-3} eV², and 151 values
³ for θ_{12} from 5° to 65° were looked over. This 3D grid of $101 \cdot 101 \cdot 151$ P_{ee} values
⁴ is then written to disk, and loaded into memory for use during the fit as a lookup
⁵ table. At run-time, as the Metropolis-Hastings algorithm samples this 3D space
⁶ the survival probability is estimated through a trilinear interpolation of the 3D
⁷ grid loaded in: a version of linear interpolation for three dimensions.

⁸ **6.2 Analysis on Scintillator-Phase data**

⁹ **6.2.1 Dataset and Livetime**

¹⁰ The data used in this analysis was chosen to be scintillator phase data after the
¹¹ end of the PPO top-up campaign that completed in April 2022. Following an
¹² initial validation of the analysis tools was performed on data between 29th April
¹³ and 10th May 2022 [165], data for the full analysis was chosen from runs taken
¹⁴ after these dates. Not all data taken during this time was considered usable
¹⁵ for this analysis, however: this is the role of *run selection*. The Collaboration’s
¹⁶ ‘Preliminary Scintillator Gold’ run selection list was used as the basis for this
¹⁷ analysis. This run list requires:

- ¹⁸ • The run type must be in ‘Physics’, as opposed to running in calibration or
¹⁹ maintenance;
- ²⁰ • The run must last at least 30 minutes;
- ²¹ • Detector electronics must be working in a stable manner without any alarms,
²² and with all crates online;
- ²³ • There are no abnormal rates of tagged muons, and the OWL PMTs are
²⁴ correctly functioning;

- There are no unusual conditions from e.g. earthquakes, blasting activity in the mine, or loss of power.

In the end, data for this analysis used ‘Gold’ runs selected between 17th May–30th November 2022, run numbers 300733–306498. The raw livetime associated with this dataset was calculated by looking at the start and end times of each run using the detector’s 10 MHz clock: 84.977 days.

Importantly, the livetime of the data actually used in the analysis ends up being somewhat less than this raw value. This is because two of the cuts used in the analysis (described in Section 6.2.2), the muon tagger and the `high-nhit` event tagger, also veto events for a time period following a tagged event. This means that any events in such a time window are automatically thrown out of consideration for analysis. An algorithm was written to determine the loss of livetime from both of these tagging processes for all the runs selected in this analysis, allowing for the net livetime to be calculated. To ensure accuracy in the value of this lost livetime, the algorithm took care to handle any overlaps in the time veto windows. This ends up being a quite common occurrence, as tagged muon events and their followers often have a very high `nhit`. The net livetime was calculated to be 80.615 days. Data processing and simulations used RAT versions 7.0.8 and 7.0.9.

As discussed in Section 6.1.8, in order to account for the impact of the MSW effect through the Earth on P_{ee} , the solar zenith angular distribution of the dataset is needed. This was achieved by taking the recorded trigger time of each event within the dataset as given by the GPS-calibrated 10 MHz clock, determining the position of the Sun at that time, and then deriving the value of $\cos \theta_z$ given that solar position. The resulting distribution of $\cos \theta_z$ is shown in Fig. 6.11. The structure of this distribution are a result of the times of day and year of the runs selected for this analysis.

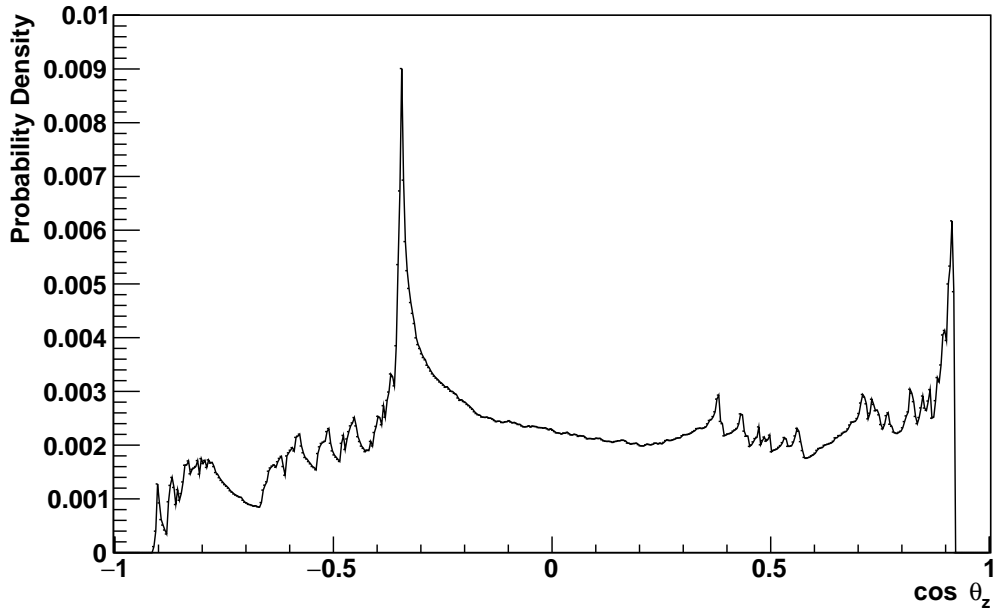


Fig. 6.11: Distribution of the cosine of the solar zenith angle, $\cos \theta_z$, for the events within this dataset. If an event has $\cos \theta_z > 0$, then at the time of that event the position of the Sun is above the detector's equator.

¹ 6.2.2 Event Selection

² Once the runs of processed data and matching MC have been selected, the next
³ step was to perform cuts on both in order to obtain our analysis ROI. The full list
⁴ of cuts used are shown in Table 6.1, most of which have already been explained in
⁵ Section 6.1.2.

⁶ Most of the other cuts used in this analysis that haven't yet been discussed
⁷ come from handling differences between data and MC. In MC, it is possible to
⁸ simulate an event but not have it trigger the detector. In this case, the stored
⁹ index of that event (`evIndex`) will be less than zero. We never see these 'events'
¹⁰ in data of course, but they do need to be removed from simulation. On the flip
¹¹ side, there are types of events that we observe in the detector but do not simulate.
¹² Many of these events are caught during 'data cleaning', which looks for a wide
¹³ variety of problems in the data when the data is being processed. Any subset
¹⁴ of the checks made during data cleaning can be chosen to consider in a given

| Cut Description | Cut |
|---|---|
| Event triggers detector | <code>evIndex ≥ 0</code> |
| Pass data cleaning | <code>ANALYSIS_MASK = 0x2100000042c2</code> |
| High-nhit veto | <code>correctedNhits ≥ 5000; veto for 20 s</code> |
| <code>ScintFitter</code> used | <code>scintFit = true</code> |
| Results of <code>ScintFitter</code> valid | <code>fitValid = true</code> |
| In energy Region of Interest | $2.5 \text{ MeV} < E < 14.0 \text{ MeV}$ |
| Fiducial Volume cut | $R < 5.0 \text{ m}$ |
| Remove BiPo Out-of-window tags | See Section 6.1.2 |
| Remove BiPo In-window tags | Tagged if $\text{alphaBeta212} > 0$ and $\text{alphaBeta214} > 0$ Tagged if $E < 5.0 \text{ MeV}$, |
| Remove External tags | $\text{extONuTimeTl208AVNaive} > -0.007$, and $\text{extONuAngleTl208AV} > -4.7$ |

Table 6.1: Cuts used in this analysis.

analysis by defining a specific ‘analysis mask’; a number that specifies for each of its binary digits whether to consider the data cleaning process associated with that bit. The mask chosen used in this analysis is the Collaboration’s current standard for the scintillator phase, 0x2100000042c2, which corresponds to:

- **00 cut:** Tags every event which has a GTID ending in 00 in hexadecimal, which is associated with a long-standing issue in the detector triggering system.
- **Junk cut:** Tags events that have channels with multiple recorded hits for that event. These are associated with so-called ‘orphaned’ hits that the event building process doesn’t know what to do with.
- **OWL cut:** Tags events that have at least three OWL PMTs hit, a sign that the event came from a cosmic-ray muon.
- **Polling cut:** Tags all events that occur during ‘polling’, a detector monitoring process.
- **CAEN cut:** Tags all events that have missing CAEN trace data.

- ¹ • **Muon cut:** Tags muon-like events.
- ² • **Muon follower cut:** Tags all events coming up to 20 s after a tagged muon event.

⁴ Beyond the formal data cleaning cuts, a high-nhit veto was used to tag and
⁵ remove various instrumental backgrounds which can generate large amounts of
⁶ light in the detector. This method also catches any muons left untagged by the
⁷ data cleaning mask. After any event with a sufficiently large number of hits, both
⁸ that event and any following it for 20 s are removed. This method is likely to be
⁹ fairly conservative, and there exist different methods for cutting flashers within
¹⁰ data cleaning. However, these were originally coordinated for the water phase,
¹¹ and had not been updated for the scintillator phase at the time of writing.

¹² The results of all these cuts can be seen for the data in Table 6.2. 654 out of
¹³ the 18,112,495,770 events within the dataset pass all cuts. These same cuts were
¹⁴ also run over the MC, with results summarised in Table 6.3. Important to note
¹⁵ was the difference between the number of physics events simulated for a given
¹⁶ process and the number of triggered events. The latter ends up being larger than
¹⁷ the former for all processes discussed here, because a given physics event in the
¹⁸ detector will often generate a retrigger event following the primary triggered event.
¹⁹ Also shown in this table are the combined cut efficiencies for each process. This
²⁰ efficiency is defined as the number of triggered events that pass all cuts, divided
²¹ by the number of simulated physics events for that process.

²² Variable bin widths in energy were chosen for this analysis: 0.1 MeV bins
²³ between 2.5 MeV–5.0 MeV, 0.25 MeV bins between 5.0 MeV–13.0 MeV, and a single
²⁴ energy bin between 13.0 MeV–14.0 MeV. Four equally-spaced bins were used in the
²⁵ parameter $r_3 = (r_{\text{reco}}/R_{\text{AV}})^3$ in the range $0 \text{ m} \leq r_{\text{reco}} < 5.0 \text{ m}$. The r_3 parameter
²⁶ was used to allow for equal volume weighting for each radial bin.

| Cut | # Events Remaining | Cut Efficiency (%) |
|---------------------------|--------------------|--------------------|
| Before cuts | 18,112,495,770 | 100.00 |
| Event triggers detector | 18,112,495,770 | 100.00 |
| Data Cleaning | 17,663,711,108 | 97.52 |
| high-nhit veto | 17,039,514,332 | 96.47 |
| ScintFitter used | 10,433,875,757 | 61.23 |
| ScintFitter results valid | 3,431,328,125 | 32.89 |
| Energy cut | 132,673 | 0.00387 |
| FV cut | 2093 | 1.58 |
| BiPo OOW cut | 817 | 39.03 |
| BiPo IW cut | 719 | 88.00 |
| Externals cut | 652 | 90.68 |

Table 6.2: Impact of each cut on the quantity of events in data.

| MC process | # Physics Events Simulated | # Triggered Events Simulated | # Remaining Events after cuts | Overall Cut Efficiency (%) |
|------------------------------------|-------------------------------|---------------------------------|----------------------------------|----------------------------|
| $^8\text{B } \nu_e$ | 2,830,425 | 5,511,568 | 929,551 | 32.8 |
| $^8\text{B } \nu_{\mu,\tau}$ | 1,898,088 | 3,675,261 | 572,949 | 30.2 |
| AV ^{214}Bi | 27,138,894 | 38,267,431 | 127 | 0.000468 |
| Ropes ^{214}Bi | 67,541,698 | 84,734,663 | 221 | 0.000327 |
| AV ^{208}Tl | 4,071,850 | 6,689,331 | 1471 | 0.0361 |
| Ropes ^{208}Tl | 6,105,956 | 8,758,457 | 2407 | 0.0394 |
| External Water ^{214}Bi | 81,300,835 | 85,056,233 | 62 | 0.0000763 |
| External Water ^{208}Tl | 36,602,319 | 38,963,663 | 2786 | 0.00761 |
| PMT $\beta - \gamma$ | 4,069,055 | 6,615,601 | 13,570 | 0.333 |
| Internal $^{212}\text{BiPo}$ | 9,761,554 | 24,331,685 | 8276 | 0.0848 |
| Internal ^{208}Tl | 816,233 | 1,626,536 | 409,629 | 50.2 |
| Internal $^{214}\text{BiPo}$ | 4,883,417 | 19,293,285 | 1030 | 0.0211 |
| Internal ^{210}Tl | 815,256 | 1,625,012 | 342,415 | 42.0 |
| Surface (α, n) (combined) | 22,627,103 | 48,834,413 | 2238 | 0.00458 |
| Internal (α, n) | 1,219,279 | 4,740,313 | 655 | 0.0537 |
| Internal ^{228}Ac | 9,764,480 | 19,294,643 | 0 | 0 |
| Internal ^{234m}Pa | 16,959,995 | 30,806,833 | 1 | 0.0000059 |

Table 6.3: Combined impact of cuts on each MC process. Overall cut efficiency is defined as the number of remaining triggered events after all cuts have been applied, divided by the number of physics events simulated for that process. Processes have been split into three general categories: signal, externals, and internals. A final category corresponds to various processes that have been considered for this analysis, but either all events are cut out, or Section 6.2.3 will show a negligible number of these events are expected in our dataset.

1 6.2.3 Expected Rates and their Constraints

2 Because this analysis is dependent on deriving the shape and size of the ${}^8\text{B}$
3 spectrum from the data observed, it is important to have expectations about the
4 number of events expected to be seen within the dataset for each process, both
5 signal and background. This is done in two stages: firstly, the expected rates for
6 each process before any cuts applied is determined, along with any constraints.
7 Then, by using the cut efficiencies calculated in the previous section, we can derive
8 estimates for the expected number of events after cuts. When combined with a
9 constraining uncertainty, this can be used as a prior within the MCMC fit. The
10 resulting expected rates before and after cuts, along with any constraints being
11 used, are shown in Table 6.5.

12 ${}^8\text{B}$ Signal

13 Starting with the ${}^8\text{B}$ signal, numerous theoretical predictions and experimental
14 measurements have been made of the ${}^8\text{B}$ flux. For this analysis, two different
15 values have been used. The SSM predicts a relatively loose constraint of $\Phi_{{}^8\text{B}} =$
16 $(5.46 \pm 12\%) \times 10^6 \text{ cm}^{-2} \text{ s}^{-1}$ [30], whereas a recent global fit of neutrino oscillation
17 experiments by Bergström *et al* leads to a much stronger constraint of $\Phi_{{}^8\text{B}} =$
18 $(5.16^{+2.5\%}_{-1.7\%}) \times 10^6 \text{ cm}^{-2} \text{ s}^{-1}$ [166]. We shall mainly use the latter result to both
19 calculate the expected rate of the signal events in the detector, and the fractional
20 uncertainties used to constrain this rate. The looser constraint coming from the
21 SSM will be used for comparison.

22 To calculate the number of electrons within the liquid scintillator, we follow
23 the method used in [79], which uses the formula:

$$\text{24} \quad n_e = \frac{(f_{\text{LAB}} n_{\text{LAB}} + f_{\text{PPO}} n_{\text{PPO}}) N_A M_{\text{LAB}}}{m}. \quad (6.6)$$

Here, f_{LAB} and f_{PPO} are the fraction by weight of the LAB and PPO within the scintillator cocktail, respectively. Because this analysis is done over data taken during the scintillator phase with a PPO concentration of 2.2 g for every litre of LAB, these take values 99.744% and 0.256%, respectively. n_{LAB} and n_{PPO} are the mean number of electrons per molecule of LAB and PPO, respectively. PPO has the chemical formula C₁₅H₁₁NO, leading to $n_{\text{PPO}} = 116$. The LAB used in SNO+ has varying alkyl chain lengths, leading to a varying number of electrons per molecule. This distribution is known to have changed between batches of LAB made by the manufacturer, and is also impacted by the distillation process used during the purification of the LAB before it was put into the AV. At the time of writing, no final molecular breakdown has been made for the LAB within the detector; for now we shall use the breakdown provided here [167], from a representative tanker truck of LAB: there $n_{\text{LAB}} = 131.68$. Finally, $N_A = 6.02 \times 10^{23} \text{ mol}^{-1}$ is Avogadro's Constant, $M_{\text{LAB}} = 780.2 \text{ t}$ is the total mass of scintillator within a sphere of radius the size of the AV, and $m = 235 \text{ g mol}^{-1}$ is the molecular weight of the scintillator. This leads to a value for the number of electron targets:

$$n_e = 2.63 \times 10^{32} \text{ electrons.}$$

We can modify Eq. 6.1 to get an equation for the total rate of solar neutrino events by flavour, before oscillations or analysis cuts are considered:

$$R_i = \Phi_{^8\text{B}} n_e \int S_\nu(E_\nu) \sigma_{\nu_i}(E_\nu) dE_\nu. \quad (6.7)$$

Note that for $i = \mu, \tau$, this rate corresponds to the interaction rate if 100% of the neutrinos have flavour $\nu_{\mu, \tau}$.

Using the cross-section formula from Eq. 1.4, the ${}^8\text{B}$ spectral shape from [29], and $\Phi_{^8\text{B}} = 5.46 \times 10^6 \text{ cm}^{-2} \text{ s}^{-1}$ ($5.16 \times 10^6 \text{ cm}^{-2} \text{ s}^{-1}$), we expect a rate before

¹ considering oscillations or cuts of:

$$\text{2} \quad R_i = \begin{cases} 2743.2(2592.5) \text{ events/yr} & \text{for } i = e, \\ 489.7(462.8) \text{ events/yr} & \text{for } i = \mu, \tau. \end{cases}$$

³ In the above rates, we have included an additional volume correction factor of
⁴ 1.0139, because in MC events are simulated within the neck of the AV in addition
⁵ to the main spherical bulk [168].

⁶ Internal Uranium- and Thorium-Chain Backgrounds

⁷ As mentioned in Section 6.1.2, $^{214}\text{Bi-Po}$ and $^{212}\text{Bi-Po}$ decays, coming from the
⁸ ^{238}U and ^{232}Th decay chains respectively, are capable of generating distinctive
⁹ delayed coincidence events. Rafael Hunt-Stokes was able to use a series of cuts
¹⁰ to isolate both types of coincidence signals [155], looking at coincidence signals
¹¹ within the same 5.0 m FV as my analysis. After correcting for his cut efficiencies,
¹² he obtained a derived rate in the whole detector of [169]:

$$\text{13} \quad \text{BiPo rate} = \begin{cases} 0.94 \text{ events/hour} & \text{for } ^{212}\text{Bi-Po}, \\ 6.06 \text{ events/hour} & \text{for } ^{214}\text{Bi-Po}. \end{cases}$$

¹⁴ These rates assume a uniform concentration of ^{222}Rn and ^{220}Rn throughout the
¹⁵ detector: this is how internal backgrounds are simulated by default in RAT. However,
¹⁶ it has been shown that this is not at all the case within SNO+; radon ingress
¹⁷ from the AV neck propagates through the bulk of the detector via convection
¹⁸ currents induced by the thermal gradient present throughout the detector [170].
¹⁹ This radon ingress also breaks the secular equilibrium of the two decay chains, so
²⁰ that one can no longer make straightforward predictions about rates for decays in
²¹ the chains above radon. Fortunately for this analysis, Table 6.3 showed that the

cut efficiencies for ^{228}Ac and ^{234m}Pa decays, both in their respective decay chain above radon, are negligible. This means that even if their decay rates were much greater than what would be predicted from the tagged BiPo rates, a negligible number of events are expected for both in the livetime of the dataset considered in this analysis.

The combination of broad coincidence tagging as well as using an in-window BiPo classifier cut ensures that the expected rate of BiPo events that survive all the cuts is 1.5 and 2.5 for $^{212}\text{Bi}-\text{Po}$ and $^{214}\text{Bi}-\text{Po}$, respectively. Because the branching ratio of $^{212}\text{Bi} \rightarrow ^{208}\text{Tl}$ is 36%, and the branching ratio of $^{214}\text{Bi} \rightarrow ^{210}\text{Tl}$ is 0.021% [171, 172], after considering the cut efficiencies in this analysis we expect 512.4 internal ^{208}Tl and 1.1 internal ^{210}Tl events.

In theory, the non-uniformity of all the radon-induced backgrounds could impact the results of the oscillation analysis. However, the rates of each after cuts have been applied mean that only the internal ^{208}Tl could plausibly have any effect. For this particular background, each slice of the binned PDF in r_3 was allowed to float independently, with no constraints. The other three related backgrounds considered in the fit (^{210}Tl , $^{212}\text{Bi}-\text{Po}$, and $^{214}\text{Bi}-\text{Po}$) did not have this splitting applied to them. A loose 25% constraint on each of these three processes' rates was applied, to account for the current uncertainty in the calculation of R. Hunt-Stokes' tagging efficiency.

(α, n) Reactions

As discussed in Section 6.1.2, (α, n) reactions are induced by α -particles generated in the detector. In the SNO+ scintillator phase, the dominant source of α -particles are decays of ^{210}Po located both within the scintillator and on the AV surfaces. Because of substantial quenching by the scintillator, the reconstructed energy of the ^{210}Po α events fall substantially below E_{\min} . The rate of the internal and

¹ surface ^{210}Po events have been tracked throughout the scintillator phase by Serena
² Riccetto and Shengzhao Yu, respectively.

³ Within the 5 m FV, S. Riccetto measured a total of 1.60×10^8 ^{210}Po events
⁴ over the runs considered for this analysis [173, 174]. Assuming the internal rate of
⁵ these events are uniform throughout the scintillator, this leads to a total rate of
⁶ 2.78×10^8 events for all the scintillator. After using a conversion rate of 6×10^{-8}
⁷ neutrons generated per α on ^{13}C in liquid scintillator [90, 175], we can derive an
⁸ expected number of internal (α, n) events before cuts to be 17. However, because
⁹ a coincidence cut is used in this analysis, the vast majority of these should be
¹⁰ removed, leading to merely 0.009 events expected after cuts.

¹¹ Similarly, S. Yu measured the surface ^{210}Po rate to vary between $2\text{--}5 \text{Bq m}^{-2}$
¹² over the time period of this analysis as well as a function of height in the detec-
¹³ tor [176]. Using the midpoint value of 3.5Bq m^{-2} , one can derive an expected
¹⁴ rate of 554.4 surface (α, n) events occurring over the dataset's livetime, before
¹⁵ cuts. Once again, the coincidence cut as well as the FV cut removes the vast
¹⁶ majority of these events, so that only 0.07 events are expected after all cuts have
¹⁷ been applied. Because both classes of (α, n) events have negligible expected rates
¹⁸ in our dataset, they were not included within the MCMC fit.

¹⁹ External Backgrounds

²⁰ During the water phase of SNO+, an analysis of the rates of the external back-
²¹ grounds was performed by Tony Zummo [177]. The results of this analysis are
²² shown in Table 6.4, giving the measured rates as a fraction of the nominal values
²³ given in [158]. Although the statistical uncertainty for these measurements were
²⁴ quite small, the total systematic uncertainty was substantial because T. Zummo's
²⁵ analysis involved looking at events in the tail of energy distributions, so that any
²⁶ uncertainty in the energy scale systematic had an outsized impact on the number
²⁷ of events observed within that energy window. These measured rates and their

| Background Type | Rate (Fraction of Nominal) |
|-----------------|----------------------------------|
| AV & Ropes | $0.21 \pm 0.009^{+0.64}_{-0.21}$ |
| External Water | $0.44 \pm 0.003^{+0.32}_{-0.27}$ |
| PMTs | $1.48 \pm 0.002^{+1.65}_{-0.60}$ |

Table 6.4: Measured rates of the external backgrounds during the water phase of SNO+, by Tony Zummo [177].

systematic uncertainties were used to predict the expected rate and constrain the external backgrounds in this scintillator phase solar analysis. For the AV, ropes, and PMTs, this seems reasonable as we do not expect there to be any substantial change in these backgrounds between the phases. The exception to this is the external water, where various aspects of the water purification process over the years since T. Zummo’s analysis dataset was taken [178]. Because of this, the water phase measured rate was used as a starting point for the fit, but no constraint was applied.

Before the expected number of triggered events can be calculated for each external background process, two subtleties must be dealt with. Firstly, MC production of the externals did not include the hold-up ropes at the time of performing the analysis. This is not a major problem, because the hold-up ropes are of substantially lower mass than the hold-down ropes, and also their average radius from the centre of the detector is much larger. This means that the expected rate of events from the hold-up ropes that manage to reconstruct inside the FV should be sub-dominant to their hold-down counterparts. For the purposes of this thesis, the combined rate for both kinds of ropes were calculated, with the overall cut efficiency and derived PDFs coming from just the hold-down ropes.

Secondly, because the attenuation length of a 2.6 MeV γ particle is 23 cm in water [179, 180], the vast majority of external backgrounds which start from a substantial distance away from the AV do not generate γ s that make it into the scintillator. As a result, an enormous amount of computational resources could be wasted on simulating events that never get into the ROI. To work around this,

| MC process | Expected # Events Pre-Cuts | Overall Cut Efficiency (%) | Expected # Events Post-Cuts | Con- straint (%) |
|----------------------------------|-------------------------------|-------------------------------|--------------------------------|---------------------|
| $^8\text{B } \nu_e$ | 572.58 | 32.8 | 187.94 | +2.5% -1.7% |
| $^8\text{B } \nu_{\mu,\tau}$ | 102.22 | 30.2 | 30.86 | +2.5% -1.7% |
| AV ^{214}Bi | 594,000 | 0.000468 | 2.78 | +304.8% -100% |
| Ropes ^{214}Bi | 140,000 | 0.000327 | 0.46 | +304.8% -100% |
| AV ^{208}Tl | 69,600 | 0.0361 | 25.14 | +304.8% -100% |
| Ropes ^{208}Tl | 79,900 | 0.0394 | 31.48 | +304.8% -100% |
| External Water ^{214}Bi | 4,490,000 | 0.0000763 | 3.42 | — |
| External Water ^{208}Tl | 190,000 | 0.00761 | 14.46 | — |
| PMT $\beta - \gamma$ | 16,800 | 0.333 | 56.12 | +111.5% -40.5% |
| Internal $^{212}\text{Bi-Po}$ | 1814 | 0.0848 | 1.54 | $\pm 25\%$ |
| Internal ^{208}Tl | 1021 | 50.2 | 512.39 | — |
| Internal $^{214}\text{Bi-Po}$ | 11,728 | 0.0211 | 2.47 | $\pm 25\%$ |
| Internal ^{210}Tl | 2.5 | 42.0 | 1.05 | $\pm 25\%$ |
| Surface (α, n) (combined) | 554.4 | 0.00458 | 0.07 | — |
| Internal (α, n) | 17.0 | 0.0537 | 0.009 | — |
| Internal ^{228}Ac | 2835 | 0 | 0 | — |
| Internal ^{234m}Pa | 11,726 | 0.0000059 | 0.0007 | — |

Table 6.5: Number of events expected both before and after cuts have been applied, along with any constraints. As in Table 6.3, processes have been split into broad categories, with the last one being processes which have negligible rates after cuts. These processes are not included within the analysis fit.

¹ PMT $\beta - \gamma$ events are modelled as 2.6 MeV γ s generated at a radius of 6.2 m (just
² outside the AV), pointing radially inwards. Making some basic assumptions about
³ these events, one can derive the expected survival rate of these γ particles as a
⁴ function of radius [180, 181], which leads to a correction factor of 1.17×10^{-6} .

⁵ Similarly, simulations of background events in the external water and ropes are
⁶ restricted from starting beyond certain maximum radii depending on the specific
⁷ process, such that there remains a negligible impact on the fraction of simulated
⁸ events that actually deposit any energy into the scintillator. This leads to rate
⁹ correction factors of 0.35 and 0.50 for external water ^{214}Bi and ^{208}Tl events, as
¹⁰ well as 0.50 and 0.35 for hold-down and hold-up ropes [182].

6.2.4 Systematics

There are a number of systematic effects in the analysis that could possibly have some impact on the resulting posterior densities of θ_{12} and Δm_{21}^2 . Consideration of these effects is important to ensure that the uncertainty in the measurement is not underestimated. However, we shall find in Section 6.3 that for this dataset, the analysis is statistically-limited, and so it is not necessary to perform exhaustive measurements to determine the contribution of all possible systematic contributions. Instead, the focus shall be on the subset of the systematics that can plausibly have the most impact on the final measurement.

In this analysis, the measurement of the oscillation parameters is based on the fitted shape and normalisation of the ${}^8\text{B}$ signal energy spectrum. Therefore, for a systematic effect to have an impact on the final measurement it must first impact the fit of the signal PDF. One straightforward way this could occur is for some background events to be misattributed as signal events within the fit (or vice versa). If the rates of signal and background processes are strongly constrained to incorrect values, then this could easily happen. This could be a result of either getting the rate pre-cuts or the cut efficiencies incorrect. In this analysis, the strongest constraint on the rate of events comes from the global fit constraint of $\Phi_{{}^8\text{B}}$. Because of this, the fit will also be run with the looser SSM constraint on the signal flux as a means of comparison.

Another class of systematic effects that can plausibly have a substantial impact come from the mismodelling of the detector response, particularly on the reconstructed energy and radius, as they are the observables used within the fit. The most important of these for this analysis is a global mismodelling of the energy calibration by some linear factor known as the energy scale, α : $E_{\text{reco}} \rightarrow \alpha E_{\text{reco}}$.

Because of this importance, it is worthwhile constraining this α parameter. This can be done by comparing the reconstructed energy distributions of ${}^{214}\text{BiPo}$

¹ events tagged by R. Hunt-Stokes [169] in the dataset to the equivalent production
² MC, in the same 5 m FV. For a given α , the energies of the tagged ^{214}Bi in MC
³ were scaled by α , and then compared to the equivalent (unscaled) distribution in
⁴ data, via a log-likelihood ratio \mathcal{L}_{Bi} :

$$\mathcal{L}_{\text{Bi}} = \sum_{i=1}^{N_{\text{bins}}} n_i^{\text{data}} \ln \frac{n_i^{\text{MC}}}{N_{\text{MC}}}. \quad (6.8)$$

⁶ Here, n_i^{data} and n_i^{MC} are the number of events for data and (scaled) MC in energy
⁷ bin i , with N_{bins} being the total number of bins and N_{MC} being the total number of
⁸ tagged events in MC. To account for the edge effects discussed in Section 6.1.7, the
⁹ first and last bins in energy were used as buffers and not considered in calculation
¹⁰ of \mathcal{L}_{Bi} .

¹¹ Values of α were scanned over, generating a log-likelihood distribution. In
¹² the usual way, a constraint on α was obtained by obtaining the energy scaling
¹³ factor which maximises the log-likelihood, followed by looking for the α values
¹⁴ with values of \mathcal{L}_{Bi} less than the maximum by 1/2. The constraint was found to
¹⁵ be $\alpha = 0.9969 \pm 0.0022$, with the data and scaled MC at the best fit value of α
¹⁶ shown in Fig. 6.12.

¹⁷ To handle energy scaling as a systematic in this analysis, we allow the energy
¹⁸ scale to be floated within the MCMC fit, with the constraint given above. The
¹⁹ first and last energy bin of the MCMC fit were used as buffer bins to let this
²⁰ floating occur; this allows for the energy scale to float in the range $\frac{13}{14} \leq \alpha \leq \frac{2.6}{2.5}$.

²¹ In addition to a global energy scaling, it is possible that the resolution of the
²² energy reconstruction could be systematically off. Because of the effects discussed
²³ in Section 6.1.1, changes to the oscillation parameters only impact the observed
²⁴ signal distribution over a broad range of energies. This means that mismodelling
²⁵ the energy resolution of the detector is only liable to have an impact on the
²⁶ measurement if that mismodelling is substantial. However, by looking again at

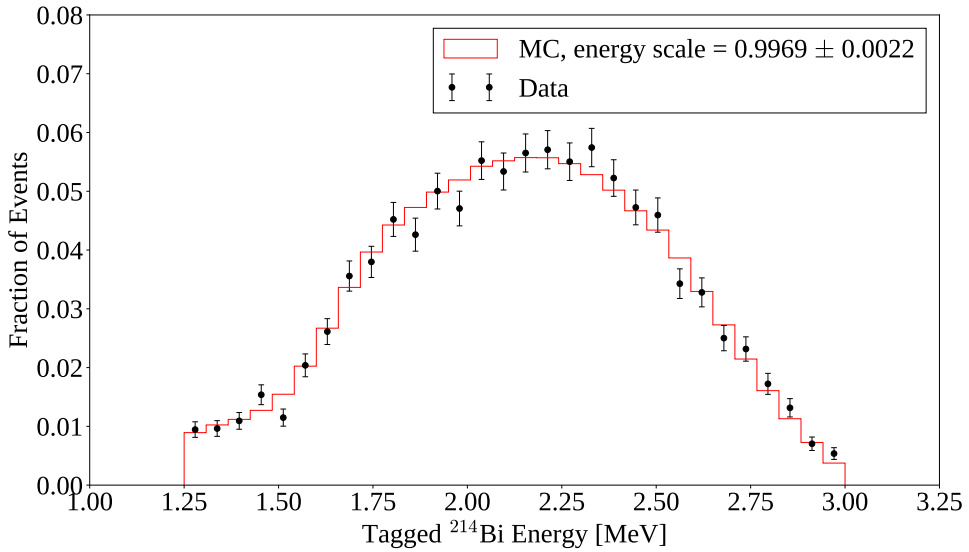


Fig. 6.12: Comparison of tagged ^{214}Bi reconstructed energy distributions between data and MC, after MC has been scaled by the best-fit factor $\alpha = 0.9969$.

Fig. 6.12 we see that there appears to be a good qualitative match of the energy resolution between data and MC for the tagged ^{214}Bi events. As a result, the systematic effect of additional energy smearing will not be considered in this thesis.

Similar to the systematics in reconstructed energy, there are also systematics possible in reconstructed position. These can be decomposed into three kinds of systematic: radial scaling, radial resolution, and position bias along each coordinate axis. The dominant effect that these systematics will have on the PDFs is to change their normalisations. Because we are floating all normalisations within the MCMC fit, and the normalisation constraints of almost all PDFs are relative large, we expect the impact of these systematics to be sub-dominant.

Finally, there can also be mismodelling of the radial distributions for given processes in MC compared to data. For example, it is known that the internal ^{208}Tl events are non-uniform as a function of radius; this is why the normalisation of each radial slice for this background is floated independently. The external backgrounds can also plausibly have PDF shape systematics, especially if the

1 assumptions made to model them (such as the use of simulation shells) are not
2 fully accurate. These shape systematics can also arise from the lack of statistics
3 in the PDFs used to model them: as an example, Table 6.3 shows that only
4 62 external water ^{214}Bi events are used in the creation of the associated PDF.
5 Handling this type of modelling uncertainties for the external backgrounds is not
6 considered in this thesis.

7 6.2.5 Results

8 Fit Validation

9 In theory, the convergence of the sampled distribution within an MCMC fit to
10 the posterior density distribution is guaranteed to eventually occur, regardless of
11 the specific shape of the multivariate Gaussian proposal distribution. However,
12 the speed of this convergence is highly dependent on the widths of the proposal
13 distribution. This is very important as in practice we can only run the MCMC fit
14 for a finite amount of time. For a given parameter within the fit, if the associated
15 width (also known as the step size) in the proposal distribution is too large, then
16 the vast majority of proposals will be to points in the parameter space where
17 the log-likelihood is less than before, and so these proposals will be consistently
18 rejected. Alternatively, if the width is chosen too small, the acceptance rate of
19 the chain will be very high, but too much time will be spent for the chain to go
20 from sampling one point in the space to another.

21 By choosing sensible width parameters for the proposal distribution, as well
22 as running the chain for as long as possible, one can attempt to maximise the
23 “effective sample size” of the MCMC fit. It has been shown that, for a wide variety
24 of situations, an appropriate size for the width of a given parameter is the standard
25 deviation of the true posterior density distribution [183]. Because knowing this
26 posterior density distribution is precisely the aim of the whole MCMC procedure,

this can make choosing these widths challenging in practice. In this analysis, an iterative approach was used: an MCMC fit was first run using width parameters that were guessed. Once this fit completed, the resulting sampled distribution marginalised onto each fit parameter were looked at to find approximately the magnitude of their standard deviations. This then informed the widths chosen for the next MCMC fit. This process was repeated until the autocorrelation of the sampled distribution for each fit parameter appeared to be minimal; this is an indication that the effective sample size has been maximised. A chain length of 1,000,000 steps was found to be sufficient to obtain large enough effective sample sizes for this analysis.

In order to guard against the possibility of a given chain missing some important part of the parameter space because of its starting position, 100 chains were run simultaneously. The initial positions of each in the parameter space were chosen randomly according to the overall prior distribution. Fig. 6.13 shows the sampled values for four different parameters in a given chain, after the tuning of the width parameters had been completed.

Given some initial start point in the parameter space, a given chain will typically take some time in finding where the region of greatest likelihood is. This leads to an initial set of steps where the chain moves a large distance in the parameter space in the same direction, so that the autocorrelation of the chain in this period is substantial. These initial samples are not representative of the actual posterior density distribution: as a result, in this analysis the first 100,000 steps of each chain were declared as a “burn-in” period. This number of steps for the burn-in was motivated in part by looking at auto-correlation plots for the MCMC chains, as seen in Fig. 6.14. By the time the number of steps differed by 100,000, the autocorrelation of parameters and the log-likelihood itself of each chain was at zero, indicating the likelihood evaluations in the chains were independent when they differed by at least 100,000 steps. The overall set

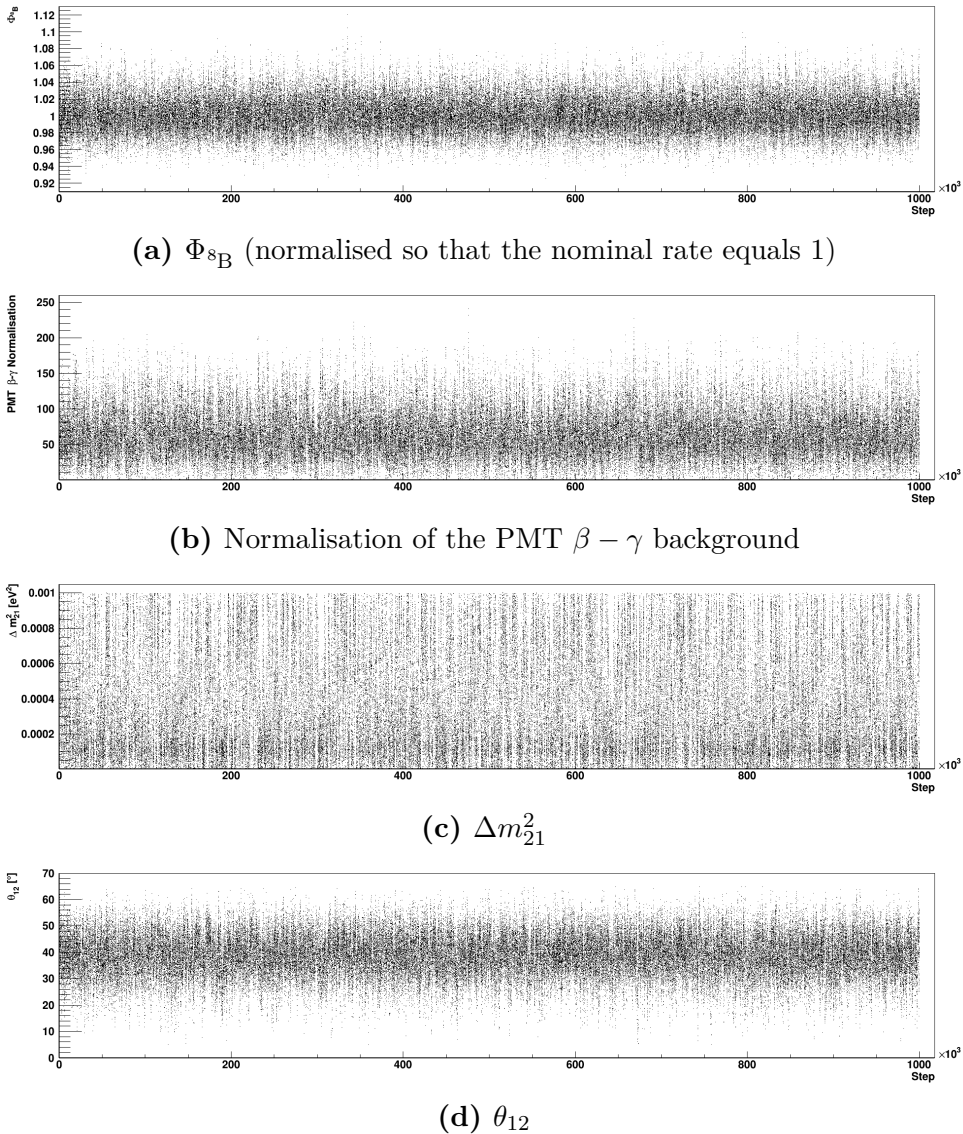


Fig. 6.13: Examples of the sampled values for parameters within a given MCMC chain as a function of the step number, after tuning the proposal distribution width parameters.

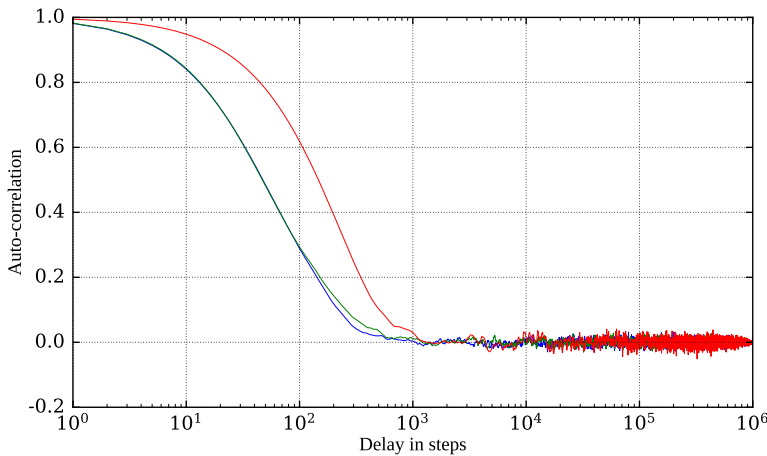


Fig. 6.14: Plot showing the auto-correlation as a function of step delay for three variables in a typical chain: log-likelihood (blue), Δm_{21}^2 (red), and θ_{12} (green).

of samples used to approximate the posterior density distribution corresponds to
1 collection of all sampled points on all the chains, after burn-in.
2

Oscillation Fit Results

Now that there is confidence in the convergence of the MCMC fit to the posterior
4 density distribution, we can look at this distribution to obtain the results of this
5 analysis. Fig. 6.15 shows the posterior density distribution, marginalised onto
6 each parameter of the fit other than the two oscillation parameters. We can see
7 that each marginalised distribution appears smooth, another qualitative indication
8 of a sufficient effective sample size in the MCMC fit. For each 1D distribution,
9 the bin centre associated with the HPD has been indicated, and the vertical band
10 indicates the Bayesian 1σ CI for that parameter. Also shown in these plots is the
11 prior distribution for each of the parameters, for comparison.
12

For a number of the parameters, the posterior distributions are more strongly
13 peaked than their associated priors. This indicates that there was enough infor-
14 mation in the dataset further constrain those parameters. One such parameter
15 is the rate of the external water ^{214}Bi . The resulting measurement of this is
16 $34.1^{+18.5}_{-18.9}$ events in the dataset. This is 10 times larger than the expected rate
17

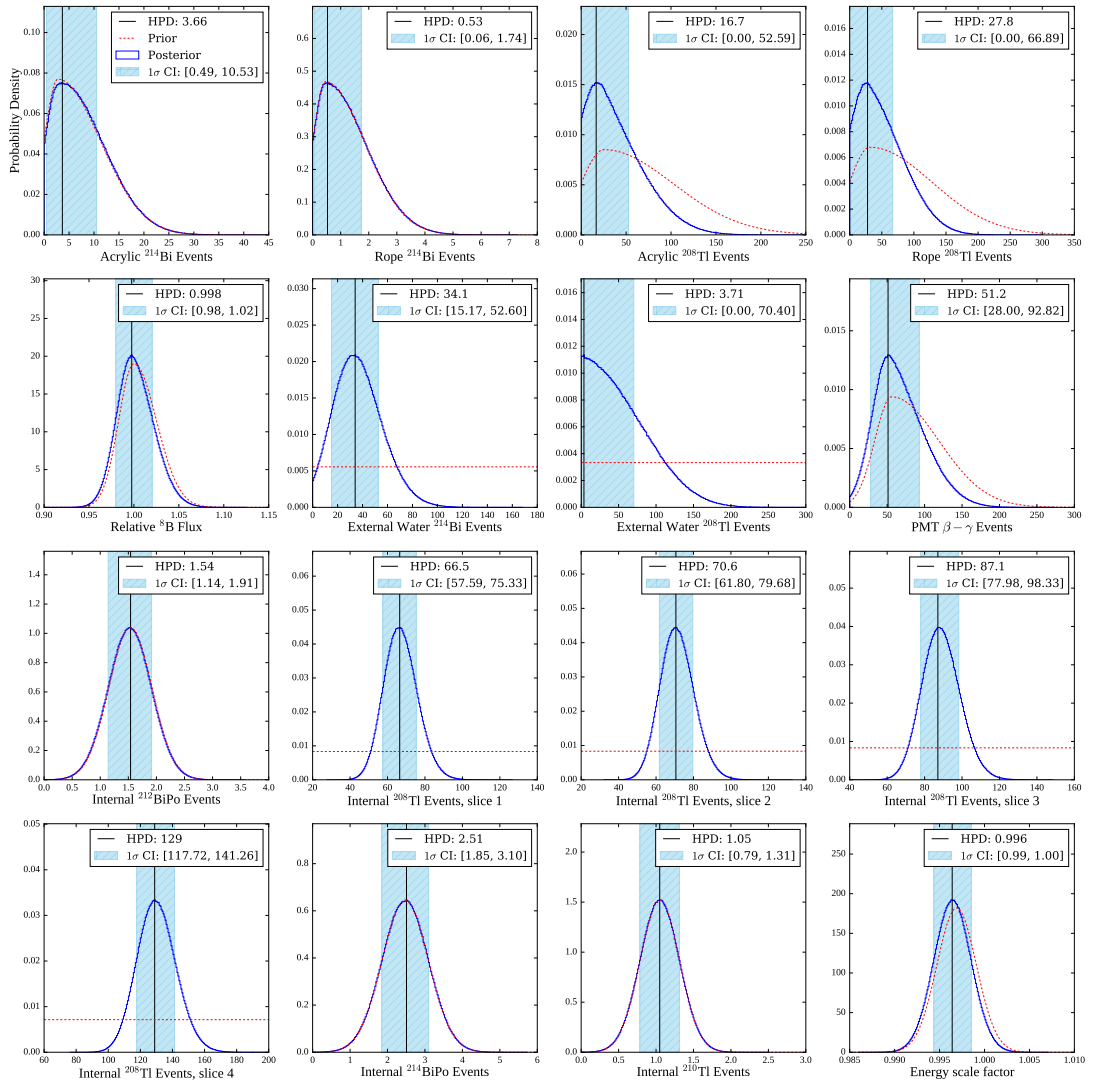


Fig. 6.15: Marginalised 1D posterior density distributions for all non-oscillation parameters, shown in blue. The HPD and 1σ Bayesian CI are shown for each parameter. Also shown in dashed red are the associated prior distributions.

shown in Table 6.5, providing good evidence for a change in the level of this particular background relative to the water phase. In contrast, all other external backgrounds have HPDs consistent with their prior expected values.

Another set of parameters that have been well-constrained in the fit are the normalisations of each of the internal ^{208}Tl slices. As expected, slices corresponding to larger radii have a greater fitted rate, with the number of events measured in the outermost radial slice to be twice that of the innermost one. However, the posteriors of the other internal ^{238}U - and ^{232}Th -chain are the same as their priors, indicating there was no evidence from data within the fit to constrain those processes any further. Similarly, the posteriors of the energy scale parameter and Φ_{sB} only show very mild differences with their strong priors.

If instead of looking only at the 1D marginalised distributions of each parameter we look at the equivalent 2D distributions for every combination of parameters, we can generate a table of correlation coefficients. This is shown in Fig. 6.16. From this, we can see that there is some clear anti-correlation between a number of the external backgrounds. This seems intuitive: the PDFs for many of these external backgrounds are similar, and so the fit struggles to distinguish between them.

The only other pair of parameters which have a substantial correlation between one another are the two oscillation parameters. Fig. 6.17 shows their 2D marginalised posterior distribution, along with contours for a number of Bayesian CIs. Because the priors on both oscillation parameters are uniform, this can be directly converted into the log-likelihood ratio $\ln L_R$ for a given bin, where $L_R = p/p_{max}$: p is the posterior density of a given bin in the 2D space, and p_{max} is the posterior density of the HPD bin, equivalent to the bin with the maximum likelihood. This allows for Frequentist CI to be derived as well. For this plot, the HPD is at $\theta_{12} = 34.1^\circ$, $\Delta m_{21}^2 = 1.80 \times 10^{-5} \text{ eV}^2$.

As can be seen from this plot, the fit has been able to successfully constrain θ_{12} to some success. However, beyond a value of $5 \times 10^{-4} \text{ eV}^2$, the posterior density

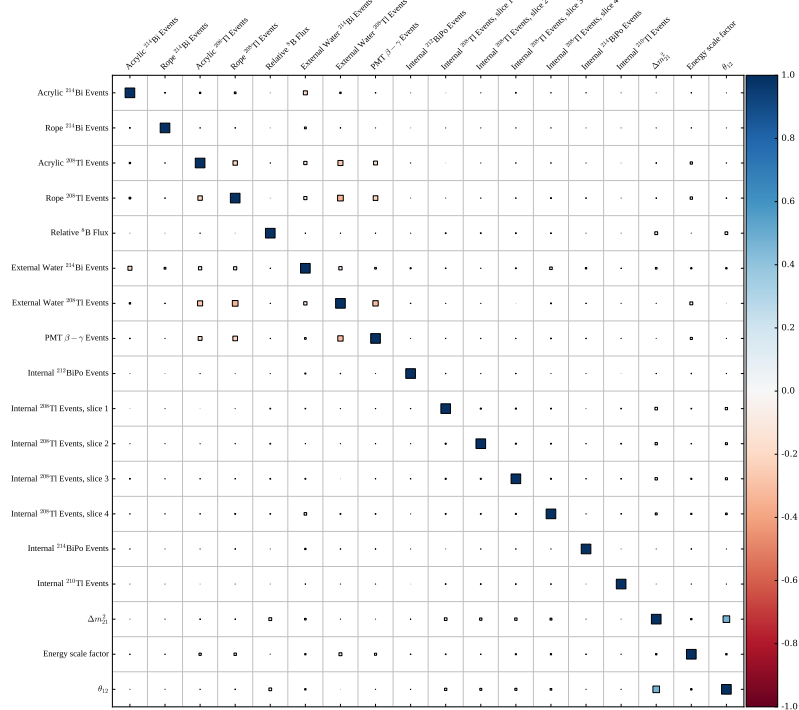


Fig. 6.16: Correlation matrix between all parameters in the MCMC fit.

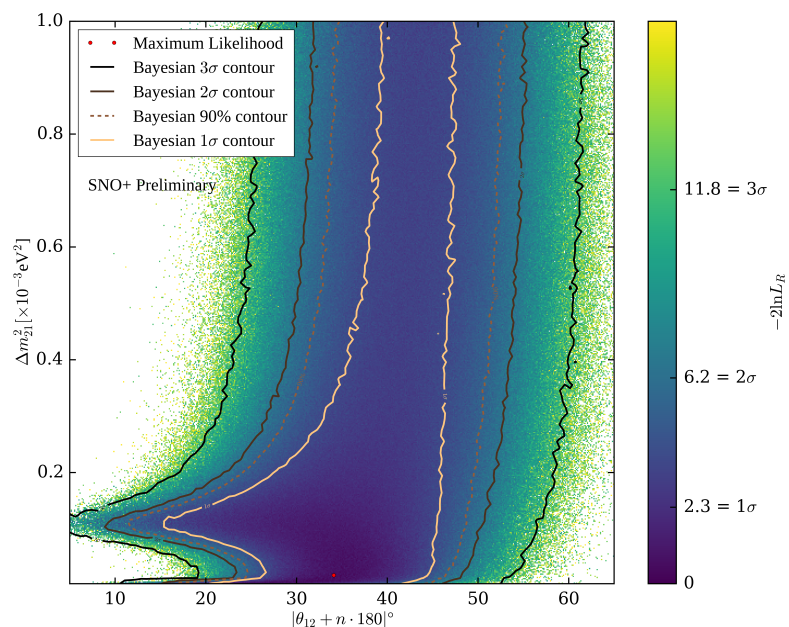


Fig. 6.17: 2D posterior density distribution marginalised onto Δm_{21}^2 and θ_{12} . The colour axis shows $-2 \ln L_R$, proportional to the natural logarithm of the posterior density, with labels corresponding to the values associated with the $N\sigma$ Frequentist CIs. Also shown, in shades of brown, are the Bayesian CIs.

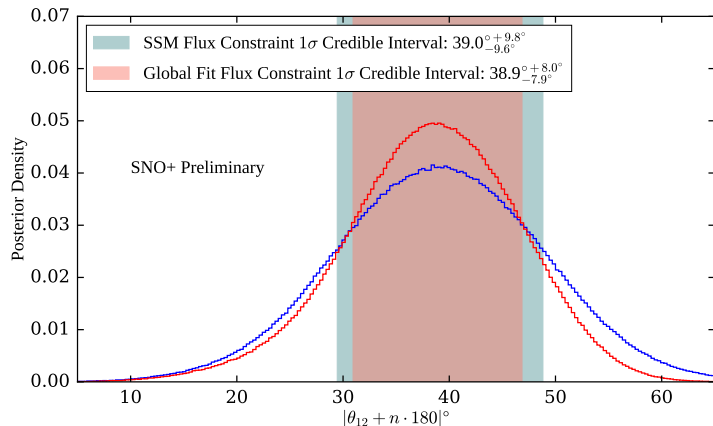


Fig. 6.18: Comparison of 1D posterior density distributions marginalised onto θ_{12} , using both forms of ${}^8\text{B}$ flux constraint. The 1σ Bayesian CI are shown for both.

appears flat as a function of Δm_{21}^2 . This implies that this dataset provides little ability to reject the possibility of large values of Δm_{21}^2 .

Given this lack of constraining power on Δm_{21}^2 , it is reasonable to only obtain a measurement for θ_{12} . The result of marginalising over Δm_{21}^2 to obtain the 1D posterior distribution in θ_{12} is shown in Fig. 6.18. From this, we can obtain a measurement of:

$$|\theta_{12} + n \cdot 180|^\circ = 38.9^\circ_{-7.9^\circ}.$$

Here, the HPD has been estimated by fitting a quadratic function to the peak of the posterior distribution, and the uncertainties by obtaining the Bayesian 1σ CI. For comparison, the NuFit 5.1 global fit results have [60]:

$$|\theta_{12} + n \cdot 180|^\circ = 33.44^\circ_{-0.74^\circ}.$$

As can be seen, the measurement made in this thesis is consistent with the global fit value, although with a substantially larger uncertainty. This is not surprising, given the limited statistics of the 80.6 days of data used.

The fact that the measured value of θ_{12} is somewhat above the global fit value also has a reasonable explanation. Looking back at Fig. 6.17, we find that the

1 preferred values of θ_{12} for large Δm_{21}^2 are somewhat greater on average than for
 2 Δm_{21}^2 values close to the global fit value of 7.4×10^{-5} eV². As a result, the final
 3 value quoted for θ_{12} is dependent on our choice of the prior distribution for Δm_{21}^2 :
 4 this is an inevitable result of using a Bayesian framework for this analysis. We
 5 can see the impact of choosing a less conservative prior for Δm_{21}^2 by ignoring all
 6 sampled points with $\Delta m_{21}^2 \geq 5 \times 10^{-4}$ eV², say. The resulting measurement of θ_{12}
 7 becomes:

8 $|\theta_{12} + n \cdot 180|^\circ = 36.4^\circ_{-7.8^\circ}{}^{+8.0^\circ}.$

9 Although there is negligible change to the uncertainty of the measurement, this
 10 change in prior shifts the HPD value down by 2.5° , in the direction of the global
 11 fit value.

12 Also shown in Fig. 6.17 is the posterior density for θ_{12} if the looser SSM flux
 13 constraint is used. Under these conditions, the measurement becomes:

14 $|\theta_{12} + n \cdot 180|^\circ = 39.0^\circ_{-9.6^\circ}{}^{+9.8^\circ}.$

15 Using this constraint has little impact on the HPD value, but does increase
 16 the uncertainty by $\sim 1.8^\circ$. This gives an indication of the extent to which the
 17 strong global flux constraint allows θ_{12} to be constrained on its own, without any
 18 information from the dataset.

19 One could naïvely expect that the point in parameter space where each fit
 20 parameter corresponds to the HPD value obtained in the above 1D marginalisation
 21 would correspond to the maximum likelihood. This is not the case, because of
 22 the correlations between parameters in the fit. Because an MCMC fit does not
 23 actually attempt to directly find this maximum likelihood point, deciding on the
 24 overall ‘best-fit’ point in parameter space is a little ambiguous. For this analysis,
 25 the sampled point in all of the chains which had the greatest log-likelihood

| Fit Parameter | 1D HPD value | Maximum likelihood value |
|---|--------------|--------------------------|
| Relative ${}^8\text{B}$ flux | 0.9975 | 1.006 |
| $\Delta m_{21}^2 [\times 10^{-5} \text{ eV}^2]$ | 11.02 | 5.50 |
| $\theta_{12} [^\circ]$ | 39.05 | 33.73 |
| AV ${}^{214}\text{Bi}$ Events | 3.66 | 8.49 |
| Ropes ${}^{214}\text{Bi}$ Events | 0.53 | 0.52 |
| AV ${}^{208}\text{Tl}$ Events | 16.71 | 19.08 |
| Ropes ${}^{208}\text{Tl}$ Events | 27.81 | 31.20 |
| External Water ${}^{214}\text{Bi}$ Events | 34.09 | 45.93 |
| External Water ${}^{208}\text{Tl}$ Events | 3.71 | 88.03 |
| PMT $\beta - \gamma$ Events | 51.22 | 46.88 |
| Internal ${}^{212}\text{BiPo}$ Events | 1.54 | 1.45 |
| Internal ${}^{208}\text{Tl}$ Events, Slice 1 | 66.52 | 68.78 |
| Internal ${}^{208}\text{Tl}$ Events, Slice 2 | 70.60 | 66.62 |
| Internal ${}^{208}\text{Tl}$ Events, Slice 3 | 87.09 | 87.33 |
| Internal ${}^{208}\text{Tl}$ Events, Slice 4 | 128.92 | 125.25 |
| Internal ${}^{214}\text{BiPo}$ Events | 2.51 | 2.56 |
| Internal ${}^{210}\text{Tl}$ Events | 1.05 | 1.00 |
| Energy Scale Factor, α | 0.9964 | 0.9970 |

Table 6.6: Comparison of the fit parameter values obtained when getting the HPD values after marginalising onto each parameter, versus looking at the sampled point with the maximal likelihood found.

was declared as the best-fit point. A comparison between the parameter values obtained at the HPD of the 1D marginalisations to the maximum likelihood point is shown in Table 6.6.

Using the maximal likelihood fit parameters, the comparison of data to MC is shown in Fig. 6.19. We see that the ${}^8\text{B}$ signal distribution only dominates above 5 MeV, as well as at low energies for the first two radial slices. This is because for larger radii, external backgrounds become the dominant processes in the 2.5–2.8 MeV region. Between 3–5 MeV, at all radii the internal ${}^{208}\text{Tl}$ shows a clear peak well above the ${}^8\text{B}$ signal. Qualitatively, the MC appears to give a good fit to the data.

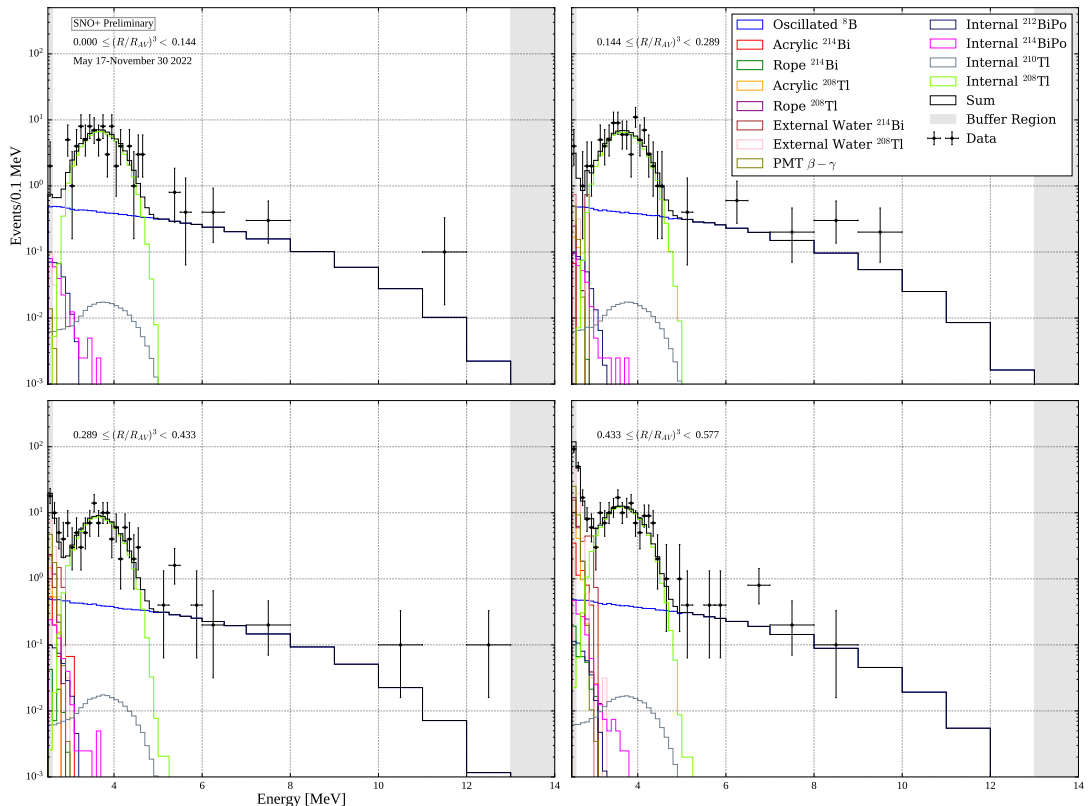


Fig. 6.19: Comparison of data to MC for each radial slice, using the best-fit parameter values derived from the MCMC results. The buffer bins used for varying the energy scale parameter within the fit are shown in grey.

6.3 Sensitivity Projections

Given the limited statistics used in the dataset analysed in Section 6.2, the question of how much better we could measure the solar oscillation parameters with more data naturally arises. In particular, it is worthwhile knowing the expected sensitivity of this analysis as a function of livetime, and hence whether SNO+ could eventually make a world-leading measurement of θ_{12} via ${}^8\text{B}$ neutrinos. Furthermore, it is useful to find out to what extent improvements such as additional background reduction could help the measurement.

To perform these sensitivity projections, the same analysis method was employed as with the real dataset. However, for each projection scenario a fake “Asimov” dataset was generated. This was a 2D histogram binned in the same way as the MC PDFs, corresponding to the total expected rate of all signal and background processes. Because the same PDFs were used to build both the MC and fake dataset, the maximum likelihood should occur when the fit parameters are identical to those which generated the fake dataset. Although this method of performing sensitivity projections leads to the slightly odd situation of having non-integer numbers of events in the bins of the fake dataset, it has been shown that this approach allows us to estimate the median sensitivity of a scenario [184].

The assumptions used to make the fake datasets are as follows. To begin with, no cuts were changed between the main analysis and this projection, and the same PDFs were used in both. Furthermore, the ${}^8\text{B}$ rate was determined by the same global fit flux value and neutrino oscillation parameters used in the rest of this analysis. Because some of the dataset used in the main analysis was taken during a time of known elevated ${}^{238}\text{U}$ - and ${}^{232}\text{Th}$ -chain backgrounds, R. Hunt-Stokes provided an additional estimate of the ${}^{214}\text{Bi-Po}$ and ${}^{212}\text{Bi-Po}$ rates in the 5.0 m FV for only the period of the dataset where the internal background levels had stabilised. Those rates went from 6.06 events per hour before excluding

1 the higher background period down to 4.87 events per hour for the ^{214}Bi –Po, and
2 from 0.94 events per hour down to 0.89 events per hour. These relative changes
3 for the two background chains were used to scale the rates from their expectation
4 in the original dataset. For the internal ^{208}Tl , the rate of each slice relative to
5 one another was taken from their fitted HPD values in the original analysis, with
6 the absolute value of those rates scaled by 0.89/0.94.

7 External backgrounds were in general set to the rates expected from T. Zummo,
8 as described in Section 6.2.3. The exceptions were the backgrounds from the
9 external water: for the ^{208}Tl component, the nominal rate without T. Zummo’s
10 correction factor was used. For the ^{214}Bi component, the higher rate as given by
11 the fitted HPD value was used instead. The same constraints on all the rates
12 were used as in the main analysis. For the energy scale parameter, because no
13 additional systematics were applied to the Asimov dataset the true and expected
14 value of α was set to 1, with the same uncertainty of ± 0.0022 as before.

15 Using this baseline set of assumptions, fake datasets were generated and fit
16 over a series of livetime scenarios between 150 days and 5 years. The results of
17 these MCMC fits, in terms of the 2D and 1D posterior densities for the oscillation
18 parameters are shown in Figs. 6.20 and 6.21. Note that the length of burn-in was
19 increased to 250,000 steps for these projections to ensure the convergence of all
20 chains. As can be seen, by ~ 2 years of livetime, there is sufficient evidence to
21 confidently reject large Δm_{21}^2 values above $2 \times 10^{-4} \text{ eV}^2$. This leads to a fairly
22 substantial decrease in uncertainty as well as less bias in the 1D HPD value for
23 θ_{12} . There does remain some bias, however: this is because of the non-Gaussian
24 “boomerang” structure seen in the 2D posterior density plots.

25 The general story told by these projections is that, assuming the same condi-
26 tions and analysis, increasing the livetime of the dataset will lead to a substantial
27 improvement to the precision of the measurement of θ_{12} , as well as the beginnings

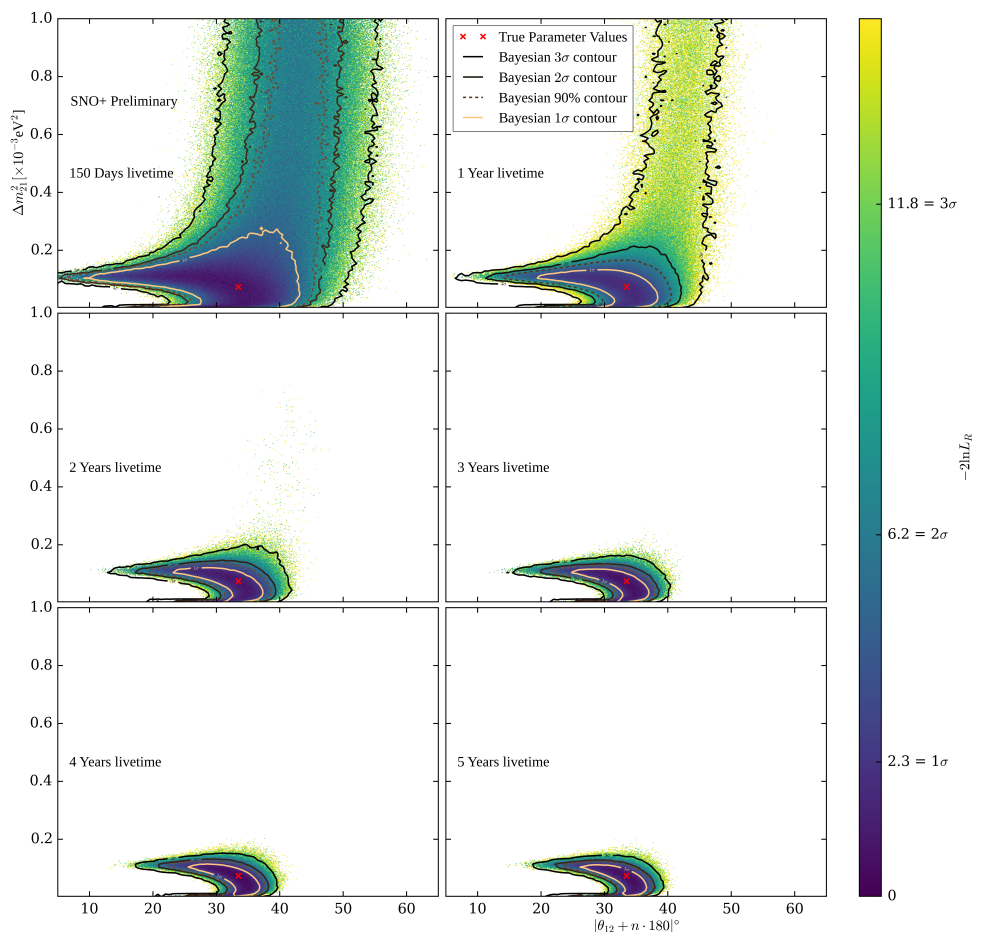


Fig. 6.20: Posterior density distributions marginalised onto the two solar oscillation parameters, for each livetime scenario in the pure scintillator phase under the current backgrounds.

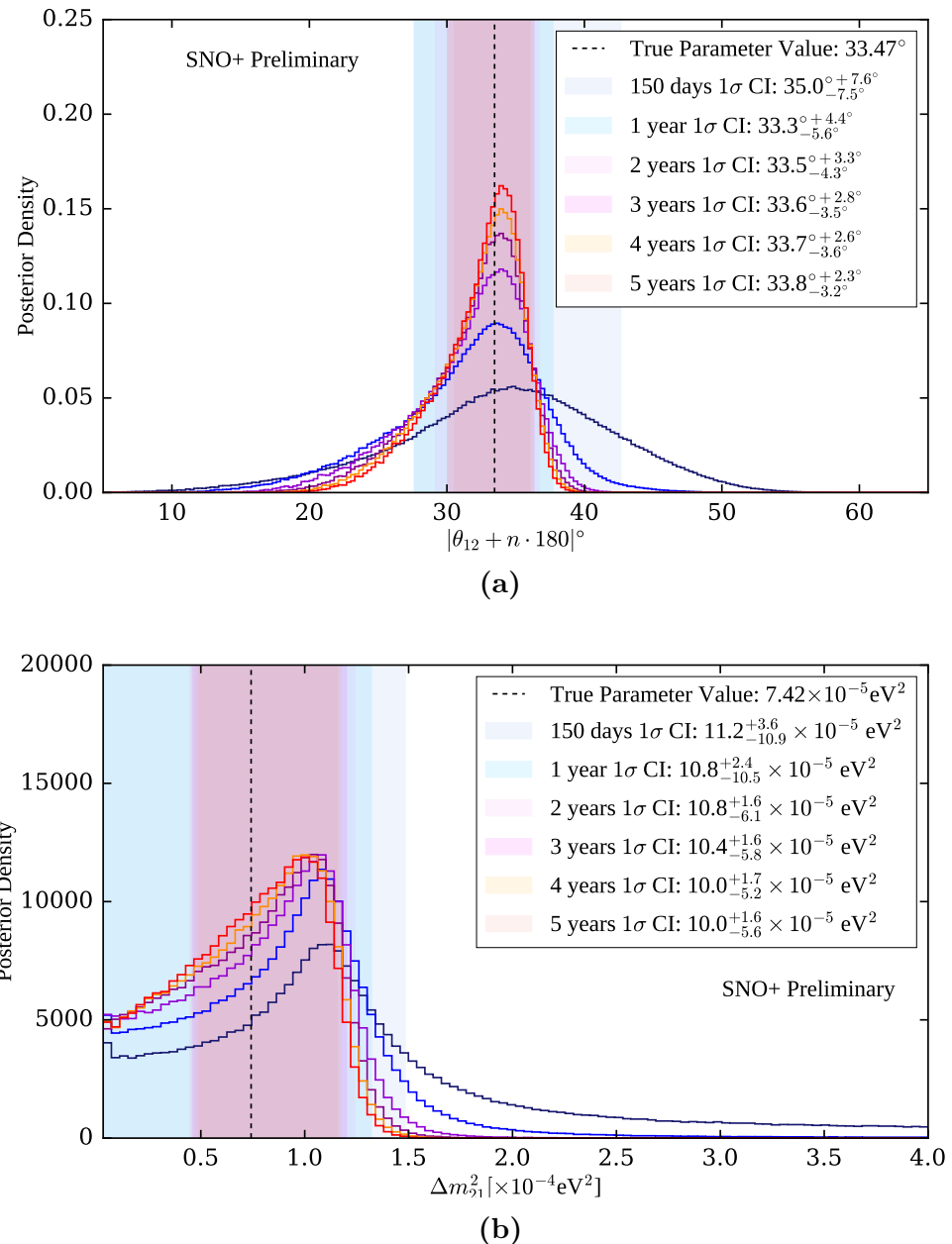


Fig. 6.21: Posterior density distributions marginalised onto each of θ_{12} and Δm^2_{21} , for each livetime scenario in the pure scintillator phase under the current backgrounds.

of a measurement of Δm_{21}^2 . However, after ~ 3 years of livetime the rate of progress slows down somewhat.

The choices of assumptions for this baseline set of projections were deliberately chosen to be fairly conservative. However, they do not account for the loading of BisMSB and TeLS into the detector that is likely to occur in the coming years. For BisMSB, the main impact is expected to be a dramatic increase in the observed light yield in the detector, leading to a smaller energy resolution and hence improved measurement [84]. Once the TeLS is also loaded, the observed light yield will likely decrease back down to levels similar to that of the current LABPPO. One of the biggest expected impact of the Te phase on this analysis will instead be to the background levels within the detector: the target rate of ^{238}U -chain backgrounds in the Te phase is ~ 100 times that of the scintillator phase [158].

Because of this, two further scenarios were considered over a period of 1 year of livetime. In one, the internal ^{238}U - and ^{232}Th -chain backgrounds were raised to the nominal level expected during the Te-loaded phase [135]. Unique to the Te phase will be a number of other background processes. These include $2\nu\beta\beta$ decay as well as cosmogenic isotopes created from the spallation of Te nuclei. Because the Q-value of $2\nu\beta\beta$ decay for ^{130}Te is 2.53 MeV, only a tiny fraction of those events should be expected to make it above this analysis' 2.5 MeV energy threshold. When the cuts described in Table 6.1 were run over the production of $2\nu\beta\beta$ MC made for the dataset used in the above analysis, no events survived. For the cosmogenics, assuming that the purification of the TeLS works as expected, less than one cosmogenic event of any kind is expected in the $0\nu\beta\beta$ ROI in a year [135]. Because of this, both of these additional backgrounds have been ignored for this scenario.

In the other background scenario, the external water backgrounds were set to the level measured by T. Zummo in the water phase, and the internal ^{208}Tl were

reduced by a factor of 10. This latter scenario reflects the possibility of better control of the radioactivity in the external water, as well as a way of using new analysis methods to cut out 90% of the internal ^{208}Tl events.

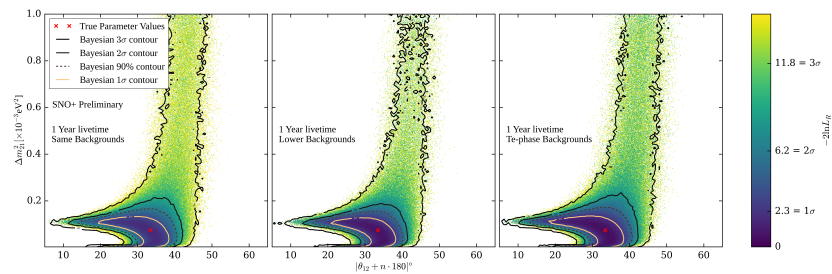
The results of running these two scenarios can be seen in Fig. 6.22. Unsurprisingly, the 1σ CI for θ_{12} is wider when backgrounds are greater, and thinner in the lower background scenario. However, the magnitudes of the change in width are somewhat different. For the high backgrounds case, the width only increases by 2%. This implies that the higher internal backgrounds expected during the Te phase should not, on their own, substantially hamper the sensitivity of the measurement of θ_{12} . With lower external water and internal ^{208}Tl backgrounds, it appears that sensitivity improvements $\mathcal{O}(10\%)$ are achievable. This is because, over 1 year of livetime, the statistical uncertainties present in the signal process still dominate.

6.4 Summary and Suggestions for Further Work

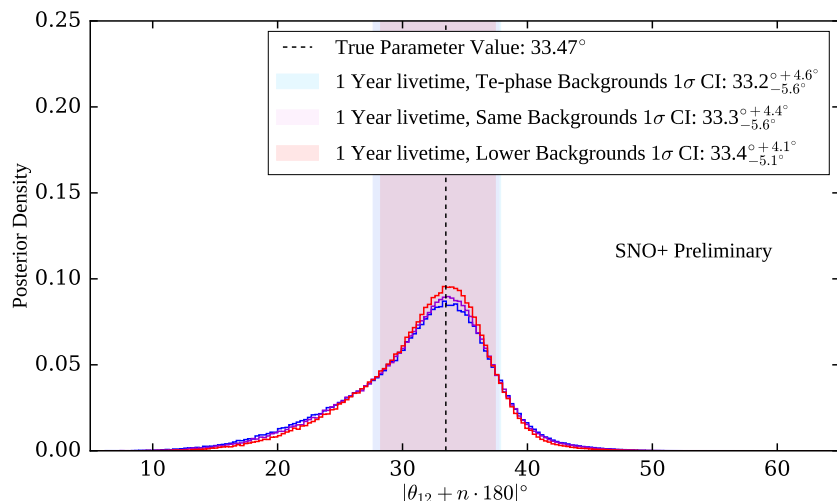
In this chapter, a full analysis for measuring the solar neutrino oscillation parameters via ^8B neutrinos was built and demonstrated on SNO+ scintillator-phase data. Using 80.6 days of livetime, assuming the global fit constraint on the ^8B flux of $\Phi_{^8\text{B}} = (5.16_{-1.7\%}^{+2.5\%}) \times 10^6 \text{ cm}^{-2} \text{ s}^{-1}$ [166], the oscillation parameter θ_{12} was measured to be $|\theta_{12} + n \cdot 180|^\circ = 38.9_{-7.9}^{+8.0}{}^\circ$.

Furthermore, assuming an identical analysis approach and similar detector conditions to those seen in the above dataset, the precision of this measurement is liable to improve by a factor of 2 in under 2 years of total livetime. This is partly because there become enough statistics to confidently reject large values of Δm_{21}^2 above $\sim 1.5 \times 10^{-4} \text{ eV}^2$.

Of course, major changes to the detector's scintillator cocktail are expected in that timeline. We have shown that the negative impacts expected from the



(a) Posterior densities marginalised onto the two oscillation parameters.

(b) Posterior densities marginalised onto θ_{12} .**Fig. 6.22:** Comparison of projections over 1 year of livetime, with different background expectations.

1 higher internal backgrounds of the Te-loaded phase should have minimal impact
2 on the sensitivity to the oscillation parameters over a livetime of 1 year. The
3 sensitivity obtained in this scenario is expected to be somewhat conservative, as the
4 scintillation emission time profile is expected to become substantially shorter [93],
5 leading to substantial improvements in the position resolution of the detector as
6 well as the discrimination power of various time-based classifiers.

7 If the external water backgrounds are able to return to the levels observed
8 during the water phase, and the event selection of internal ^{208}Tl events improves
9 substantially, there is some scope for improvement to the measurement of θ_{12}
10 when considering 1 year of livetime. There are three main possibilities for removal
11 of internal ^{208}Tl events. Firstly, these β -decays come as the delayed partner to
12 the α -decay branch of ^{214}Bi nuclei. Therefore, a coincidence tagging approach to
13 remove these events could be possible. Furthermore, alongside the β -decay of ^{208}Tl
14 are typically γ s, which should modify the observed time residual spectrum these
15 events compared to a single-site event like the signal process. As a result, creating
16 a custom multi-site classifier to exclude internal ^{208}Tl events from single-site
17 events could help further. Finally, solar neutrino and ^{208}Tl events can in theory
18 be distinguished by their direction. Via a method such as the one developed
19 in [91, 92], it might be possible to gain some discrimination power of the solar
20 signal over this background.

21 On the subject of classifiers, the choice of cuts used for the externals classifiers
22 were chosen to be deliberately conservative. By tuning those cuts, it is possible
23 that the sensitivity could be improved through the increased rejection of external
24 events. An even more sophisticated approach would be to include these classifiers
25 as dimensions of the PDFs. This method yielded substantial improvements in the
26 $0\nu\beta\beta$ study performed in [135].

27 Of course, what has been seen in this analysis is that the greatest barrier to
28 greater precision is simply the signal statistics. This is a function of exposure,

not just livetime. Therefore, substantial improvements are likely to be made by increasing the FV used for this analysis. For example, if the maximum radius used in this analysis was moved from 5.0 m out to 5.7 m, then the increased volume leads to an increased rate of signal events of 48%. Admittedly, for energies below ~ 3.0 MeV at larger radii we expect external backgrounds to completely dominate over the signal, so the benefits in the signal statistics will mostly be seen above 5 MeV.

Because the time of day impacts the extent to which solar neutrinos will be travelling through the Earth, there is expected to be some additional power in considering the difference between events observed during the day versus the night. This approach was used to boost the expected sensitivity for the solar oscillation analysis to be used on the JUNO experiment, for example [185, 186]. Also considered in that sensitivity study were additional interaction modes of solar neutrinos with a liquid scintillator, such as the CC interaction of ν_e on ^{13}C within the detector. These modes could provide further sensitivity.

Finally, analysis of neutrino oscillations from reactor anti-neutrinos in SNO+ is expected to lead to a world-leading limit of Δm_{21}^2 in under 4 years of livetime [90]. Although both analysis approaches have sensitivity to Δm_{21}^2 and θ_{12} , the reactor anti-neutrino method is more sensitive to Δm_{21}^2 whilst the solar analysis shown above is more sensitive to θ_{12} . Because of this complementarity, it is possible that a combined analysis using both types of oscillating neutrino signal incident on SNO+ will lead to even better measurements of both oscillation parameters.

Chapter 7

1

Conclusions

2

Say what has been achieved in this thesis! In particular:

3

- Substantial improvement to the SMELLIE generator in terms of speed and dynamic range 4
- A much stronger understanding of the discrepancies between data and MC in SMELLIE 6
- The creation of two analyses of SMELLIE data, designed explicitly around being robust to these systematics 7
- A measurement of the extinction length of scintillator *in-situ* with SMELLIE at 375 nm, monitored over time 9
- A first measurement of the scattering length of the scintillator *in-situ*, monitored over time 10
- The creation of an analysis of ^8B solar neutrinos in the scintillator phase to measure the solar neutrino oscillation parameters 11
- The first measurement of θ_{12} using ^8B neutrinos in SNO+ 12
- Projections of this solar analysis' precision at longer livetimes 13

14

15

16

17

¹ [3 PAGES TOTAL]

References

- [1] S. L. Glashow, Partial-symmetries of weak interactions, Nuclear Physics **22**, 579 (1961). 1
2
3
- [2] S. Weinberg, A Model of Leptons, Physical Review Letters **19**, 1264 (1967). 4
- [3] A. Salam, Weak and electromagnetic interactions, in *Selected Papers of Abdus Salam*, , World Scientific Series in 20th Century Physics Vol. Volume 5, pp. 244–254, WORLD SCIENTIFIC, 1994. 5
6
7
- [4] **UA1 Collaboration**, G. Arnison *et al.*, Experimental observation of isolated large transverse energy electrons with associated missing energy at s=540 GeV, Physics Letters B **122**, 103 (1983). 8
9
10
- [5] **UA2 Collaboration**, M. Banner *et al.*, Observation of single isolated electrons of high transverse momentum in events with missing transverse energy at the CERN pp collider, Physics Letters B **122**, 476 (1983). 11
12
13
- [6] **UA1 Collaboration**, G. Arnison *et al.*, Experimental observation of lepton pairs of invariant mass around 95 GeV/c² at the CERN SPS collider, Physics Letters B **126**, 398 (1983). 14
15
16
- [7] C. L. Cowan, F. Reines, F. B. Harrison, H. W. Kruse, and A. D. McGuire, Detection of the Free Neutrino: A Confirmation, Science **124**, 103 (1956). 17
18
- [8] F. Reines and C. L. Cowan, The Neutrino, Nature **178**, 446 (1956). 19
- [9] G. Danby *et al.*, Observation of High-Energy Neutrino Reactions and the Existence of Two Kinds of Neutrinos, Physical Review Letters **9**, 36 (1962). 20
21
- [10] **DONUT Collaboration**, K. Kodama *et al.*, Observation of tau neutrino interactions, Physics Letters B **504**, 218 (2001). 22
23
- [11] **Gargamelle Collaboration**, F. J. Hasert *et al.*, Observation of neutrino-like interactions without muon or electron in the Gargamelle neutrino experiment, PHYSICS LETTERS (1973). 24
25
26
- [12] **Gargamelle Collaboration**, F. Hasert *et al.*, Search for elastic muon-neutrino electron scattering, PHYSICS LETTERS **46** (1973). 27
28
- [13] **Gargamelle Collaboration**, F. J. Hasert *et al.*, Observation of neutrino-like interactions without muon or electron in the Gargamelle neutrino experiment, Nuclear Physics B **73**, 1 (1974). 29
30
31

- ¹ [14] **Gargamelle Collaboration**, J. Blietschau *et al.*, Evidence for the leptonic
² neutral current reaction $N\mu + e^- \rightarrow \nu\mu + e^-$, Nuclear Physics B **114**, 189 (1976).
- ³ [15] M. Goldhaber, L. Grodzins, and A. W. Sunyar, Helicity of Neutrinos,
⁴ Physical Review **109**, 1015 (1958).
- ⁵ [16] **The ALEPH, DELPHI, L3, OPAL and SLD Collaborations**, Precision
⁶ electroweak measurements on the Z resonance, Physics Reports **427**,
⁷ 257 (2006).
- ⁸ [17] P. Janot and S. Jadach, Improved Bhabha cross section at LEP and the
⁹ number of light neutrino species, Physics Letters B **803**, 135319 (2020).
- ¹⁰ [18] F. F. Deppisch, Chapter 2: Neutrinos in the Standard Model, in *A Modern*
¹¹ *Introduction to Neutrino Physics*, IOP Concise Physics, pp. 1–25, Morgan
¹² & Claypool Publishers, 2019.
- ¹³ [19] F. Englert and R. Brout, Broken Symmetry and the Mass of Gauge Vector
¹⁴ Mesons, Physical Review Letters **13**, 321 (1964).
- ¹⁵ [20] P. W. Higgs, Broken Symmetries and the Masses of Gauge Bosons, Physical
¹⁶ Review Letters **13**, 508 (1964).
- ¹⁷ [21] G. S. Guralnik, C. R. Hagen, and T. W. B. Kibble, Global Conservation
¹⁸ Laws and Massless Particles, Physical Review Letters **13**, 585 (1964).
- ¹⁹ [22] **ATLAS Collaboration**, G. Aad *et al.*, Observation of a new particle in
²⁰ the search for the Standard Model Higgs boson with the ATLAS detector
²¹ at the LHC, Physics Letters B **716**, 1 (2012).
- ²² [23] **CMS Collaboration**, S. Chatrchyan *et al.*, Observation of a new boson at
²³ a mass of 125 GeV with the CMS experiment at the LHC, Physics Letters
²⁴ B **716**, 30 (2012).
- ²⁵ [24] **Particle Data Group**, R. L. Workman *et al.*, Review of Particle Physics:
²⁶ Review 14 - Neutrino Masses, Mixing, and Oscillations, PTEP **2022**, 083C01
²⁷ (2022).
- ²⁸ [25] **KATRIN Collaboration**, M. Aker *et al.*, Direct neutrino-mass measurement
²⁹ with sub-electronvolt sensitivity, Nature Physics **18**, 160 (2022).
- ³⁰ [26] E. Di Valentino, S. Gariazzo, and O. Mena, Most constraining cosmological
³¹ neutrino mass bounds, Physical Review D **104**, 083504 (2021).
- ³² [27] J. N. Bahcall, *Neutrino Astrophysics* (Cambridge University Press, 1989).
- ³³ [28] **Borexino Collaboration**, M. Agostini *et al.*, Comprehensive measurement
³⁴ of pp-chain solar neutrinos, Nature **562**, 505 (2018).
- ³⁵ [29] W. T. Winter, S. J. Freedman, K. E. Rehm, and J. P. Schiffer, The B8
³⁶ Neutrino Spectrum, Physical Review C **73**, 025503 (2006), arxiv:nucl-
³⁷ ex/0406019.
- ³⁸ [30] N. Vinyoles, A. Serenelli, and F. L. Villante, The B16 Standard Solar
³⁹ Models, Journal of Physics: Conference Series **1056**, 012058 (2018).

-
- [31] N. Grevesse and A. Sauval, Standard Solar Composition, *Space Science Reviews* **85**, 161 (1998). 1
2
- [32] M. Asplund, N. Grevesse, A. J. Sauval, and P. Scott, The Chemical Composition of the Sun, *Annual Review of Astronomy and Astrophysics* **47**, 481 (2009). 3
4
5
- [33] R. Davis, D. S. Harmer, and K. C. Hoffman, Search for Neutrinos from the Sun, *Physical Review Letters* **20**, 1205 (1968). 6
7
- [34] B. T. Cleveland *et al.*, Measurement of the Solar Electron Neutrino Flux with the Homestake Chlorine Detector, *The Astrophysical Journal* **496**, 505 (1998). 8
9
10
- [35] C. Pena-Garay and A. Serenelli, Solar neutrinos and the solar composition problem, 2008, arxiv:0811.2424. 11
12
- [36] J. N. Abdurashitov *et al.*, Measurement of the solar neutrino capture rate with gallium metal. III. Results for the 2002–2007 data-taking period, *Physical Review C* **80**, 015807 (2009). 13
14
15
- [37] M. Altmann *et al.*, Complete results for five years of GNO solar neutrino observations, *Physics Letters B* **616**, 174 (2005). 16
17
- [38] J. N. Bahcall, M. Kamionkowski, and A. Sirlin, Solar neutrinos: Radiative corrections in neutrino-electron scattering experiments, *Physical Review D* **51**, 6146 (1995). 18
19
20
- [39] K. Abe *et al.*, Solar neutrino measurements in Super-Kamiokande-IV, *Physical Review D* **94**, 052010 (2016). 21
22
- [40] **SNO Collaboration**, J. Boger *et al.*, The Sudbury Neutrino Observatory, *Nuclear Instruments and Methods in Physics Research Section A* **449**, 172 (2000). 23
24
25
- [41] **SNO Collaboration**, B. Aharmim *et al.*, Electron energy spectra, fluxes, and day-night asymmetries of $\hat{8}$ B solar neutrinos from measurements with NaCl dissolved in the heavy-water detector at the Sudbury Neutrino Observatory, *Physical Review C* **72**, 055502 (2005). 26
27
28
29
- [42] **Super-Kamiokande Collaboration**, Y. Fukuda *et al.*, Evidence for Oscillation of Atmospheric Neutrinos, *Physical Review Letters* **81**, 1562 (1998). 30
31
32
- [43] **IMB Collaboration**, R. Becker-Szendy *et al.*, Electron- and muon-neutrino content of the atmospheric flux, *Physical Review D* **46**, 3720 (1992). 33
34
- [44] **Kamiokande Collaboration**, Y. Fukuda *et al.*, Atmospheric $\nu\mu/\nu e$ ratio in the multi-GeV energy range, *Physics Letters B* **335**, 237 (1994). 35
36
- [45] **Super-Kamiokande Collaboration**, Y. Ashie *et al.*, Evidence for an Oscillatory Signature in Atmospheric Neutrino Oscillations, *Physical Review Letters* **93**, 101801 (2004). 37
38
39

- [46] **LamLAND Collaboration**, A. Gando *et al.*, Reactor on-off antineutrino measurement with KamLAND, Physical Review D **88**, 033001 (2013).
- [47] **Daya Bay Collaboration**, D. Adey *et al.*, Measurement of the Electron Antineutrino Oscillation with 1958 Days of Operation at Daya Bay, Physical Review Letters **121**, 241805 (2018).
- [48] **T2K Collaboration**, K. Abe *et al.*, Improved constraints on neutrino mixing from the T2K experiment with 3.13×10^{21} protons on target, Physical Review D **103**, 112008 (2021).
- [49] **Double Chooz Collaboration**, H. de Kerret *et al.*, Double Chooz Θ_{13} measurement via total neutron capture detection, Nature Physics **16**, 558 (2020).
- [50] **RENO Collaboration**, G. Bak *et al.*, Measurement of Reactor Antineutrino Oscillation Amplitude and Frequency at RENO, Physical Review Letters **121**, 201801 (2018).
- [51] **NOvA Collaboration**, P. Adamson *et al.*, Constraints on Oscillation Parameters from ν_e Appearance and ν_μ Disappearance in NOvA, Physical Review Letters **118**, 231801 (2017).
- [52] **T2K Collaboration**, K. Abe *et al.*, Observation of Electron Neutrino Appearance in a Muon Neutrino Beam, Physical Review Letters **112**, 061802 (2014).
- [53] **NOvA Collaboration**, P. Adamson *et al.*, First Measurement of Electron Neutrino Appearance in NOvA, Physical Review Letters **116**, 151806 (2016).
- [54] **T2K Collaboration**, K. Abe *et al.*, Constraint on the matter–antimatter symmetry-violating phase in neutrino oscillations, Nature **580**, 339 (2020).
- [55] **NOvA Collaboration**, M. A. Acero *et al.*, First measurement of neutrino oscillation parameters using neutrinos and antineutrinos by NOvA, Physical Review Letters **123**, 151803 (2019).
- [56] **OPERA Collaboration**, N. Agafonova *et al.*, Final Results of the OPERA Experiment on $\nu\tau$ Appearance in the CNGS Neutrino Beam, Physical Review Letters **120**, 211801 (2018).
- [57] Z. Maki, M. Nakagawa, and S. Sakata, Remarks on the Unified Model of Elementary Particles, Progress of Theoretical Physics **28**, 870 (1962).
- [58] B. Pontecorvo, Neutrino Experiments and the Problem on Conservation of Leptonic Charge, Soviet Physics JETP **26**, 1717 (1968).
- [59] F. F. Deppisch, Chapter 3: Neutrino Oscillations, in *A Modern Introduction to Neutrino Physics*, IOP Concise Physics, pp. 1–27, Morgan & Claypool Publishers, 2019.
- [60] I. Esteban, M. Gonzalez-Garcia, M. Maltoni, T. Schwetz, and A. Zhou, The fate of hints: Updated global analysis of three-flavor neutrino oscillations, Journal of High Energy Physics **2020**, 178 (2020).

-
- [61] L. Wolfenstein, Neutrino oscillations in matter, Physical Review D **17**, 2369 (1978). 1
2
- [62] S. P. Mikheyev and A. Yu. Smirnov, Resonant amplification of ν oscillations in matter and solar-neutrino spectroscopy, Il Nuovo Cimento C **9**, 17 (1986). 3
4
- [63] C. Giunti and C. W. Kim, Chapter 9: Neutrino Oscillations in Matter, in *Fundamentals of Neutrino Physics and Astrophysics*, pp. 322–351, Oxford University Press, 2007. 5
6
7
- [64] C. Giunti and C. W. Kim, Chapter 13: Phenomenology of Three-Neutrino Mixing, in *Fundamentals of Neutrino Physics and Astrophysics*, pp. 452–483, Oxford University Press, 2007. 8
9
10
- [65] **LSND Collaboration**, A. Aguilar *et al.*, Evidence for neutrino oscillations from the observation of $\{\overline{\nu}_e\} \rightarrow \{e\}$ appearance in a $\{\overline{\nu}_\mu\} \rightarrow \{\nu_\mu\}$ beam, Physical Review D **64**, 112007 (2001). 11
12
13
14
- [66] **MiniBooNE Collaboration**, A. A. Aguilar-Arevalo *et al.*, Updated MiniBooNE neutrino oscillation results with increased data and new background studies, Physical Review D **103**, 052002 (2021). 15
16
17
- [67] **MicroBooNE Collaboration**, P. Abratenko *et al.*, First Constraints on Light Sterile Neutrino Oscillations from Combined Appearance and Disappearance Searches with the MicroBooNE Detector, Physical Review Letters **130**, 011801 (2023). 18
19
20
21
- [68] S. Weinberg, Baryon- and Lepton-Nonconserving Processes, Physical Review Letters **43**, 1566 (1979). 22
23
- [69] P. Minkowski, $M \rightarrow e\gamma$ at a rate of one out of 109 muon decays?, Physics Letters B **67**, 421 (1977). 24
25
- [70] E. Majorana, Teoria simmetrica dell'elettrone e del positrone, Il Nuovo Cimento (1924-1942) **14**, 171 (1937). 26
27
- [71] W. H. Furry, On Transition Probabilities in Double Beta-Disintegration, Physical Review **56**, 1184 (1939). 28
29
- [72] M. Goeppert-Mayer, Double Beta-Disintegration, Physical Review **48**, 512 (1935). 30
31
- [73] **CUORE Collaboration**, D. Q. Adams *et al.*, Measurement of the $2\nu\beta\beta$ Decay Half-Life of $\hat{^{130}\mathrm{Te}}$ with CUORE, Physical Review Letters **126**, 171801 (2021). 32
33
34
35
- [74] **GERDA Collaboration**, M. Agostini *et al.*, Results on $\beta\beta$ decay with emission of two neutrinos or Majorons in $^{76}\mathrm{Ge}$ from GERDA Phase I, The European Physical Journal C **75**, 416 (2015). 36
37
38

- [75] **KamLAND-Zen Collaboration**, A. Gando *et al.*, Precision Analysis of the $\hat{136}\mathrm{Xe}$ Two-Neutrino $\beta\beta$ Spectrum in KamLAND-Zen and Its Impact on the Quenching of Nuclear Matrix Elements, *Physical Review Letters* **122**, 192501 (2019).
- [76] **NEMO-3 Collaboration**, R. Arnold *et al.*, Measurement of the $2\nu\beta\beta$ decay half-life of $\hat{150}\mathrm{Nd}$ and a search for $0\nu\beta\beta$ decay processes with the full exposure from the NEMO-3 detector, *Physical Review D* **94**, 072003 (2016).
- [77] F. Kondev, Nuclear Data Sheets for $A = 206$, *Nuclear Data Sheets* **109**, 1527 (2008).
- [78] J. Schechter and J. W. F. Valle, Neutrinoless double- β decay in $SU(2) \times U(1)$ theories, *Physical Review D* **25**, 2951 (1982).
- [79] A. S. Inácio, *Data Analysis of the Water and Scintillator Phases of SNO+: From Solar Neutrino Measurements to Double Beta Decay Sensitivity Studies*, PhD thesis, Universidade de Lisboa, 2022.
- [80] M. Agostini *et al.*, Final Results of GERDA on the Search for Neutrinoless Double- β Decay, *Physical Review Letters* **125**, 252502 (2020).
- [81] **CUPID-Mo Collaboration**, E. Armengaud *et al.*, New Limit for Neutrinoless Double-Beta Decay of $\hat{100}\mathrm{Mo}$ from the CUPID-Mo Experiment, *Physical Review Letters* **126**, 181802 (2021).
- [82] **CUORE Collaboration**, D. Q. Adams *et al.*, Search for Majorana neutrinos exploiting millikelvin cryogenics with CUORE, *Nature* **604**, 53 (2022).
- [83] **KamLAND-Zen Collaboration**, S. Abe *et al.*, Search for the Majorana Nature of Neutrinos in the Inverted Mass Ordering Region with KamLAND-Zen, *Physical Review Letters* **130**, 051801 (2023).
- [84] **SNO+ Collaboration**, V. Albanese *et al.*, The SNO+ experiment, *Journal of Instrumentation* **16**, P08059 (2021).
- [85] **SNO+ Collaboration**, M. Anderson *et al.*, Optical calibration of the SNO+ detector in the water phase with deployed sources, *Journal of Instrumentation* **16**, P10021 (2021).
- [86] **SNO+ Collaboration**, M. Anderson *et al.*, Measurement of the B 8 solar neutrino flux in SNO+ with very low backgrounds, *Physical Review D* **99**, 012012 (2019).
- [87] **SNO+ Collaboration**, A. Allega *et al.*, Evidence of Antineutrinos from Distant Reactors using Pure Water at SNO+, *Physical Review Letters* **130**, 091801 (2023), arxiv:2210.14154.

- [88] **SNO+ Collaboration**, M. Anderson *et al.*, Search for invisible modes of nucleon decay in water with the SNO+ detector, Physical Review D **99**, 032008 (2019). 1
2
3
- [89] **SNO+ Collaboration**, A. Allega *et al.*, Improved search for invisible modes of nucleon decay in water with the SNO+ detector, Physical Review D **105**, 112012 (2022), arxiv:2205.06400. 4
5
6
- [90] I. Morton-Blake, *First Measurement of Reactor Antineutrinos in Scintillator at SNO+ and Study of Alternative Designs for Large-Scale Liquid Scintillator Detectors*, DPhil Thesis, University of Oxford, 2021. 7
8
9
- [91] SNO+ Collaboration, A. Allega *et al.*, Event-by-Event Direction Reconstruction of Solar Neutrinos in a High Light-Yield Liquid Scintillator, 2023, arxiv:2309.06341. 10
11
12
- [92] J. Paton, *Directional Reconstruction in Liquid Scintillator Neutrino Detectors*, DPhil Thesis, in preparation, University of Oxford, 2023. 13
14
- [93] D. J. Auty *et al.*, A Method to Load Tellurium in Liquid Scintillator for the Study of Neutrinoless Double Beta Decay, Nuclear Instruments and Methods in Physics Research Section A **1051**, 168204 (2023), arxiv:2212.12444. 15
16
17
- [94] I. Frank and Ig. Tamm, Coherent visible radiation of fast electrons passing through matter, Compt. Rend. Acad. Sci. URSS **14**, 109 (1937). 18
19
- [95] T. Kaptanoglu, L. Segui, A. Mastbaum, N. Barros, and I. T. Coulter, Optics Overview and Proposed Changes to RAT, 2016, SNO+ Internal Document DocDB #3461. 20
21
22
- [96] T. Kaptanoglu, Documentation for Attenuation Studies, 2022, SNO+ Internal Document DocDB #7608. 23
24
- [97] J. B. Birks, Chapter 3: The Scintillation Process in Organic Materials I, in *The Theory and Practice of Scintillation Counting*, pp. 39–67, Pergamon Press, , 2nd ed., 1967. 25
26
27
- [98] R. Hunt-Stokes, Emission Timing Tuning - 2.2 g / L Optical Model, 2022, SNO+ Internal Document DocDB #7621. 28
29
- [99] A. LaTorre, New Measurements for the Timing Spectrum of Electrons and Alphas in LAB+PPO, 2016, SNO+ Internal Document DocDB #4081. 30
31
- [100] J. B. Birks, Chapter 6: The Scintillation Process in Organic Materials II, in *The Theory and Practice of Scintillation Counting*, pp. 185–234, Pergamon Press, , 2nd ed., 1967. 32
33
34
- [101] S. Riccetto, RAT optics 2.2g/L - after CM_Aug2022, 2022, SNO+ Internal Document DocDB #7571. 35
36
- [102] G. Mie, Contributions to the Optics of Turbid Media, particularly of Colloidal Metal Solutions, Annalen der Physik **25**, 377 (1908). 37
38
- [103] L. Lorenz, Sur la lumière réfléchie et réfractée par une sphère (surface) transparente, Oeuvres scientifiques de L. Lorenz , 403 (1898). 39
40

- ¹ [104] H. C. van de Hulst, *Light Scattering by Small Particles* Structure of Matter Series (Dover Publications, New York, 1981).
- ³ [105] L. Rayleigh, On the transmission of light through an atmosphere containing small particles in suspension, and on the origin of the blue of the sky, The London, Edinburgh, and Dublin Philosophical Magazine and Journal of Science **47**, 375 (1899).
- ⁷ [106] J. D. Jackson, Section 10.1: Scattering at Long Wavelengths, in *Classical Electrodynamics*, Wiley, , 3rd ed., 1998.
- ⁹ [107] X. Zhou *et al.*, Rayleigh scattering of linear alkylbenzene in large liquid scintillator detectors, Review of Scientific Instruments **86**, 073310 (2015), arxiv:1504.00987.
- ¹² [108] N. G. Jerlov and E. S. Nielsen, *Optical Aspects of Oceanography : [Collection of the Papers Presented at the Symposium on Optical Aspects of Oceanography ... Held at the Institute of Physical Oceanography in Copenhagen, 19th-23rd June 1972]* (Academic Press / Symposium on Optical Aspects of Oceanography (1972 : Copenhagen), London ; New York, 1974).
- ¹⁷ [109] A. Einstein, Theory of Opalescence of Homogeneous Fluids and Liquid Mixtures near the Critical State, Annalen der Physik **338**, 1275 (1910).
- ¹⁹ [110] M. S. Smoluchowski, Molecular kinetic theory of gases in critical opalescence state, as well as some related phenomena, Annalen der Physik , 205 (1908).
- ²¹ [111] J. Cabannes, Relationship between the degree of Polarisation and the intensity of light Scattered by anisotropic molecules. New determination of the Avogadro constant, Journal de Physique et Le Radium **1**, 129 (1920).
- ²⁴ [112] J. F. Eykman, Recherches réfractométriques (suite), Recueil des Travaux Chimiques des Pays-Bas **14**, 185 (1895).
- ²⁶ [113] B. Moffat, *The Optical Calibration of the Sudbury Neutrino Observatory*, PhD thesis, Queen's University, Kingston, Canada, 2001.
- ²⁸ [114] E. Turner, *A Measurement of Scattering Characteristics of the Detection Medium in the SNO+ Detector*, DPhil Thesis, University of Oxford, 2022.
- ³⁰ [115] M. Chen and I. T. Coulter, Optical properties in RAT, 2012, SNO+ Internal Document DocDB #1664.
- ³² [116] L. Segui, Scintillator Model: Comparison between new data and old model and its performance in RAT, 2015, SNO+ Internal Document DocDB #2774.
- ³⁵ [117] Y. Liu, Attenuation and Scattering of TeBD and the Cocktail, 2016, SNO+ Internal Document DocDB #3880.
- ³⁷ [118] Q. Liu *et al.*, Rayleigh scattering and depolarization ratio in linear alkylbenzene, Nuclear Instruments and Methods in Physics Research Section A: Accelerators, Spectrometers, Detectors and Associated Equipment **795**, 284 (2015).

-
- [119] M. Yu *et al.*, Measurements of Rayleigh Ratios in Linear Alkylbenzene, arXiv:2203.03126 [hep-ex, physics:physics] (2022), arxiv:2203.03126. 1
2
- [120] R. Boardman, *The Detection of Cherenkov Radiation from Neutrino Interactions*, DPhil Thesis, University of Oxford, 1992. 3
4
- [121] H. W. C. Tseung and N. Tolich, Ellipsometric measurements of the refractive indices of linear alkylbenzene and EJ-301 scintillators from 210 to 1000 nm, *Physica Scripta* **84**, 035701 (2011), arxiv:1105.2101. 5
6
7
- [122] E. Hecht, Section 4.6.2: The Fresnel Equations, in *Optics*, Pearson, , 4th ed., 2014. 8
9
- [123] M. E. Moorhead, *Reflectors in Cherenkov Detectors*, DPhil Thesis, University of Oxford, 1992. 10
11
- [124] S. D. Biller, N. A. Jelley, M. D. Thorman, N. P. Fox, and T. H. Ward, Measurements of photomultiplier single photon counting efficiency for the Sudbury Neutrino Observatory, (1999). 12
13
14
- [125] J. Dunger and E. Turner, Occupancy Analysis for Multiple-Hit Corrections in Large Scintillation Detectors, 2016, NuPhys 2016 poster; SNO+ Internal Document DocDB #4107. 15
16
17
- [126] M. Howe *et al.*, Sudbury neutrino observatory neutral current detector acquisition software overview, *IEEE Transactions on Nuclear Science* **51**, 878 (2004). 18
19
20
- [127] J. C. Loach, *Measurement of the Flux of 8B Solar Neutrinos at the Sudbury Neutrino Observatory*, DPhil Thesis, University of Oxford, 2008. 21
22
- [128] M. Dragowsky *et al.*, The 16N calibration source for the Sudbury Neutrino Observatory, *Nuclear Instruments and Methods in Physics Research Section A: Accelerators, Spectrometers, Detectors and Associated Equipment* **481**, 284 (2002). 23
24
25
26
- [129] S. Valder *et al.*, A Laserball Calibration Device for the SNO+ Scintillator Phase, in preparation. 27
28
- [130] P. G. Jones, *Background Rejection for the Neutrinoless Double Beta Decay Experiment SNO+*, DPhil Thesis, University of Oxford, 2011. 29
30
- [131] I. T. Coulter, *Modelling and Reconstruction of Events in SNO+ Related to Future Searches for Lepton and Baryon Number Violation*, DPhil Thesis, University of Oxford, 2013. 31
32
33
- [132] W. Parker, MultiPDF Method for Position Reconstruction, 2021, SNO+ Internal Document DocDB #7257. 34
35
- [133] W. Parker, Recoordinating ScintEffectiveSpeed & MultiPDF with Updated 2.2 g/l Optics, 2023, SNO+ Internal Document DocDB #7636. 36
37
- [134] M. Mottram, Updated functional form energy reconstruction: EnergyR-ThetaFunctional, 2015, SNO+ Internal Document DocDB #3488. 38
39

- ¹ [135] T. Kroupová, *Improving the Sensitivity to Neutrinoless Double Beta Decay in SNO+*, DPhil Thesis, University of Oxford, 2020.
- ³ [136] J. R. Sinclair, *Positioning and Timing Calibration of SNO+*, PhD thesis, University of Sussex, 2015.
- ⁵ [137] K. Majumdar, *On the Measurement of Optical Scattering and Studies of Background Rejection in the SNO+ Detector*, DPhil Thesis, University of Oxford, 2015.
- ⁸ [138] L. Cavalli *et al.*, The SMELLIE Hardware Manual, 2016, SNO+ Internal Document DocDB #3511.
- ¹⁰ [139] S. Langrock, *Measurement of the Rayleigh Scattering Length and Background Contributions during Early Data Taking Phases at SNO+*, PhD thesis, Queen Mary, University of London, 2016.
- ¹³ [140] J. Lidgard, Supercontinuum addition to SMELLIE.RATDB, 2018, SNO+ Internal Document DocDB #4816.
- ¹⁵ [141] D. Fibreoptics, 30dB Precision Variable Attenuator Specifications, 2017, URL: <https://www.diconfiberoptics.com/products/scd0069/SCD-0069C.pdf>, accessed 28/07/2023.
- ¹⁸ [142] Corning, Corning Infinicor 50 Mm Optical Fibres Product Information, 2007, URL: <http://www.princtel.com/datasheets/Infinicor50.pdf>, accessed 28/07/2023.
- ²¹ [143] K. J. Clark, ELLIE Fibre Radioactivity, 2011, SNO+ Internal Document DocDB #1223.
- ²³ [144] C. Jones, *Future Searches for Rare Astrophysical Signals and Detector Commissioning in SNO+*, DPhil Thesis, University of Oxford, 2016.
- ²⁵ [145] S. S. Wilks, The Large-Sample Distribution of the Likelihood Ratio for Testing Composite Hypotheses, *The Annals of Mathematical Statistics* **9**, 60 (1938).
- ²⁸ [146] **SNO+ Collaboration**, M. Anderson *et al.*, Development, characterisation, and deployment of the SNO+ liquid scintillator, *Journal of Instrumentation* **16**, P05009 (2021).
- ³¹ [147] B. Tam, Benchtop Attenuation Measurements, 2022, SNO+ Internal Document DocDB #7448.
- ³³ [148] S. Riccetto, Full Fill 210 NHits and Radial Profile, 2022, SNO+ Internal Document DocDB #7489.
- ³⁵ [149] P. Khaghani, Neck sense rope system and leaching studies for SNO+, Master's thesis, Laurentian University of Sudbury, 2015.
- ³⁷ [150] P. Khaghani, *16N Calibration and Background Studies for SNO+*, PhD thesis, Laurentian University of Sudbury, 2022.

-
- [151] B. Tam, Attenuation Measurements, 2022, SNO+ Internal Document DocDB #7481. 1
2
- [152] J. Caravaca, SNO+ Sensitivity to Standard Solar Neutrino Oscillations, 3
2020. 4
- [153] J. Dunger, *Topological and Time Based Event Classification for Neutrinoless Double Beta Decay in Liquid Scintillator*, DPhil Thesis, University of Oxford, 5
2018. 6
7
- [154] J. R. Wilson, BiPo Rejection Factors Summary, 2017, SNO+ Internal Document DocDB #4183. 8
9
- [155] R. Hunt-Stokes, Uranium and Thorium Background Analysis, 2022, SNO+ Internal Document DocDB #7664. 10
11
- [156] E. Marzec, BiPo Event Reduction using Likelihood Ratio Cut, 2013, SNO+ Internal Document DocDB #1994. 12
13
- [157] Z. Ye, Tagging in-window BiPo events with AlphaBetaClassifier – Recoordinated for 2.2 g/L LABPPO new optics, 2022, SNO+ Internal Document DocDB #7659. 14
15
16
- [158] **SNO+ Collaboration**, S. Andringa *et al.*, Current Status and Future Prospects of the SNO+ Experiment, Advances in High Energy Physics **2016**, 1 (2016). 17
18
19
- [159] W. Feller, *An Introduction to Probability Theory and Its Applications* Wiley Series in Probability and Mathematical Statistics. Probability and Mathematical Statistics, 3rd ed., rev. printing. ed. (Wiley, New York ; Chichester, 1968). 20
21
22
23
- [160] S. D. Biller and S. M. Oser, Another look at confidence intervals: Proposal for a more relevant and transparent approach, Nuclear Instruments and Methods in Physics Research Section A: Accelerators, Spectrometers, Detectors and Associated Equipment **774**, 103 (2015). 24
25
26
27
- [161] C. Sanderson and R. Curtin, Armadillo: A template-based C++ library for linear algebra, Journal of Open Source Software **1**, 26 (2016). 28
29
- [162] C. Sanderson and R. Curtin, A User-Friendly Hybrid Sparse Matrix Class in C++, in *Mathematical Software – ICMS 2018*, edited by J. H. Davenport, M. Kauers, G. Labahn, and J. Urban, Lecture Notes in Computer Science, pp. 422–430, Cham, 2018, Springer International Publishing. 30
31
32
33
34
- [163] N. Barros, *Precision Measurement of Neutrino Oscillation Parameters: Combined Three-Phase Results of the Sudbury Neutrino Observatory*, PhD thesis, Universidade de Lisboa, 2011. 35
36
37
- [164] A. M. Dziewonski and D. L. Anderson, Preliminary reference Earth model, Physics of the Earth and Planetary Interiors **25**, 297 (1981). 38
39

- ¹ [165] D. Cookman, Solar Oscillation Analysis Update, 2023, SNO+ Internal
² Document DocDB #7707.
- ³ [166] J. Bergström *et al.*, Updated determination of the solar neutrino fluxes from
⁴ solar neutrino data, Journal of High Energy Physics **2016**, 132 (2016).
- ⁵ [167] M.-P. Lebeuf, LAB Certificate of Analysis, 2020, Example of document
⁶ provided by CEPSA for each tanker of LAB used to fill SNO+. SNO+
⁷ Internal Document DocDB #7572.
- ⁸ [168] J. Caravaca, Validation of SNO+ Production Signal, 2019, SNO+ Internal
⁹ Document DocDB #5519.
- ¹⁰ [169] R. Hunt-Stokes, Private Communication, 2023.
- ¹¹ [170] J. D. Wilson, Thermally-driven scintillator flow in the SNO+ neutrino
¹² detector, Nuclear Instruments and Methods in Physics Research Section
¹³ A: Accelerators, Spectrometers, Detectors and Associated Equipment **1055**,
¹⁴ 168430 (2023).
- ¹⁵ [171] M. J. Martin, Nuclear Data Sheets for $A = 208$, Nuclear Data Sheets **108**,
¹⁶ 1583 (2007).
- ¹⁷ [172] M. Shamsuzzoha Basunia, Nuclear Data Sheets for $A = 210$, Nuclear Data
¹⁸ Sheets **121**, 561 (2014).
- ¹⁹ [173] S. Riccetto, Private Communication, 2023.
- ²⁰ [174] S. Riccetto, Full Fill Internal Po-210 Collaboration Meeting Update, 2023,
²¹ SNO+ Internal Document DocDB #7733.
- ²² [175] V. Lozza and O. Chkvorets, Neutron sources and backgrounds in SNO+,
²³ 2015, SNO+ Internal Document DocDB #2497.
- ²⁴ [176] S. Yu, AV Surface Po210 Analysis, 2023, SNO+ Internal Document DocDB
²⁵ #7733.
- ²⁶ [177] A. Zummo, External Background Box Analysis Plot/Results, 2022, SNO+
²⁷ Internal Document DocDB #7329.
- ²⁸ [178] T. Kaptanoglu, First look at external backgrounds in the scintillator phase,
²⁹ 2023, SNO+ Internal Document DocDB #7817.
- ³⁰ [179] M. J. Berger *et al.*, XCOM: Photon Cross Sections Database, NIST (2009).
- ³¹ [180] W. J. Heintzelman, Survival to Radii Inside the PSUP of Γ s from PMT β - γ
³² Events, 2012, SNO+ Internal Document DocDB #1729.
- ³³ [181] W. J. Heintzelman, Angular distribution of surviving Γ s from PMT β - γ
³⁴ events, 2013, SNO+ Internal Document DocDB #1712.
- ³⁵ [182] A. S. Inácio, Using a Smaller Shell when Simulating Bi214 and Tl208 in the
³⁶ External Water and Ropes, 2019, SNO+ Internal Document DocDB #5154.

-
- [183] A. Gelman *et al.*, Chapter: 11: Basics of Markov chain simulation, in *Bayesian Data Analysis*, , 3 ed., 2013. 1
2
 - [184] G. Cowan, K. Cranmer, E. Gross, and O. Vitells, Asymptotic formulae for likelihood-based tests of new physics, *The European Physical Journal C* **71**, 1554 (2011), arxiv:1007.1727. 3
4
5
 - [185] JUNO Collaboration, A. Abusleme *et al.*, Feasibility and physics potential of detecting 8B solar neutrinos at JUNO, 2020, arxiv:2006.11760. 6
7
 - [186] JUNO Collaboration, J. Zhao *et al.*, Model Independent Approach of the JUNO 8B Solar Neutrino Program, 2022, arxiv:2210.08437. 8
9